

Dynamics and Force Generation of  
Flagellum and Pili in  
*Caulobacter crescentus*

**Inauguraldissertation**

zur

Erlangung der Würde eines Doktors der Philosophie

vorgelegt der

Philosophisch-Naturwissenschaftlichen Fakultät

der Universität Basel

von

**Nora Sauter**

aus Kradolf-Schönenberg TG, Schweiz

Basel, 2019

Originaldokument gespeichert auf dem Dokumentenserver der Universität Basel

[edoc.unibas.ch](http://edoc.unibas.ch)

Genehmigt von der Philosophisch-Naturwissenschaftlichen Fakultät auf  
Antrag von:

**Prof. Dr. Urs Jenal**

**Dr. Thomas Pfohl**

**Dr. Thomas Braun**

Basel, den 22.05.2018

**Prof. Dr. Martin Spiess**

Dekan

## ABSTRACT

---

Surface attachment of bacteria is the first step of biofilm formation and biofilms are associated with infections and bacterial resistance. Surface attachment of bacteria is often mediated by extracellular appendages, for example flagellum and pili. The flagellum is a cork-screw like structure used for swimming and surface sensing. Pili are filamentous structures and have a wide variety of functions, among them attachment on surfaces. Because of the small diameter of flagellum and pili, direct observations of flagellum and pili are challenging under physiological conditions. *C. crescentus*, a model organism for biofilm formation, has an asymmetric life cycle. The sessile and stalked mother cell produces a motile daughter cell that is equipped with a flagellum and pili at the free pole.

In this work we investigated the dynamics and force generation of the flagellum and pili of *C. crescentus* under physiological conditions employing a label-free method. We built an optical tweezers set-up, combined it with a light microscope and took advantage of *C. crescentus* ability to attach to nearly any surface. For parallel imaging and force measurements *C. crescentus* cells were attached onto polystyrene beads and the beads were held in the optical tweezers in a microfluidic channel. The impact of the flagellum and the pili could be directly observed and analyzed.

We found that the rotation of the flagellum already starts 3 - 4 minutes before cell separation is completed and the daughter cell is released from the mother cell. The flagellum is fully assembled before the immediate onset of the rotation and switches its rotation direction approximately every second. A rough 2/3 to 1/3 distribution of clockwise and counterclockwise rotation direction of the flagellum is reflected in the fraction of cells that are released from the mother cell swimming forward, respectively backwards. The flagellum generates on average a force of roughly 1.0 pN, but peak forces up to 1.5 pN were measured in the optical tweezers. The forces generated by the flagellum are strong enough to induce a bending-motion of the surface attached predivisional cell. Just a few seconds before cell separation, the daughter cell starts to rotate around its long axis, while still connected to the mother cell. This change in the flagellum-induced motion is due to the progression of cell separation. After the completed separation of the rigid peptidoglycan layer the daughter cell is only softly connected to the mother cell via the outer membrane. The torque induced by the flagellum is now causing the daughter cell to rotate. The two cells separate when the separation of the outer membrane is completed.

Moreover, we found that pili activity in the predivisional cell starts roughly one minute before the completion of cell separation. With measurements in microfluidic flow channels and in the optical tweezers, we confirmed that the pili of *C. crescentus* are dynamic, they can attach to surface, retract, and release. The retraction speed, net displacement and attachment duration of the pili are load dependent, a larger load decreases retraction speed, displacement, and attachment duration. Pili can exert a force of up to 8 pN, but the average force of an individual pilus is roughly 2 pN. Even in presence of the rotating flagellum pili are capable of surface attachment and keeping the cell in position. The rotating flagellum decreases the attachment duration of single pili, probably because of the additional hydrodynamic load induced by the flagellum. Interestingly, the rotating flagellum increases the attachment rate of pili. The rotation of the flagellum brings the piliated pole of the predivisional cell closer to the surface, thereby facilitating attachment of the pili. Several cycles of pili attachment and release are possible before cell separation is completed. In between the attachment of individual pili, the cell performs a purely flagellum induced gyrational motion in the optical tweezers. Together with the finding that the release of a pilus is roughly 10x faster than retraction, this observation strongly encourages a release-model of the pilus where release is achieved by detachment or breakage of the pilus.

# CONTENTS

---

<b>1</b>	<b>INTRODUCTION</b>	<b>1</b>
1.1	Motility at low Reynolds Numbers	2
1.2	<i>Caulobacter Crescentus</i>	2
1.3	Optical Trapping	7
<b>2</b>	<b>MICROSCOPE AND OPTICAL TWEEZERS SET-UP</b>	<b>10</b>
2.1	Microscope Set-up	10
2.2	Optical Tweezers Set-up	11
2.3	Considerations for Choosing the Objective	14
2.4	Considerations for Choosing the Trapping Laser	14
2.5	Calibration of the Optical Tweezers	15
<b>3</b>	<b>MATERIALS AND METHODS</b>	<b>18</b>
3.1	Microfluidic Fabrication	18
3.2	Cell Culturing	20
3.3	Image Analysis	25
<b>4</b>	<b>FLAGELLUM DYNAMICS DURING CELL SEPARATION</b>	<b>27</b>
4.1	Abstract	27
4.2	Introduction	28
4.3	Materials and Methods	32
4.4	Results	35
4.5	Discussion	58
<b>5</b>	<b>DYNAMIC ROLE OF TAD PILI IN CAULOBACTER CRESCENTUS SURFACE COLONIZATION.</b>	<b>64</b>
5.1	Abstract	65
5.2	Introduction	66

5.3	Results	69
5.4	Discussion	83
5.5	Methods	85
5.6	Acknowledgements	88
5.7	Supplemental Figures	89
<b>6</b>	<b>INTERPLAY OF PILI AND FLAGELLUM DURING CELL SEPARATION</b>	<b>95</b>
6.1	Abstract	95
6.2	Introduction	96
6.3	Materials and Methods	98
6.4	Results	100
6.5	Discussion	112
<b>7</b>	<b>LIVE CELL X-RAY IMAGING OF AUTOPHAGIC VACUOLES FORMATION AND CHROMATIN DYNAMICS IN FISSION YEAST</b>	<b>114</b>
7.1	Abstract	115
7.2	Introduction	116
7.3	Results	117
7.4	Conclusions	123
7.5	Acknowledgements	124
7.6	Author contributions	124
7.7	Additional Information	124
7.8	Methods	125
7.9	References	128
<b>8</b>	<b>CONCLUSION</b>	<b>131</b>
<b>9</b>	<b>REFERENCES</b>	<b>134</b>
<b>10</b>	<b>ACKNOWLEDGMENTS</b>	<b>142</b>

<b>11 APPENDIX</b>	<b>143</b>
11.1 Media	143
11.2 Matlab Scripts	144



# 1 INTRODUCTION

---

Microbial cells are found in almost every environment on earth<sup>1</sup>. Their adaptation to nearly every niche has led to an abundant number of different microbial strains. Microbes are heavily involved in forming the biosphere of earth. Without microbes, the growth of plants would not be possible, plants and microbes influence each other and are interdependent<sup>2</sup>. For example, the ever so important nitrogen fixation from air that enables plant growth, is enabled by bacterial cells<sup>3</sup>. Likewise, microbes can also have a negative impact on plants, leading for example to losses in food harvest<sup>4</sup>. Microbes do not only colonize plants, but also all animals, including humans. Microbes can live in symbiosis with the animal or human host, affecting the metabolism and immune system positively<sup>5</sup>. A vast number of microbial cells from different strains is colonizing the human gut, the aggregation of all the microbes together is called the human microbiome. The microbes in the microbiome extract energy from otherwise indigestible polysaccharides, enabling the host to access these calories as well<sup>6</sup>. Microbial cells can also act as pathogens, colonizing the host and leading to infections and other diseases. For host infection, many species require the assistance of specialized surface structures, for example flagellum and pili in bacterial cells. Among other functions they enable surface attachment and motility of bacterial cells. Upon surface contact, many bacterial cells undergo a transformation from motile cells to sessile cells. They form biofilms, communities of microorganisms attached to surfaces and are protected by a layer of extracellular polymers. Biofilms are found on nearly any surfaces that are exposed to aqueous solutions or high humidity. They can be formed by a single species or contain a wide variety of different microorganisms. Bacterial biofilms are a source of infection<sup>7</sup> and are associated with increased bacterial resistance<sup>8</sup>. Because of the importance of microbes in our lives a thorough understanding of microbes is essential. The study of initial bacterial attachment on surfaces is of special interest to prevent biofilm formation. Most of the processes involved in microbial growth are dynamic at various time and length scales. To study the dynamic processes, techniques that allow real time imaging of the processes are required. Ideally these techniques enable the imaging of the microbes in their physiological environment, without the need of fixation or labelling of the sample and without inducing damage to the cells, for example by radiation or heat.

Here we studied the dynamics and force generation of pili and the flagellum of a bacterial cell under physiological conditions using microfluidics and different label-free methods. We also present a method that allows label-free visualization of chromatin oscillations in fission yeast<sup>9</sup>.

## 1.1 MOTILITY AT LOW REYNOLDS NUMBERS

A vast variety of microbes lives in aqueous environments and they have developed means of motility. Motility allows the microbes to actively colonize new environments and move into more favorable habitats. The means of motility for microbes differ significantly to the means employed in the macroscopic world because microbes live in a low Reynolds number regime. The Reynolds number gives the ratio of inertial forces to viscous forces and is defined as:

$$Re = \frac{f_i}{f_v} = \frac{v \cdot l \cdot \rho}{\eta} \quad (1.1)$$

With  $v$  the typical velocity,  $l$  the typical length scale,  $\rho$  the density and  $\eta$  the viscosity of the fluid.

For a bacterium swimming at  $30 \mu\text{m/s}$  and with a length of  $2 \mu\text{m}$  (in water:  $\rho = 10^3 \frac{\text{kg}}{\text{m}^3}$  and  $\eta = 0.001 \frac{\text{Pa}}{\text{s}}$ ) the Reynolds number is  $Re = \frac{30 \frac{\mu\text{m}}{\text{s}} \cdot 2 \mu\text{m} \cdot 10^3 \frac{\text{kg}}{\text{m}^3}}{0.001 \frac{\text{Pa}}{\text{s}}} = 6 \cdot 10^{-5}$ .

For comparison, the Reynolds number is  $\sim 10^5$  for humans. At the low Reynolds number of bacteria and other microorganisms, viscous forces dominate<sup>10</sup>. Because of the lack of inertial forces, swimming with a reciprocal motion does not lead to a net displacement of the swimmer. Displacement of the swimmer can only be achieved by a non-reciprocal swimming movement. For example the rotation of one or several cork-screw-like structures located at the outside of the cell wall<sup>11</sup>. The cork screw like structure is called flagellum and is a common way of swimming employed by microbes<sup>12,13</sup>. The lack of inertial forces also leads to an immediate stop of the moving microorganism when the rotation of the flagellum is stopped.

## 1.2 CAULOBACTER CRESCENTUS

The gram-negative *alphaproteobacterium* *Caulobacter crescentus* (*C. crescentus*) belongs to the genus of *Caulobacter* and was first described in 1935<sup>14</sup>. It is ubiquitously found in fresh water and is adapted to very nutrient scarce environments<sup>15</sup>. The origin of *C. crescentus* name comes from its characteristic curved shape. The shape is formed by a cytoskeleton like protein, crescentin<sup>16-19</sup>. *C. crescentus* divides asymmetrically and is therefore a widely used model organism for studying cellular differentiation and development. The freshly formed daughter cells can be divided from the mother cells by density centrifugation<sup>20</sup>, leading to a synchronized cell cycles on a population level. This allows the study of the progressing cell cycle in a precise time dependent manner.

### 1.2.1 Life cycle

*C. crescentus* has an asymmetric life cycle. The freshly formed daughter cell is a replication inert, motile swarmer cell (Figure 1.1A). In this stage the cell is equipped with a flagellum (orange) for motility and pili (blueish) for reversibly attaching to surfaces (B). The pili and the flagellum are located at the same pole. Upon surface contact or after a defined period of time, the flagellum and the pili are shed and the formation of a holdfast is initiated at the same pole (C). This attaches the cell irreversibly to the surface (D). The cell starts growing a stalk and becomes replication competent (E). DNA replication is initiated and a new daughter cell is formed at the pole opposite of the stalk<sup>21</sup> (F). The predivisional daughter cell is already equipped with a flagellum and pili at the pole opposite of the stalk before the cell separate (G). After completion of cell separation, the daughter cell is released as a replication inert, motile swarmer cell (H).

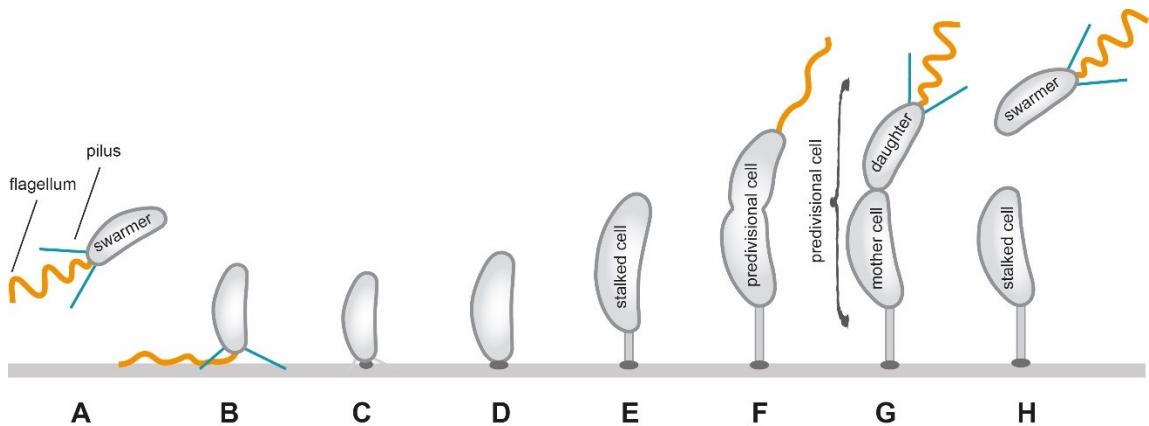


**Figure 1.1: Cell cycle of *C. crescentus*.** The life cycle of a *C. crescentus* cell starts as a replication inert swarmer cell. It is equipped with a flagellum (orange) and pili (blueish). After a defined period of time or when the cell contacts a surface, it sheds its pili and flagellum and instead forms a holdfast for surface attachment. Subsequently the stalk is formed. The cell transits from a replication inert cell into a replication competent stalked cell and produces a new swarmer cell at the pole opposite of the stalk. The motile swarmer cell is again equipped with pili and a flagellum, while the stalked cell remains attached to the surface.

When the predivisional daughter cell encounters a surface while still attached to the mother, it can also already form a holdfast. This process irreversibly attaches the daughter cell to a site in close proximity to its mother cell even before cell separation is completed (not shown in the figure, discussed more in detail in Chapter 6)<sup>22</sup>. The characteristic curved shape of the cells facilitates surface contact of the predivisional daughter cell and therefore supports surface colonization<sup>23</sup>. After cell division, the stalked mother cell remains replication competent and immediately starts a new reproducing cycle, while the daughter cell explores the environment until it irreversibly attaches to a surface and become a stalked cell itself.

### 1.2.2 Flagellum

Many microorganisms are equipped with organelles that enable locomotion. Active movement allows the organism to move towards more favorable habitats and to avoid disadvantageous or harmful areas. In bacteria, locomotion can be achieved by the flagellar apparatus. A reversibly rotary motor is connected to a long and thin cell appendage, the flagellar filament, via a universal joint, the hook<sup>24</sup>. The rotary motor is embedded in the cell envelope and powered by an ion flux (protons for most neutrophils<sup>25–28</sup>, among them *C. crescentus*<sup>29</sup>, sodium ions for alkophiles<sup>30</sup> and marine *Vibrio*<sup>28</sup>). The rotary motor converts the ion flux into a torque that rotates the flagellar filament. The filament is a corkscrew like appendix at the outside of the cell wall and generates a pushing or pulling force that propels the cell when it rotates<sup>12</sup>. In *C. crescentus* the flagellar filament has a length of 6  $\mu\text{m}$ <sup>29</sup>, a diameter of 14 nm<sup>31</sup> and has a right handed helical form<sup>31</sup>. The filament is a long, hollow tube and is formed by thousands of copies of the protein flagellin<sup>28</sup>. The helical shape is achieved by variations in the packing of the flagellin subunits<sup>32</sup>. The hook that connects the filament to the rotary motor is slightly thicker and more flexible than the filament<sup>33</sup>. Bacterial cells can be equipped with a single flagellum (monotrichous) or with multiple flagella (peritrichous). Every flagellum is powered by its own rotary motor. The mode of swimming and how the bacteria change their swimming direction depends on whether the cell is monotrichous or peritrichous<sup>34</sup>.

The flagellar apparatus of *C. crescentus* is not only used for swimming, there is also strong evidence that the flagellar motor acts as surface sensor to initiate holdfast synthesis. Surface contact of the rotary motor interferes with the rotor-stator components, generating a signaling cascade that leads to a burst of c-di-GMP, which in turn activates holdfast synthesis<sup>35</sup>.

### 1.2.3 Pili

Similar to flagella, pili are also long and thin protein-based appendixes located at the outside of the cell wall, however they differ structurally and mechanically. Pili are used for a wide variety of functions, among them is surface attachment and motility on surfaces<sup>36–38</sup>. Pili can mediate adherence and migration of bacterial cells in the host<sup>39</sup> and act as surface sensors, regulating the transcription of genes involved in virulence<sup>40</sup>. Therefore they play a crucial role in surface colonization, biofilm formation and pathogen spreading<sup>41,42</sup>. One of the most refined class of pili are the type IV pili. These are dynamic machines widespread in bacteria and archaea that can undergo cycles of retraction and extension by the disassembly and assembly of pilin subunits<sup>43–45</sup>. Assembly and disassembly of the pilin subunits is powered by ATPases that induce rotational movement of the assembly platform. The assembly platform is located in the inner

cell membrane and integrates or extracts pilin subunits into the pili-forming helical filaments<sup>41,46</sup>. Type IV pili are divided into two subclasses, type IVa and type IVb. Type IVa pili are a uniform class and are found in human pathogens like *Pseudomonas aeruginosa* and *Vibrio cholerae*. Type IVb pili are less uniform and best studied in enteropathogenic *Escherichia coli* or *V. cholera*<sup>47</sup>. A subclass of type IVb pili are called tight adherence pili (Tad) and are widely found in Gram positive and negative bacteria, among them *C. crescentus*. They promote surface colonization, biofilm cohesion and virulence in pathogens<sup>47-49</sup>. Although the gene clusters encoding the Tad pili lack a ATPase gene, Tad pili can still show a dynamic retraction<sup>50</sup>. In *C. crescentus* Tad pili enable the reversible attachment of the swarmer cell onto a surface. They also seem to play a crucial role in surface sensing. The surface is likely sensed either by obstruction of the pilus retraction<sup>50</sup>, or via the interference of the surface with the rotary motor of the flagellum that is positioned close to the surface by pili<sup>35</sup>.

#### 1.2.4 Stalk and Holdfast

The genus of *Caulobacter* was initially defined by their ability to form stalks<sup>51</sup>. A stalk is a cell envelope extension that can be polar or apolar<sup>51</sup>. In the case of *Caulobacter* it is always polar. In *C. crescentus* cells, only replication competent cells have a stalk. The stalk lacks most of the proteins that are present in the cell body, but contains proteins necessary for the uptake of nutrients<sup>52</sup>. The form of the stalk, long and thin with a large surface, facilitates the uptake of diffusing nutrients<sup>15,53</sup>. At the end of the stalk a strong adhesive holdfast is secreted, that allows the cell to irreversibly attach to surfaces<sup>53,54</sup>. The holdfast is formed by polysaccharides<sup>54,55</sup> and some additional, yet unknown components<sup>54,56,57</sup> and can resist detachment forces up to 2  $\mu\text{N}$ <sup>53</sup>, making it the strongest ever measured biological adhesive. Via the holdfast, *C. crescentus* is able to permanently attach to nearly any surface<sup>58</sup>. One exception are the cell bodies of other *C. crescentus* cells. However, holdfasts can attach to other holdfasts, several cells joined together form characteristic rosettes of stalked cells<sup>58</sup>.

#### 1.2.5 Motility and Chemotaxis

The best studied example of locomotion in bacteria is *E. coli*. It is equipped with several (usually between three and eight) flagella that are randomly distributed on the cell body<sup>59</sup>. When all rotary motors are rotating counter clock wise (CCW), all flagella are aligned and form a bundle. The cell is propelled in an almost straight line and moves at a speed of 10 – 30  $\mu\text{m/s}$ <sup>60</sup>. Upon the rotation reversal of at least one of the rotary motors to clock wise (CW) direction, the flagella-bundle falls apart, which leads to a tumbling motion and a random reorientation of the cell<sup>59</sup>. During normal swimming, tumbling happens about every second<sup>59</sup>. To move towards attractants

or away from repellants, cells are equipped with receptors to sense concentration variations. When the cell is moving upwards an attractant gradient, it prolongs its runs, leading to a biased random walk towards the attractant<sup>61</sup>. In the presence of a repellent, reversals from CCW to CW rotation of the motor are increased, leading to more tumbling and more reorientations of the cell until conditions improve<sup>62</sup>.

In *C. crescentus*, only the swarmer cell is equipped with a single flagellar filament that has a length of roughly  $6\ \mu\text{m}$ <sup>29</sup>. The filament has a right handed helical form and a diameter of  $14\ \text{nm}$ <sup>31</sup>. The rotary motor is powered by protons. When the flagellum is rotating CW, the flagellum pushes the cell body forwards<sup>31</sup> and when the flagellum is rotating counterclockwise (CCW), the flagellum pulls the cell body<sup>63</sup>. The swimming speed does not depend on the direction, it is in both directions around  $40 - 60\ \mu\text{m/s}$ <sup>29,64</sup>. The rotation rate of the flagellum is determined by the rotation rate of the motor and depends on the medium. It is around 270 Hz in a medium with enough nutrients (peptone yeast extract (PYE)) and around 200 Hz in extremely low nutrients levels (deionized water)<sup>29</sup>. To maintain zero net torque, the cell body counterrotates. In PYE the cell body counterrotates at 80 Hz<sup>29</sup>. The stall torque generated by the rotary motor is around  $350\ \text{pN nm}$ <sup>29</sup> and depends on the swimming direction, the motor generates more torque when the cell swims backwards (CCW rotation of flagellum)<sup>65</sup>. The stall torque of *C. crescentus* is thereby much smaller than the stall torque of *E. coli* and *V. alginolyticus*<sup>66,67</sup>. The motor rotates at a constant torque up to the rotation rate in swarmer cells, while in *E. coli* and *V. alginolyticus* the motor torque of free swimming cells is much lower than the stall torque<sup>66,67</sup>. This fact makes *C. crescentus* an efficient swimmer and perfectly adapted to environments with scarce nutrients levels<sup>29</sup>. Because the *C. crescentus* cell has only one single flagellum, changes in the swimming direction cannot be achieved by tumbling. The curvature of the cell body by itself leads to a curved trajectory when the cell is swimming backwards<sup>68</sup>. To further improve the cells ability for reorientation and therefore improved chemotaxis, the cells exhibit a behavior called “the flick”<sup>34,69</sup>. The flick occurs shortly after the onset of a forward run. The drag force of the cell body and the propulsion force of the flagellum apply a compressive force on the hook, causing a buckling of the hook and an off-axis deformation of the flagellum that in turn results in a reorientation of the cell. The buckling and the subsequent flick of the cell reorients the swimming direction by about 90 degrees<sup>34,69</sup>. The probability of a flick and the reorientation angle depend on the swimming speed of the bacteria and the cell body size<sup>70</sup>. When moving up a gradient of attractant, *C. crescentus* cells prolong the duration of their forward runs, leading to less reorientations and a more directed motion<sup>71</sup>.

### 1.2.6 c-di-GMP

Cyclic diguanylate (c-di-GMP) is a second messenger found in many bacterial cells and plays an important role in controlling bacterial life style and cell cycle progression<sup>72</sup>. It consists of two guanine bases that are linked to form a cycle by ribose and phosphate<sup>73</sup>. Because c-di-GMP plays such an important role in controlling cell cycle progression, it needs to be tightly regulated. Production of c-di-GMP is mediated by diguanylate cyclases, while the removal of c-di-GMP is achieved by phosphodiesterases that hydrolyze c-di-GMP<sup>74,75</sup>. The asymmetric cell cycle of *C. crescentus* is regulated by c-di-GMP. Swarmer cells have low levels of c-di-GMP, while stalked and predivisional cells have higher level of c-di-GMP<sup>76</sup>. This is also found to be true for other species, low levels of c-di-GMP promote motility, while a rise in c-di-GMP promotes a sessile lifestyle and biofilm formation<sup>77</sup>. Mutants of *C. crescentus* that are lacking all diguanylate cyclases lose all phenotypes typical for *C. crescentus*, they do not form stalks, holdfast, pili or flagellum and show no cell polarity and have severe cell division defects<sup>78</sup>.

## 1.3 OPTICAL TRAPPING

The principle of optical trapping relies on the interaction of light with matter. When a photon hits a particle, they interact. Light can be either refracted, reflected, deflected or absorbed (Figure 1.2). The material of the particle and the incident angle of the photon determine the way of interaction.

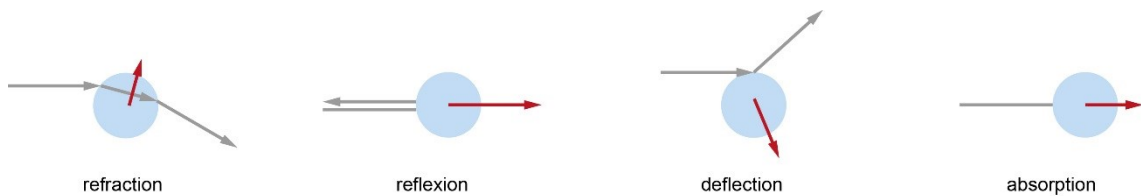


**Figure 1.2: Different modes of interaction of photons and matter.** The photon can be refracted, reflected, deflected and absorbed. The path of the photon is depicted in grey, whereas the direction of the transferred momentum is depicted in red.

Because the photon does not have a rest mass, the force and the momentum of the photon cannot be described by Newton's second law. Instead, the momentum of the photon is described via its energy. Einstein showed that every photon has a discrete energy  $E$  and a momentum  $p$  that depends on the wavelength  $\lambda$  of the photon<sup>79</sup>. The momentum is given by

$$p = \frac{E}{c} = \frac{h}{\lambda} \quad (1.2)$$

with  $h$  the Planck constant and  $c$  the speed of light. Because the momentum of a single photon is very small ( $\sim 10^{-25}$  kg·m/s), and the transferred momentum onto the particle cannot be larger

than the initial momentum of the photon, a massive amount of photons is needed to have an impact onto even a micron sized object. This amount of photons can only be produced by a technique called “light amplification by stimulated emission of radiation”, also known as “laser”. With a laser it is not only possible to produce a massive amount of photons, the output is also stable over a long time, the photons have all the same wavelength and hence the same energy, and are coherent. For efficient trapping of a particle, a gradient of photons is needed. Photons emitted from a laser already form a lateral gradient, more photons are emitted from the center than from the edges. Ashkin was the first to observe that microspheres dissolved in water and placed in the laser beam were not only pushed along the axis of the light propagation, but also experienced a lateral force towards the center of the beam<sup>80</sup>. Depending on the wavelength of the laser and the size of the trapped object, two different models were established to describe the forces acting on the trapped particle:

1: **Rayleigh-regime**, with particle diameter  $\ll \lambda$ . Because the particle is small compared to the trapping wavelength, the particle is considered a dipole and Maxwell’s equations are used to describe the forces acting on the particle<sup>81</sup>.

2: **Mie-regime**, with particle diameter  $\gg \lambda$ . The particle diameter is much larger than the wavelength of the trapping laser. In this case, ray optics can be used to describe the resulting forces on the particle<sup>82</sup>.

Often, an intermediate state has to be considered where the particle diameter  $\approx \lambda$ .

In our case, the trapping happened in the Mie-regime and can therefore be described with ray optics.

A particle in the laser beam will experience a force due to the scattering of the incident photons. This force consists of two components: 1: a scattering force that points towards the direction of the light propagation, and 2: a gradient force, that points towards the more intense part of the photon gradient. These two forces together will position the particle in the center of the laser beam, but the particle will still move along the axis of the light propagation<sup>81</sup>. There are two ways to stabilize the bead also in axial position. In the early days of optical trapping this was done using two opposing laser, pointing at each other. The two laser form an optical potential well where the two scattering forces cancel each other out and the particle is stabilized<sup>80</sup>. Nowadays most optical tweezers are formed by tightly focusing the laser beam. The momentum change of the focused beam generates a force towards the focus point, both when the particle is in front or behind the focus (Figure 1.3). Because of the scattering force, the particle is

positioned slightly behind the focus point, where the gradient force compensates the scattering force. The advantage of this method is that only one laser is needed and the laser can be conveniently focused with the same objective that is used for imaging the sample.

Trapping works best when the refractive index of the particle and the surrounding media differ as much as possible. However, optical tweezers also have a wide application in biology where the aqueous medium and the biological specimen that also mostly consists of water have only a slight difference in the refractive index. Optical tweezers are capable of holding and manipulating biological  $\mu\text{m}$ -sized objects in their physiological environment. Optical tweezers are a versatile and powerful tool for many biological applications, for example force measurements of microbes or sorting of small objects.

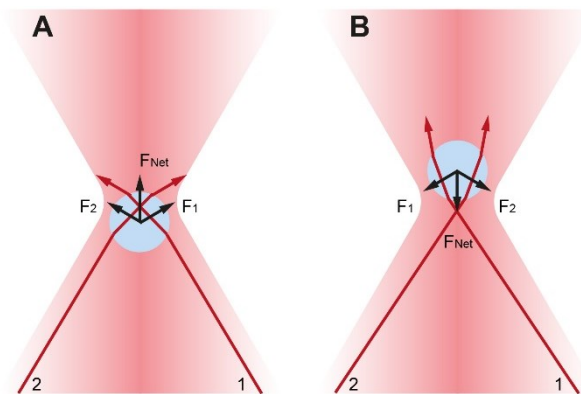


**Figure 1.3: Ray optics schematics of a sphere in a focused laser beam.** Momentum change of rays when the bead is in front (A) or behind (B) the laser focus (direction of light propagation: from bottom to top). The momentum change of the refracted rays forces the bead towards the center of the focused laser beam. Because of the scattering force that counteracts the gradient force the equilibrium position of the bead is slightly behind the focus. The photon gradient keeps the bead laterally in the center of the beam.

## 2 MICROSCOPE AND OPTICAL TWEEZERS SET-UP

---

We constructed our own light microscope and combined it with an optical tweezers set-up. The set-up was built in a modular way, making it very versatile and flexible. For example, filters and the camera can be exchanged quickly. The set-up was easy to assemble, comparably low-priced and well suited for the experiments. Implementing microfluidic channels enables the continuous recording of living bacterial cells under physiological conditions. The optical tweezers set-up allows the manipulation and force measurement of the bacteria.

### 2.1 MICROSCOPE SET-UP

The light microscope was built on an optical table (aluminum thread-bore plate: Nexus, heavy duty passive frame: Thorlabs), and all components were mounted using the Linos Microbench system (Qioptiq). We used high precision aluminum cubes and plates that can be mounted on rails that are fixed on the thread-bore plate. The optical components were then mounted inside of the cubes and plates. The individual parts were connected via hardened steel rods for added stability. The Microbench system allowed for rigid and precise rectangular assembly of optical components in a very flexible manner. Customized parts were used where needed and fabricated by the mechanical workshop of the Physical Chemistry of the University of Basel. The microscope consisted of the following parts:

- 1.) Köhler bright field illumination for sample inspection and imaging consisting of a collector lens ( $f = 16$ ) and a condenser lens ( $f = 27$ ). Two irises were placed 16 mm and 32 mm after the collector lens. The condenser lens was placed 43 mm after the collector lens. (Lenses: Qioptiq, irises: D20S, Thorlabs)
- 2.) Movable sample stage (MP-285, Sutter Instruments), including a customized sample holder (mechanical workshop)
- 3.) Objective (60x water, 1.20, Uplansapo, Olympus), for sample imaging and focusing of the laser beam
- 4.) 45° tilted mirror to transform the light path from vertical to horizontal propagation
- 5.) Lens system for image magnification. Two lenses (Qioptiq) with  $f = 50$  and  $f = 120$ , positioned 140 mm apart.
- 6.) Iris (D20S, Thorlabs) for the removal of stray lights
- 7.) Low pass filter (HC 680/SP, AHF) for filtering out any remaining light of the trapping laser
- 8.) High speed camera (Phantom Miro eX4, Vision Research)

Additionally, a fluorescence illumination path was added. It consisted of the following parts:

- 9.) Illumination lamp (PhotoFluor II NIR, 89 North) for the fluorescence illumination
- 10.) Liquid light guide (5 mm, 89 North)

- 11.) 5x beam expander (Thorlabs)
- 12.) Filter cube with a filter set of the desired wavelength. (GFP: Thorlabs, emission filter: MF525-39, excitation filter: MF469-35, dichroic mirror: MD498. TRITC: Thorlabs, emission filter: MF620-52, excitation filter: MF542-20, dichroic mirror: MD568. DAPI: Chroma, emission filter: AT650/50m, excitation filter: AT375/28x, dichroic mirror: AT415dc)

To retain as much light as possible when working with bright field, the fluorescence filters were only mounted when fluorescence illumination was required. This was especially important when recording at very high frame rates that resulted in low illumination times.

## 2.2 OPTICAL TWEEZERS SET-UP

The optical tweezers set-up consists of two laser diodes that form two independent traps. The power output of the main laser diode is adjustable, allowing the easy adjustment of the stiffness of the optical tweezers. The laser for the optical tweezers is coupled into the microscope via a dichroic mirror. The laser beam passes through the back aperture of the objective. This leads to a focused laser beam in the focal plane of the sample. The optical tweezers consists of the following parts:

- 13.) Diode mount (LDM90/M, Thorlabs), also acts as laser controller and laser cooler
- 14.) Laser diode (1 W, 830 nm, LD830-MA1W - 830 nm, Thorlabs)
- 15.) Collimation lens
- 16.) Anamorphic prism pair (3.5x PS881-B, Thorlabs) for the transformation of the elliptical laser beam into a circular laser beam
- 17.) Tilt-able gold mirrors (ME1-M01, Thorlabs) for the laser beam alignment and adjusting the position of the focused laser beam at the sample plane
- 18.) Iris (D20S, Thorlabs) for the removal of stray lights
- 19.) Polarization cube (CM1-PBS252, Thorlabs), for the coupling of a second laser beam for a double-tweezers set-up
- 20.) Lens system to expand the laser beam so that it slightly overfills the back aperture of the objective ( $f = -40$  and  $f = 80$ , placed 40 mm apart)
- 21.) Dichroic mirror (T750SPXRXT, AHF) for the coupling of the trapping laser into the light path

### 2.2.1 Double Tweezers Set-up

A second laser diode was added to the device to generate a double tweezers set-up with two independent traps. The intensity of the second laser beam is controlled via neutral density filters. The alignment of the laser beam is only done via one mirror instead of two. This leads to an impaired adjustability of the position of the optical trap. The second laser set-up consists of the following parts:

- 22.) Collimated laser diode (200 mW, 830 nm, Schäfter+Kirchhoff)
- 23.) Tilt-able gold mirror (ME1-M01, Thorlabs) for the laser beam alignment and adjusting the position of the focused laser beam at the sample plane

The two laser beams are combined in the polarization cube (N° 19) and coupled into the microscope via the dichroic mirror (N° 21). The double tweezers set-up was built for future experiments – for the experiments presented in this work, solely the tunable laser diode was used.

A schematic of the set-up is shown in Figure 2.1, and a picture of the set-up is shown in Figure 2.2.

Next to the optical set-up and close to the microfluidic device (N° 24), a microfluidic pump system (neMESYS low pressure syringe pump V2, 14:1 gear; Cetoni GMBH) for injecting liquids into the microfluidic channels was placed.

The sample stage, pump, camera, fluorescence illumination and the diode controller for the tunable laser diode (ITC4005, Thorlabs) are all controlled via the same computer and their factory-software. All lenses were taken from the Linos Microbench set “Optics” (G062004000, Qioptiq)

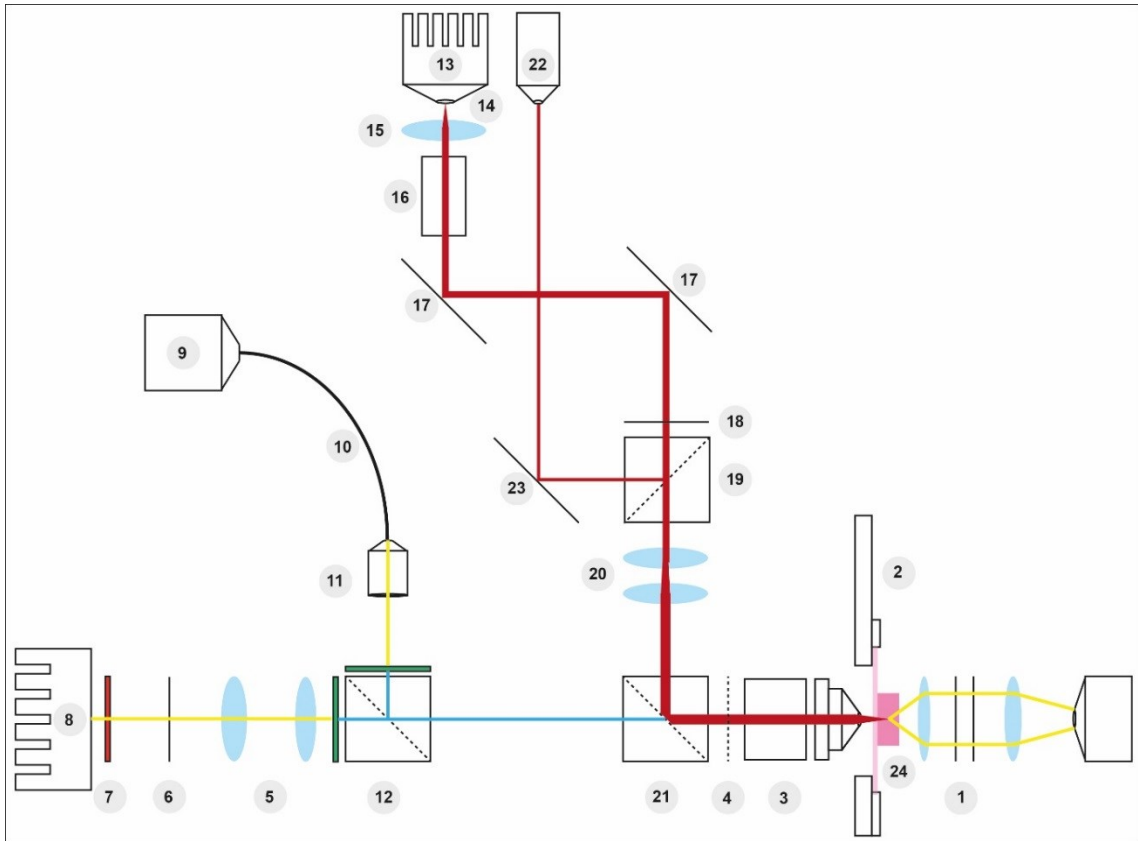


**Figure 2.1: Schematic of the microscope and optical tweezers set-up.** Red indicates the path of the laser light coming from two laser diodes. In yellow and blue the paths of the bright field illumination and the fluorescence illumination are shown. Light blue represents lenses and the microfluidic device is colored in pink.

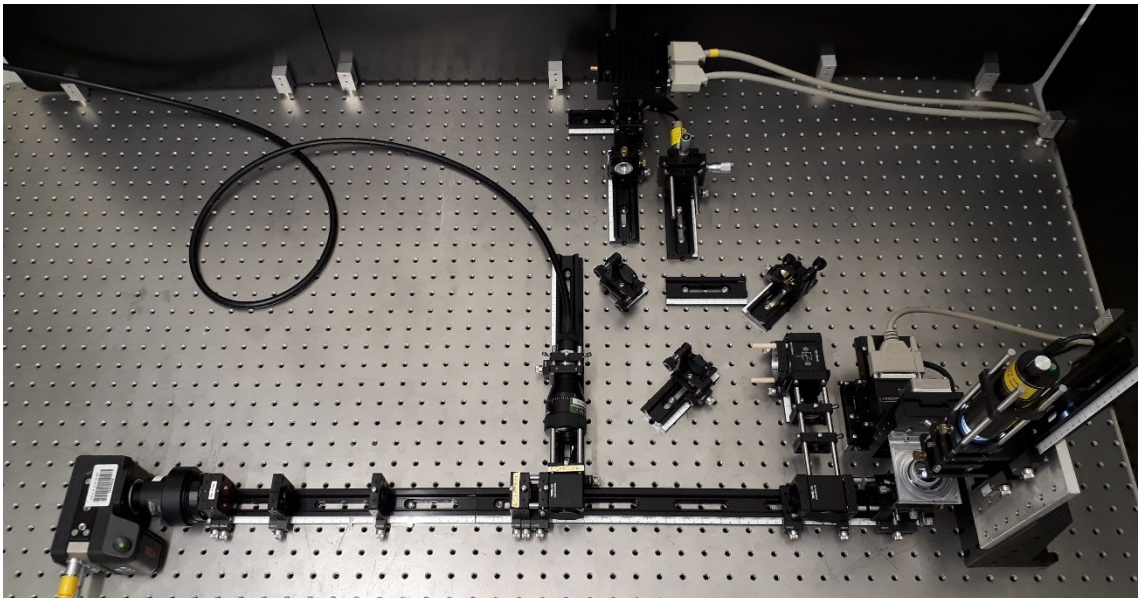


**Figure 2.2: Picture of the microscope and optical tweezers set-up.** The set-up was mounted on an aluminum thread-bore plate and all components were mounted via the Linos Microbench system. The optical components were mounted inside of the cubes and plates.

### 2.3 CONSIDERATIONS FOR CHOOSING THE OBJECTIVE

The objective used to focus the laser beam is one of the most important parts of an optical tweezers set-up. It not only determines the quality and resolution of the bright field images, but also determines the overall efficiency and trapping depth of the optical tweezers. The overall efficiency is determined by trap stiffness versus input power and is a function of the NA (numerical aperture) and transmittance of the objective. The higher the NA, the steeper is the light gradient and the stronger the optical trap becomes. The NA needs at least to be high enough to generate a photon gradient steep enough to overcome the scattering force (typically about 1.2 - 1.4 NA)<sup>81</sup>. Therefore, an objective with both an NA and transmittance as high as possible is favorable. The transmittance of different objectives varies a lot, depending on the purpose of the objective. An objective with a good transmittance at the wavelength of the trapping laser should be chosen for efficient trapping<sup>83,84</sup>. Another important point to consider is the working distance. The higher the working distance of the objective, the further away from the cover slip is the focused beam spot and therefore the trapping position of the object. Typically oil immersion objectives have a short working distance and the large refractive index mismatch between the immersion oil and the aqueous medium leads to spherical aberrations<sup>85</sup>. With water immersion objectives, typically a deeper trapping position can be achieved because there is no refractive index mismatch between the immersion medium and the aqueous trapping medium and the working distance of water immersion objectives is longer<sup>85</sup>. Because we wanted to be able to trap rather large particles and make sure there are no interfering wall effects, a water immersion objective with a long working distance was chosen.

### 2.4 CONSIDERATIONS FOR CHOOSING THE TRAPPING LASER

The trapping laser needs to be strong enough to trap particles with a low refractive index mismatch in an aqueous environment, but also have a stable power output to keep noise as low as possible. Apart from output power and stability, the wavelength is of fundamental importance, especially when working with biological samples. In the near infrared, between the absorption of proteins and the absorption of water is a window of relative transparency (~ 750 - 1200 nm)<sup>83</sup>. For bacterial cells of *E. coli*, damage minima at 830 nm and 970 nm were found<sup>84</sup>. We chose a relatively high laser power because we wanted to be able to trap swimming cells. For cost reasons we chose a 1 W diode laser with a wavelength of 830 nm. The drawback of the diode is that the laser beam is not circular, but elliptical and its shape need to be transformed

into a circular beam by an anamorphic prism pair. However, even after correction the beam was not perfectly circular, which resulted in a slightly anisotropic trap potential.

## 2.5 CALIBRATION OF THE OPTICAL TWEEZERS

To determine the forces generated by the optical tweezers at various laser powers, the optical tweezers need to be calibrated. We used the fluctuation method for the calibration and calculated the spring constant  $\kappa$  via the mean square displacement (MSD) of the bead in the optical tweezers.

### 2.5.1 Fluctuation Calibration

The optical potential in the optical tweezers can be described with a spring and the Hookean spring model. In this model, the spring is fixed in the center of the optical tweezers. When the object is also in the center of the optical tweezers, no force is acting on the object. But the further away the object gets from the center of the tweezers, the stronger is also the force pulling the object back. The force acting on the object can be described with

$$F = \kappa \cdot r \quad (2.1)$$

where  $F$  is the force,  $\kappa$  is the stiffness of the optical tweezers and  $r$  is the displacement in the  $x$ - $y$ -plane of the object from the center. With the mean square displacement,  $MSD$ , of the particle in the optical tweezers, the trap stiffness

$$\kappa = \frac{4 \cdot k_B \cdot T}{MSD} \quad (2.2)$$

can be determined, where  $k_B$  is the Boltzmann constant and  $T$  is the temperature of the system. The force acting on the particle then linearly depends on the displacement of the particle from the center of the trap. Because a slightly elliptic laser beam profile was used, the potential of the optical tweezers was not perfectly symmetrical. Therefore, we calculated two trap stiffnesses,  $\kappa_X$  and  $\kappa_Y$ .

$$\kappa_X = \frac{2 \cdot k_B \cdot T}{MSD_X} \quad (2.3)$$

and

$$\kappa_Y = \frac{2 \cdot k_B \cdot T}{MSD_Y} \quad (2.4)$$

## 2.5.2 MSD Determination

In order to determine the MSD of a particle at different laser powers, a particle was held in the optical tweezers and different laser powers were applied. For each power, the particle was recorded with a frame rate of 1000 Hz for 64 s. The position of the bead in every frame was determined with a self-written Matlab (MathWorks, Inc.) tracking software (Appendix). The data was plotted as a position distribution (Figure 2.3A). The position distribution shows that the optical trap is not perfectly symmetrical. The bead is more confined in  $x$ - than in  $y$ -direction. Furthermore, the position distribution of the bead depends on the applied laser power, at a higher laser power (grey) the bead is more confined than at a lower laser power (blue). The position of the bead was also plotted as the trajectory of the bead (Figure 2.3B). Here the bead hold at the higher laser power (grey) is more confined than the bead hold with the lower laser power (blue). For clarity, only the trajectory in one direction per laser power is shown. The  $MSD$  in  $x$ - and  $y$ -direction was calculated with a self-written Matlab script (Appendix) from the trajectories of the bead (Figure 2.3C). The anisotropy in the  $x$ - and  $x$ -direction of the optical trap is reflected in the  $MSD$  as well. At a larger laser power, the bead is confined in a narrower space.

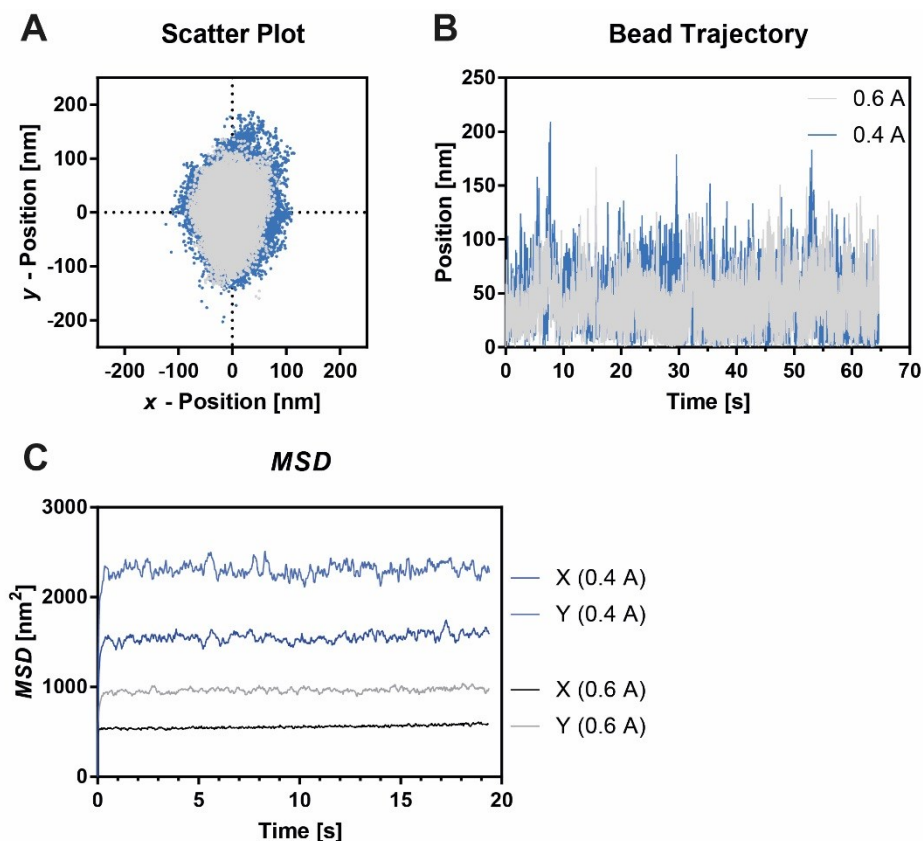


**Figure 2.3: Dependence of particle position on laser power.** **A:** Scatter plot of the bead position for 0.4 A (blue) and 0.6 A (grey). **B:** Trajectory of the bead for two different laser powers. Displacement at lower laser power is stronger than at higher laser power. **C:**  $MSD$  in  $x$ - and  $y$ -direction of a particle at 0.4 A (blue) and 0.6 A (grey). The anisotropy of the optical tweezers is reflected in the  $MSD$ . The confinement of the bead is stronger at 0.6 A than at 0.4 A.

### 2.5.3 Trap Stiffness $\kappa$

For each laser power,  $\kappa_x$  and  $\kappa_y$  were determined by the MSD using equation 2.2. To account for background noise, beads tightly attached to the surface of the device were recorded and analyzed using the same settings.  $\kappa_x$  and  $\kappa_y$  were corrected by considering the obtained background values. The trap stiffness  $\kappa_x$  and  $\kappa_y$  depends linearly on the applied laser power (Figure 2.4).

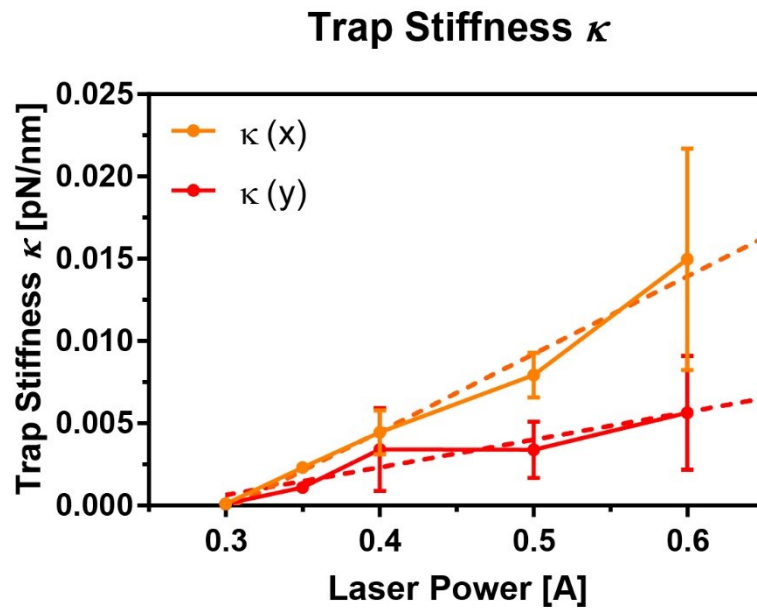


**Figure 2.4: Trap stiffness  $\kappa$  for different laser power.** The trap stiffness  $\kappa$  is separately determined for the  $x$ - and  $y$ -direction. Both  $\kappa_x$  and  $\kappa_y$  depend linearly on the applied laser power, but  $\kappa_x$  is larger than  $\kappa_y$  for all applied laser powers. Data shown are the average of 4 – 7 independent measurements  $\pm$  standard deviation. Stippled line: linear fit.

## 3 MATERIALS AND METHODS

---

### 3.1 MICROFLUIDIC FABRICATION

The single-use polydimethylsiloxane (PDMS) replicas were fabricated from a master that could be re-used many times. The master was fabricated in the clean room facility of the Department of Physics, University of Basel, while the device fabrication can be done in any regular laboratory. The replicas contained a main channel with a width of 10  $\mu\text{m}$ . On both ends of the channel, an inlet/outlet was placed for the injection of cells and media. Along the channel, side chambers of various sizes and shapes were placed, as previously described<sup>86</sup>. The sizes of the chambers ranged from several  $\mu\text{m}^2$  to hundreds of  $\mu\text{m}^2$ . The height of the chambers and the channel was 10  $\mu\text{m}$ .

#### 3.1.1 Master Fabrication to Produce Devices with a Channel Height of 10 $\mu\text{m}$

A silicon wafer with native oxide layer (Si-Mat, Kaufering, Germany) was rinsed with isopropanol and pre-baked at 200 °C for 10 min. The wafer was placed inside the spin coater and SU-8 3010 photoresist (Microchem, Newton, MA, USA) was applied equally and without bubble formation onto the wafer. The photoresist was spin-coated onto the wafer, first at 500 rpm for 10 s with fast ramping, then at 5000 rpm for 30 s with slow ramping. The height of the channel is determined by the choice of photoresist and the chosen spinning speed. The wafer was then soft-baked at 95 °C for 3 min and cooled to room temperature. Subsequently, the wafer was placed in a MJB4 mask aligner (SUSS MicroTec AG, Garching, Germany) and exposed to UV light (365 nm) through the corresponding mask with the desired structure (ML&C GmbH, Jena, Germany) for 5 s (depends on the intensity of the lamp. Desired value:  $\sim 33 \text{ mW/cm}^2$ ). Post-exposure baking was done at 95 °C for 1 min before the wafer was submerged in SU-8 developer for 4 min and then rinsed with isopropanol. These steps led to the removal of all photoresist that was not exposed to the UV light. The wafer was blow-dried and post-baked at 200 °C for 15 min. After cooling to room temperature the wafer was ready to use.

#### 3.1.2 PDMS Casting

To create the single-use PDMS replica, the master was placed into a petri dish of the corresponding size with the photoresist-treated side facing upwards. PDMS and cross linker (both Sylgard 184, Dow Corning GmbH, Wiesbaden, Germany) were well mixed in a ratio of 9:1. The mixture was poured into the petri dish until the master was covered. The height of the poured PDMS layer determines the height of the final PDMS replica. A too thick layer makes the

punching of the inlets and outlets more difficult, while a too thin layer makes handling of the replica more difficult. For general applications, the most convenient height is about 5 mm. The liquid PDMS was degassed and cured at 80 °C for a minimum of 4 h, either in an oven or on a hotplate. The structure formed by the photoresist is now imprinted into the PDMS.

### 3.1.3 Single Use Microfluidic Device Fabrication

The cured PDMS replica was cut out, peeled off the master and holes were punched (Harris Unicore, 0.75 mm diameter) for the inlets and outlets. A glass slide was rinsed with isopropanol and blow dried with nitrogen. The glass slide and the PDMS replica were plasma-treated for 30 s at 2 mbar in a plasma-cleaner (Harrick Plasma, NY, USA) and immediately brought into contact after the treatment. After some minutes, covalent linkage between the PDMS and the glass was established. To avoid evaporation of the medium during the experiment and to facilitate the creation of a no-flow environment, the PDMS replica was submerged in aqueous solution during the experiment. To this means, a plastic ring (50 mL falcon tubes, cut into rings with heights of about 1 - 2 cm in the mechanical workshop) that fit over the replica was dipped into liquid PDMS and placed around the replica<sup>87</sup>. After solidifying of the PDMS connecting the ring and the glass slide, the tubing (polytetrafluoroethylene, Adtech, outer diameter 0.76 mm) was inserted into the inlets and outlets. The device was then ready to use.

### 3.1.4 Thermal Aging

Right after plasma-bonding, the PDMS surface is hydrophilic, this leads to easier filling of the device, and formation of less air bubbles. To prolong the hydrophilicity, the device can be thermally aged<sup>88</sup>. This also leads to the loss of low molecular weight chains that diffuse from the bulk of the PDMS block and are harmful for cells. The thermal aging was done at 150 °C on the hotplate for 4 h and, to increase this effect, the devices were stored at 80 °C until use. This procedure also decreased sticking of the polystyrene beads to the surface.

### 3.1.5 Bovine Serum Albumin Coating

In order to prevent sticking of the polystyrene beads to the surface even further, the microfluidic devices were coated with bovine serum albumin (BSA, Sigma, Art. Nr. A-2512). 1 mg/ml BSA was dissolved in deionized water. The device was rinsed with medium, then the BSA solution was pumped through the device for several minutes. Then the device was rinsed with medium again.

### 3.1.6 Equilibration of the Device

PDMS is permeable to water which leads to a permeation driven flow and changes in salt concentrations. For some applications it is also necessary to maintain a strictly flow free

environment. The easiest way to achieve a flow free environment is to submerge the total PDMS replica into the same aqueous solution as is filled into the microchannels. For this reason, the plastic ring around the PDMS replica was mounted. During the experiment, the ring was filled with aqueous solution and the tubing was removed after injection of the contents. Importantly, the filling of the ring has to cover the inlets and outlets.

## 3.2 CELL CULTURING

The cell culturing techniques established in the Jenal lab were followed. All media and plates used came from the media kitchen (4<sup>th</sup> floor, Biozentrum, University of Basel). For a list of the media see the Appendix.

### 3.2.1 Culturing on Plate

Bacteria were kept in stock at -80 °C. For cell culturing, a small amount of frozen cells was scrapped off and plated on solidified peptone yeast extract (PYE. The cells were evenly distributed on the agar plate, either using a sterile pipette-tip or a sterile glass loop. The plates were incubated at 30 °C or on the bench for several days, until colonies arose. The plates were then stored in the fridge at 4 °C and could be used up to 2 weeks.

### 3.2.2 Liquid Culture

For the liquid culture, a single colony from the plate was picked and incubated in 2 - 3 ml liquid PYE at 30 °C overnight. Healthy cells reached a density of about  $1.4 \cdot 10^9$  cells per ml. Depending on the experimental set-up, cells were diluted before the experiment.

### 3.2.3 Freezing

For long-term storage, cells were shock-frozen in liquid nitrogen and kept at -80 °C. The desired strain was grown in liquid culture overnight as described above. 1 ml of the overnight culture was well mixed with 100 µl dimethyl sulfoxide DMSO (Sigma, Art. Nr. 41640), subsequently plunge frozen in liquid nitrogen and transferred to the storage at -80 °C.

### 3.2.4 Bacterial Conjugation

Our assay with cells attached to a glass slide or a bead only works because of the ability of *C. crescentus* to irreversibly attach to nearly any surface via the formation of a holdfast and stalk. However, due to a mutation in the holdfast *hfsA* gene, the common NA1000 wild-type lab strain does not form a holdfast. To reintroduce the functioning *hfsA* gene onto the chromosome, tri-parental conjugation with *E. coli* S17 and an *E. coli* strain with the RP4 plasmid to increase efficiency was carried out as described before<sup>89</sup>. In this acceptor-donor system, the acceptor

*C. crescentus* strain carries the mutated *hfsA* gene, and the donor *E. coli* S17 strain is carrying a pNPTS138 suicide vector. The pNPTS138 plasmid carries an intact *hfsA* gene, a resistance cassette against kanamycin (Kn) to allow the selection for conjugated *C. crescentus* cells, and the *sacB* gene for an additional selection step. The S17 strain is also able to transfer the plasmid to the acceptor. This transfer is mediated by F-pili. These pili establish the initial contact between donor and acceptor cells, enabling the transfer of the pNPTS138 plasmid. To increase conjugation efficiency, the helper strain *E. coli* MT607 was added, carrying the conjugative RP4 plasmid which increases pili production.

The donor strain (*E. coli* S17) was grown overnight in LB supplemented with 1.6 µl/ml Kn (Applichem, Art. Nr. A1493.0025) The helper strain (*E. coli* MT607) was also grown in LB overnight, supplemented with 1.5 µl/ml chloramphenicol (Cm, Fluka, Art. Nr. 23275). The acceptor *C. crescentus* strain was grown in PYE overnight. The cell density was then measured using a photo spectrometer (Ultrospec 2100 pro, Amersham Biosciences) and set to 0.25 for the acceptor cells and 0.4 for the donor and helper cells by dilution. 1.2 ml of acceptor cells were mixed with 100 µl donor cells and 120 µl helper cells. The cells were centrifuged at 600 rpm for 2 min, then the supernatant was discharged and the cell pellet was re-suspended in 100 µl PYE. The re-suspended cells were placed drop by drop on a filter paper that was on top of a vacuum tube to accumulate the cells, facilitating the transfer of the plasmid. When the area with the cells started to dry from the edge, the filter paper was placed on a PYE plate and incubated at 30 °C for 4 - 5 h.

#### 3.2.4.1 First Selection (Plasmid Acceptance and First Recombination)

After incubation the cells were scratched off the filter paper, and plated on a PYE plate, containing nalidixic acid (20 µg/ml, Sigma, Art. Nr. N-4382-5g) and Kn (20 µg/ml). The plate was then incubated at 30 °C until colonies arose. Under these conditions, only *C. crescentus* cells that integrated the pNPTS138 plasmid, carrying the Kn resistance cassette, were able to grow. The remaining *C. crescentus* cells were inhibited by Kn. The *E. coli* cells were inhibited by nalidixic acid, as it is toxic to *E. coli* but not *C. crescentus*. To remove the integrated suicide plasmid and integrate the functioning *hfsA* gene, a second recombination and selection step had to be carried out.

#### 3.2.4.2 Second Selection (Second Recombination)

The pNPTS138 plasmid carries not only a resistance against Kn, but also a *sacB* gene that produces a toxic by-product in the presence of sucrose. When the genome recombination was

successful, the *sacB* gene, together with the Kn resistance cassette, is removed with the pNPTS138 suicide vector. This allows the selection of cells that have successfully recombined the plasmid. For every acceptor strain, 5 single colonies were picked from the plate used for the first selection and grown in PYE overnight. From every tube 5  $\mu$ l cell suspension was taken and spread on a separate PYE plate with 0.3% sucrose (Fluka, Art. Nr. 84100). The plate was incubated at 30 °C until colonies arose. Cells that by chance mutated the *sacB* gene, but did not undergo a second recombination, are able to grow on this plate, but are still resistant against Kn. To check for these cells, a parallel “pick and patch” was performed. From each PYE/sucrose plate, a small amount of cells was taken with a toothpick from 36 individual colonies and first streaked on a PYE plate and then carefully at the same position on a PYE/Kn (20  $\mu$ g/ml) plate (Figure 3.1). The plates were then incubated at 30 °C until colonies arose. The PYE only plate and the PYE/Kn plate were compared and all colonies that only formed on the PYE plate, but not on the PYE/Kn plate, were picked for overnight culture. These colonies are not resistant against Kn, indicating that they successfully inserted the plasmid into the genome during the first recombination and lost the suicide vector during the second recombination. As the cells do not necessarily incorporate the new DNA sequence from the pNPTS138 plasmid but can recombine to the original chromosome, an attachment assay was performed to verify that the *hfsA* gene was restored.

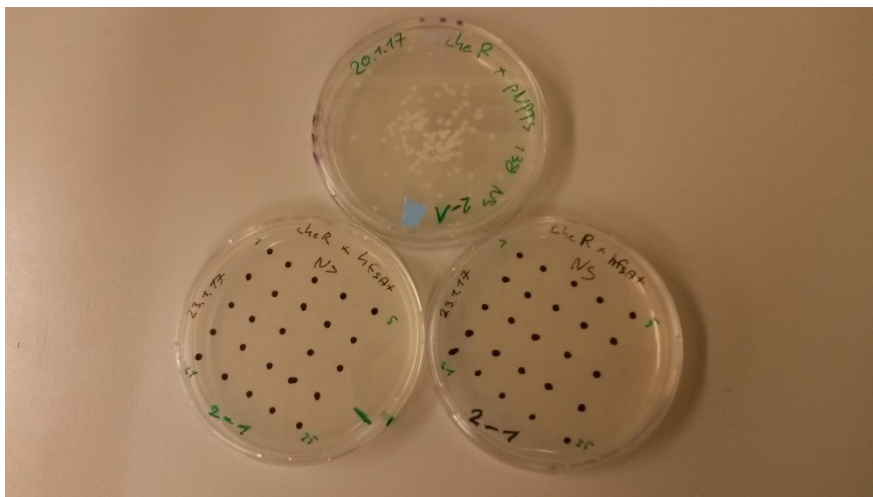


**Figure 3.1: Second selection:** Cells growing on a plate containing 0.3% sucrose (top) were parallel streaked on clearly indicated and traceable spot on a PYE plate only (right) and on a PYE plate plus antibiotics (left). Only cells that could grow solely on the PYE plate, but not on the PYE plus antibiotic plate did successfully undergo the second recombination.

### 3.2.5 Attachment Assay

To verify that the introduction of the plasmid that gives cells the ability to form holdfasts was successful, we checked the cells ability to form biofilms. Biofilms can only be formed when the cells are able to permanently attach to a surface. A sufficient number of 96-well plates were filled with 160  $\mu$ l PYE. With a toothpick a small amount of the colonies that grew on the PYE only plate from the second selection was picked, dipped into a well and streaked on a fresh PYE plate. Each colony was placed in a new well. The 96-well plate and the corresponding streak on the fresh PYE plate were arranged that each well had a corresponding streak. The 96-well plate was placed on a shaker and incubated at 30 °C overnight. The PYE plate was also incubated at 30 °C. The next morning, the liquid content of the well plate was discharged and 180  $\mu$ l of 0.1 % crystal violet (Sigma, Art. Nr. C-3886) in de-ionized water were added in each well. The 96-well plate was placed on a shaker for 30 min, then the content was discharged and the well plate was rinsed with water. The wells that contained cells that were able to form biofilms stayed colored, while in the other wells the dye was quickly washed out (Figure 3.2). The corresponding streaks on the PYE plate were marked, these cells were now confirmed to have successfully restored the function of the *hfsA* gene and therefore holdfast production. The cells could be used directly from the PYE plate for experiments or could be grown as liquid culture and frozen for further experiments.

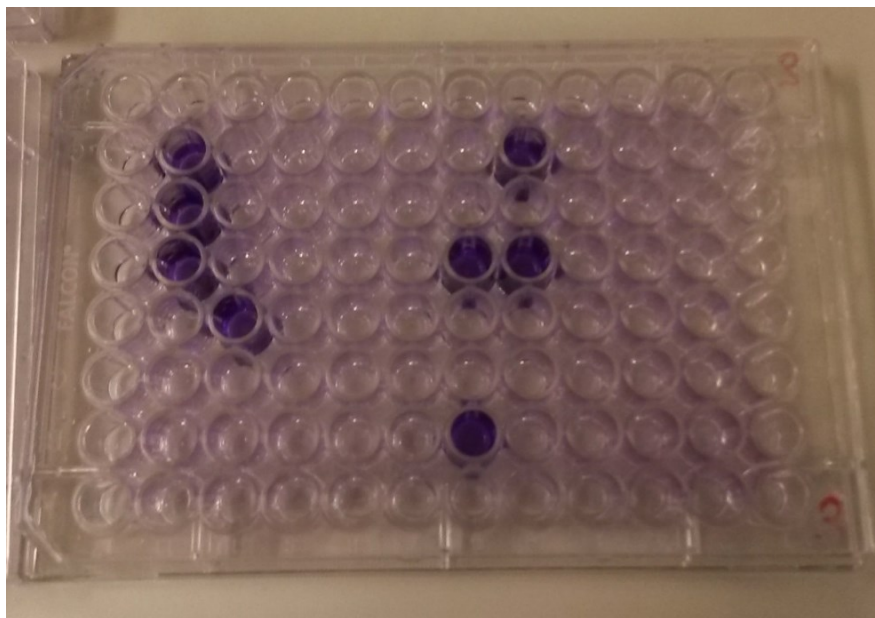


**Figure 3.2: Attachment assay.** Only the wells colored in deep violet contained cells that were able to form holdfasts.

### 3.2.6 Strains Used in this Study

The strains used for experiments or for the bacterial conjugation are listed in Table 3.1. The strain referred to as wildtype (WT) in this work is NA1000 *hfsA*<sup>+</sup>, which has a functional flagellum, produces pili and is able to form a holdfast upon surface contact. Strain NA1000 *hfsA*<sup>+</sup>  $\Delta creS$  is a rod-shaped cell, due to a deletion of the crescentin gene (CC3699). The function of the flagellum remains unchanged. Strain NA1000 *hfsA*<sup>+</sup>  $\Delta cheYII$  has a clean deletion of CC0437. The flagellum does not change the rotation direction, it remains rotating in CW direction (CCW rotation direction of the cell body). The same is the case for the strain NA1000 *hfsA*<sup>+</sup>  $\Delta cheR$ . The clean deletion of CC0435, CC598 and CC3472 only allows the flagellar motor to rotate in CW direction. The opposite is the case for the strain NA1000 *hfsA*<sup>+</sup> CC0440. In this case, the motor switches direction more often than in the WT because of the clean deletion of CC0440. The strain NA1000 *hfsA*<sup>+</sup>  $\Delta flgDE$  does not have a flagellum at all due to the deletion of flagellar hook genes. The function of the pili and holdfast remained unchanged for all strains.

Strain	Genotype	Description	Reference/source
<b><i>E. coli</i></b>			
SöA898	S17, pNPTS138 <i>hfsA</i> <sup>+</sup>	Donor, carries plasmid to form holdfast	Sören, A.
UJ2295	MT607	Increases efficiency of plasmid transfer	Alley, D.
<b><i>C. crescentus</i></b>			
UJ5511	NA1000 <i>hfsA</i> <sup>+</sup>	WT, pili, flagellum, holdfast	Friedrich, E.
UJ5145	NA1000 $\Delta creS$	Pili, flagellum, in-frame deletion of <i>creS</i> (CC3699), therefore rod-shaped, no holdfast	Heinritz, J. and Cabeen, M.T. <sup>90</sup>
UJ8653	NA1000 $\Delta cheYII$	Pili, flagellum, no holdfast, no change in rotation direction, clean deletion of CC0437	Hug, I.
UJ6884	NA1000 $\Delta cheR1, 2, 3$	Pili, flagellum, no holdfast, no change in rotation direction, clean deletion of CC0435, CC0598 and CC3472	Briegel, A. <sup>91</sup>
UJ5673	NA1000 $\Delta CC0440$	Pili, flagellum, no holdfast, fast change in rotation direction, clean deletion of CC0440	Nesper, J.
UJ9822	NA1000 $\Delta CheYII$ (UJ8653) <i>hfsA</i> <sup>+</sup>	Pili, flagellum, holdfast, no change in rotation direction	Sauter, N.
UJ9823	NA1000 $\Delta CheR1, 2, 3$ (UJ6884) <i>hfsA</i> <sup>+</sup>	Pili, flagellum, holdfast, no change in rotation direction	Sauter, N.
UJ9824	NA1000 CC0440 (UJ5673) <i>hfsA</i> <sup>+</sup>	Pili, flagellum, holdfast, fast change in rotation direction	Sauter, N.
	NA1000 <i>hfsA</i> <sup>+</sup> $\Delta creS$	Pili, flagellum, holdfast, rod-shaped	Sangermani, M.
UJ8177	NA1000 <i>hfsA</i> <sup>+</sup> $\Delta flgDE$	Pili, holdfast, no flagellum because of knock-out of <i>flgDE</i>	Hug, I.

**Table 3.1: Strains used in this work.**

### 3.2.7 Attachment of Bacterial Cells on Glass Slides

To attach *C. crescentus* cells onto the surface of the microfluidic device, cells from an overnight culture were diluted 1:1 with fresh PYE and injected into the device. The flow was stopped and the cells were left to attach onto the surface of the microfluidic device for several minutes. The remaining cells were flushed by injection of fresh PYE at a high flow rate ( $\sim 0.1 \mu\text{l/s}$ ). This procedure also supplied the attached cells with fresh medium. After 20 - 30 min, the flow was stopped, the tubing removed and the PDMS replica was submerged in PYE to create a strict no-flow environment and to avoid evaporation<sup>87</sup>. Recording of the cells was started about 2 h after injection and stopped about 8 h after injection. At later time points, the device was overgrown by bacteria.

### 3.2.8 Attachment of Cells on Beads

To attach cells onto colloidal beads, cells were grown overnight in liquid culture, diluted 1:10 with fresh PYE and put back at 30 °C for 2 h. The cells were then further diluted 1:2 and the appropriate amount of beads (Polysciences, Inc., Warrington USA.) were added and well mixed with the pipette tip. For the 3  $\mu\text{m}$  beads, 25  $\mu\text{l}$  bead solution ( $1.68 \times 10^9$  particles/ml) of carboxy-coated polystyrene beads was used per ml cell suspension. For the 1  $\mu\text{m}$  beads 1  $\mu\text{l}$  bead solution ( $4.55 \times 10^{10}$  particles/ml) of uncoated polystyrene beads per ml cell suspension was used. The solution was left to incubate for 2 min, then a small amount was placed on a coverslip and the number of cells per bead was checked. When the desired number of beads with 1 - 2 attached cells was reached, the cell suspension was diluted 1:1 with fresh PYE and injected into the device. The last dilution step served two reasons: firstly, it prevented further attachment of cells on the beads at least partially, as the density of both is cut in half, and secondly, it provides enough nutrients without the need to replace the medium for several hours. The tubing was removed and the device was submerged in PYE to create a strict no-flow environment and to avoid evaporation<sup>87</sup>. Recording of the cells was started about 2 h after injection and stopped about 8 h after injection. At later times, the device was overgrown by bacteria.

## 3.3 IMAGE ANALYSIS

Images were recorded at the appropriate frame rates (50 - 75 Hz for the cells attached to 3  $\mu\text{m}$  beads, 10 - 50 Hz for cells attached to 1  $\mu\text{m}$  beads, 200 - 300 Hz for cells attached to the surface of the device) in a \*.cine format. The difference in the frame rates is due to the wider field of view that is needed when the imaged object has a larger size, as in the case of the cells attached to the 3  $\mu\text{m}$  beads, or is capable of freely moving, as in the case of the cells attached to the

1  $\mu\text{m}$  beads. The \*.cine format was converted to \*.tiff, the movies were cropped and shortened to the relevant sequences, and brightened if necessary. The movies with the surface attached cells were analyzed manually to determine the duration of the flagellar activity and the rotation direction. The movies with cells attached to 1  $\mu\text{m}$  beads were analyzed using the Fiji plugin “Manual Tracking”<sup>92</sup> to track the position of the bead. Fiji is an image processing package of ImageJ (supported by NIH, Maryland), bundling and regularly updating plugins. The “Manual Tracking” plugin allows for quantifying movements of objects between individual frames of a temporal stack. The onset of the flagellar rotation, the softening of the connection between the two cells and cell separation were determined. The position of the 3  $\mu\text{m}$  bead hold by the optical tweezers was determined via a custom-made Matlab (MathWorks, Inc.) script (see Appendix). The position of the cell was determined via a second custom-made Matlab script (see Appendix). With these scripts it was possible to determine the onset of the flagellar rotation, angular velocity, reversion of the rotation direction, the softening of the connection between the two cells and the moment of cell separation.

## 4 FLAGELLUM DYNAMICS DURING CELL SEPARATION

---

### 4.1 ABSTRACT

*C. crescentus* cells divide asymmetrically, a stalked mother cell produces a motile daughter cell that is equipped with a rotating flagellum. The flagellum does not only allow swimming of the daughter cell, the flagellar motor also seems to be essential for surface sensing. In this work, we investigated the dynamics of the flagellum of the predivisional cell. We established a method that allows the label-free imaging of the impact of the flagellum under physiological conditions. We show that the rotation of the flagellum starts 3 – 4 min before cell separation is completed. The flagellum has an immediate onset of the rotation and is already fully assembled before the rotation starts. The flagellum of the predivisional daughter cell switches its rotation direction regularly. We found a 2/3 to 1/3 distribution of clockwise and counterclockwise rotation direction of the flagellum, that is also reflected in the fraction of cells that leave the mother cell swimming forward, respectively backwards. We measured the forces generated by the flagellum via optical tweezers and the swimming speed of differently seized swimmer cells. The flagellum exerts an average force of about 1.0 pN when the cell is swimming in a straight line, but can reach peaks up to 1.5 pN in the optical tweezers. The forces generated by the flagellum induce a bending-motion of the predivisional cell. Just seconds before the release of the daughter cell, the daughter cell starts to rotate around its long axis, while it is still connected to the mother cell. We assign the change in the flagellum-induced motion to the progression of cell separation. After the separation of the peptidoglycan the connection between the two cells is soft enough that the torque of the flagellum induces rotation of the daughter cell. Cell separation is completed and the daughter cell is released after the separation of the outer membrane.

## 4.2 INTRODUCTION

Motility is important for a wide range of living organisms. For example, bacteria have developed various strategies, adapted to their habitat, for controlled motility. In liquids bacteria swim and on surfaces they swarm, glide, walk and twitch. Commonly, motility is mediated by flagella and pili. Pili are hair-like structures located at the outside of the cell envelope and used among other functions for surface attachment and motility on surfaces<sup>93–95</sup>. The flagellum is a corkscrew-like structure also located at the outside of the cell that is used for swimming<sup>12</sup> and in some species also plays a role in surface attachment<sup>35,94–96</sup>. The best-studied flagellar swimmer is *E. coli* with its “run-and-tumble” swimming behavior. *E. coli* has 3 - 8 flagellar filaments at randomly distributed positions on the cell body<sup>59</sup>. Each flagellum is powered by a separate rotary motor. The rotary motor itself is powered by a proton gradient across the inner cell membrane<sup>97,98</sup>. When all rotary motors rotate counterclockwise (CCW), all flagella are bundled in a single fiber and the cell swims forward in a straight motion, also called “run”, at a speed of roughly 25  $\mu\text{m/s}$ <sup>60</sup>. When at least one of the rotary motors reverses its rotation direction to clockwise (CW), the fiber of bundled flagella falls apart and the flagella are unbundled, which leads to a “tumbling” motion and a random reorientation of the cell<sup>59</sup>. During normal swimming, a tumbling event happens about every second<sup>59</sup>. For chemotaxis, the cells prolong their run-times compared to the unbiased state, when going towards an attractant and tumble more often in presence of a repellent<sup>61,62</sup>. Not all bacterial cells are equipped with several flagella to perform a “run-and-tumble” motion. It is estimated that 90% of all motile marine bacteria are equipped with only a single flagellum<sup>99</sup> and therefore cannot use the same tumble-mechanism for reorientation as *E. coli*. Instead, the reversal of the single rotary motor leads to a reversal in the swimming direction of about 180°<sup>100</sup>. The cells change swimming direction when switching from being pushed by the flagellum to being pulled by the flagellum and back. But this effect alone results mainly in swimming forward and backwards nearly on the same line. In order to change their angular orientation, these cells exhibit a flicking motion<sup>34,69</sup>. The flick was first reported for *V. alginolyticus*, it performs a three-step swimming pattern, that consists of the steps forward, reverse, and flick<sup>34</sup>. The run-reverse-flick pattern has now also been reported for *P. haloplanktis*<sup>34</sup> and *V. coralliilyticus*<sup>69</sup>. The flick was also observed in a mixed seawater community<sup>69</sup>, indicating the widespread distribution of the flick in seawater bacteria. The flick is caused by an off-axis deformation of the flagellum that results in a reorientation of the cell. Shortly after the onset of a forward run, the drag force of the cell body and the propulsion force of the flagellum generate a compressive force on the hook. The compressive force causes a

buckling of the hook and the flagellum is deformed. The buckling instability and the subsequent flick of the cell reorients the swimming direction by about 90°<sup>69</sup>.

One bacterium that is equipped with only a single flagellum is *Caulobacter crescentus*. It swims forward and backwards by switching the rotation direction of the flagellar motor<sup>101</sup>. When the cell changes from backwards swimming to forward swimming, the flicking motion was also reported<sup>68</sup>. The flagellum filament has a right handed, helical form and when it rotates CW, it pushes the cell body forward<sup>31</sup>. To maintain torque balance, the cell body itself counter rotates in CCW direction. About every few seconds, the flagellar motor reverses its rotating direction<sup>64</sup>. This forces the flagellum to change its rotation direction as well. Consequently, the swimming direction is reversed, and the flagellum is now pulling the cell. Also, the counter rotation of the cell body changes from CCW to CW. The swimming velocity of the cells is around 40 – 60 μm/s and is the same for swimming forward and backwards<sup>64</sup>. While the swimming behavior of the swarmer cell of *C. crescentus* is well characterized<sup>29,64</sup>, little is known about the onset of flagellum activity and the flagellar activity in predivisional cells.

*C. crescentus* is a model system for the study of the bacterial cell cycle and cell polarity because of its asymmetric life cycle. The newborn daughter cell is a motile swarmer cell and replication inert (Figure 4.1A). In this stage, the cell is equipped with a flagellum for swimming and pili for reversibly attaching to surfaces (Figure 4.1B). Upon surface contact or after a defined period of time (ca. 20 min<sup>102</sup>), the flagellum is shed and the pili are disassembled (Figure 4.1C), the formation of a holdfast (Figure 4.1C – E) and later a stalk is initiated. The cell can now irreversibly attach to a surface via the holdfast and becomes a replication competent stalked cell. DNA replication is initiated (Figure 4.1E) and a fresh daughter cell is formed at the pole opposite of the stalk (Figure 4.1F, G)<sup>21</sup>. After completion of cell separation (Figure 4.1H), the fresh cell is released as a replication inert, motile swarmer cell (Figure 4.1G, A). The stalked mother cell remains replication competent and starts a new reproducing cycle (Figure 4.1E). The characteristic curved shape of the cells, that also is the origin of *C. crescentus* name, was found to facilitate surface contact of the predivisional daughter cell under flow and therefore promoting surface colonization<sup>23</sup>.

When monitoring the cell separation of *C. crescentus* in microfluidic experiments under flow, often a rotation of predivisional WT daughter cells that are still connected to the mother cells along their long axis can be observed<sup>35</sup>. The flow in the channel serves two purposes: It aligns the cells parallel to the glass slide, therefore improving imaging conditions, and it facilitates surface contact of the pole of the daughter cell. The fate of the daughter cell depends on

whether the cell rotates in the last seconds before cell separation or not. When the cell rotates, the cell is most likely to swim away after cell separation. When the cell does not rotate during the last seconds of cell separation, the cell is much more likely to attach to the surface. The cells that stay attached are held in place by pili and are able to form a holdfast even before cell separation was completed<sup>22,35</sup> (for a detailed view on pili dynamics, see chapter 5). The onset of the rotation of predivisional daughter cells was observed just seconds before cell separation<sup>35</sup>. The rotation of the predivisional daughter cell is caused by the flagellum. When the flagellum is rotating in a certain direction, the cell body is rotating in the opposite direction to maintain torque balance. The motor rotation rate of a free swimming predivisional WT cell in PYE is around 270 Hz<sup>29</sup> and the counter-rotation of the cell body was found to be around 80 Hz<sup>29</sup>.

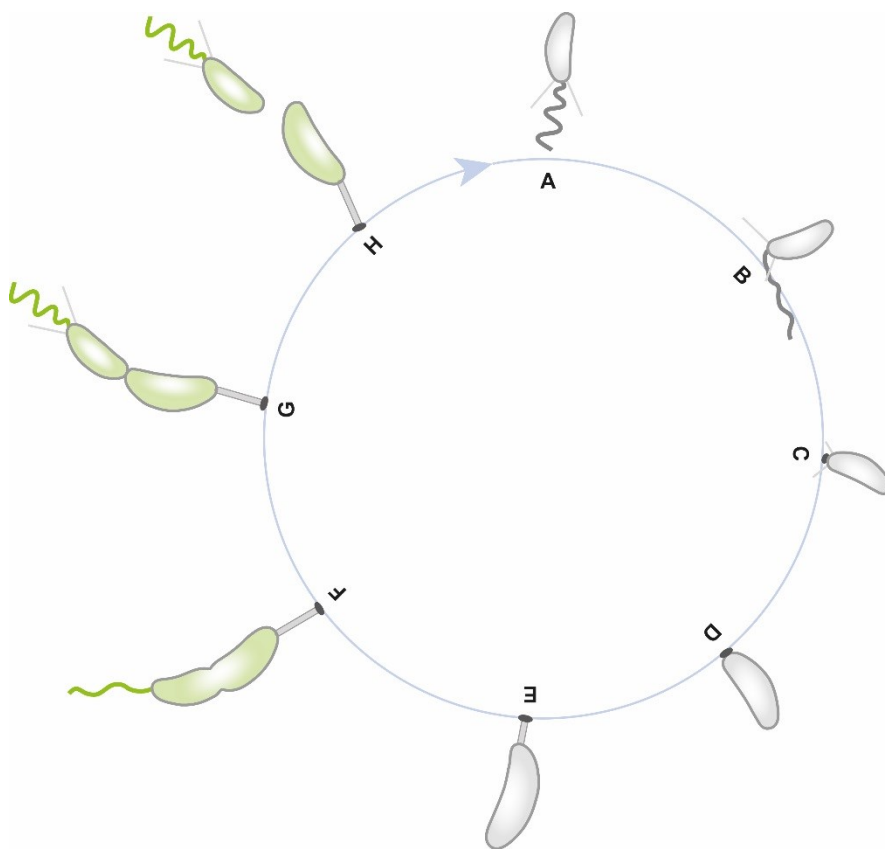


**Figure 4.1: Cell cycle of *C. crescentus*.** The life of a *C. crescentus* cell starts as a replication inert swarmer cell. It is equipped with a flagellum for motility and pili for reversible attachment (A). After a defined period of time, or earlier if it contacts a surface (B), it forms a holdfast for permanent surface attachment (C). The pili are disassembled, the flagellum is shed (C) and the cell becomes replication competent (D). The stalk is formed (E) and the stalked cell produces a new swarmer cell (F). The swarmer cell is again equipped with pili and a flagellum at the free pole (G). After cell separation, the swarmer cell swims away while the stalked cell remains attached to the surface (H) and initiates a new cycle of reproduction. In the presented work, we investigated the role of the flagellum during cell separation. The stages in the cell cycle which were relevant for our studies are highlighted in green.

In this work, we investigate the role and the activity of the flagellum during cell separation (highlighted in green in Figure 4.1). We have established experimental methods that allow us to precisely determine the onset of the flagellar rotation in the predivisional cell and the rotation direction of the flagellum. Furthermore, we observed the softening of the initially stiff connection between the mother and the daughter cell and the final release of the daughter cell and determined the forces generated by the flagellum.

## 4.3 MATERIALS AND METHODS

### 4.3.1 Cell Preparation

Cells were grown overnight in peptone yeast extract<sup>103</sup> (PYE, in-house media kitchen, see Appendix for composition) under agitation at 30 °C. To attach cells onto the surface of a microfluidic device an overnight culture of cells (roughly  $1.4 \times 10^9$  cells/ml) was diluted 1:1 with fresh PYE and manually injected into the microfluidic device. The flow was stopped and the cells were left to attach onto the surface of the microfluidic device for 2 – 3 minutes. The remaining, non-attached cells were flushed by injection of fresh PYE at a flow rate of roughly 0.1  $\mu$ l/s. This also supplied the attached cells with fresh media. After 20–30 min the flow was stopped, the tubing removed and the PDMS (Polydimethylsiloxane) replica was submerged in PYE to create a strict no-flow environment and to avoid evaporation<sup>87</sup>. To attach cells to colloidal beads, the overnight culture was diluted 1:10 with fresh PYE and put back at 30 °C for 2 h. The cells were then further diluted 1:2 with PYE and the appropriate amount of polystyrene beads (Polysciences, Inc., Warrington USA) were added and well mixed with the pipette tip. For the beads with a diameter of 3  $\mu$ m 25  $\mu$ l bead solution ( $1.68 \times 10^9$  beads/ml) of carboxy-coated polystyrene beads was used per ml cell suspension and for the beads with a diameter of 1  $\mu$ m 1  $\mu$ l bead solution ( $4.55 \times 10^{10}$  beads/ml) of uncoated polystyrene beads per ml cell suspension was used. The solution was incubated for 2 min, then a small amount was placed on a coverslip and the numbers of attached cells per bead were checked. When the desired number of beads with about 1 – 2 attached cells was reached, the cell suspension was diluted 1:1 with fresh PYE and injected into the device. The tubing was removed and the device was submerged in PYE to create a strict no-flow environment and to avoid evaporation<sup>87</sup>. Recording of the cells was started about 2 h after injection and stopped about 8 h after injection. At later time points, the device was overgrown with bacteria.

#### 4.3.1.1 Strains Used

The strain NA1000 *hsfA+* is referred to as wildtype (WT). It has a flagellum and 2 - 3 pili. The flagellum changes its rotation direction regularly. The strain NA1000 *hsfA+  $\Delta$ cheYII ( $\Delta$ cheYII)* is also equipped with a flagellum and pili. The rotation direction of the flagellum is locked in the CW direction and never changes<sup>104</sup>. This is done by the deletion of the gene *cheYII*, rendering the cell unable to produce CheYII. The phosphorylated response regulator CheY~P changes the direction of the rotor via interaction with the flagellar switch proteins FliM and FliN<sup>105,106</sup>. When CheY is not present, the rotation direction of the motor is not switched. The strain NA1000 *hsfA+  $\Delta$ fliGDE ( $\Delta$ fliGDE)* does not have the outer parts of the flagellum due to the deletion

of flagellar hook genes. All strains form holdfasts, otherwise the experiments could not have been performed.

#### 4.3.2 Microfluidic Devices

Standard photolithography and PDMS casting was performed as described in chapter 3.1. After covalently binding the PDMS replica to a glass slide, a small plastic ring that fit over the replica was dipped into liquid PDMS and placed around the replica. The devices were thermally aged to render the surface inside the device more hydrophilic and to get rid of any remaining low molecular weight polymer chains<sup>88</sup>. The devices were placed on a hotplate for 4 h at 150 °C and stored at 80 °C until use. This procedure also decreased a sticking of the polystyrene beads to the surface.

To prevent sticking of the polystyrene beads to the surface further, the microfluidic devices were coated with 1 mg/ml bovine serum albumin (BSA, Sigma) dissolved in deionized water. After rinsing the device with PYE, the BSA solution was pumped through the device for several minutes, followed by a rinsing step with PYE to prepare the cell injection.

#### 4.3.3 Recording and Optical Tweezers

All experiments were performed on the custom-built bright field microscope described in chapter 2. A high-speed camera (Phantom Miro eX4, Vision Research) was used for all recordings. The cells that were attached to the solid surface were recorded at 200 – 300 Hz, cells attached to 3  $\mu\text{m}$  beads at 50 – 100 Hz and the cells attached to 1  $\mu\text{m}$  beads at 10 – 20 Hz. The maximum frame rate inversely correlates to the number of pixels imaged, therefore a lower frequency of imaging is imposed when choosing a larger field of view. The larger field of view was needed for larger scaled objects (cells attached to 3  $\mu\text{m}$  beads) and for objects that could freely move (cells attached to 1  $\mu\text{m}$  beads).

The optical tweezers set-up is described in chapter 2. It consisted of a tunable laser diode (1 W, 830 nm, LD830-MA1W - 830 nm, Thorlabs) and a lens system to collimate, align, and expand the laser beam to overfill the back aperture of the objective. The laser beam was focused through the back aperture of the objective (60x water, 1.20, Uplansapo, Olympus). The experiments were performed in position clamp mode at a constant laser power. The optical tweezers were calibrated via fluctuation calibration. For more information on the calibration, see chapter 2.5.

#### 4.3.4 Data Analysis

The recorded images of cells attached to a solid surface were analyzed manually to determine the duration of the flagellar activity and the rotation direction in Fiji. Fiji is an image-processing

package of ImageJ (supported by NIH, Maryland), bundling and regularly updating plugins. The recorded images with cells attached to 1  $\mu\text{m}$  beads were analyzed using the Fiji plugin “Manual Tracking”<sup>92</sup> to track the position of the beads. The “Manual Tracking” plugin allows to quantify the movement of objects between individual frames of a temporal stack. The moments of onset of the flagellar rotation, the softening of the connection between the two separating cells and the moment of cell separation were determined using this plugin. The positions of the 3  $\mu\text{m}$  beads held by the optical tweezers was determined via a custom-made Matlab script (Appendix). The positions of the cells attached to the beads were determined via a second custom-made Matlab script (Appendix). With these scripts it was possible to determine the onset of the flagellar rotation, angular velocity, reversion of the rotation direction, the softening of the connection between the two cells, and the moment of cell separation.

## 4.4 RESULTS

### 4.4.1 The Impact of the Flagellum during Cell Separation – The Natural Set-up

Because the fate of the daughter cell depends largely on whether the cell rotates in the last seconds before cell separation or not, we want to further investigate and characterize the rotational behavior of predivisional cells. We intend to determine the exact onset of the flagellar rotation and the duration of the flagellar activity before cell separation is completed. The most straightforward way to determine the onset of flagellar rotation and the activity of pili would be to image the flagellum and pili directly. This is not possible under physiological conditions by light microscopy because the flagellum and pili are too thin to image. Labeling of the flagellum and pili is challenging and also prone to alter the dynamic behavior<sup>107</sup>. We therefore established a method to determine the onset of flagellar rotation by observing the movement that the active flagellum induces on the predivisional cell body.

In our experiments, we ensured that cells were attaching to the glass surface of a microfluidic device via their holdfast (mimicking the natural environment of *C. crescentus*, therefore termed “the natural set-up”). Rinsing the channel provided the attached cells with fresh medium and washed away any remaining non-attached cells. The flow was stopped and the predivisional cells were recorded with a high-speed camera with 200–300 Hz to resolve the frequency of the rotating cell bodies. Because the cells were attached and changed their position only a bit, the field of view could be kept small, enabling continuous recording for several minutes. Strict no-flow conditions were maintained in the microfluidic chamber to prevent any flow-induced impact onto the cell. In some cases, we observed a “bending movement” of the predivisional cells before the onset of the rotation of the daughter cell. During the bending movement, the two connected predivisional parts of the cell bent alternately towards the curvature and away from it (Figure 4.2A). The amplitude and the duration of the bending in a certain direction varied over time. The maximal displacement of non-attached cell pole could reach several  $\mu\text{m}$ .

The bending movement was subsequently followed by the rotation of the predivisional daughter cells around their long axis while still connected to the mother cell (Figure 4.2B). The rotation of the daughter cells could only be observed until the two cells completed cell separation and the daughter cells were released from the mother cells and quickly swam out of the field of view (Figure 4.2C). The mother cell with the stalk remained attached on the surface. During the bending movement the position of the flagellated pole of the daughter cell was tracked in x- and y-directions (black dots) and plotted in Figure 4.2D. The bending of the cell occurred mostly in

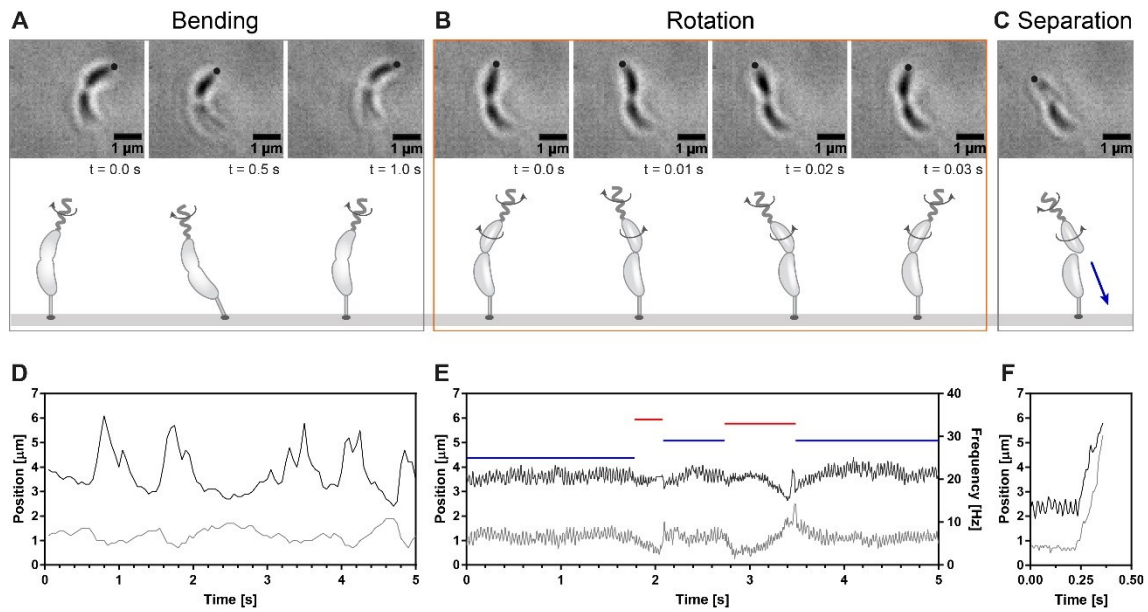


**Figure 4.2: Single cell example of a predivisional surface attached cell.** A-C: Bright field images and scheme of the bending movement (A), rotation (B) and cell separation (C, the blue arrow indicates the swimming direction of the daughter cell) of a WT cell attached to the surface of a device in PYE. The black dots indicate the tracking position for figures D-F. **D:** Example trajectory of the bending movement in  $x$ - and  $y$ -directions (black:  $x$ -direction, grey:  $y$ -direction). **E:** Example trajectory of the rotating daughter cell. On the left ordinate axis, the  $x$ - and  $y$ -positions of the daughter cell are plotted (black:  $x$ -direction, grey:  $y$ -direction). The right ordinate axis shows the corresponding rotation direction and frequency of the daughter cell. Blue: CCW rotation of cell body, red: CW rotation. **F:** Example trajectory of the last rotations and cell separation (black:  $x$ -direction, grey:  $y$ -direction).

the  $x$ -direction, as the cell was aligned nearly parallel to the  $y$ -axis. The position of the flagellated pole of the daughter cell was also tracked in  $x$ - and  $y$ -directions (black dots) to determine the rotation frequency of the predivisional daughter cell. It was also possible to determine the rotation direction of the cell because the cell has a distinct curved (banana-like) shape. We found that during the rotation around its long axis, the daughter cell can change its rotation direction. The rotation direction of the cell body depends on the rotation direction of the flagellum. When the flagellum rotates CW (from outside the body), the daughter cell counter-rotates CCW to maintain torque balance. When rotating CW, the flagellum generates a pushing force<sup>31</sup>. In the other case, when the flagellum rotates CCW, the cell counter-rotates CW and the flagellum generates a pulling force<sup>63</sup>. An example trajectory of the rotation of one single daughter cell around the long axis is shown in Figure 4.2E. Changes in the rotation direction were often, but not always, accompanied by a sharp shift of the position of the cell. While rotating in a given direction, the rotation frequency of the cell body remained stable. When the cell body changed its rotation direction, a shift in the frequency was observed. The rotation frequency of the daughter cell was found to be around 30 Hz when the cell rotated CCW and around 35 Hz when it rotated CW. The duration of the CCW sequences tends to last longer than the sequences in CW direction. The last 10 rotations and the subsequent release of the daughter cell are plotted

in *x*- and *y*-direction in Figure 4.2F. The newly born swarmer cell swims towards the mother (as sketched in Figure 4.2C), indicating a pushing movement of the flagellum (CW rotation of flagellum, CCW rotation of swarmer cell).

We determined the total duration of the observed movement activity for several cells from the first bending movement until cell separation and found that the overall activity lasted on average ( $123.4 \pm 110.9$ ) s, with a peak of cells around 60 s, but the observed duration could go up to 7 min (Figure 4.3A, left). The total activity period was split into a bending movement part, lasting from the first observed bending movement until rotation of the daughter cell began, and a rotation part, lasting from the first observed rotation of the daughter cell until cell separation was completed. The duration of the bending movement lasted on average ( $114.0 \pm 112.3$ ) s with a peak of cells also around 60 s, but the observed duration could also go up to 7 min (Figure 4.3A, center). The duration of the average bending movement is very similar to the total flagellar activity because the last part, rotation of the daughter cell, is comparably short. The rotation of the daughter cell lasted on average ( $11.2 \pm 15.6$ ) s until cell separation occurred; sometimes the rotation lasted up to 60 s (Figure 4.3A, right). For better visualization the duration of the rotation is also plotted as a histogram in Figure 4.3B. The fastest 40 % of the observed cells rotated less than 5 s before cell separation occurred (on average ( $1.7 \pm 1.4$ ) s) and the fastest 75 % of the cells rotated less than 15 s (on average ( $4.4 \pm 4.3$ ) s).

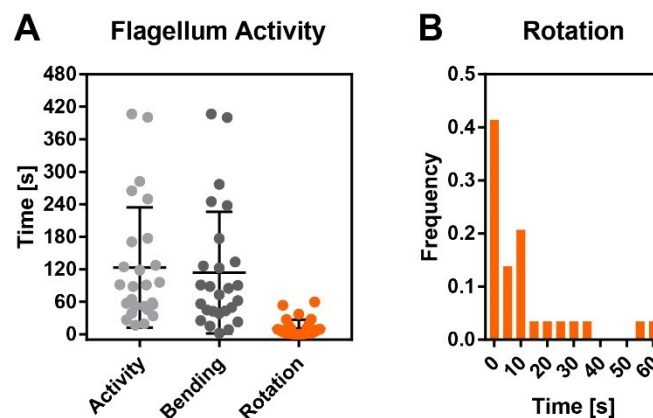


**Figure 4.3: Movement duration.** **A:** The overall activity ( $N = 26$ ) from first bending movement until cell separation (left) is divided into two parts, the bending part, where the predivisional cell shows a movement of the two cells together (center,  $N = 26$ ), and the rotation part, where the daughter cell rotates around its axis (right,  $N = 29$ ). **B:** Histogram of the rotation duration. Bin width: 5 s.

The bending movement of several predivisional cells from the first observed bending movement until the start of the rotation of the daughter cells was analyzed. We found that for the first observed bending movement ( $64 \pm 17$ ) % of the cells bent outwards, and ( $36 \pm 10$ ) % inwards relative to the cell curvature (Figure 4.4, Bending and Figure 4.5 for scheme of the assignment).

The duration of individual bending sequences was measured and we found that on average the outwards bending lasted ( $2.3 \pm 1.8$ ) s and the inwards bending lasted ( $0.4 \pm 0.2$ ) s (Figure 4.5, Bending).

When analyzing the rotational behavior of the daughter cells it was found that ( $67 \pm 19$ ) % of the observed cells started rotating around the long axis with rotating the cell body CCW, and the remaining ( $33 \pm 10$ ) % started CW (Figure 4.4, Rotation). The average rotation duration in CCW direction was ( $1.1 \pm 0.7$ ) s with 70 % of the cells rotating on average ( $0.8 \pm 0.5$ ) s. In CW direction the average duration was ( $0.6 \pm 0.6$ ) s with 90 % of the cells rotating on average ( $0.5 \pm 0.2$ ) s in CW direction (Figure 4.5, Rotation). More than half of the cells (58 %) made less than 50 rotations before separation (Figure 4.6A) and almost half of the cells (47%) did not change their rotation direction or changed the rotation direction once (33 %) until they separated from the mother cell. (Figure 4.6B). Many cells changed the rotation direction not more than once simply because they rotated only for a very short time before cell separation. The rotation trajectory in Figure 4.2E corresponds to the exceptional cell that rotated 450x around the long axis and made 10 reversals. The rotation frequency was lower when the cell rotated CCW than when it rotated CW. The average rotation frequency when rotating CCW was ( $20.4 \pm 15.0$ ) Hz and ( $29.9 \pm 25.6$ ) Hz when rotating CW (Figure 4.6C). The individual rotation speeds varied from cell to cell, but for every cell observed, the rotation in CW was faster than in CCW.

In the moment of cell separation ( $74 \pm 15$ ) % of the observed cells were rotating CCW and ( $26 \pm 5$ ) % were rotating CW (Figure 4.4, Separation). The finding that, for the first onset of rotation as well as the moment of cell separation, more than half of the cells rotated CCW raised the question whether rotating CCW is somehow beneficial to overcome the forces that are holding the cells together. CCW rotation might first allow the cells to perform their first rotation and then also helps to complete cell separation and release of the daughter cell.

It seems to be obvious that the activity of the flagellum is not only the reason for the rotation of the daughter cell, but also causes the observed bending movement of the predivisional cell. This would mean that the onset of the flagellar rotation takes place even before the rotation of the daughter cell is observed. Moreover, the change in the bending direction can be attributed to changes in the flagellum rotation direction. We analyzed the direction of the bending movement more closely and assigned the bending direction of the predivisional cell with a possible pulling or pushing movement of the flagellum, based on the geometry of the predivisional cell and the position of the flagellum. When the flagellum is pushing, it is likely to bend the predivisional cell

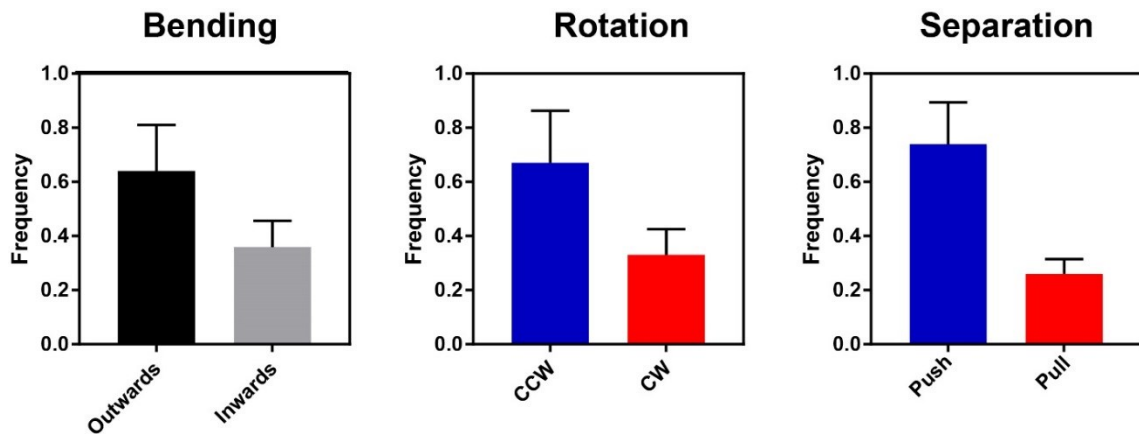


**Figure 4.4: Bending:** Normalized first observed bending direction (N = 14). **Rotation:** Normalized fraction of cells that start the rotation of the daughter cell in CCW, resp. CW direction (N = 12). **Separation:** Normalized fraction of cells that leave the mother right after cell separation as pushing cells (rotating CCW) respectively as pulling cells (rotating CW) (N = 23).

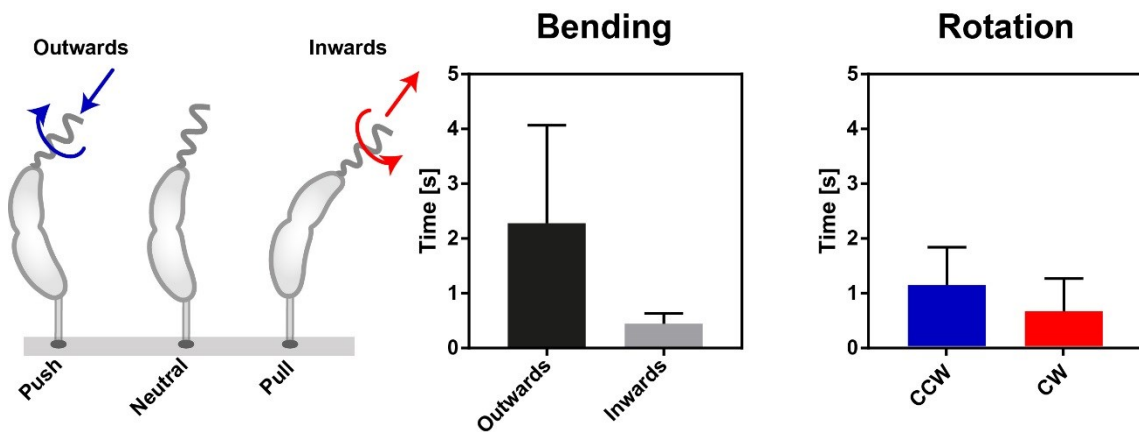


**Figure 4.5: Schematic representation:** Impact of flagellar rotation direction on bending of the cell body. **Bending:** Average duration of the flagellum pushing outwards or pulling inwards (N=2, 12 measurements per direction). **Rotation:** Average duration of the CCW and CW sequences of the predivisional daughter cell (N = 10, 17 sequences in CCW and N = 7, 11 sequences in CW).

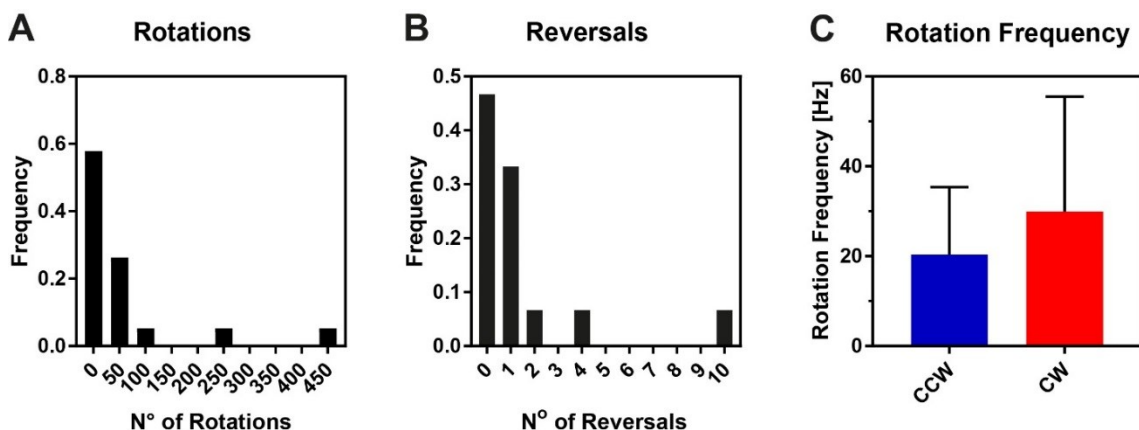


**Figure 4.6: Characterization of rotating daughter cells. A:** Normalized number of completed rotations of the predivisional cell before cell separation (N = 19). **B:** Number of changes in the rotation direction before cell separation (N = 15). **C:** Average rotation frequency of sequences in CCW, respectively CW direction (CCW: N = 11, CW: N = 7).

outwards, while the cell is bent inwards when the flagellum is pulling (Figure 4.5, scheme). The average outwards movement lasted 2.3 s and the average inwards movement lasted 0.4 s (Figure 4.5, Bending). We compared these times to the average durations of CCW and CW rotation of the rotating daughter cells. The average rotating duration was 1.1 s in the CCW direction and 0.6 s in the CW direction (Figure 4.5, Rotation). The similar length of the outwards movement sequences and the CCW rotation, and of the inwards movement sequences and CW rotation, respectively, is an indication that indeed the bending movement is caused by the rotation of the flagellum and that also during the bending movement the flagellum regularly changes its rotation direction. In both cases, the pre-rotational bending movement and the rotation, the pushing activity of the flagellum lasted longer than the pulling activity. This suggests that the distribution of the first rotation direction and the leaving direction (more cells in CCW mode) simply reflect the natural frequency of the two different rotation directions of the flagellum and are not an indication that CW rotation of the flagellum is more beneficial to overcome the forces that are holding the cells together, or to facilitate the rotation of the daughter cell and the subsequent cell separation. The duration of the observed pre-rotational bending movement is in the range of minutes, while the rotation of the daughter cells lasts seconds. It is also noteworthy, that the rotating flagellum has enough force to bend the non-attached pole of the predivisional cell several  $\mu\text{m}$ .

The assigning of the flagellar rotation direction to the bending direction of the predivisional cell is arduous because it depends on the geometry of the individual cell. Especially the exact determination of a switch, when the flagellum changes its rotation direction, is challenging because when the cell is going back in its neutral position it is impossible to tell whether the cell goes back in its relaxed state or whether it is actively forced by the flagellum. Therefore, we were in need for another method to better determine the rotation direction of the flagellum when the two cells are still stiffly connected. We also wanted to employ a method that allows the determination of the forces generated by the flagellum.

#### 4.4.2 Hydrodynamics of the Flagellum – The Loaded Swimmer

To better resolve the duration of the pushing and pulling sequences of the flagellum during the bending movement and to understand the hydrodynamic conditions, we developed a method which is more sensitive to flagellum-induced forces. Instead of focusing on cells attached onto the surface of the microfluidic device, we observed cells attached onto micrometer-sized polystyrene beads (“loaded swimmers”), recorded the predivisional cells and analyzed the duration and magnitude of the flagellum induced motion. Because the beads with the attached cells were suspended in liquid and could change their local positions a wider field of view was necessary. This demanded a reduction of the recording frame rate. To capture the duration of the total flagellar activity, the frame rate was decreased to 10 – 20 Hz. The cells were able to move in all three dimensions, leading to images of cells that were not always in focus. The exact position of the predivisional cells could still be determined via the beads they were attached to. Even in cases where a cell was out of focus, the position of the bead could be clearly determined. The only drawback of this method was that the start of the rotation of the daughter cell and the rotation direction could not always be determined because of the low frame rate and because the cells were not in focus enough.

##### 4.4.2.1 Attachment of Cells on Beads

We made use the ability of *C. crescentus* to “readily and happily” attach to nearly any available surface and ensured that the cells attached to small polystyrene beads with different surface properties. We found that the cells attach easily and quickly onto the beads and that the attachment efficiency for permanent attachment, that means holdfast formation, depends on the surface properties of the bead. Three differently functionalized surfaces were tested: non-functionalized surfaces (polystyrene), carboxylate groups (carboxylate) or primary amine groups (amino). Cells showed the highest attachment rate for carboxy-coated beads, followed by non-functionalized polystyrene beads and amino-coated beads (Figure 4.7A). The number of cells per bead increased over time. First attachment of cells on beads was already observed within minutes after addition of the beads to the cell suspension. The number of cells attached to a bead was not only determined by the surface coating and the incubation time, but also by the size of the bead (Figure 4.7B). Larger beads accommodate more cells. Up to 15 cells were found to be attached on beads with a diameter of 3  $\mu\text{m}$  (about 1 cell per 1.9  $\mu\text{m}^2$ ) and up to 7 cells were found on beads with a diameter of 1  $\mu\text{m}$  (about 1 cell per 0.45  $\mu\text{m}^2$ ).

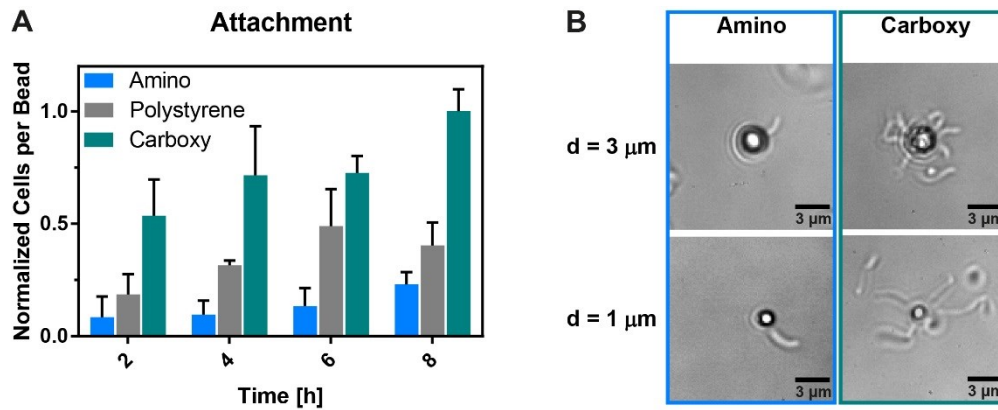


**Figure 4.7: Surface attachment efficiency.** **A:** Normalized numbers of attached cells per bead. **B:** The number of cells attached to a bead depends on the size and the surface coating of the bead. Shown are amino- and carboxy-coated beads, with a diameter of 3 μm (top) and 1 μm (bottom).

#### 4.4.2.2 Hydrodynamics of the Loaded Swimmer

We found that cells permanently “self”-attached to 1 μm beads via a holdfast and subsequently formed a stalk, transitioning from swarmer cells to stalked cells, as if they were attached to a flat, solid surface (Figure 4.1). Surprisingly, cells reaching the late predivisional stage started to swim, dragging the attached bead with them. A sequence of bright field images of a swimming cell attached via a stalk and a holdfast to a colloidal bead is shown in Figure 4.8A. Because the cell can only be attached to the bead via the pole that contains the holdfast and stalk, the mother cell is the cell closer to the bead while the daughter cell is the cell further away from the bead. The flagellum is located at the free pole of the daughter cell (Figure 4.8B and arrow indicating the flagellated pole in the first frame of Figure 4.8A). This condition simplifies the determination of the swimming direction and therefore the rotation direction of the flagellum to a large extent. When the flagellum is rotating CW, it generates a pushing movement and the cell swims forward. When the flagellum is rotating CCW, it generates a pulling movement and the cell swims backwards. In Figure 4.8 and Figure 4.9 forward swimming is indicated in blue and backward swimming in red. We tracked the position of the bead over time. An example trajectory of two forward and two backward swimming sequences is shown in Figure 4.8C. The swimming speed and the directions are plotted in Figure 4.8D. When swimming backwards (CCW rotation of the flagellum), the cell swam slightly faster than forward (CW rotation of the flagellum). Forward swimming speed was on average  $(12.8 \pm 6.1) \mu\text{m/s}$  and backward swimming speed was on average  $(17.7 \pm 6.5) \mu\text{m/s}$ . The cell spent about 2/3 of its swimming time swimming forward and about 1/3 swimming backwards. The distribution of swimming forward and backwards respectively CCW and CW rotation of the flagellum is in good agreement with what was found for cells attached to a solid surface and published data for free swarmer cells<sup>64</sup>.

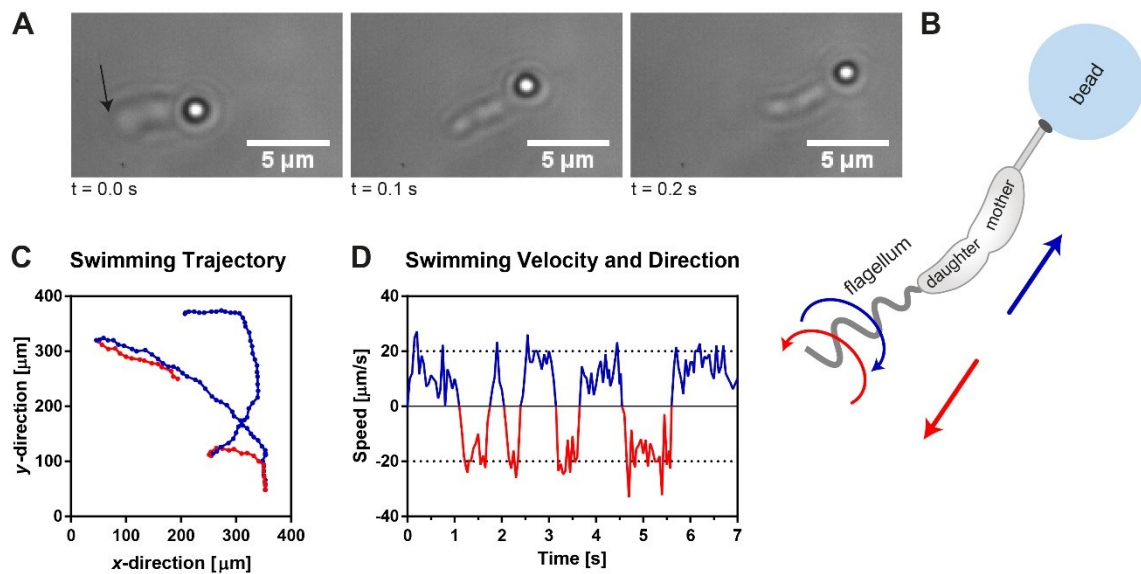


**Figure 4.8: Example of a swimming predivisional cell attached to a small bead.** **A:** Consecutive bright field images of a swimming predivisional WT cell attached to a polystyrene bead with diameter 1  $\mu\text{m}$  in PYE. The arrow indicates the flagellated pole. **B:** Scheme of the predivisional cell attached to the bead (CW rotation of flagellum, causing forward swimming: blue. CCW rotation of flagellum, causing backward swimming: red) **C:** Example trajectory of the swimming cell. Forward swimming: blue, backward swimming: red. **D:** Swimming velocity of the cell attached to the bead. Forward swimming: blue, backward swimming: red.

We observed two different behaviors in the swimming of the predivisional cells. At the onset of the swimming the connection between the mother and the daughter cell is stiff and the predivisional cell halves do not change their positions relative to each other. Just a few seconds before cell separation, the daughter cell starts to rotate around its long axis while still connected to the mother cell. This indicates a weakening of the connection between the two cells. The stiff connection that enabled the stable swimming of the cell attached to the bead is weakened and the interface between the two cells becomes soft enough to allow the rotation of the daughter cell. Cell separation is completed when the daughter cell swims off, while the mother cell stays attached to the bead and does not exhibit any motion anymore except of Brownian motion. The two different stages during the flagellar activity before cell separation resembled what we have found for the cells attached to a solid surface. There, the overall movement could also be classified in two different stages, the bending movement, where the connection between the predivisional cells was still strong, and the rotation movement of the daughter cell, where the connection between the two cells was softened and allowed the rotation of the daughter cell.

We determined the duration of the different movement behaviors for several cells. The overall flagellar activity, from the onset of swimming until cell separation lasted on average ( $99.8 \pm 57.3$ ) s, with durations ranging from 40 s up to 3 min (Figure 4.9A, left). The pre-rotational movement, when mother and daughter cell are still firmly connected lasted

( $89.1 \pm 71.3$ ) s on average (Figure 4.9A, center) and had similar duration as was found for the total flagellar activity. The observed swimming of the predivisional cell consisted mainly of the stage when the connection between mother and daughter is still stiff. The short part when the daughter cell is free to rotate but is not yet separated from the mother was found to last on average ( $10.3 \pm 7.6$ ) s (Figure 4.9A, right) and ranged from 2 s up to 17 s. The exact determination of the onset of the rotation of the daughter cell was difficult because the cells were free to move in 3D and were often not in focus enough to determine whether the daughter cell was rotating or not.

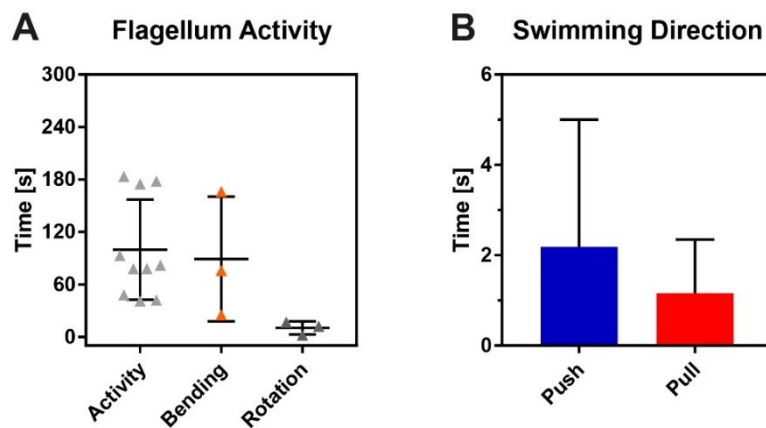


**Figure 4.9: Characterization of predivisional cells attached to small beads.** **A:** Flagellar activity before cell separation. The overall activity ( $N = 10$ ) from first observed swimming until cell separation (left) is divided into two parts, the swimming part (center,  $N = 3$ ), and the rotation part (right,  $N = 29$ ). **B:** Average duration of individual forward (push) and backward (pull) swimming sequences ( $N=3$ , 39 measurements per direction).

We found that in this set-up the average pushing sequence (CW rotation of the flagellum) lasted ( $2.2 \pm 2.8$ ) s with 90 % of the measured pushing sequences lasting on average ( $1.5 \pm 1.6$ ) s. The average pulling sequence (CCW rotation of the flagellum) lasted ( $1.2 \pm 1.2$ ) s with 90 % of the pulling sequences lasting on average ( $0.9 \pm 0.7$ ) s (Figure 4.9B). A rough distribution of about 2/3 pushing and 1/3 pulling, which is very similar to the distribution of the rotation direction in Figure 4.5, is obtained. The determination of the flagellar rotation direction and duration when the cells are still strongly connected is straightforward in this system and less challenging than the assignment of the flagellar rotation direction to the bending direction when cells are attached to a solid surface. Especially the exact moment of the flagellar rotation switch could be better resolved. We found that the flagellum is indeed already active 2 - 3 minutes before we can observe the rotation of the daughter cell.

#### 4.4.2.3 Force Generated by Free Swimming Cells

To determine the forces that are generated when the flagellum is propelling a cell, we determined the swimming speed of swarmer cells, predivisional cells and predivisional cells attached to small polystyrene beads. We calculated the friction factor  $\gamma$  for the different cell shapes and sizes and determined the average force  $\vec{F}$  with the following formula where  $v$  is the average swimming speed:

$$\vec{F} = \gamma \cdot \vec{v} \quad (4.1)$$

The cell is not only moving translational, but also rotates around its own axis at a certain frequency. The rotational friction coefficient is small ( $9.1 \cdot 10^{-22} \frac{\text{N} \cdot \text{m} \cdot \text{s}}{\text{rad}}$ )<sup>29</sup> compared to the translational friction coefficient  $\gamma_{\text{cell}} = 6.8 \cdot 10^{-9} \frac{\text{N}}{\text{m}} \text{s}$ <sup>29</sup>, therefore the rotational part was neglected when calculating the flagellar force  $\vec{F}$  used for swimming.  $\gamma_{\text{cell}}$  was previously determined by Li et al.<sup>29</sup> in the following way: The most critical parameter for the determination of the translational friction coefficient is the cell half-width. It cannot be measured directly because of the crescent-shaped cell body, that requests a nominal half-width instead of the actual half width of the cell body<sup>29</sup>. To calculate the nominal half width, the torque of the motor was determined via tethered cells and the friction factor of the flagellum was determined using published data<sup>31</sup> and the finding that the average length of a filament is  $6 \mu\text{m}$ <sup>29</sup>. The torque of the motor was calculated from the experimentally determined swimming speed and rotation rate of the cell body. From the motor torque finally the nominal cell half-width was obtained and from this  $\gamma_{\text{cell}}$  was calculated<sup>29</sup>. The translational drag coefficient of the flagellum was obtained in a similar way by Li et al.<sup>29</sup> and was found to be  $\gamma_{\text{flag}} = 9.8 \cdot 10^{-9} \frac{\text{N}}{\text{m}} \text{s}$ <sup>29</sup>. Again, the rotational drag coefficient was small ( $2.0 \cdot 10^{-22} \frac{\text{N} \cdot \text{m} \cdot \text{s}}{\text{rad}}$ )<sup>29</sup> compared to the translational drag coefficient and therefore neglected.

We used the published value of  $\gamma_{\text{cell}}$  and  $\gamma_{\text{flag}}$  to calculate the forces of swimming cells. For swarmer cells we found an average swimming speed of  $v_{FS} \approx 60 \frac{\mu\text{m}}{\text{s}}$ . The net propelling force of the flagellum was then calculated as  $F_{FS} = (\gamma_{\text{cell}} + \gamma_{\text{flag}}) \cdot v_{FS} \approx 1.0 \text{ pN}$ .

When cells do not find a surface to attach during the swarmer phase, they enter the replication phase nonetheless. The flagellum of the newly formed daughter cell is active several minutes before cell separation, during this time-window non-attached predivisional cells are able to swim. We found an average swimming speed of  $v_{PD} \approx 25 \frac{\mu\text{m}}{\text{s}}$  and the friction factor  $\gamma_{PD}$  was

approximated by  $\gamma_{PD} \approx 2 \cdot \gamma_{cell} + \gamma_{flag}$ , obtaining a net propelling force of the flagellum in swimming direction of about  $F_{PD} = \gamma_{PD} \cdot v_{PD} \approx 0.59$  pN.

For predivisional cells attached to a polystyrene bead of 1  $\mu\text{m}$  diameter, we found an average swimming speed of  $v_{CB} \approx 20 \frac{\mu\text{m}}{\text{s}}$ . The friction factor was approximated by  $\gamma_{CB} \approx 2 \cdot \gamma_{cell} + \gamma_{flag} + \gamma_{bead}$ , where the friction factor of the bead is calculated with  $\gamma_{bead} = 3\pi\eta d = 9.4 \cdot 10^{-9} \frac{\text{N}}{\text{m}}\text{s}$  with the viscosity of the medium  $\eta = 1.0 \text{ mPa} \cdot \text{s}$  and the diameter of the bead  $d = 1 \mu\text{m}$ . From this we calculated the net propelling force  $F_{CB}$  of the flagellum in swimming direction of about  $F_{CB} = \gamma_{CB} \cdot v_{CB} \approx 0.66$  pN.

The swimming speed, friction factor and generated forces for the different cell shapes and sizes are shown in Figure 4.10. The higher force generated by the flagellum of the swarmer cell is probably due to better stability of the single cell compared to the predivisional cell and the predivisional cell attached to a bead.

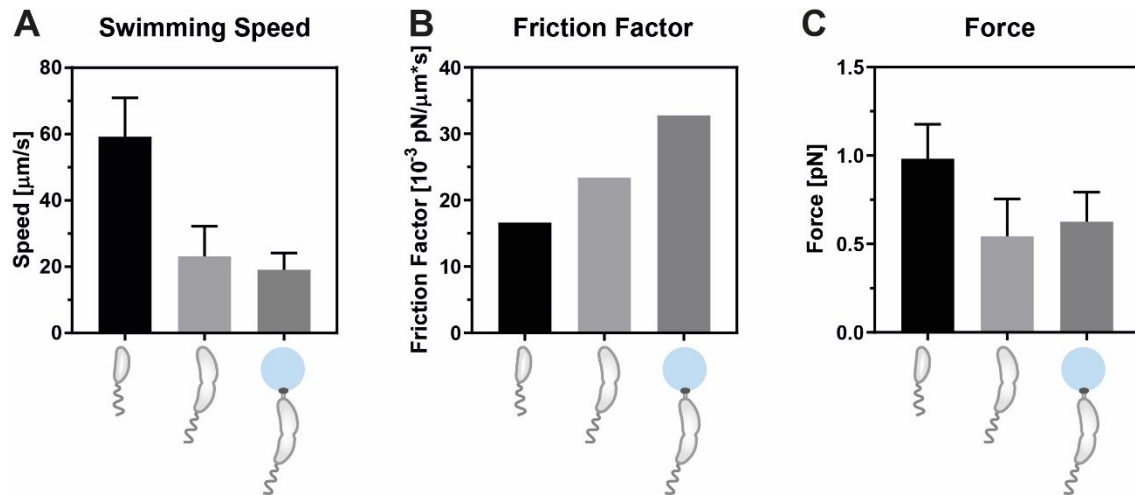


**Figure 4.10: Forces generated by the flagellum.** **A:** Average swimming speed of a swarmer cell, a predivisional cell and a predivisional cell attached to a bead (from left to right). **B:** Friction factor of the corresponding cell shapes and sizes. **C:** Net force generated by the flagellum to propel the indicated cell shapes and sizes forward at the average swimming speed.

#### 4.4.3 Force Generation and Hydrodynamics – The Trapped Swimmer

To better resolve the forces generated by the flagellum over time, parallel force measurements and imaging of the dynamics during cell separation of *C. crescentus* cells with a high temporal and spatial resolution were carried out by optical trapping. In this approach, we ensured that the cells attached to polystyrene beads and additionally immobilized the bead by optical tweezers in a microfluidics channel (“trapped swimmer”). A strict no flow regime was installed. A scheme of the method is shown in Figure 4.11A. The set-up allows for immobilization of the bead and force measurements via the optical tweezers, while the bright-field microscope enables fast imaging of the position of the bead and cell as well as the movement of the cell. The cells were recorded with 50–100 Hz. For the analysis, the position of the bead was tracked, indicated by the yellow ring in the top view scheme (Figure 4.11A). Beads with carboxylate groups coated surfaces with a diameter of 3  $\mu\text{m}$  were chosen as substrate. Using the larger beads, the attached cells are further away from the focused laser beam, therefore decreasing the amount of stray light that could inflict damages on the cells.

A series of bright field images of a predivisional cell attached to a polystyrene bead is shown in Figure 4.11B. Two cells are attached to the bead, the predivisional cell is indicated by an arrow in the first image in the first panel. In the first panel (top most, from left to right) the flagellum of the predivisional cell is not yet active and the only motion observed is Brownian motion. In the following panel (2<sup>nd</sup>), the flagellum is active, the predivisional cell changes actively its position and moves in a gyrating way in CW direction. When the connection between the two predivisional cells is softened, the daughter cell rotates around its axis (3<sup>rd</sup> panel). The last step is cell separation (4<sup>th</sup> panel), the daughter cell swims away (indicated by an arrow in frames 1 and 2 on the 4<sup>th</sup> panel). After cell separation the bead does not show any other movement except of Brownian motion. This strongly indicates that the active flagellum of the predivisional cell was the only source for the gyrating motion. The trajectories of the bead for each of the four described states are shown in Figure 4.11C. When the flagellum is not active, the bead shows only little displacement (black curves, before flagellar rotation starts and after cell separation). When the flagellum is active the movement of the cell can be seen in the displacement of the bead (red-orange for the stiff cell connection, yellow-orange for the soft cell connection) because the cell exerts gyrational and translational forces inside the optical tweezers. The observed trajectory displays the net of the effective gyrational and translational forces. Corresponding schemes, illustrating the individual stages of cell separation shown in B and C are shown in Figure 4.11D.

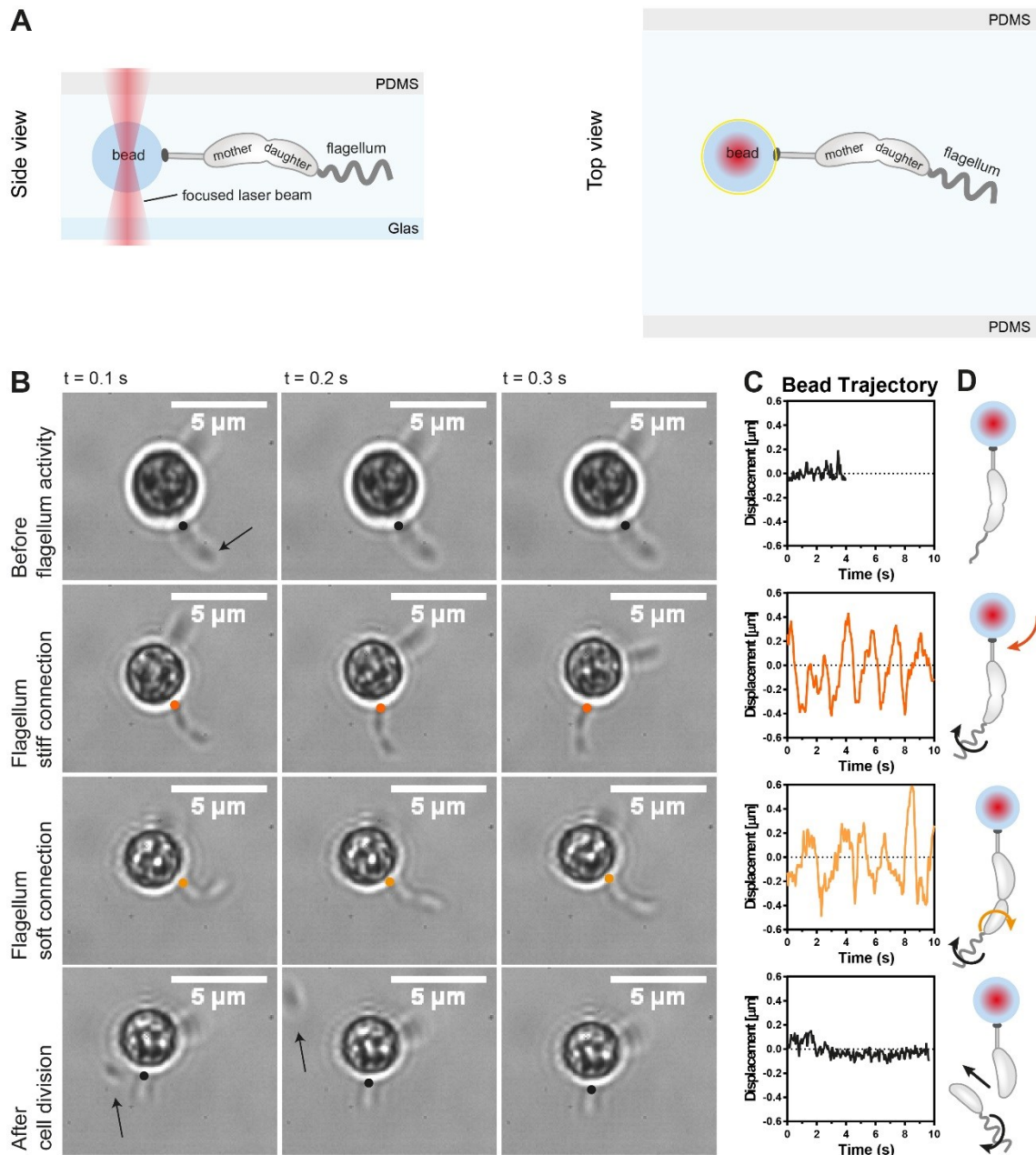


**Figure 4.11: Predivisional cell attached to a bead in optical tweezers.** **A:** Scheme of the technical set-up. A bead (blue) with a predivisional cell attached is held by optical tweezers (red) in a microfluidic channel (grey for the PDMS part, light blue for the glass slide). In yellow, the outline of the bead is highlighted in the top-view. **B:** Bright field images of two WT cells attached to a bead in the optical tweezers. The predivisional cell is indicated by an arrow in the first frame in the first panel. The dots indicate the position of the stalk. First panel: No active flagellum, the only movement is Brownian motion. Second panel: Rotation of the flagellum, the cell and the bead show a gyrational motion. 3<sup>rd</sup> panel: Connection between mother and daughter cell is loosened; the daughter rotates around its long axis. 4<sup>th</sup> panel: Cell separation is finished; the daughter cell swims off (first and second image, indicated by an arrow). The bead with the two remaining cells attached shows Brownian motion. **C:** Trajectories of the bead for the corresponding states described in B. **D:** Scheme illustrating the cell separation process. The red-orange indicates the stiff cell connection, the yellow-orange indicates the soft cell connection.

We introduce a new read-out that allows us to decouple the translational movement from the rotational movement. For the determination of the rotational movement, the position of the cell over time is followed and displayed. For a Gyratograph, a ring-shaped line is placed on a stack of images, covering the cell, but not the bead. For each frame the intensity for each pixel under the ring-shaped line is determined. The ring is cut open and the intensities along the ring for each frame are displayed on a line from 0 to  $2\pi$  (Figure 4.12A). The time is displayed along the x-axis. This allows the determination of the cell position independently of the displacement of the bead. When the cell is not moving, a horizontal line is displayed on the Gyratograph, as the cell does not change its position over time. The line is a bit blurred due to thermal noise in the system. When the cell starts gyrating around the center of the optical tweezers, a straight diagonal line is formed, because the gyration speed is constant (Figure 4.12B). The steepness of the slope depends on the angular velocity of the cell, the faster the cell gyrates, the steeper the slope. The sign of the slope is determined by the direction of the gyration of the cell. For validation of the Gyratograph, we manually tracked the position of the stalk and found that the direction of the gyration around the center changed after several seconds from CW to CCW and back. We assigned a pushing movement of the flagellum to a CW gyration direction and a pulling movement to a CCW gyration (this assignment is only valid for the example cell presented here, for other cells it may be inverted, because it depends on the orientation of the attached cell). An example trajectory where the cell and the bead switches from gyrating CW (pushing, blue) to gyrating CCW (pulling, red) and back to gyrating CW (pushing, blue) is shown in Figure 4.12C. For better visualization and to also display the duration of the individual sequence, the x- and y-positions of the tracked stalk are plotted against time in Figure 4.12D. Changes in the gyration direction are indicated with stippled lines and the colors represent the assigned directional movement of the flagellum. The corresponding Gyratograph of the same sequence is shown in Figure 4.12E. Reversals in the gyration direction change the direction of the slope and are indicated with yellow triangles for better visualization. A close-up of four reversals is shown in Figure 4.12F. From the slope, the gyration speed can be directly calculated. We found that the gyration speed in both directions is roughly the same, around 0.8 revolutions/s. CW gyration is highlighted in blue, while CCW gyration of the bead is highlighted in red. We found that for the example cell presented here the duration of the assigned pushing sequences is usually longer (around 4 s) than the duration of the assigned pulling sequences (around 1 s).

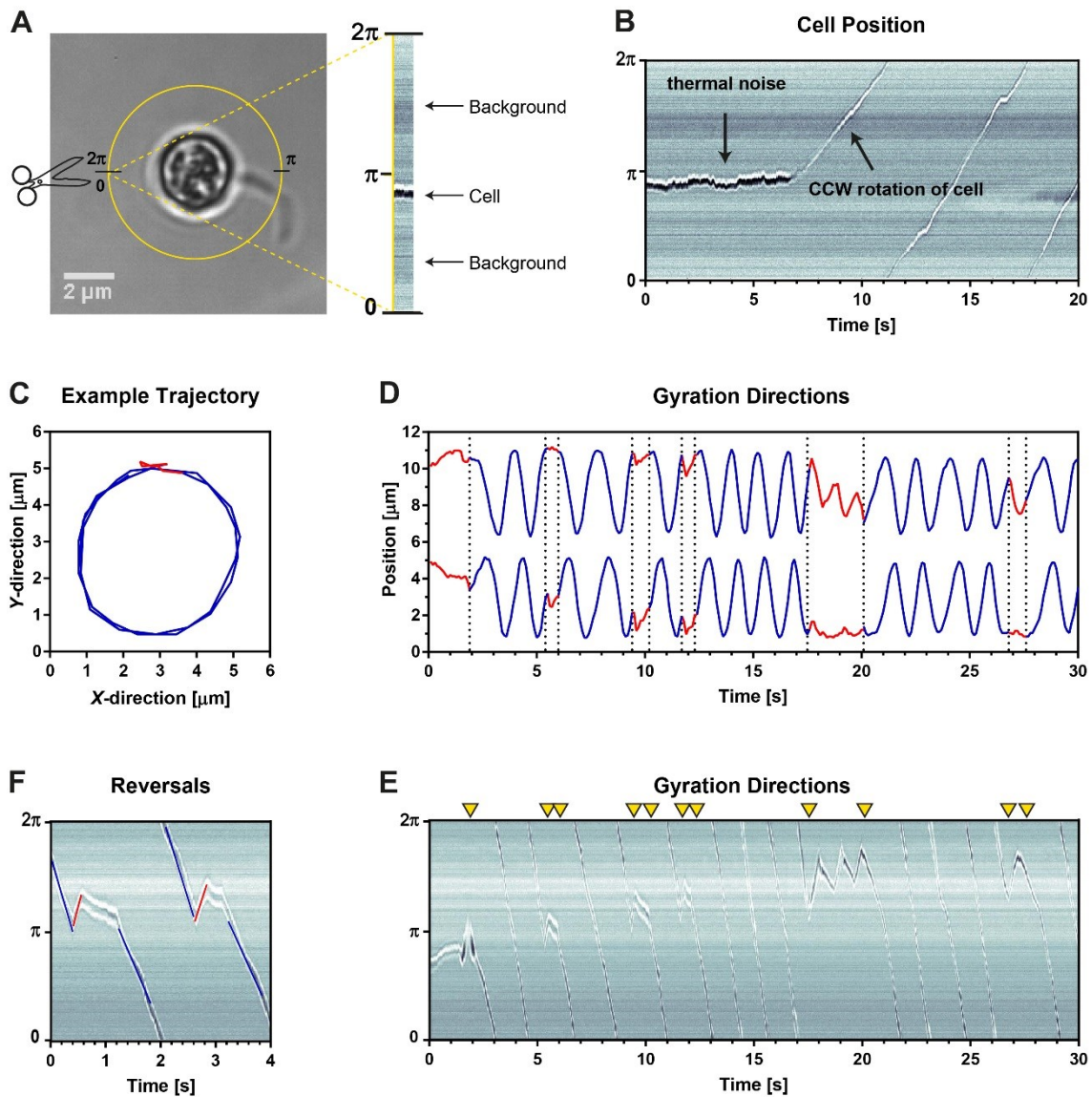


**Figure 4.12: Reversals in the circular movement.** **A:** Generation of a Gyratograph. For each frame, the intensity for each pixel on the circular ring is determined. The ring is cut open and linearized. The intensities of each frame are displayed on a line from 0 to  $2\pi$ . **B:** When the cell is not moving, a horizontal line is formed. Thermal noise causes a blurring of the line. When the cell is gyrating, the plot shows a diagonal line. **C:** Example trajectory of the gyrating movement including a direction change from outwards movement (blue) to inwards movement (red) and back to outwards movement (blue). **D:** Gyration direction of the cell around the center of the optical tweezers. The displacements in  $x$ - and  $y$ -directions are plotted separately (top:  $x$ -direction, bottom:  $y$ -direction). Changes in the direction are indicated with stippled lines. **E:** Gyratograph of the same sequence as in D. Changes in the gyration direction are indicated with yellow triangles. **F:** Inset with four direction changes. When the cell changes its gyration direction, the slope of the changes its sign. The colors indicate the assigned movement of the flagellum.

For verification that the gyrational movement is induced by the rotating flagellum and that the changes in the gyration direction are induced by a rotation change of the flagellum, cells with a mutated flagellum were tested for their behavior in the optical tweezers. We tested cells with a flagellum that could only rotate CW and never changed its rotation direction ( $\Delta cheYII$ ) and cells with a mutation that did not allow the assembly of the outer parts of the flagellum ( $\Delta flgDE$ ). A comparison of the bead trajectories and Gyratographs of WT (A and B),  $\Delta cheYII$  (C and D) and

$\Delta flgDE$  (E and F) is shown in Figure 4.13. In the WT Gyration graph several reversals can be observed until cell separation occurs (stippled line). In the Gyration graph of the  $\Delta cheYII$  mutant no change of the gyration direction could be detected. For the  $\Delta flgDE$  cell, that does not have a flagellum at all, no difference in the bead trajectory before and after cell separation is visible. Whereas the WT and  $\Delta cheYII$  daughter cell is not visible anymore in the Gyration graph after cell separation (indicated by the stippled line) because it swims away, the  $\Delta flgDE$  cell remains on the Gyration graph for several seconds until it diffuses away.

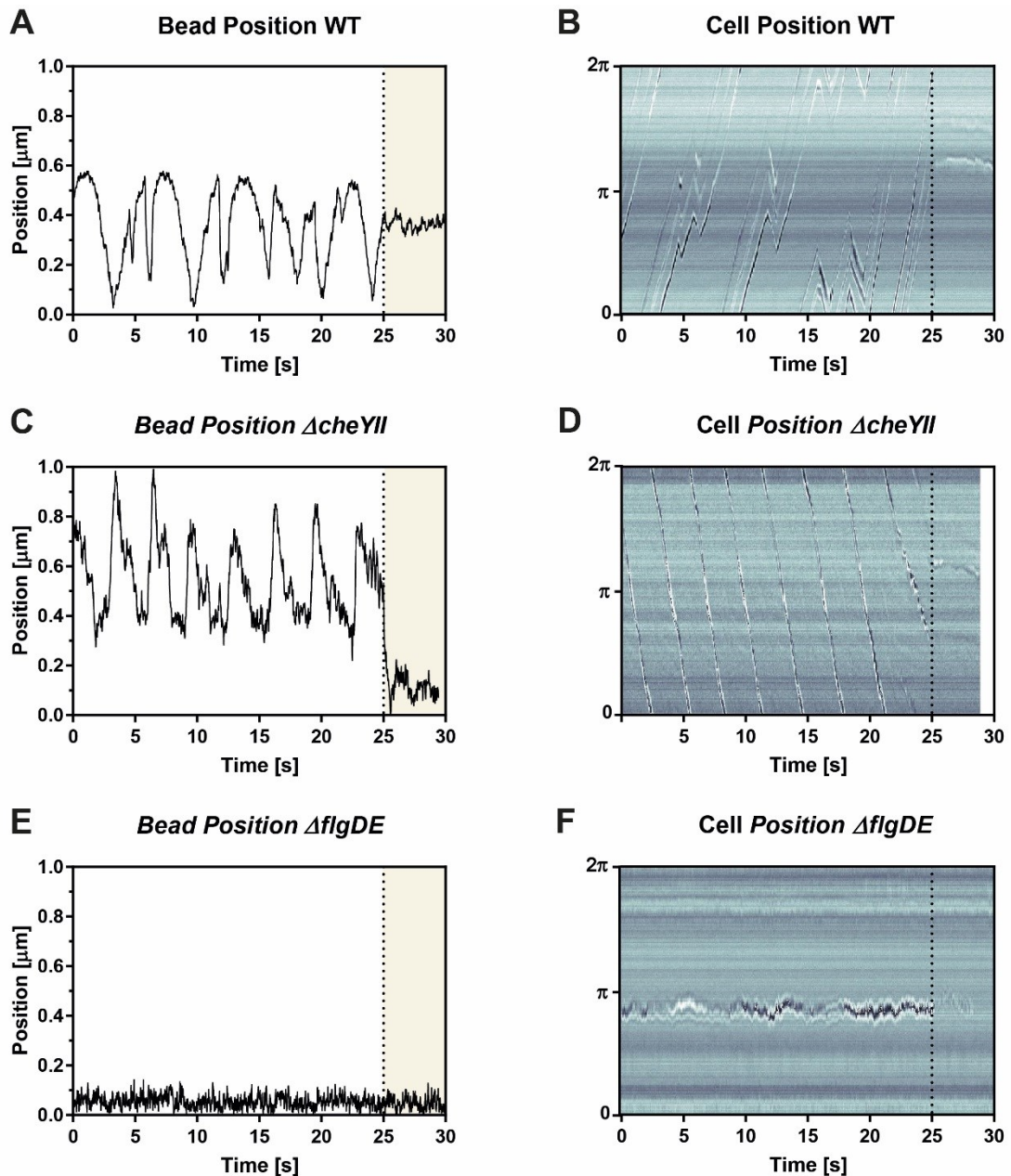


**Figure 4.13: Bead and cell position of different mutants:** A, C and E: Bead trajectory for WT,  $\Delta cheYII$ , and  $\Delta flgDE$ . White area: the daughter cell is not yet separated from the mother. Beige area: completed cell separation. B, D and F: Gyration graph of WT,  $\Delta cheYII$ , and  $\Delta flgDE$ . Cell separation is indicated by a stippled line.

When analyzing different cells attached to beads, the total observed duration of the gyrational movement, from the onset of flagellar rotation until cell separation, was found to last on average ( $202.7 \pm 140.4$ ) s while the duration differs a lot from cell to cell, ranging from 20 s to 7 min of total predivisional movement (Figure 4.14A, left). We observed two different stages during the gyrational movement of the predivisional cell. During the first stage the two predivisional cells were still firmly connected and the outline of the cell shape did not change during gyration. This stage lasted on average ( $194.5 \pm 139.8$ ) s and the distribution is very similar to the duration found for the total activity duration (Figure 4.14A, center). In the second stage, the connection between the cells was softened and the daughter cell rotated around its long axis. This stage lasted from the first observed rotation of the daughter cell until the cells completed cell separation and was on average ( $6.7 \pm 11.8$ ) s (Figure 4.14A, right). Most of the cells rotated less than 10 s before cell separation occurred. The duration of the overall flagellar activity and the time intervals of the two different stages are pretty similar to the results for the solid surface attached cells and for the cells attached to the smaller beads. With this method, the cell moved preferentially in 2D and was easier to be kept in focus compared to the cells attached to the  $1 \mu\text{m}$  beads. Because of that, the onset of the flagellar rotation and the transition from stiff cell connection to soft cell connection and rotation of the daughter cell could be determined more exactly.

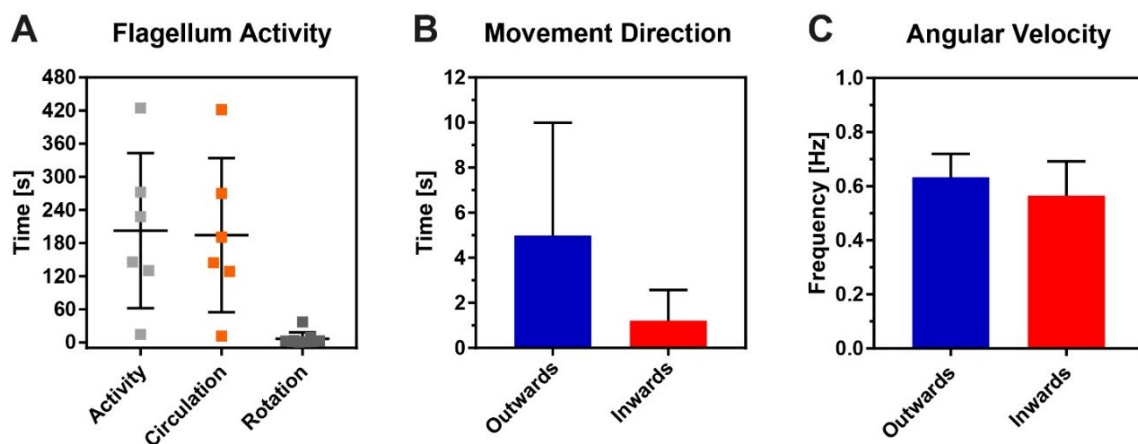


**Figure 4.14: Characterization of predivisional cells attached to beads in optical tweezers.** **A:** The overall activity ( $N = 6$ ) from first observed gyrational movement until cell separation (left) is divided into two parts, the gyrational part, where the predivisional cell shows a movement of the two cells together (center,  $N = 6$ ), and the rotation part, where the daughter cell rotates around its own axis. ( $N = 6$ ). **B:** Average duration of individual sequences, pushing outwards (blue) and pulling inwards (red), ( $N=3$  cells, 36 measurements for pushing sequences, 31 measurements for pulling sequences). **C:** Angular velocity for sequences pushing outwards (blue) or pulling inwards (red), ( $N = 3$ ,  $n = 19$  for pushing sequences,  $n = 15$  for pulling sequences).

We analyzed the duration of the assigned pushing (outwards movement) and pulling (inwards movement) sequences for several cells and found that the assigned pushing sequences lasted longer than the assigned pulling sequences (Figure 4.14B). The average push sequence lasted  $(5.0 \pm 5.0)$  s and the average pull sequence lasted  $(1.2 \pm 1.4)$  s. While the duration of the pulling sequences was comparable to the duration found for the natural set-up and trapped swimmers, the duration of the pushing sequence was longer for the cells in the optical tweezers. The difference could be due to the geometry of the cells attached to the beads. Because the force induced by the flagellum acts tangential onto the bead it is possible that a change of the rotation direction of the flagellum does not in every case induce a change in the direction of the gyration.

The angular velocity of the gyrating cell around the center of the optical tweezers was  $(0.63 \pm 0.09)$  Hz when the cells showed an outwards movement and  $(0.57 \pm 0.13)$  Hz when the cells showed an inwards movement to the curvature (Figure 4.14C).

#### 4.4.3.1 Force Generated by Trapped Cells

The forces that are generated by the flagellum cause a gyration of the trapped swimmer within the optical tweezers, overlaid by periodically arising translational displacements (Figure 4.11). The net force used for the gyration can be approximated by calculating the rotational force at the surface of the bead in tangential direction:  $F_{\text{rot}} \approx 2\pi\eta d^2\omega$  with the viscosity of the medium  $\eta = 1.0$  mPa · s and the diameter of the bead  $d = 3.0$   $\mu\text{m}$ . With the rotation frequency of  $\omega = \frac{2\pi}{T} \approx 5.2 \frac{1}{\text{s}}$  with  $T = 1.2$  s per revolution, a net rotational force of  $F_{\text{rot}} \approx 0.29$  pN can be calculated. The calculated force is most likely underestimated in this case, because the drag induced by the cell body was neglected.

The periodically arising translational displacements can locally reach displacements up to 300 - 400 nm. The translational forces  $F_{\text{trans}}$  can be calculated by considering the stall force of the optical tweezers:  $F_{\text{trans}} = \kappa \cdot \Delta r$  where  $\kappa$  is the stiffness of the optical tweezers and  $\Delta r$  is the displacement of the bead from the center of the optical tweezers. With maximal displacements of  $\Delta r = 300 - 400$  nm and  $\kappa = 0.003$  pN/nm maximal peak translational forces of  $F_{\text{trans}} = 1.2 - 1.5$  pN can be reached.

The calculated net rotational force generated by the flagellum of about 0.3 pN is similar to the calculated net propulsion forces for the swimming cells (single, predivisional, predivisional attached to bead). However, the maximal generated forces of the flagellum depend on effective directions and positions and can be higher.

#### 4.4.4 Immediate Onset of Flagellar Rotation

To determine the onset of the flagellar rotation, we analyzed the displacement of the bead over time just right before the rotation of the flagellum was manifested by a gyrational and translational displacement of the bead (Figure 4.15A and B). In some cases, the onset of flagellar rotation could be determined clearly from the trajectory of the bead. The stage with no gyration could be clearly distinguished from the gyration part, therefore the start of the flagellar rotation could be clearly identified (Figure 4.15A). The grey area indicates no flagellar rotation (purely Brownian motion in the optical trap), while the zone with the white area indicates the impact of flagellar rotation onto the bead position. In other cases, the exact onset of the flagellar rotation was not obvious, as exemplified in Figure 4.15B. The transition from no flagellar rotation to clearly distinguishable circular movement caused by the flagellar rotation took longer and was noisier. This raised the question whether the start of the flagellar rotation happens immediately or gradually. To better resolve this question, we used the Gyrotograph to display the position of the bead and uncouple the rotational position of the cell from the displacement of the bead. The Gyrotograph of the two cells that are shown in Figure 4.15A and B are shown in Figure 4.15C and D. One single cell is attached to the bead that is shown in Figure 4.15A and C, this results in one single line on the Gyrotograph in Figure 4.15C. The transition from no flagellar rotation to gyrational motion caused by the flagellar rotation is indicated by a stippled line. The slope of the line indicates the speed of the gyration, the steeper the slope, the faster is the gyration. Four cells were attached to the bead shown in Figure 4.15B and D and the position of three of these cells was analyzed on the Gyrotograph (one of the cells was too short to fit in the ring). Therefore, three lines are visible in the Gyrotograph at any given time point. The intensity of the lines varies because the cells were not always in the same focus. The distances between the lines do not change because the position of each cell is fixed on the bead and the distances between the cells do not change. From the analysis of the Gyrotograph we found that there is no transition area between no movement and full speed gyration. Instead, gyration immediately starts with its final speed. This indicates an immediate onset of the flagellar rotation with its final rotational speed. This means that the flagellum is already fully assembled when the rotation of the flagellum starts, as an increasing length of the flagellum would lead to an increasing gyration speed. It is unlikely that a varying length of the flagellum and motor rotation speed would linearly depend on each other. Therefore, the data suggests a two-step process: First, flagellum assembly, and second, the onset of flagellar rotation. The difference in the way the rotational start was manifested in the two presented bead trajectories (Figure 4.15A and B)

could be due to different geometries of the attached cells. The stalk could have a different length or the angles with which the cell is attach to the bead might be different.

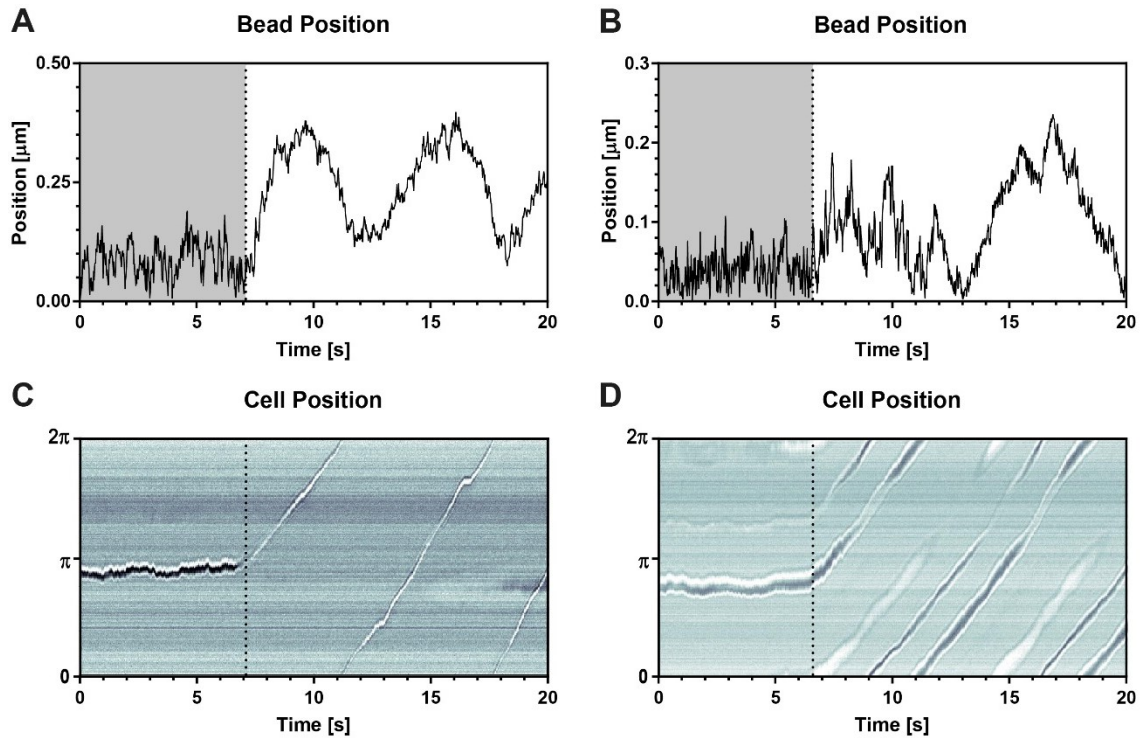


**Figure 4.15: Start of the flagellar rotation.** **A** and **B**: Position of the bead in the optical tweezers. The inactive flagellum has a grey background, the active flagellum has a white background. **C** and **D**: Gyratographs of the cells shown in **A** and **B**. The onset of the flagellar rotation is indicated by a stippled line.

#### 4.4.5 Weakening of the Connection between Mother and Daughter Cells

Predivisional cells undergo a transition from a stiff connection between the two cells to a soft connection between the two cells. The flagellum is already active before this transition takes place. Depending on the state of connection between the two cells, the motion induced by the flagellum varies. When the predivisional cells are still firmly connected, the two cells move together, causing gyration of the bead in the optical tweezers. When the connection is softened, the daughter cell is still attached to the mother cell, but rotates around its long axis. A trajectory of the bead at the transition from stiffly connected to softly connected is shown in detail in Figure 4.16A. In the white area, the predivisional cells are still firmly connected, in the dark grey area the daughter cell rotates around its long axis, and in the beige area cell separation is completed, the daughter cell is leaving the mother cell. The same sequence as in **A** is displayed in a Gyration in Figure 4.16B. An inset of the bead displacement is shown in Figure 4.16C. The solid blue lines show the approximated maximal bead displacement when the connection between the cells is still stiff (dark blue) and when the connection between the two cells is weakened (light blue). The maximal bead displacement is reduced by roughly 100 nm. The

reduced displacement corresponds to a reduced force of about 0.5 pN acting on the bead when the daughter cell is rotating around its long axis (Figure 4.16D). An inset in the Gyration graph is shown in Figure 4.16E. The transition from stiff cell connection to soft cell connection where the daughter cell rotates around its long axis (dark grey area in C, in between the stippled lines in E) and the subsequent release of the daughter cell (beige area in C and after the second stippled line in E) is clearly visible. The rotation frequency of the daughter cell is around 0.3 Hz and is nicely displayed as a wobbly line in Figure 4.16E. The gyration of the bead continues, but is slowed down when the daughter cell rotates around its own axis. The slope of the cell position in the Gyration graph is decreased by nearly 50%, this corresponds to a reduced angular velocity from around 0.3 revolutions/s to 0.15 revolutions/s when the connection between the two cells softens and rotation of the daughter cell starts. As another readout for the transition from stiff cell connection to soft cell connection, the position of the non-stalked end of the mother cell and of the flagellated pole of the daughter cell was tracked (Figure 4.16G, scheme). The difference of the position of the mother and daughter cell in  $x$ - and  $y$ -direction is plotted in Figure 4.16. While the distance remains nearly constant when the cells are still firmly connected (white area), the distance between the two cells varies when the daughter cell is free to rotate around its long axis (dark grey area). When cell separation is completed and the daughter cell swims away (beige area), the distance between mother and daughter cell quickly increases.

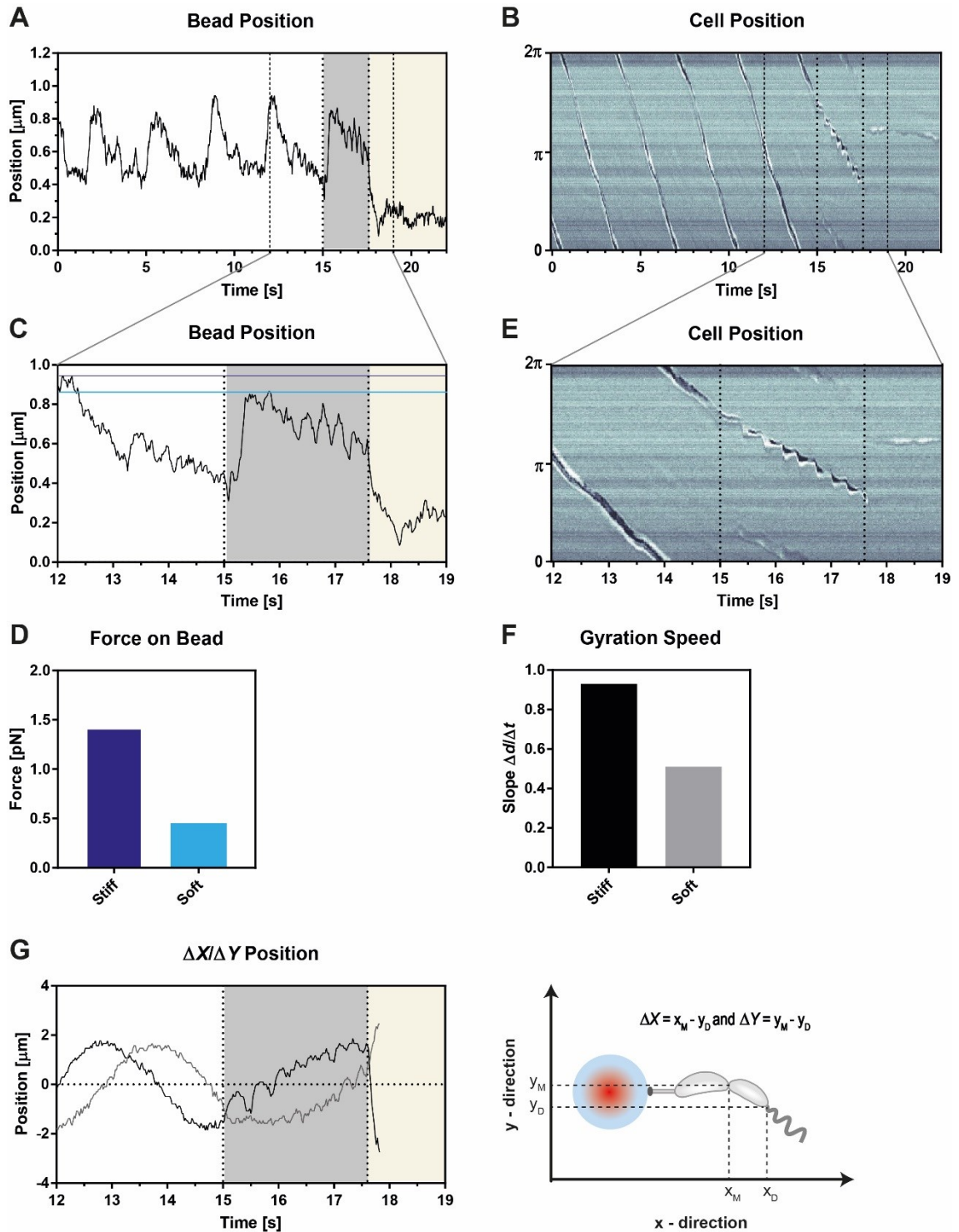


**Figure 4.16: Transition from stiff cell connection to soft cell connection.** **A:** Trajectory of the bead during the transition from stiff connection between the predivisional cells to soft connection. The stiff connection is indicated with white background, the duration of the rotation of the daughter cell in dark grey and the period after cell separation in beige. **B:** Gyratograph, of the same sequence as in A. **C:** Inset into the trajectory of A, showing more clearly the displacement of the bead when the daughter cell rotates around its own axis. **D:** Maximal translational force on the bead when the connection is still stiff (dark blue) or softened (light blue). **E:** Inset into the Gyratograph of C. The difference between stiff cell connection (cell forms a straight line) and soft cell connection (cell forms a wobbly line) is clearly visible. **F:** Average Angular velocity of the cell when the connection is still stiff (black) or softened (grey). **G:** Distance between mother and daughter cell in x- (grey) and y- (black) directions and scheme of which points are plotted.

## 4.5 DISCUSSION

We analyzed the behavior of the flagellum in the predivisional daughter cell. The flagellum starts rotating several minutes before cell separation is completed. At the beginning of the predivisional flagellum activity, the two predivisional cells are stiffly connected and the rotating flagellum is inducing a bending or swimming movement onto the cell. When the connection is softened, the daughter cell can rotate around its own axis to maintain torque balance, but is still connected to the mother cell. This stage lasts several seconds and is terminated by the separation of the daughter cell. The flagellum regularly changes its rotation direction (for numbers, see Figure 4.17 and Table 4.1).

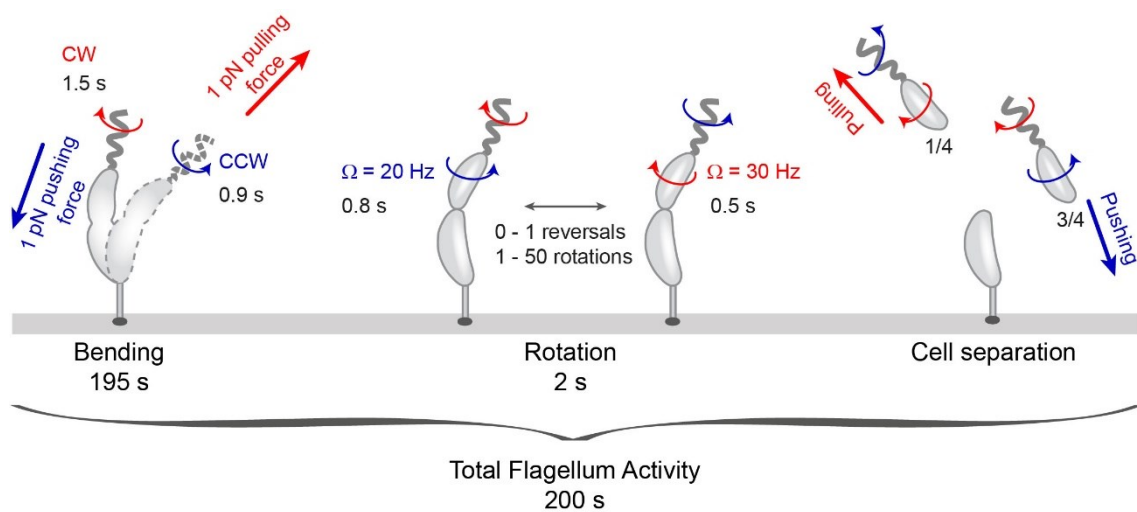


**Figure 4.17: Overview of the flagellar activity in the predivisional cell.** The flagellum is active several minutes before cell separation. In the bending stage, the mother and daughter cell are still firmly connected and the rotation of the flagellum results in a movement of the whole cell. In the rotation stage, the connection between the cells is softened and the daughter cell rotates around its long axis. This stage lasts roughly 2 seconds until the daughter cell is released and cell separation is completed.

When the connection between the predivisional cells is still stiff (Figure 4.18A), the force generated by the rotating flagellum is transferred onto the whole body of the predivisional cell. Depending on the experimental set-up, the force generated is causing different kinds of movement. In the loaded- and the trapped swimmer case it creates a swimming movement. Most notably, in the natural set-up, the force generated by the flagellum is strong enough to induce a bending of the whole predivisional cell. To allow for the subsequent rotation of the daughter cell, the mechanical properties of the connecting part between the cells need to undergo a transition. The connection could become more elastic, the rotation of the flagellum and the daughter cell would then lead to an over-twisting of the elastic connection between the two cells (Figure 4.18B). We did not observe a decrease in the rotation speed of the rotating daughter cells towards the end of a sequence in a certain direction. Therefore, over-twisting is

unlikely. Another possible explanation is the formation of a liquid-like capillary bridge in between the two cells (Figure 4.18C). In this case the daughter cell would be able to rotate without over-twisting. The formation of a capillary bridge fits best to our data. During the cell rotation, the capillary bridge is gradually constricting until the daughter cell is separated.

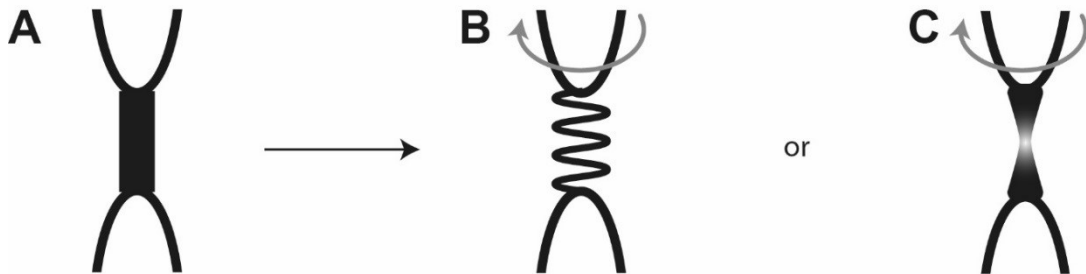


**Figure 4.18: Physical model of bending and rotational movement.** A: Stiff connection between the cells. B: Over-twisting of the connection between the cells. C: Capillary bridge between the two cells.

The transition from stiff cell connection to soft cell connection can be well explained by the composition of the cell wall of the gram-negative *C. crescentus*. The cell wall consists of an inner and an outer membrane, and a peptidoglycan layer in between. The inner and the outer membranes are lipid bilayers and consist mostly of lipoproteins and phospholipids. The peptidoglycan is a polymer formed by sugars and amino acids and gives the cell structural strength. It is proposed that the *C. crescentus* cell divides by a progressive constriction until the two predivisional cells are separated<sup>108</sup>. The cytoplasmic compartmentalization is an important step for the creation of two cells with different cell fates. The compartmentalization of the cytoplasm was found to be completed about 18 min before cell separation in a 135 min cell cycle<sup>109</sup>. In the medium used for our experiments, cell cycle progression is roughly 1.5 times faster, therefore compartmentalization of the cytoplasm is expected to be completed roughly 12 min before cell separation in our experiments. It was also found that the constriction and fission of the inner and outer membrane are two distinct and consecutive events<sup>110</sup>. We relate the two different stages (bending and rotation) that were induced by the rotating flagellum to the progressing cell separation. When the cytoplasmic compartmentalization did not yet happen, the flagellum is also not rotating (Figure 4.19A), because compartmentalization is estimated to be completed 12 min before cell separation and we found that the onset of the flagellar rotation is about 3 min before cell separation. After the compartmentalization of the inner membrane is completed, the flagellum starts rotating. The active flagellum combined with the stiff connection between the cells results in the observed motion of the two cells together. The peptidoglycan layer is not yet divided (Figure 4.19B). Only after the rigid peptidoglycan layer

is divided, and the cells are solely connected by the outer lipid membrane, the daughter cell is able to rotate around its axis (Figure 4.19C). This stage was found to last 11 s on average, with most of the cells rotating only a very few seconds. When the separation of the outer membrane is completed, cell separation is finished and the daughter cell is released from the mother cell (Figure 4.19D).

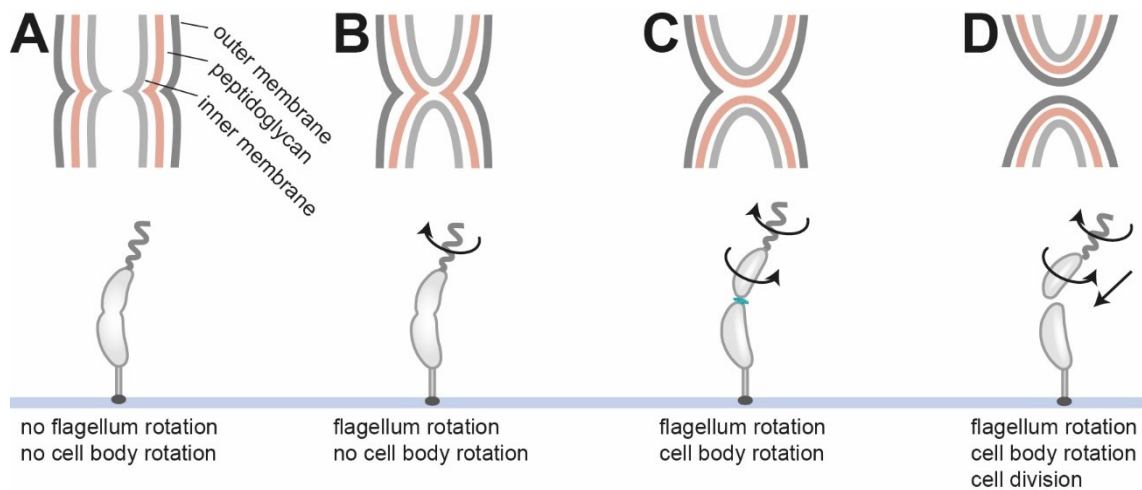


**Figure 4.19: Biological model of cell separation and flagellar rotation.** **A:** Inner membrane, peptidoglycan and outer membrane are connected. No flagellar rotation. **B:** Compartmentalization of the cytoplasm is completed by the separation of the inner membrane. Start of flagellar rotation. **C:** Completed separation of the peptidoglycan. The two cells are only connected via the outer membrane. The daughter cell is free to rotate around its axis. **D:** Completed separation of the outer membrane, finished cell separation.

We found an immediate onset of the flagellar rotation, the speed of gyration did not change as long as the predivisional cells were still firmly connected. This indicates that the flagellum is already fully assembled when the motor rotation starts. The flagellum of the predivisional daughter cell changes its rotation direction regularly, and the changes in the rotation direction do not alter during the transition from stiff connection to soft connection and subsequent cell separation. The sequences of the flagellar rotation in CW direction last longer than in CCW direction and are in good agreement to the durations found for free swarmer cells<sup>64</sup>. The rotation direction of the flagellum when the predivisional cell was stiffly connected was determined via the swimming direction of the loaded swimmer. When the connection between the two cells was softened, the rotation direction of the flagellum was directly determined from the rotation direction of the daughter cell in the natural set-up. The rotation frequency of the daughter cell was faster when the flagellum was rotating CCW, than when rotating CW.

We found that the rotation frequency of the cell body of the daughter cell depends on the load on the daughter cell. The rotating daughter cell in the natural set-up had a higher frequency as the trapped swimmer. For a free swimming swarmer cell, the cell body rotation frequency was

found to be 80 Hz<sup>29</sup> and the motor rotation frequency was 350 Hz<sup>29</sup>. The motor rotation frequency is the sum of the rotation frequency of the cell body and the rotation frequency of the flagellum. Therefore the rotation frequency of the flagellum for free swarmer cells was calculated to be 270 Hz<sup>29</sup>. We did not interfere with the flagellum in our experiments, therefore we assume that the rotation frequency of the flagellum remains constant. For the cells in the natural set-up we found a rotation frequency of 20 Hz for CCW rotation of the cell body (CW rotation of the flagellum) and 30 Hz for CW rotation of the cell body (CCW rotation of the flagellum). The roughly 4x decreased rotation speed is due to the additional load that the daughter cell experiences, the capillary bridge holding the two predivisional cells together. A free swarmer cell has rotational drag coefficient of  $9 \cdot 10^{-22} \frac{\text{N m s}}{\text{rad}}$ <sup>29</sup> and a rotation rate of 80 Hz<sup>29</sup> ( $\sim 500 \frac{\text{rad}}{\text{s}}$ ). This leads to a torque acting on the cell body of  $4.6 \cdot 10^{-19} \text{ N m}$ . For the cells that are still connected to the mother cell, the rotation frequency of the cell body is 4x decreased, therefore also the torque acting on the cell body is 4x decreased and is  $1.1 \cdot 10^{-19} \text{ N m}$ . We assume that the motor always produces the same torque and that the torque of the flagellum remains constant. Therefore the difference in the torque of free swarmer cells and cells that are still connected to the mother cell is the torque needed to overcome the viscous forces of the capillary bridge between the cells. This is roughly  $3.5 \cdot 10^{-19} \text{ N m}$  which equals to 350 pN nm. For the trapped swimmers, the rotation frequency of the cell body is even lower, around 5 Hz. In this case, the torque is not only acting on the cell body and the liquid like connection between the cells, but also on the mother cell and the bead in the optical tweezers, reducing the rotation frequency of the cell by about 10x.

We found that the flagellum of the predivisional cell generates a force of around 1.0 pN when swimming straight, but could reach peaks of up to 1.5 pN. While similar swimming speeds for backward and forward swimming of the free swarmer cell were reported<sup>64</sup> we found that the loaded swimmer is faster when swimming backwards than forward. This could be due to the higher torque generated by the motor when the cell swims backwards<sup>65</sup>. For the trapped swimmer, forward and backward movement had the same speed. It is possible that because of the short duration of the backward movement sequences the higher speed could not be resolved during the recording.

The onset of the flagellar rotation before the completion of cell separation could serve several purposes: The flagellum is known to be involved in surface sensing<sup>35</sup>, the active flagellum could therefore help the daughter cell to sense the surface and initiate holdfast formation before cell separation is completed, hence increasing attachment probability of the daughter cells. Because

the flagellum is also capable of bending the attached predivisional cell, the surface sampling area of the flagellum is increased (Figure 4.20). It is also possible that the hydrodynamic drag induced by the rotating flagellum facilitates the last steps of cell separation, leading to a faster cell separation compared to cells where the flagellar rotation starts after cell separation. We could not proof or disproof this hypothesis in this work because of the comparatively long cell cycle (90 min) compared to the possible shortening of the last separation steps (roughly 3 min). To address this question in the future, a cell cycle checkpoint close to cell separation should be determined, for example the completed separation of the inner membrane<sup>109,110</sup>. The impact of the flagellar rotation onto the speed of cell separation can then be assessed by the comparison of the duration from the checkpoint until completed cell separation for strains with and without a rotating flagellum.

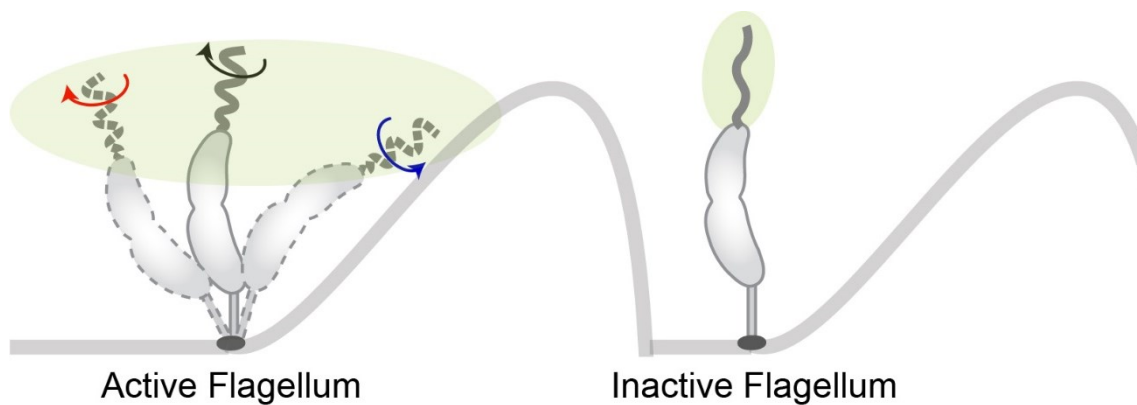


**Figure 4.20: Surface sampling area of the predivisional daughter cell with (left) and without (right) an active flagellum.** Because the rotating flagellum can bend the predivisional cell, the surface sampling area is increased when an active flagellum is present.

Measured Property	Value	System
Flagellar activity before cell separation	$(202.7 \pm 140.4) \text{ s}$	Trapped swimmer
Activity duration with stiff cell wall	$(194.5 \pm 139.8) \text{ s}$	Trapped swimmer
Pushing sequence duration	$(2.2 \pm 2.8) \text{ s}$	Loaded swimmer
90 % of the cells	$(1.5 \pm 1.6) \text{ s}$	
Pulling sequence duration	$(1.2 \pm 1.2) \text{ s}$	Loaded swimmer
90 % of the cells	$(0.9 \pm 0.7) \text{ s}$	
Activity duration with softened cell wall	$(11.2 \pm 15.6) \text{ s}$	Natural set-up
Fastest 40 % of cells	$(1.7 \pm 1.4) \text{ s}$	
Fastest 75 % of cells	$(4.4 \pm 4.3) \text{ s}$	
CCW rotation frequency	$(20.4 \pm 15.0) \text{ Hz}$	Natural set-up
CW rotation frequency	$(29.9 \pm 25.6)$	Natural set-up
CCW rotation sequence duration	$(1.1 \pm 0.7) \text{ s}$	Natural set-up
70 % of the cells	$(0.8 \pm 0.5) \text{ s}$	
CW rotation sequence duration	$(0.6 \pm 0.6) \text{ s}$	Natural set-up
90 % of the cells	$(0.5 \pm 0.2) \text{ s}$	
Release in forward swimming mode	$(74 \pm 15) \%$	Natural set-up
Release in backward swimming mode	$(25 \pm 5) \%$	
Average force generated by the flagellum	0.5 pN – 1.0 pN	Loaded swimmer
Peak force generated by the flagellum	1.5 pN	Trapped swimmer

**Table 4.1: Summary of flagellar activity before cell separation.**

## 5 DYNAMIC ROLE OF TAD PILI IN CAULOBACTER CRESCENTUS SURFACE COLONIZATION.

---

Matteo Sangermani<sup>1,2</sup>, Isabelle Hug<sup>1</sup>, Nora Sauter<sup>2,3</sup>, Thomas Pfohl<sup>2,3,4</sup>, and Urs Jenal<sup>1\*</sup>

### Affiliations:

<sup>1</sup> Biozentrum, University of Basel, Klingelbergstrasse 50/70, 4056 Basel, Switzerland.

<sup>2</sup> Department of Chemistry, University of Basel, Klingelbergstrasse 80, 4056 Basel, Switzerland.

<sup>3</sup> Swiss Nanoscience Institute, 4056 Basel, Switzerland.

### <sup>4</sup> Current addresses:

Institute of Physics, University of Freiburg, Hermann-Herder-Str 3, 79104 Freiburg, Germany.

### Key Words:

Tad pili, T4c pili, *Caulobacter crescentus*, surface attachment, microfluidics, c-di-GMP

### Author contribution:

---

Constructed the optical tweezers set-up, designed and performed the optical tweezers experiments and analysed the data.

## 5.1 ABSTRACT

Prokaryotes are capable of forming multicellular communities adhering and growing on surfaces. Many prokaryotes as single cells express filamentous appendages called pili and use them to attach on surfaces. In this work, we investigate how Tad pili promote surface attachment in *Caulobacter crescentus*. We show that Tad pili in *C. crescentus* are dynamic and are able to retract, contrary to the behaviour of other T4c pili. Using microfluidic controlled flow conditions to mimic natural environments, we found a non-linear attachment and detachment behaviour. We measured the surface attachment in flow conditions and found that flow speed of 0.75 mm/s promotes the highest attachment level, while lower or higher flow speeds affect surface colonization negatively. Using optical tweezers we measured forces generated by pili retraction and found the maximum force at about 8 pN. After surface contact cells used pili to reposition their body in a horizontal position, in respect to the attached surface, for secretion and adhesion of the holdfast, a glue-like substance that promote long-term attachment. We found that pili are active before cell division and are used for around 20 minutes after cell separation. Our results suggest that dynamic pili are necessary to promote surface attachment. We also found that second messenger c-di-GMP can regulate pili activity and increase pili-mediated attachment at low concentrations. On the other hand, higher concentrations can abolish surface adhesion. Lastly, we show that a single mutation causing lower cohesion of the holdfast caused the bacteria to walk upright for small distances, a novel phenotype specific to this strain.

## 5.2 INTRODUCTION

Bacteria have evolved effective mechanisms to colonize abiotic and biotic surfaces in order to scavenge nutrients or assemble into refractory communities called biofilms. A pivotal role in this process is played by adhesive pili, also called fimbriae, protein-based filaments exposed on the surface of bacteria that have adopted a variety of functions including adherence, motility, electron transfer, acquisition of DNA and protein secretion<sup>37,38</sup>. Accordingly, pili are crucial virulence factors during infection processes<sup>111</sup>. They mediate direct contact between pathogens and specific host tissues, promote pathogen spreading and cellular invasion<sup>41–43,112,113</sup>. The most sophisticated class of these filaments, the Type IV pili, are dynamic machineries that can undergo cycles of extension and retraction through the rapid assembly and disassembly of pilin subunits at the proximal end of the structure<sup>43,44</sup>. Extension and retraction are powered by specific cytoplasmic ATPases, which power rotational movements of the assembly platform in the inner membrane that incorporate pilin subunits into or extract them from the helical filaments<sup>41,46</sup>. Single retracting pili are able to generate forces ranging from 50 to 150 pN<sup>42,47,93,94</sup>. Through the coordinated extension and retraction of multiple polar pili, single cells are able to twitch and walk on surfaces and explore their environments<sup>37,45,114</sup>.

Type IV pili are widespread in bacteria and archaea<sup>45,46</sup>. Distinctive features divide these structures into two classes, called Type IVa and Type IVb. Type IVa represent a uniform class that is found in important human pathogens like *Pseudomonas aeruginosa*, *Vibrio cholerae* or *Neisseria* spp. and in environmental bacteria like *Myxococcus xanthus*, *Shewanella putrefaciens* or *Bdellovibrio bacteriovorus*. The Type IVb subclass is less homogenous and best-characterized for enteropathogenic *Escherichia coli* or *V. cholerae*<sup>47</sup>. A subclass of Type IVb are the tight adherence pili (Tad) (Figure 1A) that are widely distributed among Gram negative and positive bacteria<sup>48,93</sup>. Tad pili, also called Flp (fimbrial low-molecular-weight protein) pili, have pilin subunits with characteristically shorter sequence as compared to other Type IV pili systems, but show similar hydrophobic intermolecular interactions providing the main force holding the fibers together<sup>47,48,114</sup>. Tad pili promote surfaces colonization, cell-to-cell aggregation, biofilm cohesion and are required for virulence in different bacterial pathogens<sup>47–49,114–116</sup>. In contrast to other Type IVa and Type IVb pili systems, Tad clusters lack a gene coding for a retraction ATPase, raising the question if these systems show a similar dynamic behaviour as other Type IV pili fibers. However, a study found that in *Vibrio cholerae* toxin-coregulated pili (TCP) are retractable, despite the lack of a retraction ATPase<sup>117</sup>. When the minor pilin TcpB is incorporated

in a growing pilus, it blocks assembly and initiates retraction, which is proposed to be a spontaneous disassembly event, rather than an enzymatic activity.

In *C. crescentus* polar Tad pili facilitate the attachment of motile planktonic cells to surfaces<sup>35,50</sup>. During *C. crescentus* division, a polarized sessile stalked cell (ST) produces a motile offspring, the swarmer cell (SW). A single flagellum and multiple pili are assembled in the predivisional cell at the pole opposite the stalk (Figure 1B)<sup>93,118</sup>. The newborn SW cell remains in a motile, non-replicating state for a defined period called G1. After this period, chromosome replication resumes coincident with cell differentiation, during which the flagellum and pili are shed and are replaced by an adhesive exopolysaccharide, the holdfast, and the stalk. While the developmental program defines the time window during which planktonic SW cells retain their motility, SW cells challenged with surface are able to transit to the sessile state within seconds<sup>22,23,35</sup>. This process is executed by a surface recognition program that involves the rotary flagellum and the polar pili. It was recently proposed that SW cells encountering surface are able to sense mechanical cues through an interference with motor components in the cytoplasmic membrane. Motor interference stimulates a motor-associated diguanylate cyclase to produce a burst of c-di-GMP, a second messenger that allosterically activates a preassembled holdfast synthesis machinery located at the same cell pole<sup>35</sup>. Thus, by rapidly activating holdfast secretion, cells irreversibly anchor to surfaces via their piliated and flagellated cell pole. Polar Tad pili are critical components of surface sensing and surface colonization in *C. crescentus*. It was postulated that initial surface adherence is mediated by pili and that pili retraction positions the flagellar pole in close contact with the surface to allow mechanosensation to occur<sup>50</sup>. A recent study demonstrate that pili in *C. crescentus* are also capable of retraction<sup>35</sup>. The alternative model proposed a more direct role for the Tad pili as mechanosensitive devices that are able to sense surfaces by using the resistance experienced when pili retract<sup>35</sup>.

To more closely define the role of Tad pili in *C. crescentus* surface recognition and colonization, we analysed their regulation and dynamic behaviour. Our results show that pili-mediated attachment on surfaces is flow depend. Flow speed above 5 mm/s were capable to abolish surface attachment, while a speed of 0.75 mm/s resulted in maximum colonization levels. Interestingly, lower flow velocity had a negative effect on surface attachment. We confirm that pili in *C. crescentus* are capable of retraction. Pili activity was found to constantly position surface attached cells in upright position. Surface attachment and upright positioning were found to be influenced by intracellular levels of c-di-GMP. Low concentrations positively affect cell adhesion, but higher concentrations have the opposite effect and can abolish pili-mediated

attachment. A strain secreting a lower cohesion holdfast was found to display the ability to walk in the flow conditions tested, an peculiar phenotype never described for *C. crescentus* and any bacteria possessing type IVc pili. Lastly we determined the maximum force generated by pili retraction by optical tweezers measurements, at about 8 pN.

## 5.3 RESULTS

### 5.3.1 Pili mediate temporary surface attachment under media flow

Surface adhesion of *C. crescentus* via their polar pili is transient and weaker as compared to the strong and long-lasting attachment via the adhesive holdfast<sup>56</sup>. To investigate the overall contribution of pili to surface attachment without interference of the holdfast, we analysed the behaviour of the *C. crescentus* “wild type” control strain (NA1000 *hfsA*-), which carries an inactivating mutation in the *hfsA* gene, rendering this strain unable to produce holdfast<sup>119</sup>. Simple flow channels were used with a single inlet supplying a culture with a constant flow of medium<sup>35</sup>. To evaluate pili-mediated attachment, time lapse images were recorded microscopically to determine the rate of colonization. Importantly, mutants lacking pili were unable to attach in such an assay (Figure 1C).

As shown in Figure 1C, different medium flow velocities resulted in different attachment rates. A plateau of attached cells per unit surface area was reached when the rate of attachment of incoming bacteria equaled the rate of detachment of cells from the substratum (Supplemental Movie 1). The average residence time of swarmer cells on the surface was about 2 min (Supplemental Figure 1A). A fraction of cells remained attached for several minutes and their proportion increased at higher flow rates (Supplemental Figure 1A). However, the probability of newly attaching cells rapidly decreased when flow rates were increased (Figure 1D). Short-lived surface attachment of swarmer cells can be described by a Langmuir-like adsorption model, taking into account the adsorption from solution with attachment and detachment rates depending on the surface density of the cells. The evolution of the colonization density  $\theta(t)$  can be fitted by a function of the form  $\phi(t) \sim \phi_{\text{eq}} \left(1 - e^{-\frac{t}{\tau}}\right)$ , where  $\phi_{\text{eq}}$  is the plateau density and  $\tau$ , characteristic time. The equilibrium constant can be determined by  $k_{\text{eq}} = \frac{k_{\text{on}}}{k_{\text{off}}} = \frac{\phi_{\text{eq}}}{(1-\phi_{\text{eq}}) \cdot c_{\text{bulk}}}$ , with the attachment rate  $k_{\text{on}}$ , the detachment rate  $k_{\text{off}}$ , and the cell concentration in the solution  $c_{\text{bulk}}$ . The detachment rate can be obtained from  $k_{\text{off}} = \frac{\phi_{\text{eq}}}{\tau \cdot (2 - \frac{1}{\phi_{\text{eq}}})}$ . The plateau values of the colonization density  $\phi_{\text{eq}}$  (Figure 1D) as well as the obtained  $k_{\text{eq}}$  and  $k_{\text{off}}$  (Supplemental Figure 1B) show a strong dependency on the flow velocity. At lower flow velocities, an increase of  $\phi_{\text{eq}}$  with increasing flow can be observed with a maximal plateau  $\phi_{\text{eq}}$  and  $k_{\text{off}}$  at a flow velocity of 0.75 mm/s. At higher medium flow rates,  $\phi_{\text{eq}}$  decreased and the  $k_{\text{off}}$  increased (Supplemental Figure 1B). This suggested that pili-mediated surface attachment depends on the flow rate with optimal adherence values observed at intermediate flow velocities. We found

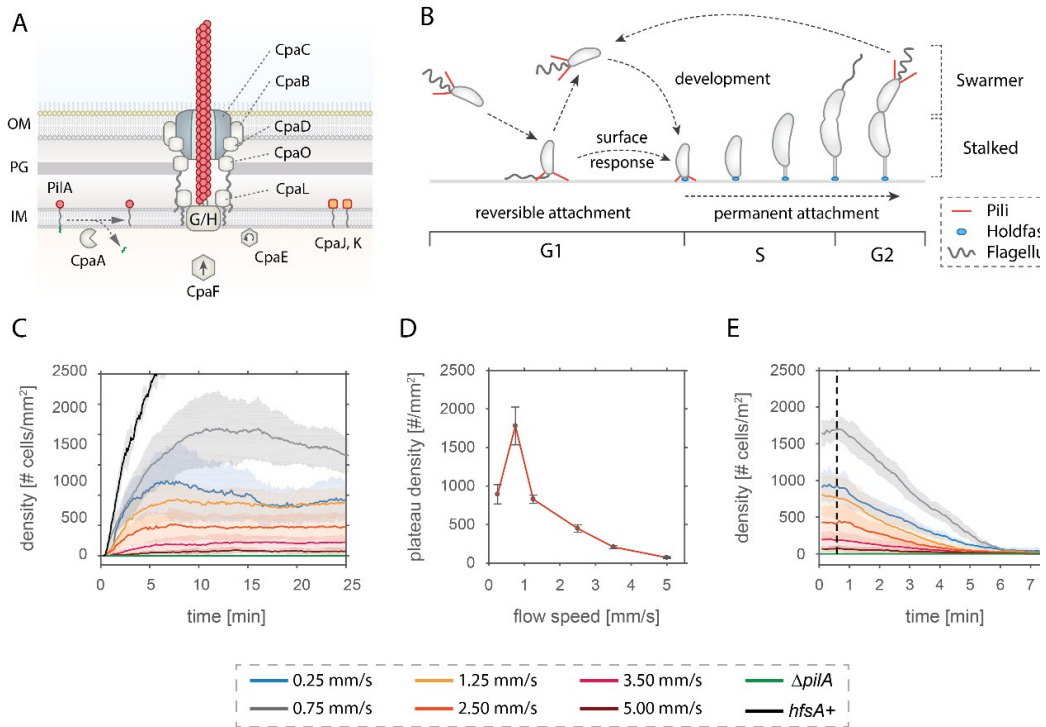


**FIGURE 1 – Pili-mediated surface attachment of *C. crescentus* cells in flow conditions**

A – Schematic model of pili machinery in *C. crescentus*. The function of most components is drawn according to comparative analysis of the *cpa* locus with other Tad pili<sup>47,120</sup>. CpaC is the secretin OM pore, which could be stabilized by CpaD and CpaB. CpaG and CpaH form the inner membrane platform that is located at the base of the filament. CpaO and CpaL aid in aligning the OM complex with the IM platform. CpaF is the functional motor protein, while the role of CpaE is yet unclear, although it is required to recruit several Cpa components to the cell pole. PilA is the major pilin subunit that matures upon removal of the signal peptide by the prepilin peptidase CpaA. Mature PilA can then be assembled into a filament by the machinery<sup>47,120</sup>.

B – Schematic of the *C. crescentus* cell cycle. Swarmer cells are born with assembled pili (red) and flagellum (grey). Upon surface encounter, pili promote temporary attachment and position the flagellated cell pole close to the surface. This triggers the secretion of an adhesive exopolysaccharide, the holdfast (blue) and results in permanent attachment of the cell. Attached cells differentiate into stalked cells and, concomitantly initiate replication and an asymmetric cell division to generate another motile swarmer cell.

C – Pili-mediated surface attachment at different flow rates. The chart shows the rate of colonization of a microfluidic channel by *C. crescentus* strain NA1000 (*hfsA*<sup>-</sup>) at different flow velocities as indicated.

D – Optimal attachment rates depend on medium flow. The plateau level of surface colonization reached at different flow velocities are plotted. Values are averages of the rates of colonization shown in C between 10 and 25 minutes after the start of the experiment.

E – Detachment of adherent cells at high flow rates. The detachment behaviour of NA1000 (*hfsA*<sup>-</sup>) from different levels of colonization as indicated in (C) is shown. The vertical dashed green line at 30 seconds marks the time point when the flow was increased to 25 mm/s. Opaque areas in panels C and E represent standard deviations. (n>3).

that flow velocities above 5 mm/s completely abolished cell attachment. To estimate the strength of pili adherence, we calculated the drag force experienced by cells close to a surface in a microchannel (Supplemental Figure 1C). A flow rate of 5 mm/s corresponds to a drag force of 40-60 pN. At optimal attachment, 0.75 mm/s, the theoretical drag force corresponds to around 7-15 pN.

To determine the detachment rates of surface attached *C. crescentus* swarmer cells, the medium flow rate was increased from a steady-state situation with constant plateau density (Figure 1C) to a very high flow rate of 25 mm/s. Under these conditions, cells were unable to attach (Figure 1C) and the surface bound cells detached following an almost exponential decay, with a decay time of roughly  $\tau_D = 2$  min (Figure 1E). Together, these observations demonstrated that pili mediate transient surface attachment of *C. crescentus* swarmer cells in devices with media flow. We conclude that pili-mediated immobilization negotiates a time window during which motile swarmer cells are able to recognize surface exposure and initiate holdfast production to undergo the transition from temporary to permanent attachment.

**5.3.2 *C. crescentus* pili are dynamic and can force attached swarmer cells into an upright position**  
Surface attached *C. crescentus* swarmer cells were most often found standing upright perpendicular to the surface, irrespective of their ability to synthesize an adhesive holdfast (Figure 2A, Supplemental Movies 1, 2)<sup>35</sup>. This is an unfavourable position considering the constant drag force from the media flow. Moreover, we observed that after landing, cells occasionally moved a few microns mostly upstream against the medium flow, as if walking upright for small distances. Since only an active force could move cells against the flow or position them in an upright orientation, we speculated that the *C. crescentus* Tad pili may be able to actively retract<sup>94</sup>. To investigate pili dynamics we first analysed strains capable of secreting an adhesive holdfast in flow channels mimicking conditions that *C. crescentus* encounters in its natural aquatic environment<sup>23</sup>. Under such conditions, offspring of attached stalked mothers are exposed to surface as a consequence of medium flow over the crescentoid dividing cells. This positions the flagellated and piliated pole in close proximity to the substratum, allowing cells to sense surface and triggering immediate holdfast production (Figure 2A)<sup>35</sup>.

To quantify the movements of newborn swarmer cells into an upright position, we measured the 2D projections of individual cells in the xz plane and used this information to infer the cells' 3D orientation (Figure 2A). The resulting tilt angle ( $\vartheta$ ) was compared five minutes before and five minutes after cell division (Figure 2B). Swarmer cells in wild type control strain (NA1000

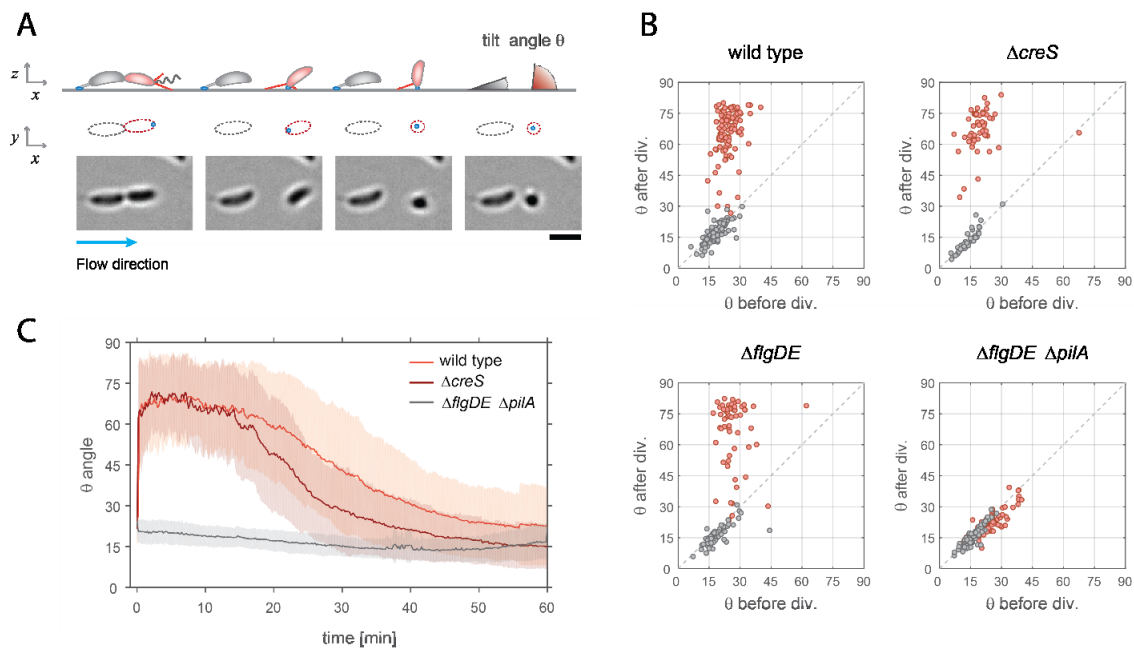


**FIGURE 2 – Pili retraction causes *C. crescentus* cells to stand up.**

A – *C. crescentus* cell division under flow. A schematic view (top) and respective light micrographs (bottom) are shown. The sequence of images illustrates a stalked mother cell, which is attached to the surface via its holdfast (blue), producing a swarmer offspring. A schematic representation of the cell outline in the xy plane is shown as identified by the program. Polar pili are highlighted (red). Upon surface sensing<sup>35</sup> the newborn SW cell produces a holdfast for surface anchoring. Newborn SW cells, but not ST mothers are able to move into a vertical position after separation. The tilt angles  $\vartheta$  (angle between the cell main body axis and the glass surface) of mother (grey) and daughter (red) were calculated from the cell contour shape (xy plane) with cells lying parallel to the glass surface and being in an upright position scoring  $\vartheta=0^\circ$  and  $\vartheta=90^\circ$ , respectively. An arrow indicates the direction of the medium flow. Scale bar: 2  $\mu\text{m}$ .

B – Pili are required for newborn swarmer cells to stand up. Scatter plots comparing the average angle  $\vartheta$  of the same cells recorded 5 minutes before and 5 minutes after cell division, respectively. The results shown were obtained with the strains indicated. Coloring of swarmer cells are in red, stalked cells are in grey).

C – Dynamics of pili-mediated standing up of swarmer cells. The chart shows the time evolution of the angle  $\vartheta$  in daughter cells of *C. crescentus* wild type (wt), the  $\Delta creS$  and the  $\Delta figDE \Delta pilA$  mutant strains. Time zero corresponds to the time when mother and daughter cells separate. Solid lines represent average values; the standard deviation is shown as an opaque area.  $n = 98$  (wt);  $n = 56$  ( $\Delta creS$ );  $n = 57$  ( $\Delta figDE$ );  $n = 75$  ( $\Delta figDE \Delta pilA$ ).

*hfsA+*) were unable to change their position as long as they were physically connected to their stalked mothers. However, upon separation, swarmer cells rapidly changed their tilt, moving into an upright position of about 80° degrees (Figure 2B). In contrast, stalked cells retained their low  $\vartheta$  value after cell division. A strain lacking the major pilus subunit ( $\Delta pilA$ ) showed extremely low attachment, making it impossible to collect statistically relevant data on the fate of newborn swarmer cells in this strain. However, we have shown earlier that cells lacking the outer components of the polar flagellum show a hypersensitive surface response with rapid deployment of the adhesive holdfast that partially alleviates the strict requirement for pili<sup>35</sup>. In agreement with this observation, cells of a strain that lacked both external flagellar structures and the major pilin subunit ( $figDE \Delta pilA$ ), occasionally attach to surfaces, but in all such instances

cells were unable to stand up (Supplemental Movie 3). In contrast, a strain lacking only the flagellar structures ( $\Delta flgDE$ ) showed wild type-like behaviour (Figure 2B). A strain lacking the crescentin cytoskeleton ( $\Delta creS$ ), has a rod-like cell shape instead of the typical curvature of *C. crescentus*. The strain  $\Delta creS$  provides a control to demonstrate that curvature does not influence the ability of attached cells to stand up (Figure 2C). Together, this strongly argued that the ability of newborn swarmer cells to move into a vertical, upright position requires the presence of dynamic, force-generating pili. The process of standing up is initiated immediately after division with piliated cells changing their tilt angle within a few seconds after cell separation (Figure 2C; Supplemental Movie 2). Despite the relatively strong medium flow, daughter cells were able to keep their upright position for about 10-15 minutes before the angle  $\vartheta$  gradually decreased. This coincides well with the timing of cell differentiation and the disappearance of pili during the SW-to-ST cell transition (Figure 1B)

### 5.3.3 Pili are active before division and can drive predivisional cell stretching

The above results demonstrated that pili are dynamic and that they are active after swarmer cells have separated from their mothers. However, pili are assembled at the flagellated pole in the predivisional cell and during division facilitate surface interaction and mechanosensation<sup>35,50</sup>. To investigate if pili are actively retracting already before cells divide, movements of surface attached dividing cells were carefully analysed. We observed that the piliated pole of late predivisional cells was pulled away from the stalked pole, stretching the typical crescentoid shape into a straight line (Figure 3A, Supplemental Movie 4). To quantify this behaviour, we determined the angle ( $\alpha$ ) between the two cell bodies five minutes and one minute before cell separation. *C. crescentus* wild type cells (NA1000 *hfsA*-) showed discrete peaks of angle  $\alpha$  at 180° and at 150° (Figure 3B). The  $\Delta creS$  mutant showed only a single peak at 180° indicating that the peak at 150° represents the natural, unstrained angle of crescentin-mediated curvature in the late predivisional stage (Figure 3B). A strain unable to assemble pili lacked the peak at 180°, but retained peaks at 150° (Figure 3B), arguing that cell stretching before division is mediated by the action of polar pili. Consistent with this, cells lacking a polar flagellum retained their stretching ability. Moreover, cell stretching became more prominent at very late stages of division, with the peak at 180° increasing at the expense of the peak at 150° (Figure 3B). Finally, we observed a striking difference between the behaviour of predivisional cells that gave birth to offspring able to attach after separation (Figure 3B, attach) and predivisional cells producing swarmer cells that were washed out after cell division (Figure 3B,

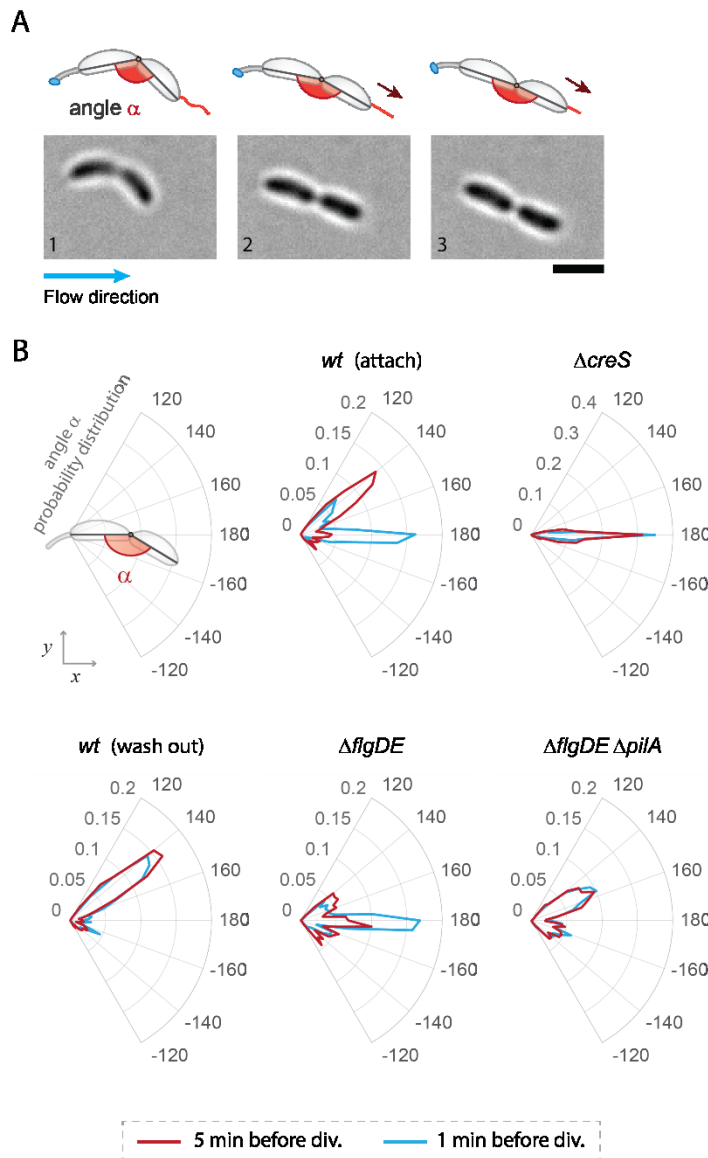


**FIGURE 3 – Pili are active before cell division.**

A – Image sequence of a crescentoid predivisional cell stretching due to activity of the pili. A schematic representation of the cell is shown above the micrographs illustrating how the angle  $\alpha$  was determined in each experiment (scale bar: 2  $\mu\text{m}$ ).

B – Angle distribution along the long axis of predivisional cells. A schematic of a dividing cell with the angle between stalked and swarmer progeny is shown on the top left as reading aid for the polar charts. Each plot shows the distribution of angle  $\alpha$  in different strains recorded five minutes (dark red) and one minute (blue) before cell division. The wild type strain NA1000 *hfsA*<sup>+</sup> has a peak at about 150° resulting from the crescentoid shape of predivisional cells at rest. A second peak is observed at 180° resulting from pili retraction at the pole opposite the surface attached stalked pole and stretch of the predivisional cell into a straight line. A lack of pili results in the absence of a peak at 180°.  $n = 130$  (wt - attach);  $n = 119$  (wt - swim);  $n = 56$  ( $\Delta creS$ );  $n = 57$  ( $\Delta flgDE$ );  $n = 75$  ( $\Delta flgDE \Delta pilA$ )

wash out). While the former showed a prominent peak at 180°, this peak was missing in dividing cells destined to produce offspring unable to attach. Instead, the latter showed a distribution of angle  $\alpha$  resembling the pilus-deficient strain (Figure 3B). This suggested that predivisional cells

unable to attach after division either lacked pili activity or were simply not successful in deploying pili for surface adherence under media flow.

Together, these experiments indicated that pili are active before cell division and that pili dynamics increases as dividing cells approach the stage where mother and daughter separate from each other. This also suggest that pili activity is instrumental for surface attachment, given it is absent in wt (wash out). We had proposed earlier that pili retraction at this stage of cell division is critical to position the flagellar mechanosensor in close proximity to the surface in order to successfully initiate biogenesis of the adhesive holdfast and therefore preventing cells from being washed out<sup>35</sup>. Of note, the orientation of the concavity of attached predivisional cells showed a strong bias to one side with respect to the flow direction (Figure 3B, Supplemental Figure 3). While the concavity distribution is expected to be random for cells with a straight C - shape, we found that cells were more likely to orient to the left with respect to the flow direction, irrespective of their position within the channel or the nature of the surface. Cells attached to the channel's ceiling showed the opposite orientation, displaying a leftward orientation with respect to the direction of the flow. Based on this, we propose that *C. crescentus* cells have a C-shape with a small helical twist (Supplemental Figure 3).

#### 5.3.4 Pili dynamics mediates swarmer cell walking against media flow

The swarmer cells analysed under flow generally moved to an upright position only once, right after cell division (Figure 2C). In contrast, the stretching behaviour of predivisional cells (Figure 3A) was observed multiple times for a single cell, arguing that pili can go through repeated cycles of extension and retraction (Supplemental Movie 5). We reasoned that consecutive activity of pili could be masked in attached swarmer cells by the rapid synthesis of the holdfast adhesin, which immobilizes cells in an upright position. To address if *C. crescentus* pili are capable of undergoing multiple cycles of extension and retraction, we used a *C. crescentus hfsK* mutant, which produces holdfast material with reduced cohesive force. We had shown earlier that this mutant secretes adherent holdfast material that was strong enough to glue cells to the surface in flow chambers, but failed to firmly anchor cells at the place of initial attachment<sup>121</sup>.

In flow chambers, this strain left trails of holdfast material, confirming the reduced cohesive properties of the adhesin material<sup>109</sup>. Intriguingly, we observed that newborn swarmer cells, after standing up, were able to move upstream against the medium flow leaving stretched trails of holdfast material behind (Figure 4A,B). This behaviour was fully dependent on the presence of pili as a  $\Delta hfsK \Delta pilA$  mutant was unable to move against the medium flow. These results indicated that active pili were able to dislodge cells that are surface attached by a weakened

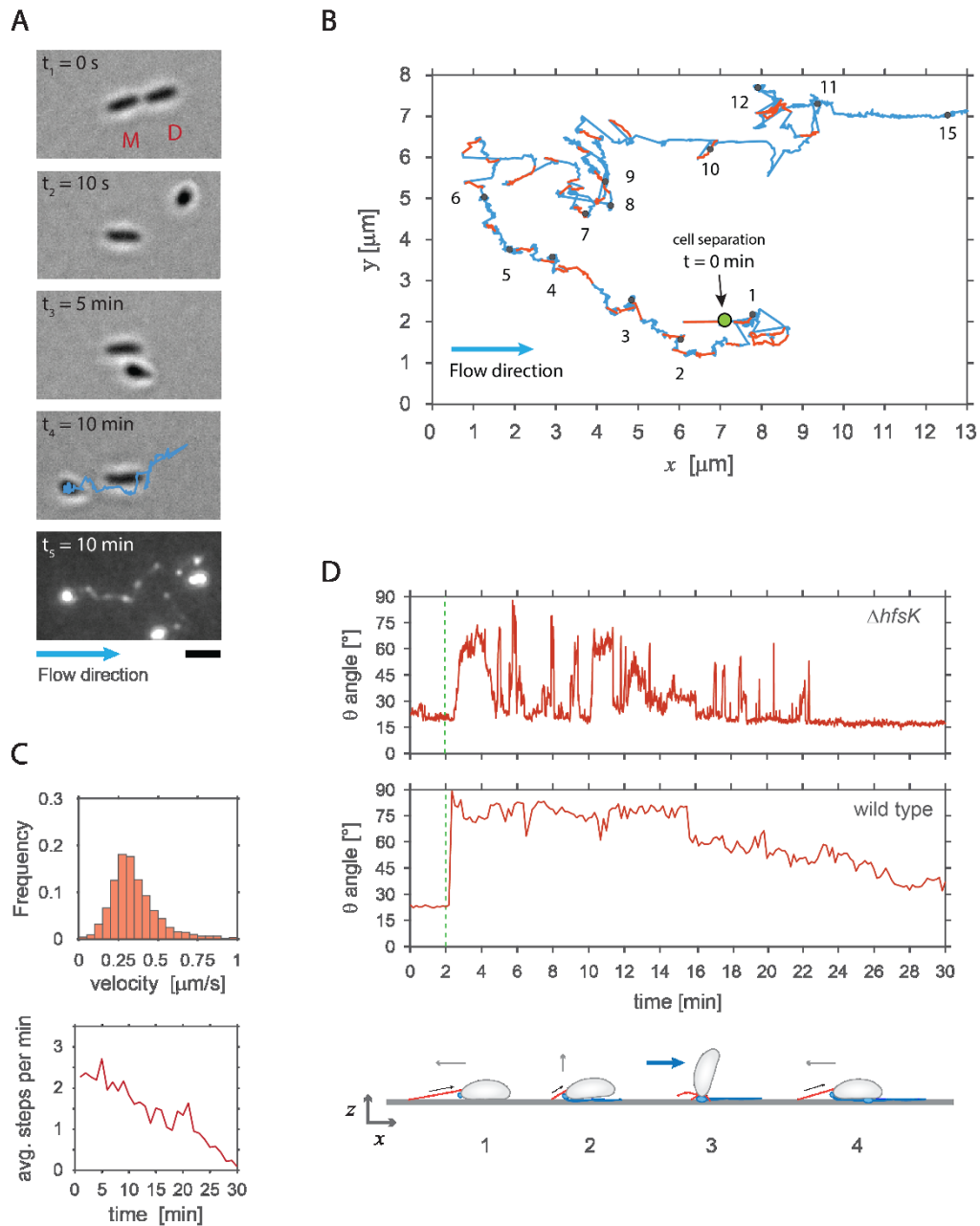


**FIGURE 4 – Dynamic pili assist walking-like movements against the medium flow.**

A – Example of a newborn swarmer cell of strain  $\Delta hfsK$  moving against the medium flow. The time after cell division is indicated. Mother (M) and daughter (D) are individually labelled. Time point 1 and 2 show the swarmer cell immediately before and after separation from its mother. After 5 min ( $t_3$ ), the cell has moved upstream and after 10 min ( $t_4$ ) the swarmer cell has moved passed its mother. The blue track indicates the trajectory of the cell recorded during its 10 min walk ( $t_4$ ). The cell track matches the trails of holdfast material left behind by the walking cell as shown by fluorescence imaging using the Oregon green labelled lectin wheat germ agglutinin ( $t_5$ ).

B – Representative trajectory of a swarmer cell after birth from its mother (cell separation). The trajectory (blue) was assembled from sequential images of an  $\Delta hfsK$  mutant strain in the microchannel. Step events were identified as fast movements against the flow and are highlighted in red. Black points in the track indicated the time passed from cell separation, in minutes.

C – Distribution of retraction velocities of pili-mediated walking movements on surfaces under flow conditions. The plots show velocity (top) and the average number of step events per minute recorded over time (bottom) in swarmer cells of the  $\Delta hfsK$  mutant strain ( $n = 56$ ).

D – *C. crescentus* swarmer cells are standing up during movements against medium flow. The tilt angle  $\vartheta$  was recorded over time in two representative examples of moving cells as shown in (B). A swarmer cell of the  $\Delta hfsK$  mutant (upper panel) and of *C. crescentus* wild type (lower panel, NA1000 *hfsA+*) are shown respectively. Movies were recorded at 1 and 0.1 frames per second for wild type and  $\Delta hfsK$  mutant, respectively. Below the charts is shown a schematic of the possible steps in the walking behaviour displayed by  $\Delta hfsK$  mutant. From a horizontal position (1) retraction of an extended pilus pull a cell forward. At the end of pili retraction a cell pull its body aright (2), against the drag force of flowing media (3). When retraction of a pilus is concluded the cell is pushed down by the flow (4) and the cycle can start again.

holdfast. Tracking the trajectories of individual cells identified the time period, step size, and speed of pili-driven movements (Figure 4B and Supplemental Movie 5). On average, each step event covered distances of up to 500 nm with an average upstream crawling speed of about 300 nm/sec (Figure 4C and Supplemental Figure 4A). Cells covered distances of several micrometers in repetitive small steps with a frequency of about 2-3 step events per minute.

While the step frequency remained high for the first 10-15 minutes after division, it gradually decreased over time and discontinued about 20 min after the daughter had separated from its mother, at which point cells had either settled or were washed away by flow (Figure 4C, Supplemental Movie 5). During their movements, swarmer cells, although unable to remain standing for longer periods of time, repeatedly moved back into an upright position (Figure 4D). This behaviour was particularly pronounced at the end of each step event (Supplemental Figure 4B), arguing that standing up against the media flow directly results from shortening of polar pili towards the end of a retraction period thereby inflicting spatial constraints that move cells into an upright position (Figure 4D). Together, these results confirmed that *C. crescentus* pili are dynamic in nature and indicated that these structures can be repeatedly employed engaging in consecutive cycles of extension and retraction.

### 5.3.5 Determining force and energy of pili retraction

To measure the forces generated by pili retraction we made use of optical tweezers. Because *C. crescentus* cells are highly susceptible to phototoxicity elicited by the strong light source used in optical traps, it was not practical to directly immobilize cells with this method. To avoid this problem we exploited the ability of *C. crescentus* predivisional cells to permanently adhere to surfaces via their adhesive holdfast positioned at the pole opposite of the piliated pole. By coupling bacteria to polystyrene beads and immobilizing the beads in the optical trap phototoxicity could be drastically reduced as cells could be kept in the optical trap for at least 1 hour without losing viability and the ability to grow and divide (Figure 5A). By exposing beads carrying predivisional cells to glass surface, pili were able to attach and, upon retraction, displace the beads from the trap (Figure 5A, Supplemental Movie 6). To avoid potential interference from the flagellum, we used a strain lacking the external parts of the rotary motor ( $\Delta flgDE$ ).

Figure 5B shows a representative example of an optical trap measurement. Initially, the bead is resting in the optical trap center, with some noise due to Brownian motion. Upon pilus attachment to the surface, Brownian motion decreases followed by bead displacement of up to 1  $\mu\text{m}$  from the center for about 20 seconds before rapidly moving back into its original position (Figure 5B). Occasionally the system backtracked to an intermediate level followed by a renewed movement out of the trap that restored the original displacement. Repeated displacements may represent detachment events of the pilus engaged, followed by the retraction of a second pilus. The varying displacement distance likely reflects the length of the pilus at the onset of the retraction event. The average speed of pili retraction was 100 nm/s (Figure 5C). From the displacement of the beads and the trap stiffness  $K_{\text{trap}}$  we calculated the maximum force applied ( $F = K_{\text{trap}} \cdot \Delta x$ ) at around 8 pN. The force determined by these experiments is proportional to the distance of bead displacement. Since electron microscopy studies showed that pili can reach a maximal length of 5  $\mu\text{m}$  (mean  $(1.14 \pm 0.92) \mu\text{m}$ ;  $n = 270$ ) (Supplemental Figure 5), most displacement events measured in the optical trap likely underestimate the dynamic range of these structures and, as a consequence, underestimate the maximal force generated by pili retraction.

Cryo-EM reconstruction of the gonococcal Type IVb pilus filament revealed 3.6 subunits per single turn of a 37 $\text{\AA}$  helix<sup>122</sup>. This amounts to a length change for the fiber of 1.05 nm per subunit added or removed. Based on this we calculated that average pili with lengths of 1.14  $\mu\text{m}$  can generate a force of  $\sim 8$  pN and have a potential energy of  $4.5 \cdot 10^{-18}$  J (or 1089  $k_B T$ ) during retraction. Assuming a 100% efficiency in energy conversion, we estimate that the pilus machinery would disassemble 20 nm of the filament per ATP hydrolyzed. However, a figure of about 1.0 nm/ATP is more realistic in line with previous structural studies<sup>43</sup>, and it results in the pilus machinery having an energy conversion efficiency of around 5%. Thus, one pilus subunit can be assembled/disassembled for each ATP hydrolyzed, which is consistent with the proposed piston model of the pili machinery<sup>123</sup>. Stronger forces measured in our experiments could be achieved if the machinery was more efficient or, alternatively, if multiple pili were employed at the same time.

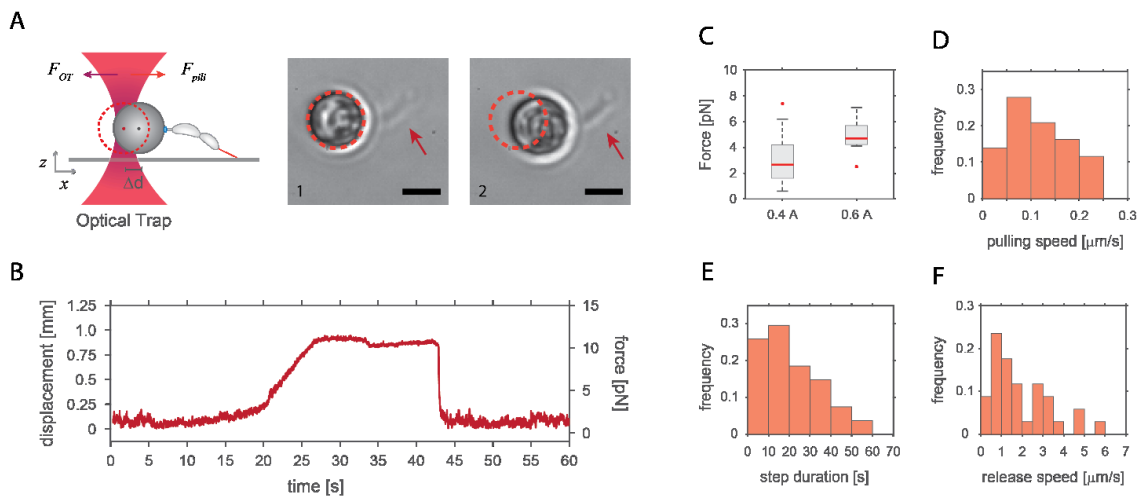


**FIGURE 5 – Measurements of pili retraction force and speed using optical tweezers**

A – Schematic representation of the experimental setup used for optical trap measurements of pili retraction forces. Beads carrying late predivisional cells attached via their holdfast adhesin were trapped by optical tweezers. Pili extending from the new pole (red) can attach to the glass surface and upon retraction, displace the bead from the trap. The two images show a representative example of a bead with one attached predivisional cell (arrow) of the mutant  $\Delta flgDE$  before (1) and after (2) retraction. The trapped bead is displaced by the retraction of pili by about 1  $\mu\text{m}$  (scale bar: 2  $\mu\text{m}$ ).

B – Pili mediated displacement of trapped beads over time. The plot is a representative example of an optical tweezers measurement, showing the displacement and the respective force generated by pili retraction.

C, D– Force and pulling velocity measurements of pili retraction at the optical tweezers. The box plots (C) show the median (red line), 25th and 75th percentiles (bottom and top edges of the box), and most extreme data points (whiskers). Outliers are plotted as red points. The measurements were conducted with the laser power of the optical trap at either 0.4 A ( $n = 100$ ) or at 0.6 A ( $n = 11$ ). (for D, laser power at 0.4A).

E - The step duration for pili retraction is defined as the time passed from the start of bead displacement to the moment the bead is released and moves back into the center of the optical trap ( $n = 28$ ).

F – The chart shows the speed at which the bead moves back into the trap, at the end of a step event ( $n = 34$ ).

### 5.3.6 c-di-GMP influences Pili activity

In the *C. crescentus* surface sensing activate the diguanylate cyclase DgcB, which boost levels of the second messenger c-di-GMP and trigger rapid surface attachment<sup>35</sup>. We assayed how components of surface sensing can influence pili-mediated colonization to test if c-di-GMP controls pili-mediated attachment. The setup employed is similar to the one described above (see Figure 1), using a flow speed of 0.75 mm/s and different strains, all unable to secrete a holdfast (*hfsA*-). The protein DgcB is a diguanylate cyclase that plays an important role in surface sensing. In the flow channel, the  $\Delta dgcB$  deletion mutant reached the same colonization level as wild type control strain (NA1000 *hfsA*-) (see Figure 6A). However, the attachment rate of  $\Delta dgcB$  was markedly slower. Wild type reached the colonization level of 1500 cells/ $\text{mm}^2$  in about 5 minutes, compared to the 20 min needed for  $\Delta dgcB$ . One possible explanation for the lower rate of attachment is that  $\Delta dgcB$  mutant are less sensitive to surface and pili activity is lower.

However, later in the experiment cells entering the microfluidic channel have been exposed to surface for long time, waiting in the upstream tubing (500  $\mu\text{m}$  in width) that connect the microdevice with the reservoir. Inside the tubing cells have time and available surface to activate secondary ways to sense surface and generate a holdfast, and then when reaching the microchannel attach seemingly just like wildtype, which instead senses and attaches on the spot. Deletion of  $\Delta\text{flgDE}$  or  $\Delta\text{motB}$  resulted in almost complete abolishment of surface attachment. This suggests that non-motile bacteria in our flow conditions were unable to reach the surface. However, cells of strain  $\Delta\text{flgDE}$  occasionally attached which resulted in a slightly higher colonization level compared to  $\Delta\text{motB}$  (see Supplemental Figure 6A). CheY-like Cle proteins can bind c-di-GMP and interact with the motor of the flagellum. Their deletion lowered the colonization levels compared to the control strain (see Figure 6A). We also created strain with mutations in minor pilins,  $\text{cc\_0832}^{\text{ESV}}$  and  $\text{cc\_2951}^{\text{ESV}}$ , modifying the critical Glu5 amino acid. A similar mutation in the minor pilin TcpB in *V. cholerae* resulted in decreased retraction of pili<sup>117</sup>. In strain  $\text{cc\_0832}^{\text{ESV}}$  the mutation had no effect on colonization levels, while in  $\text{cc\_2951}^{\text{ESV}}$  it decreased the colonization levels to half that of wild type (see Supplemental Figure 6B).

We also directly manipulated the levels of c-di-GMP inside the cells by regulating the expression of an exogenous diguanylate cyclase (*dgcZ*) in the strain NA1000 *hfsA- rcdG<sup>0</sup> dgcZ*<sup>78</sup>. Without induction intracellular c-di-GMP concentrations were similar to wild type due to leaky expression. However, colonization efficiencies under flow were lower than wild type. Small levels of induction of *dgcZ* increased attachment efficiency, with 0.5  $\mu\text{M}$  of IPTG reaching closest to wild type. Further increase of the intracellular c-di-GMP concentration diminished the density of attached cells in the flow. Induction at 100  $\mu\text{M}$  IPTG, the highest level tested, completely abolished cell attachment. The results suggest that low c-di-GMP concentrations promote pili-mediated surface attachment until a tipping point is reached, after which a further c-di-GMP increase negatively interferes with attachment.

We also quantified the movements of newborn swarmer cells into an upright position, as described above (Figure 6D). The  $\Delta\text{dgcB}$  mutant strain behaved similar to wild type, but a higher proportion of cells had intermediate  $\vartheta$  after division, between 30° to 60° degrees. The measured tilt angles of cells in from this strain were generally slightly lower compared to wild type but followed the same trend (Supplemental Figure 6C). In contrast,  $\Delta\text{motB}$  swarmer cells had low  $\vartheta$  value after cell division and only a few cells stood up above 60° degrees. Interestingly, this initial low  $\vartheta$  value increased 5-10 minutes after cell division and then followed similar values as wild type (Figure 6E). This suggests that pili activation may be delayed.

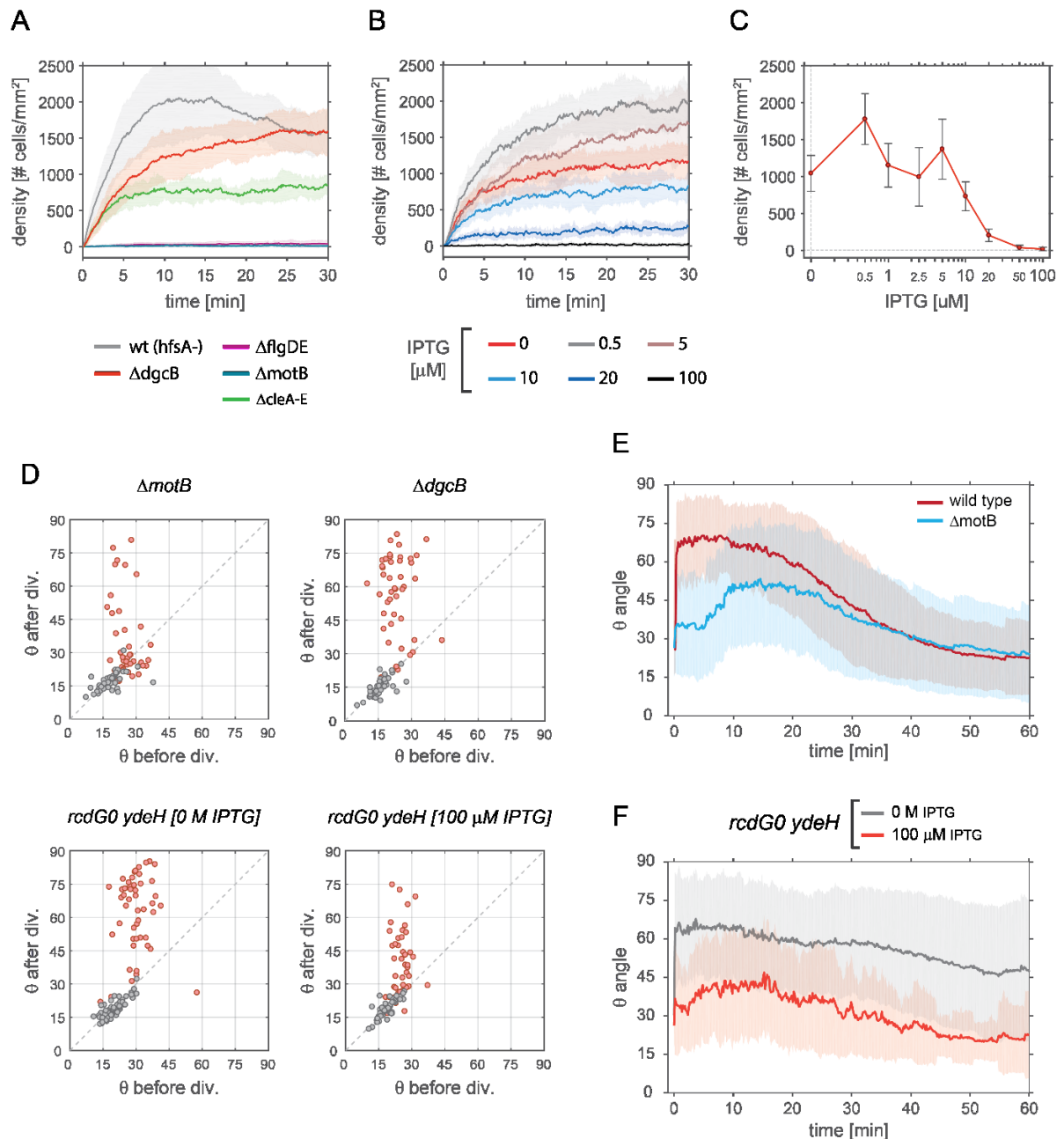


**FIGURE 6 – Effect of c-di-GMP on attachment behaviour.**

A, B - Pili mediated attachment efficiency in *C. crescentus* is measured as colonization levels at a constant flow of 0.75 mm/s. We tested several deletion mutants (A) and for the strain NA1000 *hfsA*- *rcdG*<sup>0</sup> *dgcZ* different levels of c-di-GMP concentrations (B), indicated as different induction levels. Shadow areas correspond to respective standard deviations.

C – Plateau levels of surface colonization with respect to c-di-GMP concentration for the strain NA1000 *hfsA*- *rcdG*<sup>0</sup> *dgcZ*. Each point is the average value of colonization levels between minute 10 and 25. Error bars are relative standard deviations.

D – Scatter plots show the average angle  $\theta$  of cells recorded 5 minutes before and 5 minutes after cell division. The results shown were obtained with the strains indicated. (Colouring of swarmer cells are in red, stalked cells are in grey) [  $n = 41$  ( $\Delta$ *motB*);  $n = 45$  ( $\Delta$ *dgcB*),  $n = 50$  (*rcdG0 dgcZ* [0 M]);  $n = 46$  (*rcdG0 dgcZ* [1  $\mu$ M]) ].

E, F – Dynamics of pili-mediated standing up of swarmer cells. The chart shows the time evolution of the angle  $\theta$  in daughter cells of *C. crescentus* wild type (wt) and  $\Delta$ *motB* (E) and *rcdG*<sup>0</sup> *dgcZ* with IPTG concentrations of 0 and 100  $\mu$ M (F). Time zero corresponds to moment of separation of mother and daughter cells. [ E:  $n = 98$  (wt);  $n = 41$  ( $\Delta$ *motB*); F:  $n = 50$  (*rcdG0 dgcZ* [0 M]);  $n = 46$  (*rcdG0 dgcZ* [1  $\mu$ M]) ].

The effect of c-di-GMP on the standing up behaviour was tested with the strain NA1000 *hfsA-rcdG<sup>0</sup>dgcZ*. Without induction (0 M IPTG), the tilt angle in the 5 minutes after division was similar to wild type. Inducing *dgcZ* with 100  $\mu$ M IPTG resulted in intermediate  $\vartheta$  values, rarely above 60° (Figure 6D). Different expression levels of *dgcZ* also influenced the time evolution of the tilt angle (Figure 6F). No induction (0 M IPTG), resulted in cells standing up for longer than 10-15 minutes. After 1 hour the average tilt angle in the population was still about 45° degrees, compared to an average  $\vartheta$  value of 20° degrees for wild type. Induction levels of with 100  $\mu$ M IPTG resulted in almost the opposite phenotype. Swarmer cells were able to stand up, but only at low  $\vartheta$  values between 20° and 45° degrees.

## 5.4 DISCUSSION

At the late predivisional stage compartmentalization between stalked and swarmer cells has already occurred and all components of the pili machinery are expressed<sup>93,109</sup>. Our results show that pili machineries are already assembled and operating before cell separation. Pili retraction can pull the new pole away from the stalked pole, supporting surface sensing (Fig 3). The short surface residence time of swarmer cells (Fig 1) suggests that pili mediate transient surface contact, offering a short time window for holdfast to be formed in order to irreversibly glue cells to the surface. Swarmer cells obtain upright position when, probably, multiple surface attached pili are pulling in different direction at the same time. The cell pole is forced down on the surface and may acts like a hinge, thereby rotating the cell body into an upright position. Despite the drag forces inflicted by the flow, the constant force of retracting pili maintains cells in such position, regardless of the presence of holdfast (see Fig 2C and Supplemental Movie 1). Pili-mediated attachment and retraction optimally positions the pole on the surface for tactile sensing and rapid anchoring of the holdfast for permanent attachment<sup>35</sup>.

Our results show that cells able to attach at higher flow rates were able to remain attached longer (Supplemental Figure 1A,B). In response to the drag force experienced by flow pili fibers may undergo conformational changes that strengthen the interaction with the surface. In line with this hypothesis in *N. gonorrhoeae* tensional stresses bring conformational changes that expose new epitopes in the filament<sup>124,125</sup>. Moreover, a bimodal behaviour has been reported to occur for the adhesion of FimH Type 1 pili of *Escherichia coli*<sup>126</sup>.

We were able to observe walking-like behaviour in the *C. crescentus* mutant  $\Delta hfsK$ , by weakening the holdfast and applying flow to force cells to orient the leading/piliated pole upstream. The ability of *C. crescentus* to walk after only a single mutation in the holdfast machinery was surprising, considering that twitching and walking have only been observed in bacteria expressing Type IVa pili. The upstream direction of walking when subjected to laminar flow has been reported in studies where *P. aeruginosa* exhibits an upstream zig-zag motion<sup>127</sup>. The reorientation induced by the flow, coupled with the polar localization of pili explains the directed walk. Our results suggest that for simple walking upright to evolve, bacteria need only to localize pili at one pole. Stochastic cycles of elongation and retraction may then be sufficient for a random walk on a surface. Cells must coordinate pili to ensure one pilus remain attached to the surface at any time, in order to prevent removal by flow. *C. crescentus* cannot do that, which is demonstrated by the small residence time and lack of walking behaviour in *hfsA*- strain

(see Supplemental Movie 1). However, the  $\Delta hfsK$  mutant can use the lower cohesion holdfast function as a weak anchor, avoiding the need of coordinating pili activity.

Using the  $\Delta hfsK$  mutant with its weakly coherent holdfast we could demonstrate that pili remain active after holdfast production and our results suggest they are capable of multiple cycles of elongation/retraction within a window of 10-20 minutes after cell separation and attachment. These results suggest that holdfast secretion does not lead to pili removal. Instead, the removal of the pili machinery may simply be a consequence of cell cycle progression and the motile-sessile switch<sup>93</sup>.

Lastly, our results suggest that pili retraction may be directed by the intracellular levels of c-di-GMP. Interestingly, deletion of *motB* has major effects. Pili-mediated standing up is not abolished, but instead delayed (Figure 6E). Swarmer cells might fail to stand up after division due to an inability to rise intracellular levels of c-di-GMP upon surface contact<sup>35</sup>. However, c-di-GMP levels increase over time due to cell cycle progression, activating pili at later point. The  $\Delta dgcB$  mutant which fails to raise c-di-GMP in response to surface contact<sup>35</sup> displays only marginally lower pili activity than wild type (Figure 6D and F). This suggests that some other downstream effectors may regulate pili activity. Our results also show that low levels of c-di-GMP improve pili mediated attachment (Figure 6B) and retraction (Figure 6F). On the other hand, higher c-di-GMP levels have the opposite effect (Figure 6B and 6F). Taken together those results may suggest that a newborn swarmer cell having low intracellular levels of c-di-GMP can express and extend pili but upon surface contact the c-di-GMP levels rise to some intermediate levels or locally at the flagellated pole which could promote surface attachment and pili retraction. As the cell cycle progresses, intracellular c-di-GMP rises up to levels that may signal cells to disassemble the pili machineries.

## 5.5 METHODS

### 5.5.1 Bacterial Strains and growth conditions

The wild type (*wt*) strain of reference was *NA1000 hfsA+*, which have functional pili and holdfast. *NA1000* is a lab adapted strain with a point mutation in gene *hfsA*, which makes it unable to secrete the holdfast, therefore the functional gene was reintroduced (*hfsA+*). Strain *NA1000 hfsA+ ΔcreS* produce rod-shaped cells, due to deletion of crescentin gene. Deletion of the major pilin subunit, *NA1000 hfsA+ ΔpilA*, make cells unable to secrete pili fibers. However, in the flow channel setting the attachment efficiency was extremely low. Therefore, the strain *NA1000 hfsA+ ΔflgDE ΔpilA* was used for testing the absence of pili. The train *NA1000 hfsA+ ΔflgDE*, resulting in cells without flagellar filaments, due to deletion of flagellar hook genes, was used as control.

*NA1000 hfsA+ rcdGO dgcZ ΔhfsK* is a mutant which secrete a holdfast having lower cohesion, resulting in weaker surface attachment. To tune the amount of holdfast generated, the *hfsK* deletion was engineered in a strain that allowed to modulate intracellular levels of c-di-GMP, the primary allosteric regulator of the holdfast secretion machinery<sup>78,121</sup>. The lack of cdGMP cyclases (*rcGO*) is compensated by the presence of exogenous *dgcZ*, which was regulated by a *lac*-promoter.

Cultures of *C. crescentus* were grown overnight at 30°C in PYE media, under agitation. They were then diluted and regrown to exponential phase, at OD<sub>660</sub> = 0.2-0.3. The culture was then used for experiments in microfluidic devices, which were all conducted at room temperature.

### 5.5.2 Microfluidic devices

Masters were fabricated via standard photolithography protocols<sup>128</sup>. PDMS (polymethylsiloxane) device were created via replica molding, and then aged via heat treatment, placing them on hotplate at 150°C for 30 min<sup>129</sup>. This treatment increases the hydrophilicity of microchannel walls during experiments. Holes were drilled at inlet(s) and outlet(s), devices were treated in oxygen plasma and covalently bound onto borosilicate cover glass. To supply the fluids inside microfluidic devices one end of a PTFE microtube (0.56 x 1.07 mm, Fisher Scientific) was connected to an inlet/outlet. The other end was connected to a 1 mL plastic syringe (Soft-ject, Henke-Sass, Wolf), via a needle (23G, 0.6 x 30 mm, B. Braun Melsungen AG). All microflow experiments were conducted in single microchannel device having a height of 20 μm and a width of 100 μm.

### 5.5.3 Microfluidics and microscopy setup

Microfluidic devices were placed on the stage of an inverted microscope (IX81, Olympus GMBH). For the colonization experiments (see Fig 1), cultures were grown at precisely  $OD_{660} = 0.15$  and loaded in a syringe. The latter was connected to the device and mounted on a syringe pump (neMESYS low pressure module V2, 14:1 gear; Cetoni GMBH). The flow was initially set at 25 mm/s for 5 min to ensure that the microchannel surface was devoid of cells. Then time lapse recording was started and the flow was set to the desired target flow for a duration of 30- 45 minutes. The flow was then switched back at 25 mm/s to test the detachment behaviour for 15 min. During the whole procedure images were recorded at 0.1 fps, using 40x oil immersion objective. In order to ensure that the concentration of supplied cell did not vary, always new batch of culture at  $OD_{660}$  of 0.15 was used to conduct each single experiment.

For experiments of single cell division events, the cells were loaded in the device and left to colonize the surface to a level where the average distance between cells was  $\geq 15 \mu\text{m}$ . This colonization required 2-10 min, depending on the attachment efficiency of the strain being used. This ensured that single cell division events would not be influenced by neighbouring cells. A syringe supplied fresh media from the inlet at a steady flow of 1 mm/s. Cells were left to growth for 1-2 h before starting recording image sequences at 1 or 5 fps, using a 100x oil immersion objective. The experiments were conducted for no more than 10-12 h. This procedure ensured steady growth conditions and no overgrowth/clogging in the inlet (see Supplementary Figure 5).

### 5.5.4 Optical Tweezers setup and force measurements

The optical tweezers experiments were performed on a custom built bright field microscope, complemented with a laser diode setup (LD830-MA1W,  $\lambda = 830 \text{ nm}$ , Thorlabs). A water immersion, high aperture objective (UPlanSApo 60x water, Olympus) was used to focus the laserbeam, trap the beads with attached bacteria, and image the fluctuations of the bead in the trap and the attached bacteria. The experiments were carried out in position clamp mode at a constant laser power. The images of the bead and the attached cell were recorded with 50 Hz and 75 Hz using a fast camera (Phantom Miro EX4, Vision Research Inc.). The images were used to determine the position change of the bead during the experiment and observe the active cell.

Calibration of the optical tweezers was carried out via fluctuation calibration. For each laser power used, an image sequence of a bead in the trap was recorded at 1000 Hz. From the fluctuation of the bead in the trap the variance  $\sigma$  was determined. The trap stiffness  $K_{trap}$  was calculated as:  $K_{trap} = k_B T / \sigma^2$ , with  $k_B$  the Boltzmann constant and  $T$  the room temperature.

An exponential culture of *NA1000 hfsA+ ΔflgDE* at OD660 of 0.2 was mixed with polystyrene beads (Fluoresbrite YG Carboxylate Microspheres 3.00 μm, Polysciences) to a final concentration of  $1.7 \cdot 10^8$  beads per mL cell suspension. The mix was let stand for 2 min, allowing the time for cells to attach to the beads. Then a 1:1 dilution with fresh PYE was injected into the device, and experiments conducted in condition of no flow inside the device. Devices used for optical tweezers measurements had chambers at the side of a main channel<sup>86,128</sup> connected by an opening of less than 10 μm. Single bead-carrying predivisional cells were chosen and placed inside the chambers where the optical tweezers measurements could be performed undisturbed by other cells.

### 5.5.5 Image analysis

Cell outline detection was carried out using Matlab-based program *microbeTracker*<sup>130</sup>. Further tracking, analysis and statistics were carried out with in-house developed Matlab scripts. Cell outline was fitted to an ellipse and we extracted the value  $\varepsilon$ , which is the eccentricity of the ellipse, the ratio between its the major and minor axes. We used the eccentricity to get the inclination of cells in respect of the surface, angle  $\vartheta$ . We place an  $\varepsilon$  value of 1 for to be an angle  $\vartheta$  of 90° and an  $\varepsilon$  value of 0.1 to be a tilt of 0°. Eccentricity value below 0.1 can be excluded as they represent very elongated ellipse, with a ratio length-to-width ratio that do not occur for single *C. crescentus* cells.

To track the trajectories of cell we choose to follow the position of the holdfast. This position would lie in a point between a vertex and a focus of the ellipse which fit the 2D projection of the cell. The position was dependent on  $\varepsilon$ , such that as the cell is upright, it coincides with the focus, and the cell lies flat, it is the close to the vertex (see Fig 4 A).

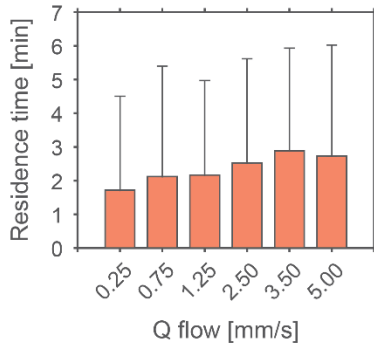
Step events in the trajectories of  $\Delta hfsK$  strain (see Fig 4 B and C) were determined as the time windows when fast upstream advancements (in the x-axis direction) occurred.

## 5.6 ACKNOWLEDGEMENTS

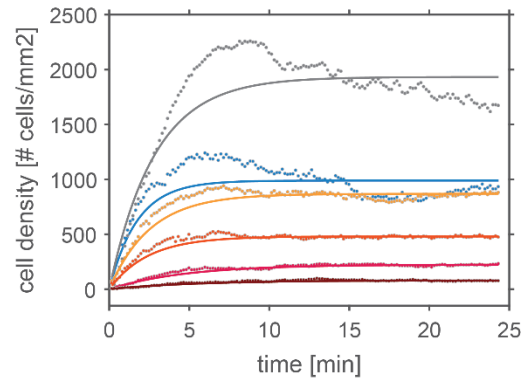
We acknowledge Ursula Sauder and Carola Alampi of the C-CINA of Imaging Core University of Basel for technical assistance with the TEM microscopy and Benoît-Joseph Laventie for fruitful discussions and critical comments on the manuscript. We gratefully acknowledge funding by the Swiss Nanoscience Institute in Basel, Switzerland (SNI PhD graduate school, Project P1302) and by the Swiss National Science Foundation (grant 310030B\_147090 to U.J.).

## 5.7 SUPPLEMENTAL FIGURES

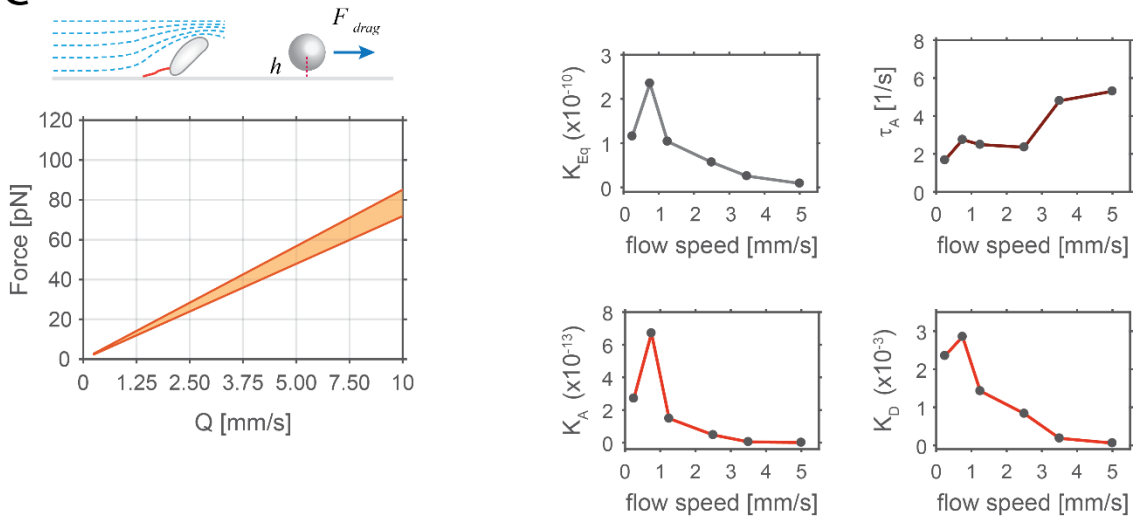
**A**



**B**



**C**



**Supplemental Figure 1**

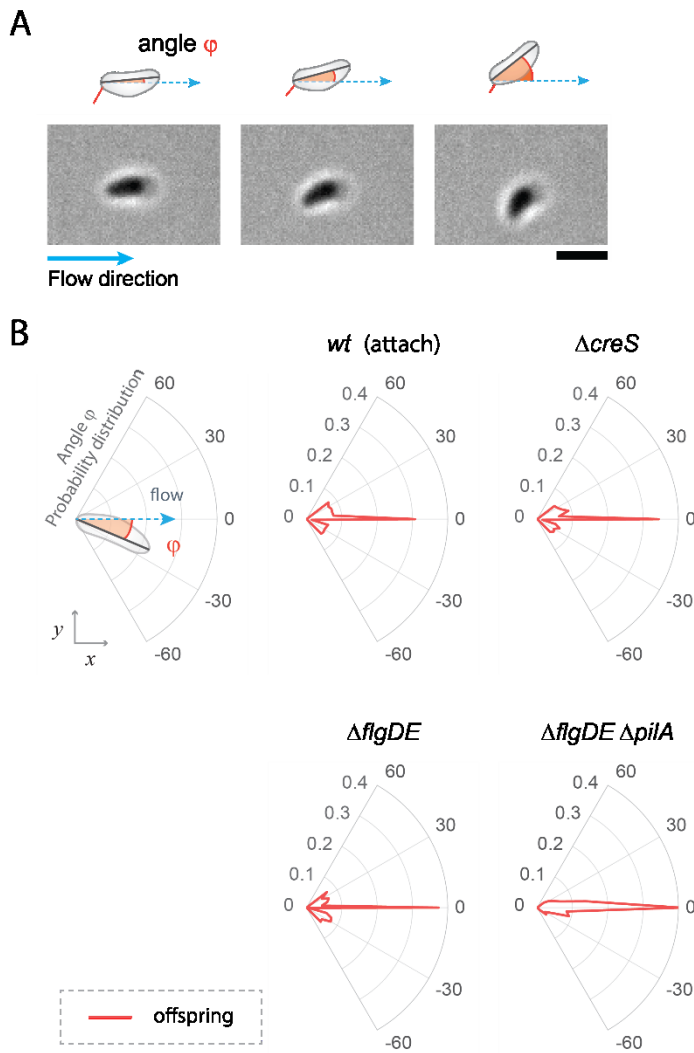
**A – Average time of residence of single cell on a surface via pili** - Pili mediate transient attachment to glass surface. Bar chart showing the average residence time on surface for swarmer cells having pili, but no holdfast (strain NA1000 *hfsA-*), under different flow rates. There is no statistically relevant difference between different flow velocities.

**B – Modelling after a Langmuir adsorption process** - The upper chart shows the colonization behaviour at different flow rates (dots) with the respective fitting after Langmuir adsorption isotherm process. The 4 lower charts show the extrapolated reaction constants ( $K_{eq}$ ,  $K_A$  and  $K_D$ ) and time constant ( $\tau_A$ ).

**C – Theoretical drag force near a surface** - The graph shows the theoretical drag force experienced by a typical swarmer cell and stalked cell attached to a surface at different flow rates. The drag force is calculated using the equation shown below. The equation the drag force experienced by a sphere near a surface, with a volume equal to the average swarmer (orange) or stalked cell (red). The two areas show the range for the sphere having a distance from the surface ( $h$ ) ranging from 0 to 0.5  $\mu\text{m}$ .

$$F_{Drag} = \frac{3\pi a \mu u_z}{2 \left( -\frac{0.0625 a^5}{h^5} - \frac{0.1758 a^4}{h^4} + \frac{0.125 a^3}{h^3} - \frac{0.5625 a}{h} + 1 \right)}$$

( $a$  = radius of the sphere with equivalent volume  $\approx 0.62 \mu\text{m}^3$  for swarmer and  $\approx 0.71 \mu\text{m}^3$  for stalked cells,  $h$  = height from the surface,  $\mu$  = viscosity,  $u_z$  = flow velocity at height  $h$  from the surface). Equation eq 7-4.37 from <sup>131</sup>.

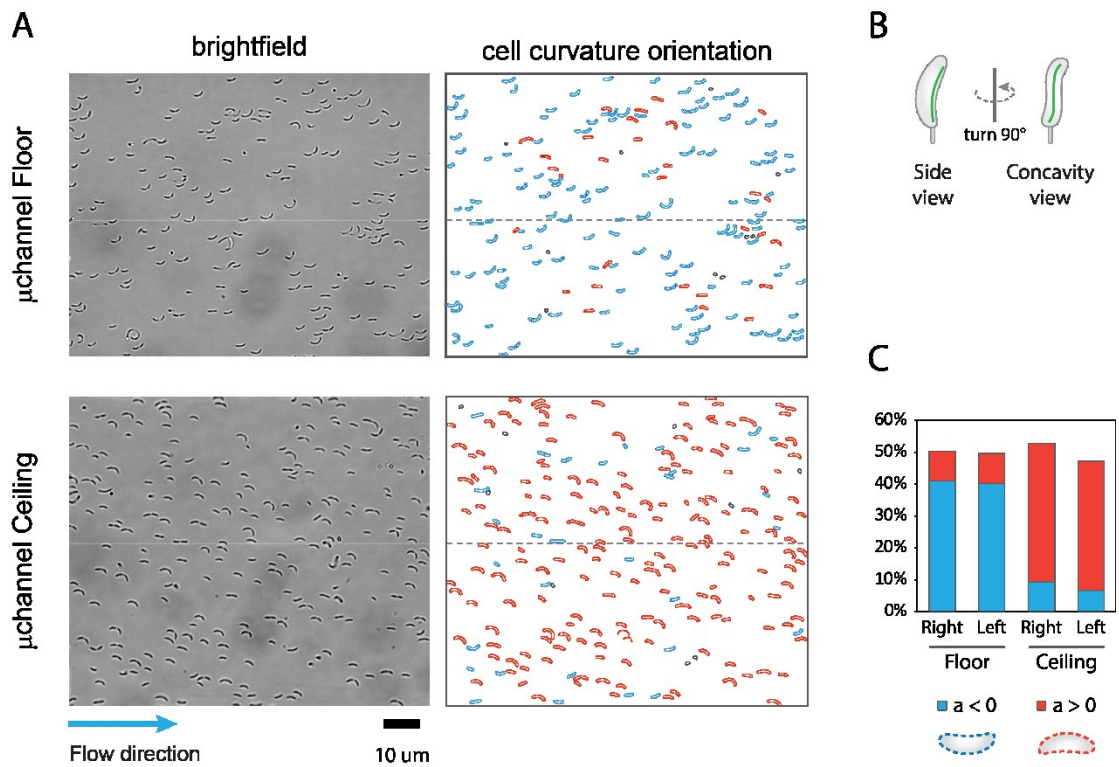


### Supplemental Fig 2

A – Image sequence interval of a swarmer cell reorienting its body away from flow lines due to the activity of polar pili. A schematic representation of the cell positioning and the angle  $\varphi$  is shown above the images.

B – Polar plots showing the distribution of angle  $\varphi$  in swarmer cells during a five-minute window after cell division. The angle  $\varphi$  describes the angle between the cell body axis and the flow line and changes in  $\varphi$  indicate the deviation from the flow. *C. crescentus* wild type cells (attach) show a prominent peak at  $0^\circ$ , since cells spend most of the time in a position parallel to flow lines. However, cells are able to deviate from this position and reorient their body with an angle of up to  $\pm 40^\circ$ . The same trend can be observed for  $\Delta creS$  and  $\Delta flgDE$  strains. In contrast, a  $\Delta flgDE \Delta pilA$  strain shows a much narrower distribution around  $0^\circ$ , indicating that cells lacking pili are unable to actively reorient.

[wt (attach),  $n = 130$ ; wt (swim),  $n = 119$ ;  $\Delta creS$ ,  $n = 56$ ;  $\Delta flgDE$ ,  $n = 57$ ;  $\Delta flgDE \Delta pilA$ ,  $n = 75$ ] (scale bar in A and C is  $2 \mu\text{m}$ )

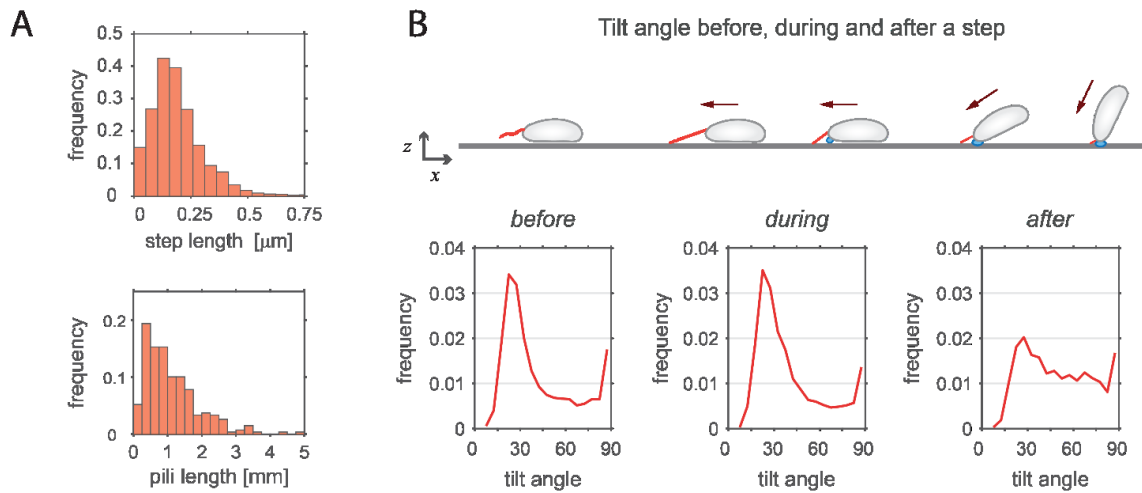


**Supplemental Fig 3**

A – Bright field images of *C. crescentus* cells attached to the floor and ceiling of a microfluidic channel. Cells with the concavity oriented to the right in the direction of the flow are shown in red, while cells oriented to the left are shown in blue.

B – Schematic drawing show the proposed cell shape of crescentoid *C. crescentus* with a small left-handed twist.

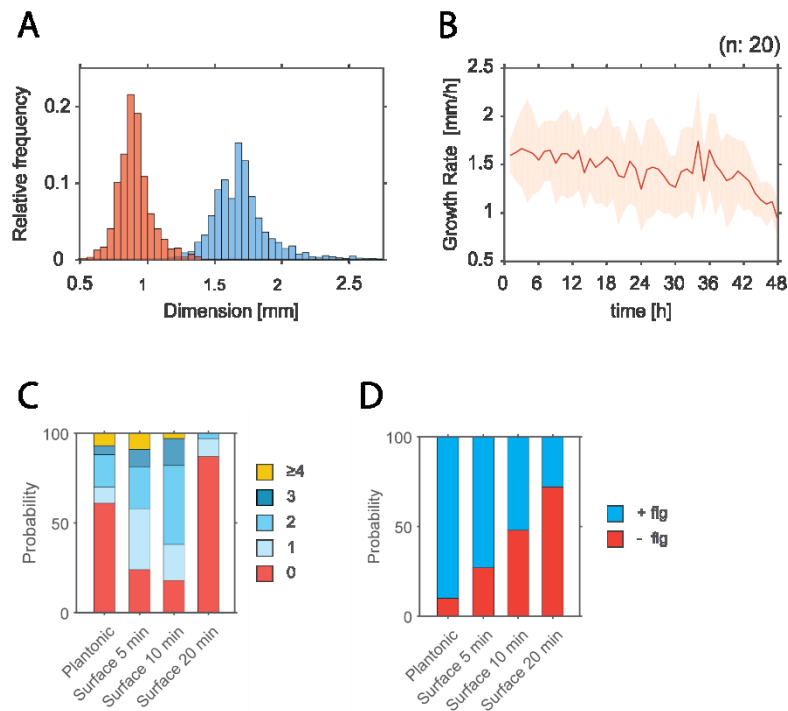
C – The chart shows the result of the analysis of three independent experiments with cells scored on  $\geq 0.3 \text{ mm}^2$ , for both ceiling and floor surfaces of a device. Concavity distribution is also scored also in respect of cells position: the right half or left half of the channel, have the same concavity distribution.



#### Supplemental Fig 4

A – Upper plot show the step length distribution for NA1000 ΔhfsK mutant strain (n = 56). The lower plot shows the distribution of pili length in wild type strain observed at TEM (n = 271). Cells in a planktonic culture were fixed with 0.1% glutaraldehyde and then spotted on a grid for electron microscope. Samples were then washed with water and negatively-stained with 0.5% uranyl acetate. Images taken at the TEM were visually inspected to locate cell-attached pili and measure their length.

B – Schematic drawing of a *C. crescentus* swarmer cell moving against the medium flow and the standing upright at the end of each dislocation step. Pili (red), holdfast (blue) and cell movement (red arrow) are indicated. The charts below the graph show the distributions of tilt angle values five seconds before (left), during (middle) and five seconds after (left) a step event. Three different flow velocities were analysed. Before and during a step event cells lie flat on the surface, while standing up upon completion of an upstream movement.

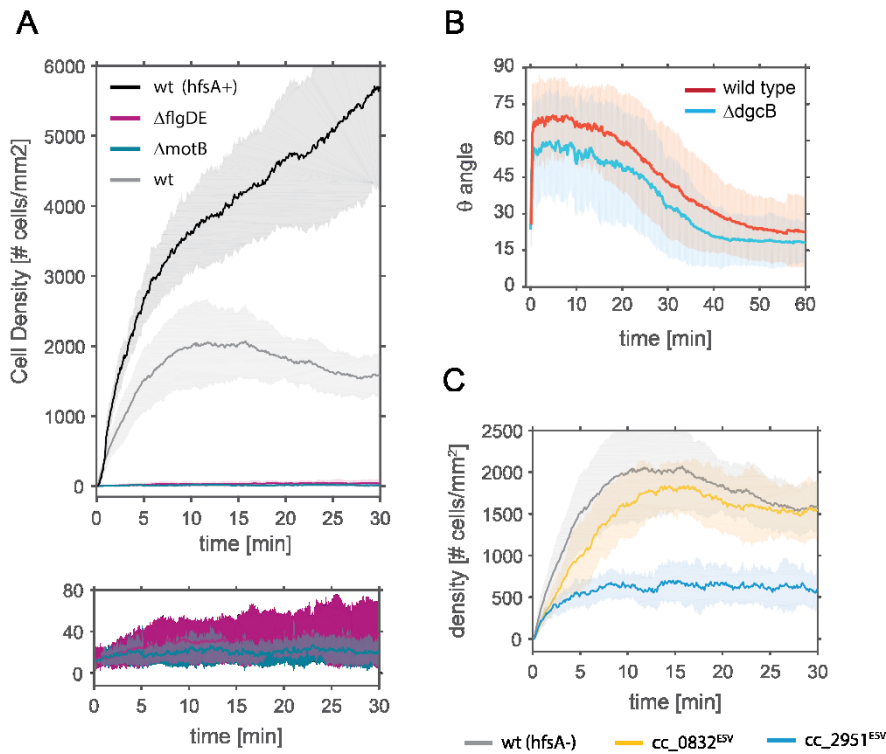


### Supplemental Fig 5

A – Distribution of the cell diameter (red) and cell length (blue) of swarmer cells at the time of separation from their stalked mothers ( $n = 130$ ).

B – Growth rate of individual cells in a microfluidic device for 3 days ( $n = 20$ ). Cells of *C. crescentus* strain NA1000 *hfsA*<sup>+</sup> *ΔpilA* attached the surface of a microfluidic channel were grown for three consecutive days under constant imaging conditions and imaged at 0.5 fpm. The red line is the average and the opaque area is the standard deviation. The results show no significant decrease in growth rate in the first 24 hours.

C and D – Number of pili (C) and the presence of flagellum (D) observed at the pole of individual *C. crescentus* swarmer cells. A cell culture was fixed with 0.1% glutaraldehyde while still in a planktonic culture, or after being spotted on the TEM grid for 5, 10 and 20 min, in order to allow them to make surface contact. Samples were then washed with water and negatively-stained with 0.5% uranyl acetate. Images taken at the TEM were visually inspected to locate swarmer cells, defined as cells with length  $< 2.4 \mu\text{m}$ . Cells were categorized in five different classes according to the number of pili (C) and the presence of attached flagellum flagellum was recorded (D).



**Supplemental Fig 6**

A – The chart is the same shown in Figure 6A. Wider y-axis range allow to appreciate differences in attachment levels between strains without a holdfast (NA1000 *hfsA*-) and strains capable with a holdfast (NA1000 *hfsA*+). In the lower part is shown an enlarged view of  $\Delta$ *motB* and  $\Delta$ *flgDE* strain.

B - Dynamics of pili-mediated standing up of swarmer cells. The chart shows the time evolution of the angle  $\theta$  in daughter cells of *C. crescentus* wild type (NA1000 *hfsA*-), and  $\Delta$ *dgcB* mutant strain. Time zero corresponds to the time when mother and daughter cells separate. (n = 98 (wt); n = 45 ( $\Delta$ *dgcB*)).

C – The chart show the colonization levels in strain cc\_0832<sup>ESV</sup> and cc\_2951<sup>ESV</sup>. Both have single amino acid substitution for the highly conserved Glu5 at N-terminal. Wild type (NA1000 *hfsA*-) is reported as control.

## 6 INTERPLAY OF PILI AND FLAGELLUM DURING CELL SEPARATION

---

### 6.1 ABSTRACT

The model organism *C. crescentus* divides asymmetrically, producing a sessile stalked cell and a motile swarmer cell. The swarmer cell is equipped with a flagellum and pili on the same pole. Pili are used for intermittent surface attachment of the cell and the flagellum is used for swimming and surface sensing. In the predivisional daughter cell, pili and the flagellum are active during the same time window. In this work we investigated the interplay of pili and the flagellum in the predivisional cell. We show that pili are capable of surface attachment and keeping the cell in position in presence of the rotating flagellum. We used an optical tweezers set-up and predivisional *C. crescentus* cells attached to polystyrene beads to visualize the dynamics of the flagellum and pili under physiological conditions. The rotation of the flagellum decreases the average attachment duration of single pili, but it increases the attachment rate of pili. This result indicates a positive hydrodynamic effect of the flagellum on pili attachment efficiency. In between pili attachment cycles, a flagellum induced gyrational motion in the optical tweezers was observed. This finding suggests a complete release of the pilus, mediated by detachment or breakage of the pilus.

## 6.2 INTRODUCTION

Swarmer cells of *C. crescentus* are equipped with a flagellum and pili. The flagellum is a corkscrew-like structure at the outside of the cell that is used for swimming<sup>12</sup>. Pili are hair-like structures also located at the outside of the cell envelope and used among other functions for surface attachment and motility<sup>36</sup>. Bacterial cells have developed a variety of different pili. One of the most sophisticated types are the type IV pili. They are widespread in bacteria and archaea and can undergo cycles of retraction and extension by the disassembly and assembly of pilin subunits<sup>43–45</sup>. Type IV pili are divided into two subclasses, type IVa and type IVb. A subclass of type IVb pili are called tight adherence pili (Tad) and are widely found in Gram positive and negative bacteria, among them *C. crescentus*. In *C. crescentus*, the flagellum and pili are located at the newly formed pole opposite of the stalk and act as counterparts. The pili act as anchor to attach and stabilize the cell onto the surface until a holdfast is formed for permanent attachment<sup>15</sup>. The flagellum on the other hand is used for motility and exploring new spaces. It is easy to see these two appendixes as natural counterparts, shaping the future of the cell.

*C. crescentus* is a widely used model organism for bacterial cell cycle and cell polarity studies, because it generates two morphologically different cells upon cell separation. The swarmer cell is replication inert and motile, it has a flagellum and pili on one pole. Upon surface contact or after a defined period of time, the formation of a holdfast and later a stalk is initiated. The cell attaches irreversibly to a surface and becomes replication competent. DNA replication is initiated and a fresh cell is formed at the pole opposite to the stalk<sup>21</sup>, harboring 2 - 3 type IV pili and a single flagellum on the free pole. After completion of cell separation, the cell is released as a replication inert, motile swarmer cell. For convenience, this cell is named daughter cell in the following. The stalked cell, termed mother cell in the following, remains replication competent and starts a new reproducing cycle right after the division of the daughter cell (Figure 6.1, CW from top). The cell cycle can be shortcut by exposing the surface attached predivisional cell to flow. This brings the free pole of the daughter cell in close proximity to the surface. Upon surface contact, about half of the daughter cells form holdfasts even before cell separation is completed and remain attached<sup>35</sup>. The other half of the cells is flushed away by the flow. The fate of the daughter cell depends on whether the cell rotates in the last seconds before cell separation or not. When the cell is rotating, this means a rotating flagellum, the cell is very likely to be flushed away after cell separation. When the cell does not rotate during the last seconds of cell separation, the cell is much more likely to form a permanent holdfast and stay attached to the surface<sup>35</sup>. The latter case of the cell not rotating could have two different reasons: Firstly,

the flagellum is simply not active and there are no forces acting on the daughter cell. The formation of the holdfast allows then the permanent attachment of the daughter cell after cell separation. Secondly, the flagellum is active and rotating, but something is holding the cell in position, preventing the rotation of the daughter cell. It is very likely that in this case the pili temporary attach the cells to the surface until a holdfast is formed.

To better resolve the activity of the flagellum and pili during the cell separation process, we established a more sensitive approach that allowed us to observe and measure the dynamics of the pili and flagellum from their onset until cell separation.

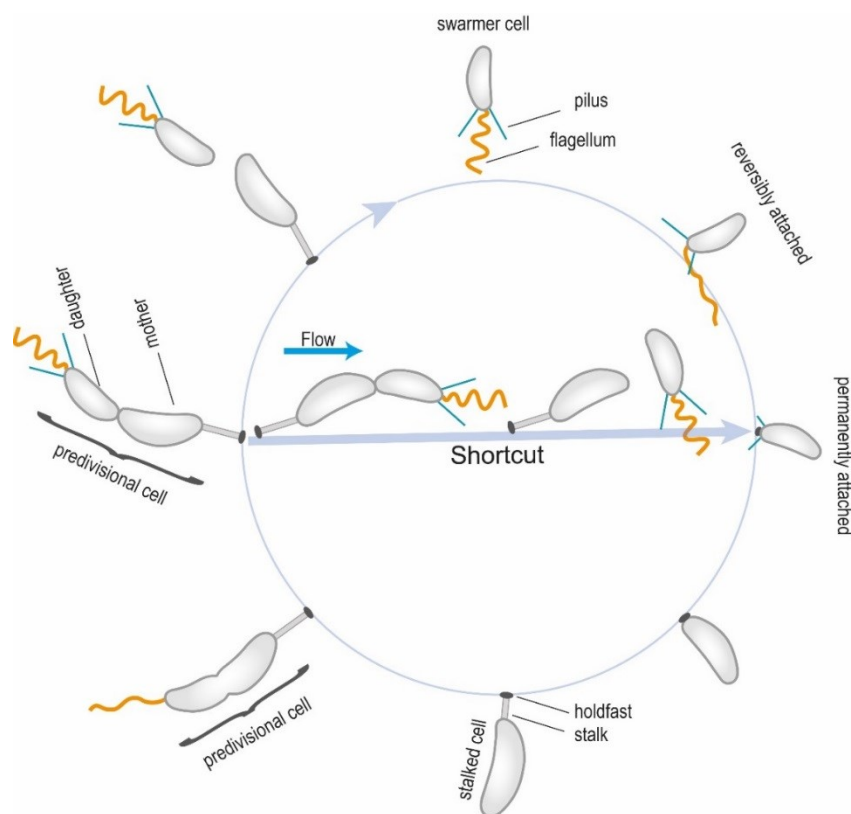


**Figure 6.1: *C. crescentus* cell cycle.** The cells have a dimorphic life cycle. Two progeny cells with different characteristics and fates are generated. The newly formed daughter cell has a flagellum and pili at the free cell pole. After cell separation, the swarmer cells swim until they reach a surface and anchor via their pili, followed by permanent attachment via holdfast. The cell cycle can be shortcut by applying a flow. The swarming phase can be omitted when the predivisional daughter cell is exposed to a surface. In this assay about 50% of predivisional cells permanently attach to the surface before cell separation is completed.

## 6.3 MATERIALS AND METHODS

### 6.3.1 Cell Preparation

Cells were grown overnight in peptone yeast extract (PYE, in-house media kitchen, see Appendix for composition) under agitation at 30 °C. To attach cells to colloidal beads, the overnight culture was diluted 1:10 with fresh PYE and put back for 2 h at 30 °C. The initial dilution led to a starting concentration of roughly  $1.4 \times 10^8$  cells/ml. The cells were then further diluted 1:2 with PYE and 25  $\mu$ l bead solution/ml cell suspension (diameter: 3  $\mu$ m,  $1.68 \times 10^9$  particles/ml, Polysciences, Inc.) was added and mixed well with the pipette tip. The solution was incubated for 2 min, then a small amount was placed on a coverslip and the number of cells per bead was checked. When an appropriate number 1 - 2 cells per bead was reached, the cell suspension was once more diluted 1:1 with fresh PYE and injected into the device. The tubing was removed and the PDMS (Polydimethylsiloxane) device was submerged in PYE to create a strict no-flow environment and to avoid evaporation<sup>87</sup>. The experiments were performed 2 – 8 h after cell injection. At a later time point, the device was too crowded with cells.

### 6.3.2 Strains Used

The strain NA1000 *hsfA+* is referred to as wildtype (WT). It has a flagellum and 2 - 3 pili. The flagellum changes its rotation direction regularly about every second. The strain NA1000 *hsfA+  $\Delta creS$  ( $\Delta creS$ )* lacks the gene for expressing crescentin, the protein that causes the cells typical curvature<sup>17</sup>. This cell is therefore rod-shaped instead of the curved crescentic shape. It has a flagellum and pili as well. The strain NA1000 *hsfA+  $\Delta flgDE$  ( $\Delta flgDE$ )* has the typical curved shape and pili, but no flagellum. All used strains form holdfasts, the ability to irreversibly attach to surfaces was indispensable for the experiments.

### 6.3.3 Microfluidic Devices

Standard photolithography and PDMS casting were performed as described in chapter 3.1. After covalently binding the PDMS replica to a glass slide, a small plastic ring that fits over the PDMS replica was dipped into liquid PDMS and was placed around the replica. The devices were thermally aged to render the surface inside the device more hydrophilic and to get rid of any remaining low molecular weight polymer chains<sup>88</sup>. To do so, the device was placed on a hotplate for 4 h at 150 °C. After this, the devices were stored at 80 °C until used. This procedure decreased sticking of the polystyrene beads.

In order to prevent sticking of the polystyrene beads to the surface further, the channels of the microfluidic devices were coated with 1 mg/ml bovine serum albumin (BSA, Sigma) dissolved in

deionized water. After rinsing the device with PYE, the BSA solution was pumped (pump module: neMESYS low pressure syringe pump V2, 14:1 gear; Cetoni GMBH) through the device for several minutes, followed by a rinsing step with PYE to prepare the cell injection.

#### 6.3.4 Optical Tweezers and Microscope

All experiments were performed on the custom-built microscope described in Materials and Methods. The optical tweezers consisted of a tunable laser diode (1 W, 830 nm, LD830-MA1W - 830 nm, Thorlabs) and a lens system to collimate, align, and expand the laser beam to overfill the back aperture of the objective. The laser beam was focused through the back aperture of the objective (60x water, 1.20, Uplansapo, Olympus). The experiments were performed in position clamp mode at a constant laser power. The optical tweezers were calibrated via fluctuation calibration. For more information, see chapter 2. A high speed camera (Phantom Miro eX4, Vision Research) was used for all recordings. The cells attached to the beads in the optical tweezers were recorded at frame rates of 50 – 100 Hz.

#### 6.3.5 Experimental Procedure

For the measurements, colloidal beads with attached cells in their late predivisional state were trapped by optical tweezers. If necessary, the beads were placed inside a microfluidic side chamber to reduce the disturbance of other cells. The beads were held in the optical tweezers at varying laser powers from 0.3 A to 0.6 A. If possible the cells and the beads were imaged and recorded until cell separation was completed.

#### 6.3.6 Data Analysis

The position of the 3  $\mu\text{m}$  bead held by the laser was determined via a self-written Matlab script (see Appendix). The script determined the position of the bead for each frame. From the trajectory, the onset of flagellar rotation and pili attachment, retraction and release events were determined. From this we calculated attachment duration and efficiency. We also have used a second script, the Gyrograph to determine and display the position of the cell for each frame.

## 6.4 RESULTS

In the WT, the swarmer cell is equipped with pili and a flagellum. We have shown that the flagellum is also already active several minutes prior to cell separation (chapter 4). We knew from experiments in a microfluidic flow channel that about half of the daughter cells managed to permanently attach to the microfluidic device, while the other half of the cells was flushed away with the flow upon cell separation<sup>35</sup>. The cells that did not attach were rotating during the last seconds before cell separation, indicating that in these cases the flagellum was freely rotating. For the other half of the cells, the ones that stayed attached, attachment had to be completed before the cells started rotating. We wanted to gain a better understanding of the interplay between the pili and flagellum in the predivisional cell. Not just a snapshot of the situation when the cells divided, but the whole picture, from the first activity of pili and flagellum until cell separation. To this means we let different strains attach to beads and recorded their behavior in the optical tweezers. We directly measured the competition between flagellum and pili with a combined set-up of light microscopy and optical tweezers. To dissect the impact of the flagellum and the cell shape onto pili activity, different mutants were tested.

### 6.4.1 Pili Dynamics Depends on Load

We established a set-up to characterize the dynamics of pili in the predivisional cell. We made use of the ability of *C. crescentus* to attach to nearly any surface and ensured the attachment of cells to beads with a diameter of 3  $\mu\text{m}$ . First, the dynamics of pili for different loads were determined. To this means, a strain without a flagellum ( $\Delta\text{flgDE}$ ) was used. In this way, the dynamics of pili are not influenced by the flagellum. The beads with the attached cells were recorded at frame rates of 50 – 100 Hz in bright field. This allowed us to track the position of the bead for the analysis of translational movement, and the position of the cell for the analysis of the rotational displacement. The bead was hold by the optical tweezers at a constant laser power and in position clamp mode (Figure 6.2A, left). When a pilus of the predivisional daughter cell attached to the glass surface and subsequently retracted, the retraction of the pilus dragged the bead out of the center of the optical tweezers (Figure 6.2A, right). When the pilus was released, the bead was dragged back into the center of the optical tweezers by the gradient force of the focused laser beam. A sequence of bright field images illustrating the difference before retraction (left), retraction (center) and after retraction (right) of a pilus is shown in Figure 6.2B. The active cell is indicated by a black arrow and the resting position of the bead is indicated with a yellow ring. The grey stippled ring indicates the tracking position of the Gyration. The direction of retraction is indicated with a yellow arrow in the second image.

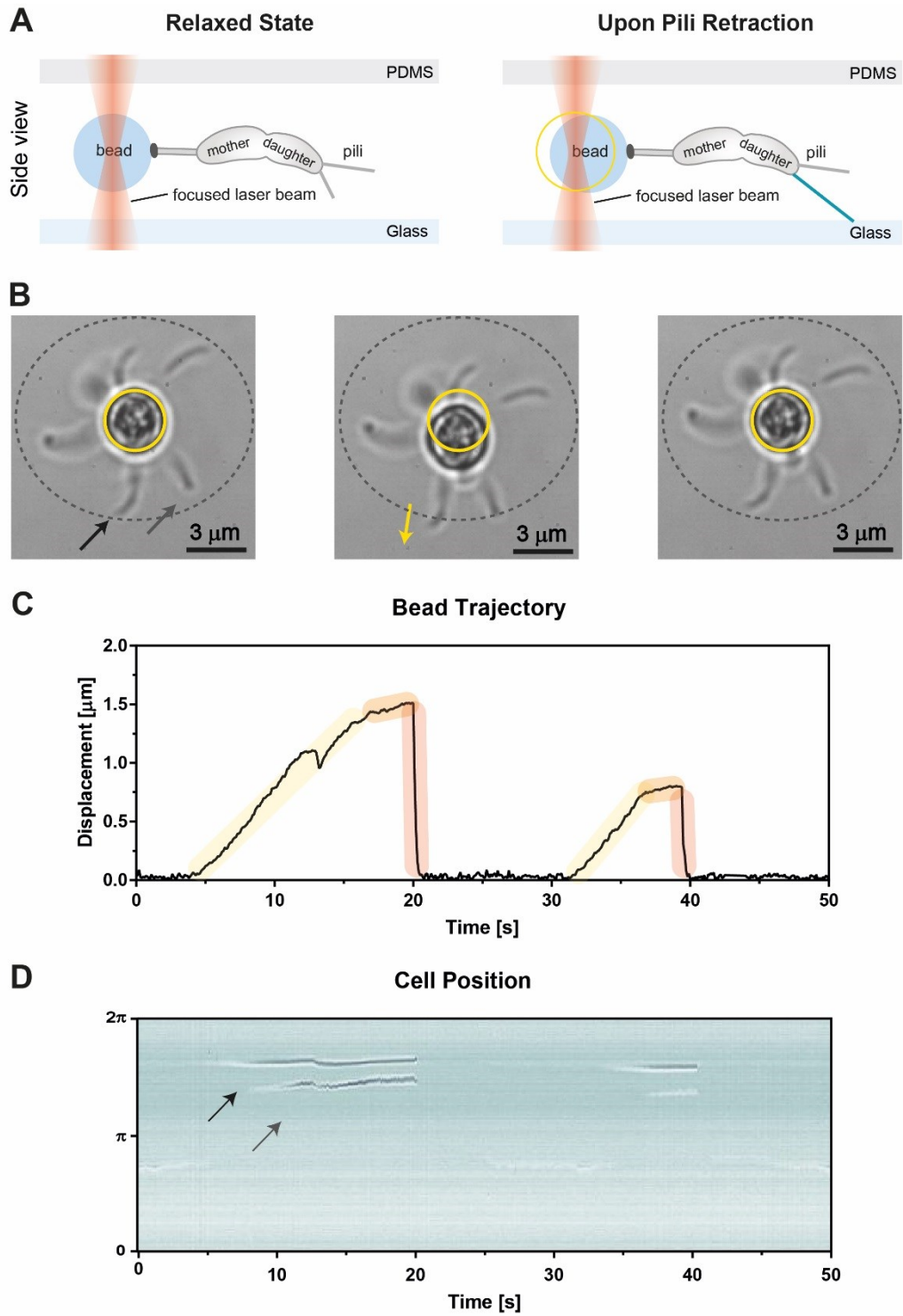


**Figure 6.2: Pili dynamics.** **A:** Sketch of the experimental set-up. In the relaxed state, the bead rests in the center of the optical tweezers (left). Upon attachment and retraction of a pilus, the bead is dragged out of the center of the optical tweezers (right). **B:** Bright field images of a bead with attached cells before (left), during (center) and after pilus retraction (right). Black arrow: active cell. Yellow arrow: Pulling direction. Yellow ring: Relaxed position of the bead. Grey stippled line: Position of the Gyratograph. Grey arrow: Second cell in the Gyratograph. **C:** Example trajectory of the bead during two consecutive attachment circles. Yellow: Retraction, orange: Hold, red: Release. **D:** Gyratograph of the same sequence as in D. Black arrow: Active cell. Grey arrow: second cell brought into the Gyratograph by the pulling of the active cell.

A trajectory of the bead during two consecutive attachment – retraction – release - cycles is shown in Figure 6.2C. Retraction of the pilus is highlighted in yellow, the plateau in orange and release of the pilus in red. From the slope of the retraction curve and the release curve, the retraction-, respectively release speed was calculated. The Gyratograph of the same sequence, displaying the position of the cell over time (Figure 6.2D), shows the successive appearance of the active cell (black arrow) during pilus retraction. During the first retraction cycle, a second cell (grey arrow) appears on the Gyratograph due to the displacement of the bead. The line of the second cell is more blurred than the line formed by the retracting cell because the second cell is not attached and shows some thermal movement. Release of the pilus causes a much sharper transition in the Gyratograph than retraction.

We characterized the dynamics for different loads by increasing the laser power. An increased laser power increases the stall force of the optical tweezers and therefore increases the load on the pilus. The maximal displacement of the bead from the center of the tweezers was determined for two different loads/laser powers. The average displacement for the lower load was  $(1.0 \pm 1.0)$  s ( $n = 42$ ) and for the larger load it was  $(0.4 \pm 0.1)$  s ( $n = 6$ ) (Figure 6.3A). The duration of single attachment-retraction-release cycles were measured for the two different loads. The duration of an attachment cycle was on average  $(144.3 \pm 107.8)$  s ( $n = 43$ ) for the lower load and  $(103.5 \pm 25.6)$  s for the higher load ( $n = 6$ ) (Figure 6.3B). The retraction speed of pili also depended strongly on the load. For the lower load, the average retraction speed was  $(144.3 \pm 107.8)$   $\mu\text{m/s}$  and for the higher load the average retraction speed was  $(103.5 \pm 25.6)$   $\mu\text{m/s}$  (Figure 6.3C). We also determined the force that the pili are able to generate for different loads. For the lower load, the average force was  $(2.9 \pm 1.6)$  pN ( $n = 100$ ) and for the higher load the average force was  $(4.5 \pm 1.4)$  pN ( $n = 6$ ). Interestingly, the maximal force generated for both loads was nearly the same, around 8 pN. The release speed was found to be 1900 nm/s and is roughly 10x higher than the retraction speed. A more detailed discussion on the dynamics of pili is presented in chapter 5.

We found that the pili are dynamic and can retract and release. Release of the pilus is roughly one order of magnitude faster than retraction. This strongly indicates that retraction and release of the pilus are not powered by the same mechanism. Release could either be performed by re-assembly of pilin subunits, elongating the pilus to its initial length and therefore enabling the bead to go back in the center of the optical tweezers, or by complete detachment from the surface.

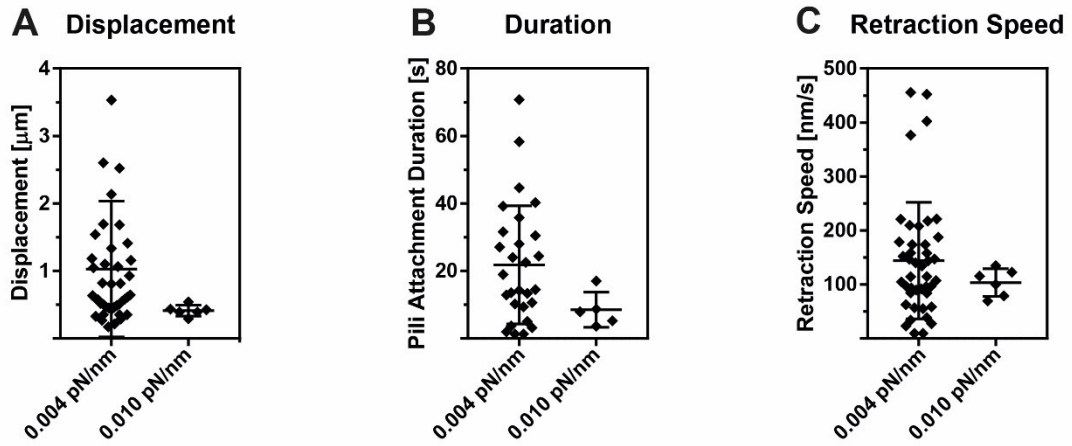


**Figure 6.3: Load dependence of pili dynamics.** **A:** Maximal displacement of the bead depending on the load. **B:** Duration of attachment depending on the load. **C:** Pili retraction speed depending on the load.

#### 6.4.2 Pili Can Attach to the Surface even when the Flagellum Is Rotating

We found that in predivisional cells the flagellum and pili are active at the same time and that pili can attach to the surface when the flagellum is rotating. A predivisional cell attached to a colloidal bead and being held in the optical tweezers showed a gyrational movement of the cell around the center of the trap because of the rotation of the flagellum (Figure 6.4A). Changes in the gyration direction were associated with the change in the rotation direction of the flagellum (see chapter 4.4.2). Suddenly the gyration stopped and the bead showed a lateral displacement. Additionally, the cell shape was distorted (Figure 6.4B). After a few seconds, the gyration of the bead was resumed (Figure 6.4C).

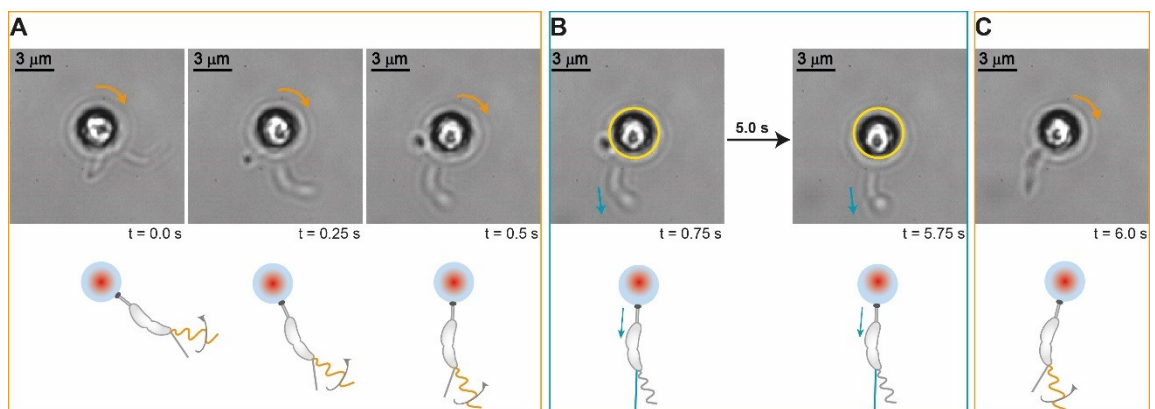


**Figure 6.4: Competition between flagellum and pili.** **A:** The active flagellum causes a rotational movement of the bead on the optical tweezers. **B:** Attachment of pili, the rotational movement is interrupted. **C:** Release of pili, the gyration is resumed.

It is unlikely that a mere stop of the flagellar rotation caused the interruption in the gyration because of the additional lateral displacement of the bead and the distortion of the cell shape. More likely is a sudden attachment of a pilus to the glass surface. Upon attachment of the pilus,

the gyration stops and the cell rests in this position until the pilus detaches and the cell resumes its gyration. A representative trajectory of the colloidal bead when both the pili and flagellum are active is shown in Figure 6.5A. When the flagellum is rotating freely, it is causing a gyration movement (white area). When a pilus is attached to the surface, it is dragging on the bead, causing a lateral displacement of the bead (grey area). Just from the trajectory of the bead the determination whether flagellum or pili are causing the observed motion is difficult. If the same sequence is plotted as Gyration graph, the assignment whether the flagellum or a pilus are causing the observed motion is facilitated (Figure 6.5B). When the flagellum is rotating freely and therefore dominating the displayed motion, diagonal lines are formed on the Gyration graph. When a pilus is attached to the surface, the cell remains in the same position for several seconds, resulting in horizontal lines in the Gyration graph. The corresponding cell appendages that cause the observed motion are highlighted in color in Figure 6.5C. The trajectory of the displacement of the bead (Figure 6.5A) serves as a further verification that the interruptions in the gyration are caused by the attachment of a pilus and not by a mere rotation stop of the flagellum. During the assigned pilus attachment sequences (grey area), the bead shows a more directed movement compared to the flagellum associated sequences (white area). Especially during the second pilus attachment sequence from 33 s until 46 s a characteristic displacement of the bead is visible. This displacement resembles clearly the displacement trajectory of  $\Delta flgDE$  cells (Figure 6.2C). The pilus slowly drags the bead out of the center of the trap, holds its position for some seconds and then the colloidal bead quickly moves back in the center of the trap. In between the two attachment cycles, the bead performed one full rotation. Interestingly, in the presented sequence, the two pili attachment cycles occurred at nearly the same position (Figure 6.5B). During the active time of pili and flagellum before cell separation, pili can attach and release one to several times, independently whether there is an active flagellum present or not. One would expect to find the pili attachment positions randomly distributed along the gyration trajectory. To prove this hypothesis, the attachment positions of several cells that displayed more than one attachment cycle were analyzed (Figure 6.6A and B). The attachment positions seem to be random, except for the last example cell (sample number 5). The biased attachment behavior of this cell could be due to some imperfection on the glass slide that facilitated attachment of the pilus at a certain spot.

The pilus can interrupt the gyration of the cell, therefore the directional forces exerted by a pilus must be larger than the forces of the flagellum. The behavior of the flagellum while the pilus is attached is unclear. Either, the attached pilus stops the flagellar rotation, or the rotation

continues. The attachment forces of the pilus are larger than the forces exerted by the flagellum and the cell is kept in place.

Release of the pilus could be accomplished in three ways: Re-assembly of pilin subunits, detachment of the pilus from the surface or breakage of the pilus. The cell is free to perform a gyrational motion in between single pili attachment cycles, and gyration is immediately resumed without a transition area. If the pilus would be elongated by reassembly of pilin subunits, the gyration of the bead and the cell would be restricted. Therefore, reassembly of pilin subunits is very unlikely. Thus, the release of the pilus is either accomplished by detaching of the pilus from the surface or breakage of the pilus. This hypothesis is also supported by the finding that the release speed is one order of magnitude larger than the retraction speed.

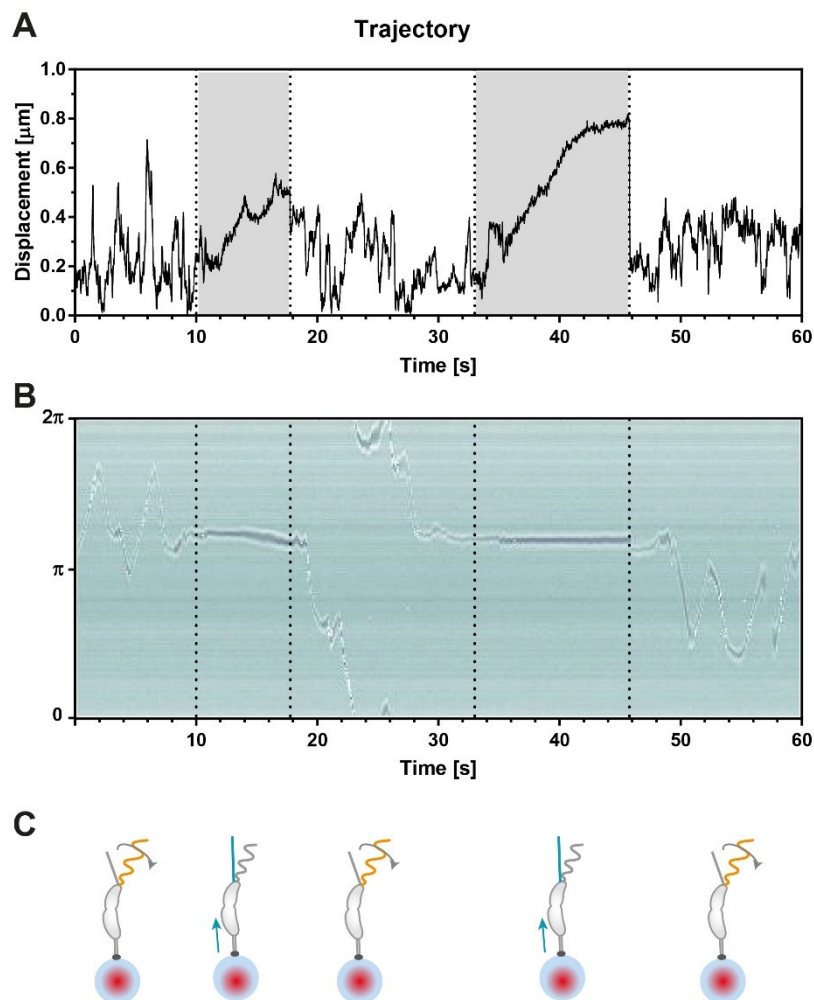


**Figure 6.5: Flagellum and pili domination alternates.** **A:** Typical trajectory of a  $\Delta creS$  predivisional cell with flagellum and pili attached on a colloidal bead in the optical tweezers. When the flagellum is rotating freely, the bead shows a gyrational movement (white area). When the pilus is attached to the surface, the bead is dragged out of the optical trap in one direction (grey area). **B:** Gyration plot of the same sequence as in A. The parts where the pili are attached are framed with dashed lines. The active flagellum causes an irregular, but gyrational movement. The active pili stabilize the cell for the duration of the attachment, resulting in a straight horizontal line. **C:** Sketches of the cell appendices. The cell appendix causing the observed motion is highlighted in colors (flagellum: orange, pilus: green).

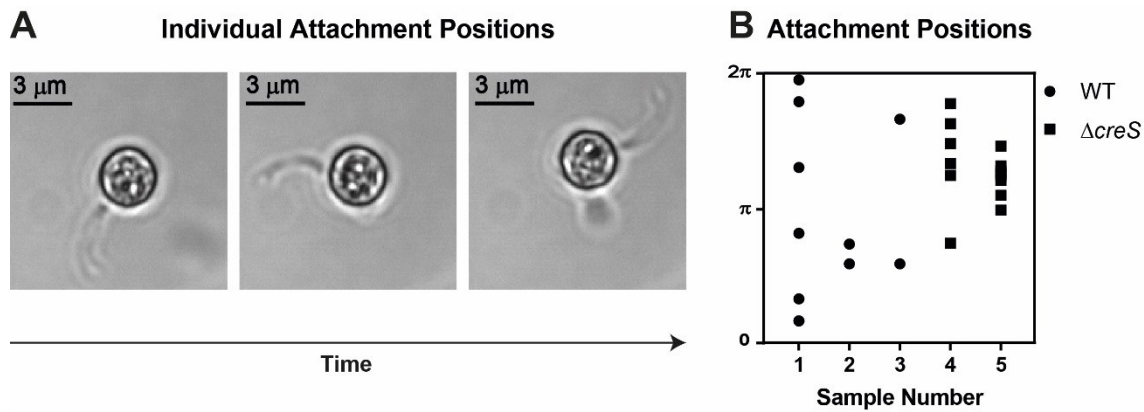


**Figure 6.6: Attachment position of single cells.** **A:** Bright field images of a cell attached to different positions. **B:** Attachment position of individual attachment cycles for several cells on the Gyrotograph.

#### 6.4.3 Flagellum Decreases Pili Attachment Duration

We found that the pilus is capable of attaching to the surface and interrupting the gyrational movement caused by the rotating flagellum. Therefore, we wanted to determine whether the attachment of the pilus stops the flagellar rotation and whether the presence of the flagellum impacts the attachment behavior of pili. To this means, we measured the duration of individual pilus attachment cycles for different strains. A cycle consists of consecutive steps: attachment, retraction, hold, and release (Figure 6.7A, blue). To determine the impact of the active flagellum onto the duration of attachment cycles, a strain without a flagellum ( $\Delta flgDE$ ), and a strain with a fully functional flagellum (WT) were compared. In addition, the duration of attachment cycles of rod-shaped cells with a flagellum ( $\Delta creS$ ) was measured to determine the impact of the cell shape on pili attachment behavior. We found that the average duration of an attachment cycle in cells without a flagellum ( $\Delta flgDE$ ) is  $(19.9 \pm 16.8)$  s ( $n = 35$ ) with a peak at 10 s and the longest attachment duration at 70 s (Figure 6.7B). For WT cells the average attachment duration is  $(12.9 \pm 11.4)$  s ( $n = 15$ ) with a distinct peak at 10 s and a sharp decrease (Figure 6.7C). For  $\Delta creS$  the average attachment duration is  $(18.1 \pm 12.9)$  s ( $n = 15$ ), (Figure 6.7C) with a peak at 10 – 20 s and the longest attachment duration of 50 s (Figure 6.7C). The presence of the flagellum in the WT clearly decreases the duration of attachment cycles. We have also found that the duration of attachment cycles depends on the load. The reduced attachment duration in presence of a flagellum could be a hint that the flagellum generates an additional load compared to the strains that miss the flagellum. The additional load could be induced by a continuous rotation of the flagellum, even when a pilus is attached. Additionally, the flagellum could also dash against the attaching pilus, leading to a decreased attachment duration of the pilus. The longer attachment duration of  $\Delta creS$  compared to WT is most likely because of the different geometry of the cells and a more favorable positioning of the flagellum and pili.

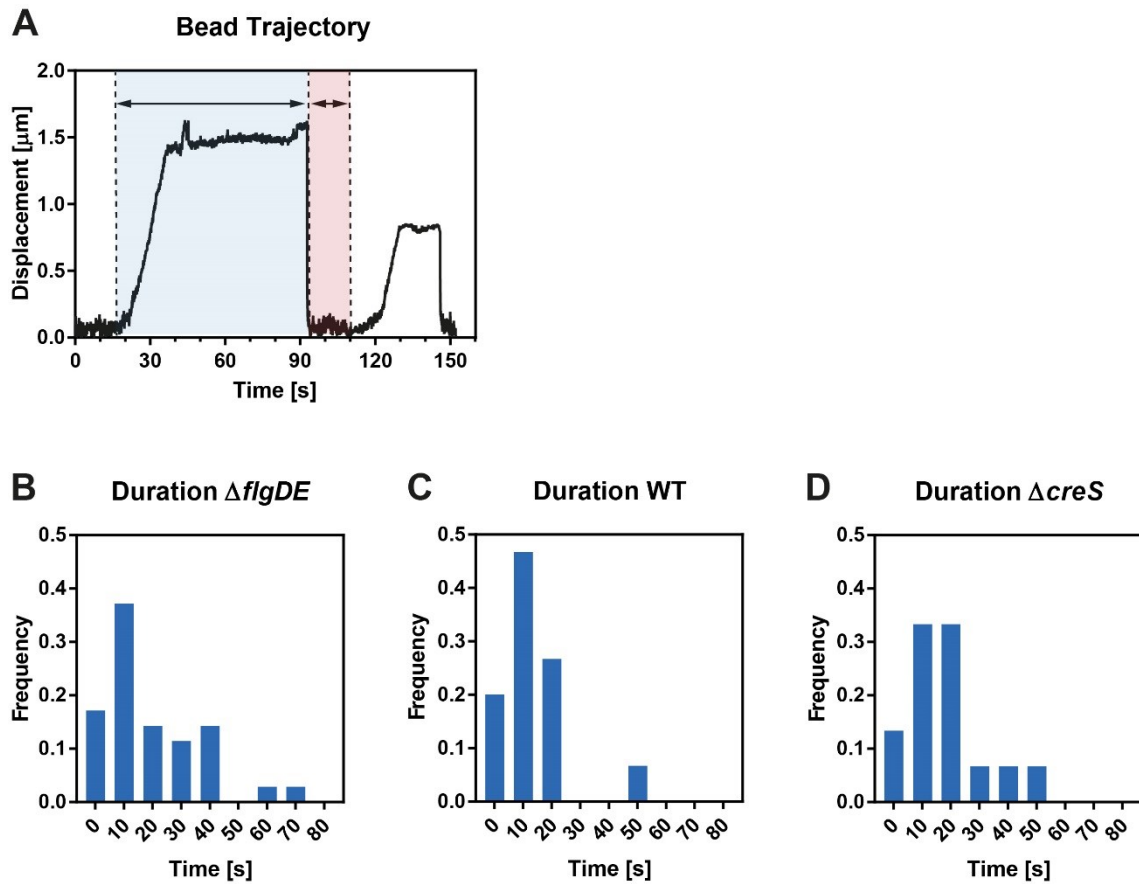


**Figure 6.7: Duration of single pilus attachment.** **A:** Trajectory of a bead with an attached  $\Delta flgDE$  cell in the optical tweezers. Two consecutive pili attachment circles are shown. Blue: Duration of one single pilus attachment cycle, red: Duration between two consecutive attachment cycles. **B-D:** Duration of individual pilus attachment cycles for  $\Delta flgDE$ , WT and  $\Delta creS$ .

#### 6.4.4 Flagellum Increases Pili Attachment Rate

To further investigate the impact of the rotating flagellum on the attachment behavior of pili, the periods between two individual pilus attachment cycles (Figure 6.7A, red) were measured for cells with (WT) and without a flagellum ( $\Delta flgDE$ ). To determine the impact of cell shape onto pili attachment behavior, we also measured the intervals between individual pilus attachment cycles for the rod-shaped strain ( $\Delta creS$ ). We found that the average period between two attachment cycles is  $(23.4 \pm 22.0)$  s ( $N = 25$ ) for  $\Delta flgDE$  cells (Figure 6.8A) with a peak at 10 s and the longest attachment-free period is 90 s. For WT cells it is on average  $(10.5 \pm 5.1)$  s ( $N = 11$ ) (Figure 6.8B) with a very distinct peak at 10 s and the longest attachment-free period is only 20 s. For  $\Delta creS$  the average period between two attachment cycles is  $(22.4 \pm 24.7)$  s ( $N = 13$ ) (Figure 6.8C) with a peak at 10 - 20 s and the longest attachment-free period is 80 s. Surprisingly, the flagellum increases the attachment rate of pili and therefore helps the pili to attach to the surface. One possible explanation for how the flagellum increases the attachment rate of pili is that the hydrodynamics of the flagellum brings the cell pole closer to the surface, therefore

increasing the probability for a pilus to encounter the surface<sup>132</sup>. We also found that the crescent shape of the cells helps to increase the attachment rate of pili compared to the rod-shaped mutants. The crescent shape allows the cell pole to be closer to the surface of the device and therefore increasing the attachment rate of pili. This is similar to the finding that the crescent cell shape promotes surface colonialization under flow<sup>23</sup>.

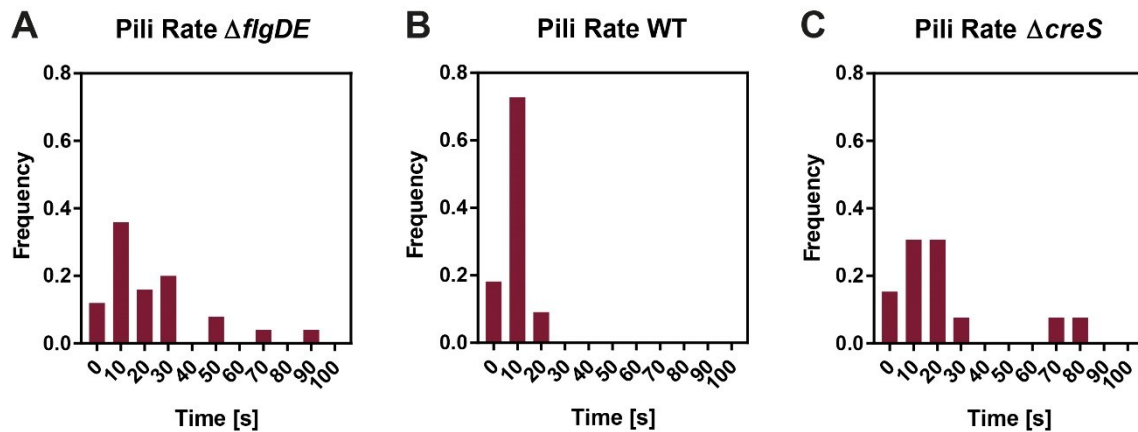


**Figure 6.8: Time between individual attachment cycles.** A-C: Period in between individual pilus attachment cycles for  $\Delta flgDE$ , WT and  $\Delta creS$ .

#### 6.4.5 Pili Activity Starts after Flagellum Activity

In every observed case (N = 4) when the predivisional cell showed activity of both, pili and flagellum, we first saw the rotation pattern of the active flagellum, followed by the pulling movement of a pilus at a later time point (Figure 6.9A). The time point of the first observed pilus attachment varied from 29 s to 345 s after the onset of the flagellar rotation. In no case we could observe an initial pulling movement of the pilus, followed by a later onset of flagellar rotation. This led to the conclusion that the flagellar activity starts before the pili activity. This idea is also supported by the finding that the flagellar rotation starts 3 -4 min before the completion of cell separation, while for  $\Delta flgDE$  cells the first pilus attachment was observed ( $73.9 \pm 95.2$ ) s (N = 9) before cell separation (Figure 6.9B).

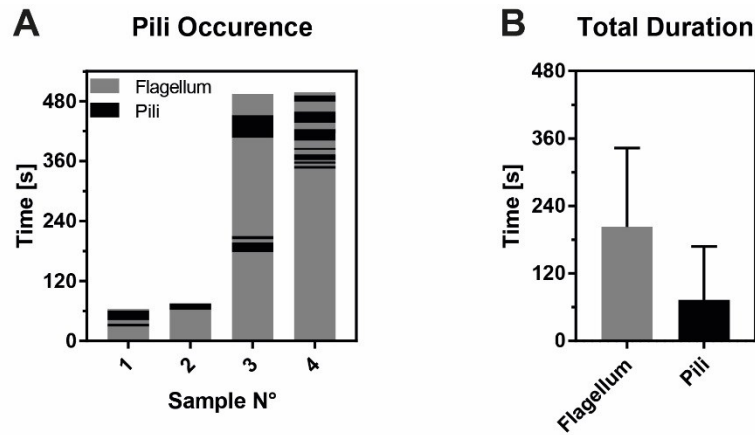


**Figure 6.9: Occurrence of pili and flagellum.** **A:** In every observed case the activity of the flagellum (grey) can be detected before the activity of pili (black). **B:** Average duration of flagellar rotation and pili activity before cell separation.

#### 6.4.6 The Flagellum can freely Rotate more than Half of the Time

We analyzed the time-wise distribution of the activity of pili and flagellum. The time when the bead showed the gyrational motion was assigned “flagellum-time”, whereas the time when a pili was dragging on the bead was assigned “pili-time”. For each analyzed cell, the flagellum-time and the pili-time were summed up and normalized to 1 to account for the varying activity time of individual cells (activity time: the time span from the first observed cell-induced movement of the bead until cell separation or stop of recording). We found that in more than half of the time the motion was assigned to the flagellum (Figure 6.10A). The flagellum caused the observed motion in  $(60 \pm 29) \%$  of the time, while the pili were the cause of the motion in  $(40 \pm 29) \%$  of the time ( $N = 9$ ). Some of the observed cells could be recorded until cell separation occurred. Cell separation can occur when the flagellum is freely rotating, or when a pilus is attaching the cell to the surface. When cell separation occurs with the cell attached to the surface, the separated daughter cell stays attached to the surface, while the bead and the mother cell are dragged back in the center of the optical tweezer (Figure 6.10B from left to right, cell separation occurs in the second image). The daughter cell then either forms a holdfast and remains attached indefinitely, or the pilus is released after some seconds and the cell swims away. When cell separation occurs while the flagellum is freely rotating, the cell immediately swims away after completion of cell separation (Figure 6.10C from left to right, cell separation occurs in the second image). The swimming direction of the freshly divided cell depends on the rotation direction of the flagellum. When the flagellum rotates CW, the cell is pushed forward, when the flagellum rotates CCW, the cell is pulled backwards. Of the 7 recorded cell separations, 4 of the cells separated when they were attached by a pilus, and 3 of the cells separated when the flagellum was freely rotating (Figure 6.10D). This result is in good agreement with a previous

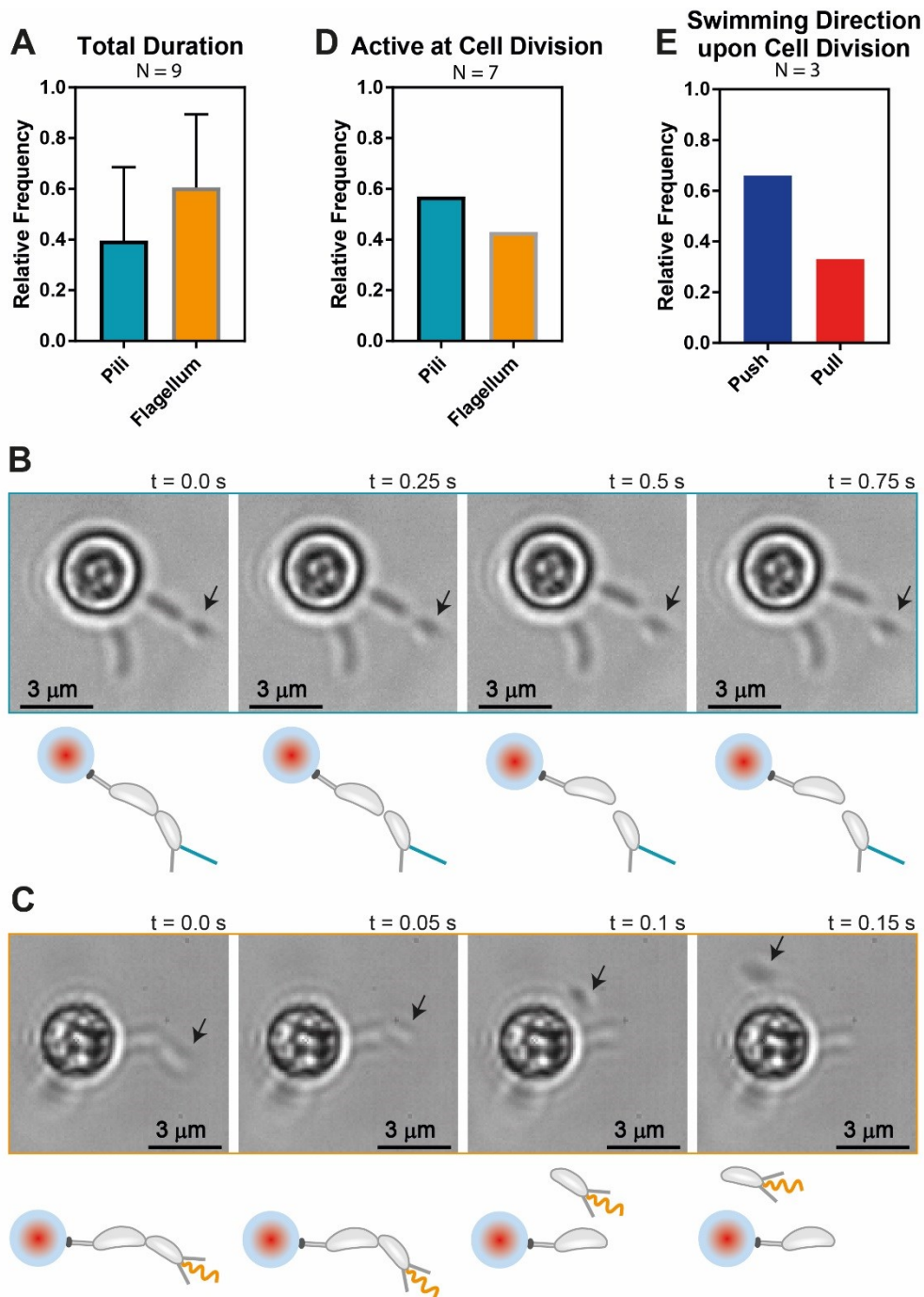


**Figure 6.10: Activity allocation.** **A:** Normalized total time when the observed movement is caused by pili or flagellum respectively. **B:** Example of a cell separating when a pilus attaches the daughter cell to a surface. The attached cell is indicated by an arrow. Cell separation occurs in the second image. **C:** Example of a cell separating when the flagellum is freely rotating. The daughter cell is indicated by an arrow. The daughter cell is pushed by the flagellum in the moment of cell separation. Cell separation occurs in the second image. **D:** From a total of 7 cells, 4 cells completed cell separation when a pilus was attached, and 3 cells completed cell separation when the flagellum was rotating freely. **E:** Of the 3 cells that separated with a free rotating flagellum, 2 cells were pushed by the flagellum and 1 cell was pulled by the flagellum.

finding that about half of the WT cells in the flow channel stay attached to the surface after cell separation, while the other half of the cells is washed away by the flow<sup>35</sup>. The 3 cells that completed cell separation when the flagellum was freely rotating were swimming and quickly left the field of view. We determined the swimming direction in the moment of cell separation and found that 2 of the cells were pushed by the flagellum and 1 cell was pulled by the flagellum (Figure 6.10E).

## 6.5 DISCUSSION

We found that Tad pili can attach to a surface, retract and be released from a surface. The attachment duration is load dependent, a larger load decreases the attachment duration. The pili of the predivisional cell can also attach to the surface when the flagellum of the cell is rotating. The flagellum most likely keeps rotating while the pilus is attached and keeps the cell in a fixed position. In this case the attachment forces of the pili need to exceed the forces generated by the flagellum. While the presence of the rotating flagellum decreased the attachment duration of pili because of the increased load generated by the rotation, it increased the attachment rate of pili. This result can be explained by a hydrodynamic effect of the flagellar rotation that brings the free cell pole closer to the surface, thereby facilitating attachment of the pili. Predivisional cells with a free pole that is initially too far away from a surface for pili to attach could get a change for attachment, therefore increasing the attachment efficiency of predivisional cells.

The fact that in between pili attachment cycles the cell can freely perform the flagellum-induced gyration indicates that the release of the pilus must be fast and complete. Together with the finding that the release of a pilus is roughly 10x faster than retraction, we conclude that the release of a pilus is achieved by a detachment or breakage of the pilus and not by elongation of the pilus via reassembly of pilin subunits.

Pili attachment could only be observed after the onset of the flagellar rotation. It is possible that the pili are active before, but never reach the surface for attachment because the rotation of the flagellum is needed to increase the attachment rate to allow successful attachment. Pili attachment could only be observed around one minute before cell separation and flagellum activity was observed roughly three minutes before cell separation. It is therefore likely that flagellum activity starts before pili activity. It is possible that flagellum activity and pili activity are linked through some unknown mechanism, the start of the flagellum might even be needed to induce pili activity.

Cell separation can occur when the cell is attached via pili or during the free gyration of the cell. We propose an “always-on” mechanism for the flagellum. Once started, the flagellum is permanently rotating until holdfast formation occurs. When a pilus attaches to the surface, the gyration is stopped and the cell is kept in a fixed position by the pilus, while the flagellum keeps rotating. We found that cells in our set-up spend more time gyrating than attachment of pili occurs. The ratio of gyration to attachment by pili can most likely be tuned by the geometry of

the set-up. Attachment time increases when the geometry favors pili attachment. For example when the piliated pole of a horizontally aligned cell is in close proximity to a vertical surface or in a microfluidic channel with flow. The flow brings the cell pole in close proximity to the glass slide, thereby enabling pili attachment, which in turn leads to enhanced surface colonization<sup>23</sup>.

## 7 LIVE CELL X-RAY IMAGING OF AUTOPHAGIC VACUOLES FORMATION AND CHROMATIN DYNAMICS IN FISSION YEAST

---

Natalja Strelnikova<sup>1</sup>, Nora Sauter<sup>1</sup>, Manuel Guizar-Sicairos<sup>2</sup>, Michael Göllner<sup>1</sup>, Ana Diaz<sup>2</sup>, Petrina Delivani<sup>3</sup>, Mariola Chacon<sup>3</sup>, Iva M. Tolić<sup>3,4</sup>, Vasily Zaburdaev<sup>5</sup>, and Thomas Pfohl<sup>1,6,7\*</sup>

<sup>1</sup>Department of Chemistry, University of Basel, Switzerland.

<sup>2</sup>Paul Scherrer Institut, Villigen, Switzerland.

<sup>3</sup>Max Planck Institute of Molecular Cell Biology and Genetics, Dresden, Germany.

<sup>4</sup>Division of Molecular Biology, Ruđer Bošković Institute, Zagreb, Croatia.

<sup>5</sup>Max Planck Institute for the Physics of Complex Systems, Dresden, Germany.

<sup>6</sup>Biomaterials Science Center, University of Basel, Switzerland.

<sup>7</sup>Present Address: Institute of Physics, University of Freiburg, Germany.

\*Email: thomas.pfohl69@gmail.com.

---

Published in *Scientific Reports* **7**, October 2017.

Doi: 10.1038/s41598-017-13175-9

### **Author contribution:**

---

Sample preparation and performed the experiments at the synchrotron together with N. S., M. G.-S., A. D., P. D., V. Z., and T. P.

## 7.1 ABSTRACT

Seeing physiological processes at the nanoscale in living organisms without labeling is an ultimate goal in life sciences. Using X-ray ptychography, we explored *in situ* the dynamics of unstained, living fission yeast *Schizosaccharomyces pombe* cells in natural, aqueous environment at the nanoscale. In contrast to previous X-ray imaging studies on biological matter, in this work the eukaryotic cells were alive even after several ptychographic X-ray scans, which allowed us to visualize the chromatin motion as well as the autophagic cell death induced by the ionizing radiation. The accumulated radiation of the sequential scans allowed for the determination of a characteristic dose of autophagic vacuole formation and the lethal dose for fission yeast. The presented results demonstrate a practical method that opens another way of looking at living biological specimens and processes in a time-resolved label-free setting.

## 7.2 INTRODUCTION

Studies of nanoscale structures and dynamics of biological matter greatly benefit from observing samples in living state using label-free methods<sup>1</sup>. X-ray ptychography enables quantitative visualization of whole biological cells with nanoscale resolution based on the natural electron density contrast of the cell content<sup>2-5</sup>. An ideal eukaryotic model organism for cellular dynamic studies is fission yeast at the horsetail stage owing to the oscillations of meiotic chromosomes in the time scale of minutes to hours<sup>6-8</sup>. Moreover, intracellular structure changes caused by X-ray radiation are of interest for a direct analysis *in situ*<sup>9</sup>. The major challenge of X-ray imaging of living cellular specimens is the very low lethal radiation dose, and owing to the intense radiation damage and a low electron density contrast, sequential X-ray imaging of live eukaryotic cells was not possible so far<sup>10-13</sup>. To record sufficient information, the samples have to be exposed to a certain amount of radiation, which has to be greater than the minimum of the required dose for imaging and less than the maximum tolerable dose for the specimen<sup>10</sup>. The limiting factor of the resolution is therefore set by the X-ray radiation dose<sup>10,11</sup>. Natural, aqueous environments of biological specimens significantly decrease the electron density contrast, thus higher X-ray flux is required, which consequently increases the radiation dose needed for a given resolution<sup>10</sup>. Radiation induced degradation can be reduced by chemical or cryo-fixation. Using cryo-fixation, X-ray ptychography<sup>2,4,14</sup> and diffraction microscopy<sup>15,16</sup> of frozen hydrated cells were accomplished. More advanced X-ray studies were realized on living cells<sup>17,18</sup> and appear to be a promising approach to analyze cellular processes *in situ*. Imaging of initially alive cells simplifies sample preparation, owing to the fact that fixation steps are not required. Imaged living cells died during the first X-ray scan<sup>18</sup> or after a free electron laser (FEL) pulse<sup>13</sup>, due to the lethal radiation dose. However, first electron density maps measured with X-rays of initially alive bacteria, which were obtained with less than a lethal dose, were recently presented<sup>12,19</sup>. X-ray ptychography is a coherent diffractive imaging (CDI) technique that combines scanning microscopy with advanced phase retrieval algorithms<sup>20-22</sup>. It relies on scanning the extended sample by the X-ray beam, collecting 2D diffraction patterns from a number of overlapping regions of the specimen and a subsequent iterative reconstruction of a single projection image, which is consistent with all recorded diffraction patterns<sup>21</sup>.

## 7.3 RESULTS

### 7.3.1 X-ray ptychography

Ptychography is an X-ray imaging technique with spatial resolution limited in principle by the spatial wavelength of the incident beam and the maximum angle at which diffracted signal can be measured with sufficient signal-to-noise ratio, although in practice the resolution can be also limited by scanning precision or radiation induced damage on the specimen under study (Figure 7.1). In living samples, the intracellular motions are happening during a single scan which can blur the images. A ptychography setup with a pinhole-defined illumination was chosen in order to achieve good contrast and high resolution with a reduced dosage of radiation (Figure 7.1a) due to the illumination broad spatial spectrum<sup>23</sup>. We obtained reconstructed images with pixel sizes of  $45 \times 45 \text{ nm}^2$  and estimated resolution in the range of 100-200 nm of live cells in aqueous environment and reduced the radiation doses down to about  $10^3$ - $10^4$  Gy per scan. These doses are two to three orders of magnitude less than  $1.8 \cdot 10^6$  Gy recorded for recent X-ray images of (initially) alive eukaryotic cells<sup>18</sup> and close to the dose of  $8.9 \cdot 10^3$  Gy used for holographic imaging of living bacteria<sup>19</sup>.

Here, we explore the dynamics of living fission yeast *Schizosaccharomyces pombe* cells during meiosis in natural, aqueous environment *in situ*. Fission yeast cells are ideal eukaryotic model organisms, because many of basic cellular principles and cell regulators are conserved from yeast to humans<sup>8</sup>. Meiosis in fission yeast is induced by depleting nitrogen sources from the culture medium and haploid cells of the opposite mating type conjugate and form a diploid “banana-shaped” zygote<sup>6</sup> (Figure 7.1b,c). At the horsetail stage of meiosis strong oscillations of chromosomes can be observed with extended periods of chromosomal back and forth motions along the cell axis<sup>25</sup>. The period of an individual oscillation is about 10 -15 min<sup>6</sup>. After several hours, at the end of the horsetail stage, the oscillations slow down and finally stop.

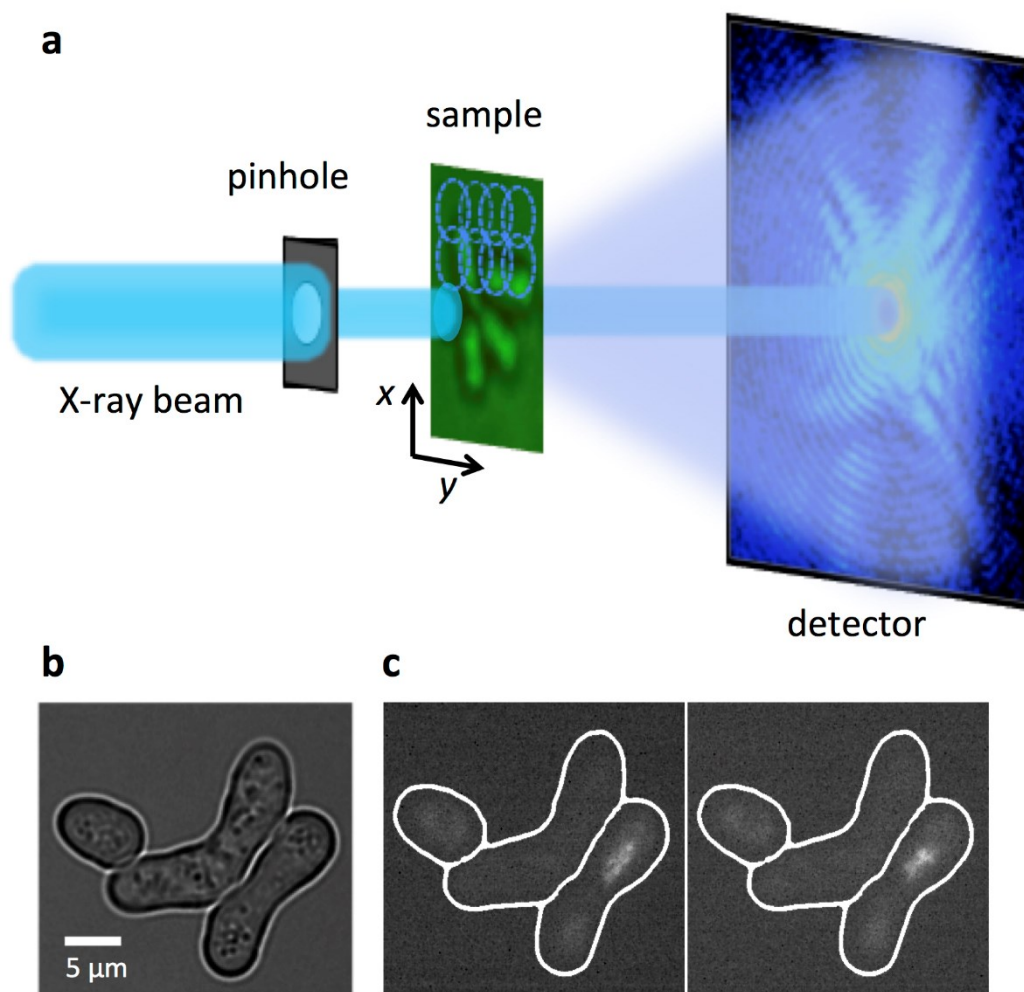


**Figure 7.1: Schematic representation of the experimental ptychography setup for imaging living cells.** (a) For the X-ray ptychography experiments, a monochromatic ( $\lambda = 0.2$  nm) beam was used to coherently illuminate a pinhole. The cell sample was scanned to collect a series of diffraction patterns from partially overlapping illuminated regions, which allow for a robust image reconstruction. The high dynamic range and count rate of the detector allows us to record the full dynamic range of the 2D diffraction patterns at the detector and avoid a loss of low spatial-frequency information that would occur if a beamstop was used. (b) A visible light bright-field optical micrograph shows three fission *Schizosaccharomyces pombe* yeast cells under nitrogen starvation conditions, where two of them were banana-shaped zygotes. (c) Corresponding fluorescence microscopy images of the same cells as in (b) in a time interval of 5 min are shown. In order to distinguish zygotes with moving chromosomes, 'nuclear oscillations', among cells with 'non-oscillating' ones, *rec25* gene was labeled with green fluorescent protein (GFP) and used as an indirect marker of DNA double strand breaks<sup>24</sup>. Here, only one of two zygotes was at the horsetail stage.

### 7.3.2 X-ray induced autophagy in fission yeast cells

X-ray ptychography micrographs of a successive image sequence of a fission yeast zygote and an analysis of the impact of ionizing radiation on the cell are shown in Figure 7.2. During the first four scans, no structural changes - almost homogenous density within the entire cell - of a zygote were observed. A further exposure of X-rays in the successive scans led to the appearance of clear, light and rounded structures in the zygote. These observed cellular structures may be a signature of a radiation induced formation of vacuoles<sup>26</sup> and autophagic bodies<sup>27</sup>, which were

described for fission yeast cells and might be a visual indication of autophagy<sup>28-30</sup>. These structural changes coincided with an overall positive shift in the phase shift histograms of zygote images showing autophagic vacuoles in comparison to zygote images without vacuoles (Figure 7.2b). Increasing the radiation dose further, a bursting of the membrane and shrinkage of the cell was observed (Figure 7.2a-ix,x), which demonstrates that after accumulating a certain amount of radiation the zygote perished. To characterize the dynamics of the autophagic vacuole formation and cell lysis, changes of the projected zygote area and of the projected area of individual vacuoles were analyzed (Figure 7.2c). In the first four ptychography scans, a slight increase of the projected area of the zygote was observed. At an accumulated dose of about  $2.2 \times 10^4$  Gy (sixth scan) for the particular scan shown in Figure 7.2c, the area decreased back to its initial size and the autophagic vacuole formation set in, a first critical dose for live fission yeast cells can be defined. Applying more X-ray radiation, the initial number of vacuoles did not change, whereas their volume (projected area) increased until the cell burst. At a dose of about  $9.2 \times 10^4$  Gy for this particular cell, the bursting of the cell membrane was concurred by a strong decrease of the projected zygote area. The observed formation of vacuoles can be attributed to ionizing effects of the X-ray radiation, which induce radiolysis of water and cause hydrogen peroxide ( $H_2O_2$ ) and hydroxyl radical ( $OH\cdot$ ) formation<sup>27</sup>. These very reactive oxygen species (ROS) activate protein kinases in yeast<sup>9</sup> and can cause autophagy<sup>31</sup>. Apart from the fact that the zygote was exposed to X-rays, yeast cells grew under nitrogen depletion, which might be a stimulus to facilitate autophagy if cells starve for several hours<sup>32</sup>. However, the autophagic vacuole formation was observed only after several ptychography scans, and was not observed in comparable experiments using optical microscopy.

In total, nine individual live fission yeast zygotes were analyzed. The average radiation dose at which autophagic vacuole formation occurred was about  $(3.30 \pm 0.74) \times 10^4$  Gy. When the radiation dosages accumulated to  $(9.6 \pm 3.2) \times 10^4$  Gy, zygotes were lysed, which can be defined as the lethal radiation dose for fission yeast. Interestingly, non-meiotic cells were more resistant to X-ray radiation, where vacuole formation occurred at higher doses of  $(8.7 \pm 3.8) \times 10^4$  Gy and cell death at about  $(1.20 \pm 0.19) \times 10^5$  Gy, indicating that the lethal radiation dose of non-meiotic cells is similar to zygotes, whereas the vacuole formation in non-meiotic cells occurs at much higher radiation doses.

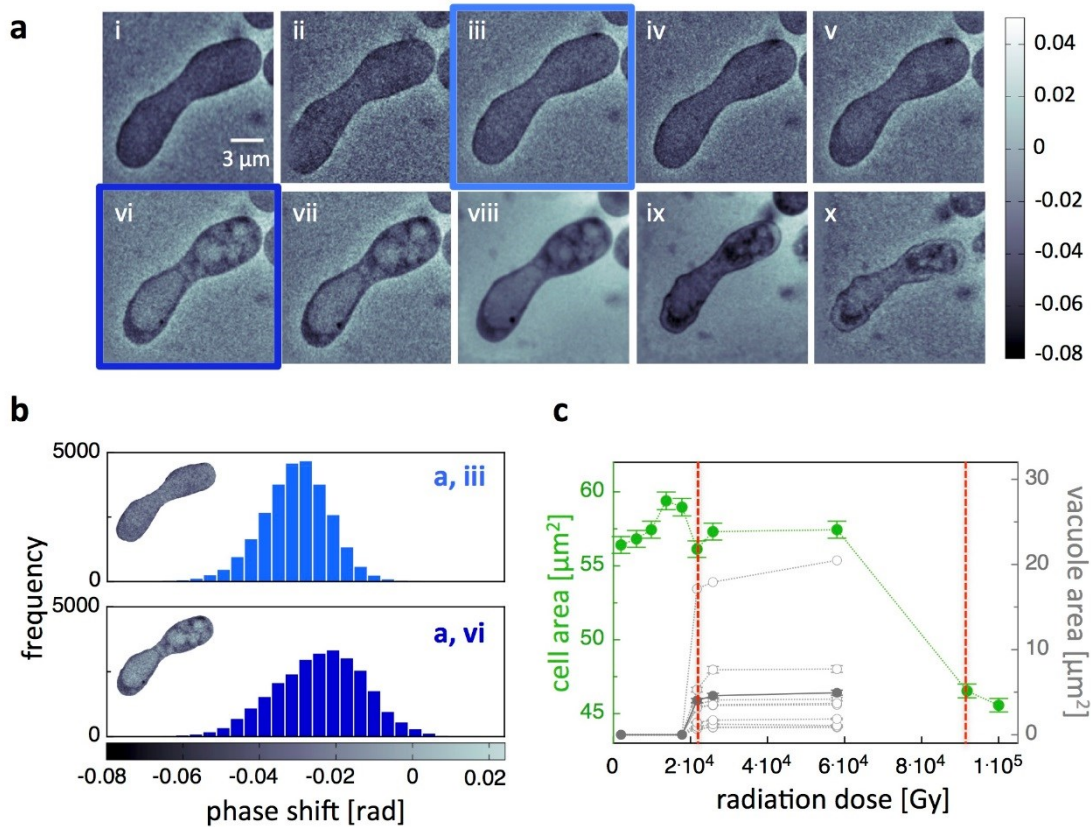


**Figure 7.2. X-ray ptychography images of a live fission yeast zygote.** (a) Successive image sequence of a live fission yeast zygote obtained by ptychographic CDI scans. (b) Phase shift histograms (plot of the number of pixels with a specific phase shift) of a zygote in the image without autophagic vacuoles (a, iii) and with autophagic vacuoles (a, vi). A positive shift corresponds to a lighter color. (c) Projected cell area and projected vacuole area versus the radiation dose calculated from the ptychographic zygote images. Each set of grey circles connected by a line corresponds to a different vacuole and the filled circles correspond to the mean area of the vacuoles. A characteristic dose of the onset of vacuole formation and a lethal dose can be identified (red dashed lines).

### 7.3.3 X-ray imaging of the chromosome motion

To further demonstrate the potential of ptychography for studying cellular dynamics, we imaged meiotic yeast zygote at the horsetail stage. During this stage, an extended movement of the whole chromatin happens, and at the same time, the motion matches the time scales of the X-ray imaging technique. Freshly prepared samples were firstly analyzed with a fluorescence microscope to find a zygote at the horsetail stage in the sample and then mounted on the X-ray ptychography setup. A temporal sequence of six X-ray ptychography images of a live fission yeast zygote in the horsetail stage is presented in Figure 7.3a. Interestingly, a darker (a more negative phase shift) and denser structure in the top part of the zygote was observed. This structure was moving during one scan to another and furthermore changed its shape. We identified this densified structure as moving chromatin, which has the same appearance as the chromosomes in the fluorescence micrograph taken before the X-ray ptychography scans (Figure 7.3b). Image processed contours of the chromosomes overlaid on the original ptychography images are shown in Figure 7.3c. The motion of the chromosomes was analyzed by calculating their center

of mass. Starting from the initial position of the chromosomes the subsequent center of mass positions showed a movement of several hundreds of nanometer away from the upper cell end in the direction of the lower part of the cell (Figure 7.3d). For further analysis, we compared the shape changes of the chromosomes over time by calculating the radius of gyration  $R_g = \sqrt{\frac{1}{N} \sum_{i=1}^N (\vec{r}_i - \vec{r}_{CM})^2}$ , where  $N$  is the number of pixels of the chromatin,  $\vec{r}_i$  are the position vectors and  $\vec{r}_{CM}$  is the center of mass of the chromosomes. The radius of gyration, which characterizes the packing and shape of the chromosomes, versus time is plotted in Figure 7.3f. Firstly, a looser packing of the chromosomes, bigger  $R_g$ , was observed, reaching a maximum of  $R_g = (1.32 \pm 0.07) \mu\text{m}$  after 10 min during their motion to the lower cell end. Afterwards,  $R_g$  steadily decreased to a minimum of  $(0.85 \pm 0.04) \mu\text{m}$ , which characterizes a strong compaction of the chromosomes. This chromosome compaction was found in conjunction with the formation of autophagic vacuoles, which could be observed after about 20 min (Figure 7.3a). The motion of the chromosomes was slowed down in comparison to the observed period of the oscillation of about 10 – 15 min<sup>6</sup>. This observed deceleration of the chromosome motion is an indication of an impact of X-ray radiation, which most probably damages the cell at the molecular level; especially the appearance of autophagic vacuoles in concurrence with the chromosomes compaction had a strong impact on the oscillating chromosomes. Moreover, due to a time-consuming sample preparation and mounting procedure, the X-ray ptychography images were presumably taken at the end of the horsetail period, when the oscillations slowed down. The appearance of autophagic vacuoles was observed, when the radiation dose accumulated to about  $1.2 \times 10^4$  Gy. This dose of the vacuole formation is less than half of the dose, which was found for normal yeast zygotes, which might be an indication that zygotes in the horsetail stage are more sensitive to X-ray radiation.

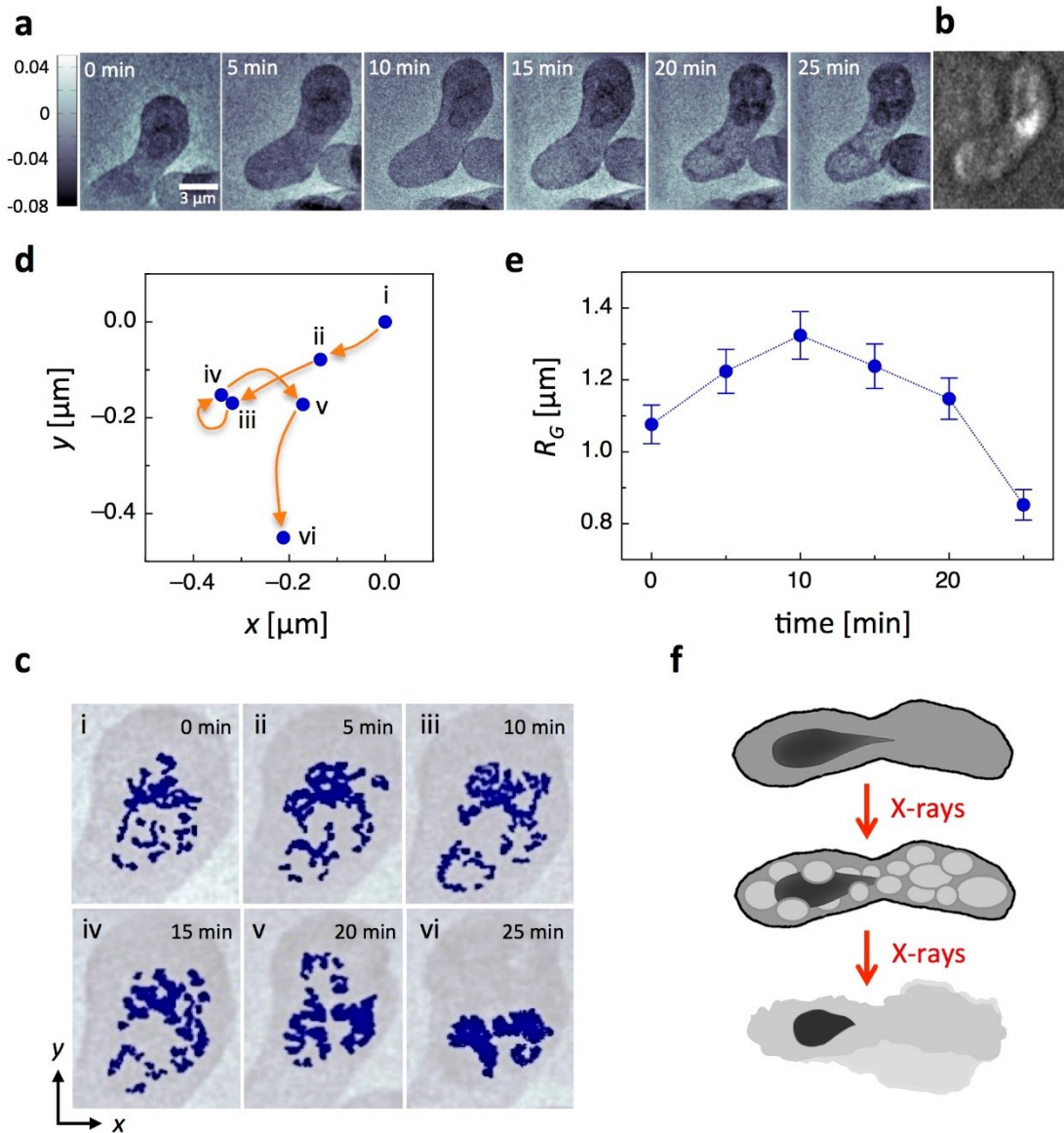


**Figure 7.3: X-ray ptychography images of chromosome motion in a live fission yeast zygote at the horsetail stage.** (a) Temporal image sequence of a live zygote in the horsetail stage obtained by X-ray ptychography. (b) Fluorescence micrograph of the zygote taken before the X-ray ptychography scans. (c) Overlay of image processed contours of the chromosomes (dark blue) on the original ptychography images. (d) Center of mass motion of chromosomes between the sequential ptychographic images. The  $x$  and  $y$ -position of the center of mass of the first scan at 0 min was set to 0,0. (e) Calculated radius of gyration of the chromosomes versus time. (f) Schematic representation of autophagic vacuoles formation and cell lysis during meiotic chromosome oscillations.

## 7.4 CONCLUSIONS

In these experiments, we optimized the sample preparation and experimental setup to successfully apply ptychography for sequential imaging – producing X-ray movies – of the live meiotic yeast cells in aqueous environment and established a method to investigate intracellular nanostructures. Based on the natural electron density contrast, this label-free imaging method allowed us to visualize cellular structures *in situ*. We discovered autophagic cell death or type II programmed cell death<sup>28</sup> and cell lysis, induced by the pathological environment due to the ionizing X-ray radiation. Autophagy in the yeast and mammalian cells is similar<sup>30</sup> and it is considered to play an important part in the response of radiation therapy<sup>33</sup>. The radiation-induced damage on the molecular level most probably occurred already during the first X-ray scan, but it did not cause visible cell changes and the cell stayed alive. Thus an average radiation dose at which visible signs of autophagy occurs by formation of autophagic vacuoles<sup>32</sup> and a characteristic dose of membrane bursting of the eukaryotic cells can be obtained. Moreover, the dynamics of denser structures, which are most likely chromatin structures at the end of their oscillatory motion during the horsetail stage of yeast zygotes, can be imaged and analyzed. However, zygotes are most likely already damaged at the molecular level by radiation. This imaging approach also simplifies sample preparation and avoids artifact formation caused by fixation, sectioning or labeling.

We believe that improved sample environments, e.g. microfluidics setup<sup>34</sup> to flush fresh medium and remove free radicals<sup>35</sup>, modified scanning protocols and adjusted ranges of interest will further advance, here demonstrated, way of seeing physiological processes of individual eukaryotic cells as well as tissues with subcellular, nanoscale resolution.

## 7.5 ACKNOWLEDGEMENTS

X-ray measurements were carried out at the cSAXS beamline of the Swiss Light Source, Paul Scherrer Institut (PSI), Villigen, Switzerland. We thank Prof. Kurt Ballmer for the use of his fluorescence microscope at PSI during our X-ray ptychography measurements, C. Martin-Castellanos for the kind gift of the Rec25-GFP strain, Zoe Swank and Raphael Urbani for their support during synchrotron experiments. Financial support by the Swiss National Science Foundation (SNF\_200020\_141270) and Swiss Nanoscience Institute is gratefully acknowledged.

## 7.6 AUTHOR CONTRIBUTIONS

N. S., M. G.-S., A. D., V. Z., and T. P. conceived the research work and designed the experiments. N. S., **N. S. (II)**, M. G.-S., A. D., P. D., V. Z., and T. P. performed the experiments. P. D., M. C. and I. M. T. contributed and modified samples and protocols. N. S., M. G.-S., M. G., V. Z., and T. P. analyzed the data. N. S., M. G.-S., V. Z., and T. P. wrote the paper with contributions from all authors.

## 7.7 ADDITIONAL INFORMATION

### **Competing financial interests**

The authors declare no competing financial interests.

## 7.8 METHODS

In order to avoid a strong background signal and to create a cytocompatible environment, we used biocompatible and X-ray resistant 200 nm thick silicon nitride ( $\text{Si}_3\text{N}_4$ ) membrane windows (frame:  $5 \times 5 \text{ mm}^2 \times 200 \mu\text{m}$ , membrane:  $1.5 \times 1.5 \text{ mm}^2 \times 200 \text{ nm}$ ; Silson Ltd, Blisworth, England)<sup>17,18,34</sup>. The  $\text{Si}_3\text{N}_4$  membrane windows were coated with lectin (Sigma-Aldrich, St. Louis, MO, USA) to increase cell adhesion to the membrane surface, which is crucial for the spatial stability of the cells and thus for the reproducibility of X-ray ptychography scans. Fission yeast *Schizosaccharomyces pombe* cells were kept in phosphate-buffered saline (PBS) medium at room temperature. For fluorescence optical imaging, we used the genotype of the fission yeast strain h90 rec25::GFP-KanMX6. The strain was a kind gift from C. Martín-Castellanos (CM62, IBFG, Salamanca, Spain). To induce meiosis, fission yeast cells were transferred to an Eppendorf tube with 100  $\mu\text{l}$  of nutrition deficient Edinburgh minimal medium (EMM-N)<sup>7</sup> and kept for 30 min at room temperature. Afterwards, a small droplet of medium with cells were put on a lectin-coated  $\text{Si}_3\text{N}_4$  membrane window and the device was covered by an uncoated  $\text{Si}_3\text{N}_4$  membrane window and accurately glued with UHU plus epoxy quick set adhesive at the edges of the membranes. The described procedure enables the preparation of hydrated living cell samples for X-ray experiments with an intercalated aqueous film of 5 to 10  $\mu\text{m}$  in thickness. The gap was determined based on bright field optical imaging where the distance between the membranes was comparable to the size of the cell as observed by changing the focus. Since the aqueous environment drastically decreases the electron density contrast of the sample, a small sample thickness is crucial to reduce the background signal caused by the medium in the device.

X-ray ptychography experiments were performed at the coherent small-angle X-ray scattering (cSAXS) beamline of the Swiss Light Source, Paul Scherrer Institut, PSI, Villigen, Switzerland. The schematic representation of the setup is shown in Figure 7.1a. An X-ray beam of 6.2 keV photon energy,  $\lambda = 0.2 \text{ nm}$ , was selected using a double crystal Si (111) monochromator. The incident beam was defined by a pinhole with a transverse diameter of about 2.5  $\mu\text{m}$  in order to obtain a coherent spatially confined illumination at the sample, which was placed 3 mm downstream of the pinhole and had at the sample position approximately the same diameter. The sample of hydrated live cells was placed on a piezoelectric scanning stage to allow for nanometer precision scanning. The coherent X-ray beam diffracted by the sample propagates through a helium flushed flight tube to a photon-counting Pilatus 2D detector<sup>36</sup>, which is located at distance of 7.412 m from the sample. The broad angular spectrum of a pinhole-defined illumination is well suited for minimizing the radiation dose while acquiring images with good contrast and a

moderately high resolution<sup>23</sup>. Before the X-ray ptychography experiments, the cell samples were imaged by fluorescent microscopy in order to identify oscillating zygotes. The membranes were then mounted on the setup and the identified cells were positioned using an on-stage bright field microscope.

In order to avoid the raster grid pathology<sup>37</sup> all scans were performed following a Fermat spiral scanning pattern<sup>38</sup>. In order to find optimal scanning parameters, different step sizes and exposure times were applied. For the measurements in Figure 7.2a a scanning field of view of  $18 \times 14 \mu\text{m}^2$  and an average step size of  $0.7 \mu\text{m}$  were used with an exposure time of  $0.1 \text{ s}$  per scanning point. For these parameters the resolution was about  $200 \text{ nm}$  with an average flux of about  $7.4 \times 10^5 \text{ photons}/\mu\text{m}^2$ . To calculate the average flux we first normalized the reconstructed illumination intensity using the total number of counts arriving at the detector after compensating for absorbing and scattering elements in the path of the beam, then we used the scanning pattern to generate a grid of the distribution of photons incident on the sample for the whole scan. The flux in  $\text{photons}/\mu\text{m}^2$  is finally calculated by integrating over an area significantly larger than the illumination and dividing by the area, in this manner we included in the calculation the total dose incident on the sample including the overlapping regions of the scan<sup>39</sup>. The corresponding dose of  $3.9 \times 10^3 \text{ Gy}$  was estimated as described in Ref.<sup>16</sup>: The dose,  $D$ , is calculated based on the surface dose equation  $D = \mu N_0 h\nu / \rho^{10}$ , where the attenuation length,  $1/\mu$ , was obtained from tabulated values<sup>40</sup> assuming an average composition of  $\text{H}_{128}\text{C}_{30}\text{N}_9\text{O}_{49}\text{S}_1$  and average density of  $\rho = 1 \text{ g cm}^{-3}$ .

In order to observe the cell behavior (death or ability to recover) between the X-ray scans, the time interval among the images was different: 5min, 25min, 20min, 20min, 50min, 30 min, 40 min, 2h, 3h. This allows us to assume that the cell death is initiated by the X-ray radiation and does not occur/continue when the X-rays are switched off. The radiation doses used for single ptychography scans in Figure 7.2a were different, the 1<sup>st</sup> scan  $1.96 \times 10^3 \text{ Gy}$ , 2<sup>nd</sup> scan  $4.01 \times 10^3 \text{ Gy}$ , 3<sup>rd</sup> scan  $3.87 \times 10^3 \text{ Gy}$ , 4<sup>th</sup> scan  $3.86 \times 10^3 \text{ Gy}$ , 5<sup>th</sup> scan  $4.09 \times 10^3 \text{ Gy}$ , 6<sup>th</sup> scan  $3.87 \times 10^3 \text{ Gy}$ , 7<sup>th</sup> scan  $4.14 \times 10^3 \text{ Gy}$ , and 10<sup>th</sup> scan  $8.20 \times 10^3 \text{ Gy}$ . The quality of the images in Figure 7.2a(viii, ix) and resolution down to about  $100 \text{ nm}$  was improved using smaller step sizes of  $0.5 \mu\text{m}$  and longer exposure times of  $0.4 \text{ s}$ , which increased the radiation dose to about  $3.3 \times 10^4 \text{ Gy}$ .

The images in Figure 7.3a were obtained with an exposure time of  $0.1 \text{ s}$  per scanning point and an average step size of  $1 \mu\text{m}$ . The flux at the sample position was  $4.2 \times 10^5 \text{ photons}/\mu\text{m}^2$  for the individual scans, corresponding to an estimated resolution of about  $100 \text{ nm}$ . The radiation doses

per scan were  $1.93 \times 10^3$  Gy (1<sup>st</sup>),  $1.83 \times 10^3$  Gy (2<sup>nd</sup>),  $2.71 \times 10^3$  Gy (3<sup>rd</sup>),  $2.70 \times 10^3$  Gy (4<sup>th</sup>),  $2.76 \times 10^3$  Gy (5<sup>th</sup>), and  $2.74 \times 10^3$  Gy (6<sup>th</sup>).

Reconstructions were carried out using the maximum likelihood method through non-linear optimization<sup>20,22</sup>. In order to reduce the noise in the reconstructions, gradient preconditioning and regularization, as described by Thibault and Guizar-Sicairos<sup>22</sup>, were used. A good estimate of the incident illumination is important to facilitate the reconstruction of weak contrast specimens<sup>41</sup>, such as the hydrated live cells presented here. For this purpose we characterized the incident illumination via ptychography before the experiments using a 2D test patterns similar to those used in<sup>42</sup>. The illumination phase and amplitude profile were stable for the duration of a single scan. For this case the resolution of the reconstruction could not be assessed via Fourier shell correlation (FSC)<sup>43,44</sup> because two identical datasets were not available due to changes or movement of the live specimens. To assess the resolution of each image we used instead a method based on the angular-averaged power spectral density (PSD) method as described in<sup>14</sup>.

X-ray ptychography images were analyzed using ImageJ (version 1.47k, Wayne Rasband, National Institute of Health, USA) and MATLAB (version R2012b, The MathWorks, Natick, USA) by applying custom developed scripts. The images were first denoised by conditional mean filtering resulting in an edge preserving smoothing. Further applying edge detection algorithms yield the contour of the cells, which acts as the range of interest in order to find the chromosomes by local thresholding.

## 7.9 REFERENCES

1. Landecker, H. Seeing things : from microcinematography to live cell imaging. *Nat. Methods* **6**, 707–709 (2009).
2. Deng, J. *et al.* Simultaneous cryo X-ray ptychographic and fluorescence microscopy of green algae. *PNAS* **112**, 2314–2319 (2015).
3. Miao, J., Ishikawa, T., Robinson, I. K. & Murnane, M. M. Beyond crystallography: Diffractive imaging using coherent x-ray light sources. *Science* **348**, 530–535 (2015).
4. Diaz, A. *et al.* Three-dimensional mass density mapping of cellular ultrastructure by ptychographic X-ray nanotomography. *J. Struct. Biol.* **192**, 461–469 (2015).
5. Hémonnot, C. J. *et al.* X-rays Reveal the Internal Structure of Keratin Bundles in Whole Cells. *ACS Nano* **10**, 3553–3561 (2016).
6. Chikashige, Y. *et al.* Telomere-led premeiotic chromosome movement in fission yeast. *Science* **264**, 270–273 (1994).
7. Forsburg, S. L. & Rhind, N. Basic methods for fission yeast. *Yeast* **23**, 173–183 (2006).
8. Patterson, J. O., Swaffer, M. & Filby, A. An Imaging Flow Cytometry-based approach to analyse the fission yeast cell cycle in fixed cells. *Methods* **82**, 74–84 (2015).
9. Spitz, D. R., Azzam, E. I., Li, J. J. & Gius, D. Metabolic oxidation / reduction reactions and cellular responses to ionizing radiation : A unifying concept in stress response biology. *Cancer Metastasis Rev* **23**, 311–322 (2004).
10. Howells, M. R. *et al.* An assessment of the resolution limitation due to radiation-damage in X-ray diffraction microscopy. *J. Electron Spectros. Relat. Phenomena* **170**, 4–12 (2009).
11. Schneider, G., Guttman, P., Rehbein, S., Werner, S. & Follath, R. Cryo X-ray microscope with flat sample geometry for correlative fluorescence and nanoscale tomographic imaging. *J. Struct. Biol.* **177**, 212–223 (2012).
12. Kimura, T. *et al.* Imaging live cell in micro-liquid enclosure by X-ray laser diffraction. *Nat. Commun.* **5**, 3052 (2014).
13. van der Schot, G. *et al.* Imaging single cells in a beam of live cyanobacteria with an X-ray laser. *Nat. Commun.* **6**, 5704 (2015).
14. Giewekemeyer, K. *et al.* Quantitative biological imaging by ptychographic x-ray diffraction microscopy. *Proc. Natl. Acad. Sci. U. S. A.* **107**, 529–534 (2010).
15. Weinhausen, B. *et al.* X-ray nano-diffraction on cytoskeletal networks. *New J. Phys.* **14**, (2012).
16. Lima, E. *et al.* Cryo-scanning x-ray diffraction microscopy of frozen-hydrated yeast. *J. Microsc.* **249**, 1–7 (2013).

17. Sedlmair, J. *et al.* Imaging of Vascular Smooth Muscle Cells with Soft X-Ray Spectromicroscopy. *Microsc. Microanal.* **17**, 991–1001 (2011).
18. Weinhausen, B. *et al.* Scanning X-ray nanodiffraction on living eukaryotic cells in microfluidic environments. *Phys. Rev. Lett.* **112**, 88102 (2014).
19. Bartels, M., Krenkel, M., Haber, J., Wilke, R. N. & Salditt, T. X-Ray Holographic Imaging of Hydrated Biological Cells in Solution. *Phys. Rev. Lett.* **114**, 48103 (2015).
20. Guizar-Sicairos, M. & Fienup, J. R. Phase retrieval with transverse translation diversity: a nonlinear optimization approach. *Opt. Express* **16**, 7264–7278 (2008).
21. Thibault, P. *et al.* High-Resolution Scanning X-ray Diffraction Microscopy. *Science* **321**, 379–383 (2008).
22. Thibault, P. & Guizar-Sicairos, M. Maximum-likelihood refinement for coherent diffractive imaging. *New J. Phys.* **14**, 63004 (2012).
23. Guizar-Sicairos, M. *et al.* Role of the illumination spatial-frequency spectrum for ptychography. *Phys. Rev. B - Condens. Matter Mater. Phys.* **86**, 1–4 (2012).
24. Fowler KR, Gutiérrez-Velasco S, Martín-Castellanos C, Smith, G. R. Protein Determinants of Meiotic DNA Break Hotspots. *Mol Cell* **49**, 983–996 (2014).
25. Vogel, S. K., Pavin, N., Maghelli, N., Jülicher, F. & Tolić-Nørrelykke, I. M. Self-organization of dynein motors generates meiotic nuclear oscillations. *PLoS Biol.* **7**, 918–928 (2009).
26. Weisman, L. S. Organelles on the move : insights from. *Nat Rev Mol Cell Biol* **7**, 243–252 (2006).
27. Li, L., Ishdorj, G. & Gibson, S. B. Reactive oxygen species regulation of autophagy in cancer : Implications for cancer treatment. *Free Radic. Biol. Med.* **53**, 1399–1410 (2012).
28. Pyo, J. O. *et al.* Essential roles of Atg5 and FADD in autophagic cell death: Dissection of autophagic cell death into vacuole formation and cell death. *J. Biol. Chem.* **280**, 20722–20729 (2005).
29. Suzuki, K. & Ohsumi, Y. Molecular machinery of autophagosome formation in yeast, *Saccharomyces cerevisiae*. *FEBS Lett.* **581**, 2156–2161 (2007).
30. Tsukada, M. Isolation and characterization of autophagy-defective mutants of *Saccharomyces cerevisiae*. *FEBS Lett.* **333**, 169–174 (1993).
31. Mahmoud, B. S. M. The effects of X-ray radiation on *Escherichia coli* O157 : H7 , *Listeria monocytogenes* , *Salmonella enterica* and *Shigella flexneri* inoculated on whole Roma tomatoes q. *Food Microbiol.* **27**, 1057–1063 (2010).
32. Mizushima, N. Autophagy : process and function. *Genes Dev* **21**, 2861–2873 (2007).

33. Palumbo, S. & Comincini, S. Autophagy and ionizing radiation in tumors: The 'survive or not survive' dilemma. *J. Cell. Physiol.* **228**, 1–8 (2013).
34. Köster, S. & Pfohl, T. X-Ray Studies of Biological Matter in Microfluidic Environments. *Mod. Phys. Lett. B* **26**, 1230018 (2012).
35. Weinhausen, B. & Köster, S. Microfluidic devices for X-ray studies on hydrated cells. *Lab Chip* **13**, 212–215 (2012).
36. Henrich, B. *et al.* PILATUS: A single photon counting pixel detector for X-ray applications. *Nucl Instr Meth Phys Res* **607**, 247–249 (2009).
37. Thibault, P., Dierolf, M., Bunk, O., Menzel, A. & Pfeiffer, F. Probe retrieval in ptychographic coherent diffractive imaging. *Ultramicroscopy* **109**, 338–343 (2009).
38. Huang, X. *et al.* Optimization of overlap uniformness for ptychography. *Opt. Express* **22**, 12634–12644 (2014).
39. Wilke, R. N. *et al.* Hard X-ray imaging of bacterial cells : nano-diffraction and ptychographic reconstruction. **20**, 4795–4797 (2012).
40. Gullikson, E. [http://henke.lbl.gov/optical\\_constants/](http://henke.lbl.gov/optical_constants/).
41. Dierolf, M. *et al.* Ptychographic coherent diffractive imaging of weakly scattering specimens. *New J. Phys.* **12**, (2010).
42. Holler, M. *et al.* X-ray ptychographic computed tomography at 16 nm isotropic 3D resolution. 1–5 (2013). doi:10.1038/srep03857
43. Heel, M. Van & Schatz, M. Fourier shell correlation threshold criteria q. **151**, 250–262 (2005).
44. Vila-comamala, J. *et al.* Characterization of high-resolution diffractive X-ray optics by ptychographic coherent diffractive imaging. **19**, 175–184 (2011).

## 8 CONCLUSION

---

The imaging of flagella and pili under physiological conditions is challenging because of the small diameter of these cell appendices. We presented a method that allows the determination of the dynamics and forces of the flagellum and pili in *C. crescentus* under physiological conditions and without labelling. By attaching predivisional cells onto polystyrene beads, parallel imaging of the cells and force measurements could be performed. The impact of the flagellum was further characterized by microscopy of cells that were either attached to smaller polystyrene beads or to the surface of a microfluidic device. The dynamics of pili were further analyzed by microfluidic experiments with tightly controlled flow conditions. Furthermore, we assessed the interplay between pili and flagellum.

The flagellum of *C. crescentus* is active roughly 3 - 4 minutes before cell separation is completed. During the predivisional flagellum activity, two different stages were observed. First, the predivisional cells are strongly connected and the forces generated by the flagellum induce a motion on the mother and daughter cell together. In the next step, the connection between mother and daughter cell is weakened and the rotation of the flagellum forces the daughter cell to rotate around its long axis while still connected to the mother cell. The two different stages during the predivisional flagellar rotation can be linked to the progressing cell separation. The daughter cell can only rotate around its axis when the separation of the peptidoglycan is completed. Complete cell separation and release of the daughter cell occurs when the separation of the outer membrane is completed. The duration of clockwise and counterclockwise rotation sequences did not change during the transition from stiff cell connection to soft cell connection and is in good agreement with the durations found for free swimming cells<sup>64</sup>. We found that the rotation of the flagellum has an immediate onset, indicating that the flagellum is already fully assembled before the rotation of the flagellum starts. Still, it remains unclear what the start signal for flagellar rotation is. Here, further experiments could be performed in the future to dissect the molecular mechanisms responsible for the start of the flagellar rotation. The flagellum generates an average force of 1.0 pN when the cell is swimming in a straight sequence, but peak forces up to 1.5 pN can be achieved during the maximal displacement of the bead from the center of the optical tweezers.

We found that the pili of *C. crescentus* are active roughly one minute before cell separation is completed. The pili are dynamic, they can attach to surface, retract and release. The attachment duration and retraction speed are load dependent, a larger load decreases attachment duration

and retraction speed. The average force exerted by a pilus is around 2 pN, with maximal measured forces of about 8 pN. The release of the pilus is mediated by breakage or detachment of the pilus. Cells can undergo several cycles of attachment–retraction–release before cell separation. It is still unclear whether the same pilus can undergo several attachment cycles, or if a new pilus is employed for every attachment cycle. Several attachment cycles per pilus would strongly suggest a detachment behavior of the pilus rather than breakage.

When pili and flagellum are present in the predivisional cell, the attachment of a pilus stop the motion induced by the flagellum. Because of the relatively short average attachment duration of about 20 s for a single pilus attachment cycle, the flagellum is rotating freely and imposing its motion onto the cell most of the time. Naturally one could think of these two cell appendices to act as counter parts. The pili can be regarded as anchors, keeping the cell in one position, while the flagellum is a “propeller”, sending the cell into the unknown. However, our data suggest that the interactions between pili and flagellum are more complex. The presence of a rotating flagellum not only shortens the attachment duration of pili, but also shortens the time between single pilus attachment cycles. This leads to an increased attachment rate of individual pili and is most likely due to hydrodynamic interactions that bring the flagellated cell pole and therefore the pili closer to the surface. This effect can be observed in the natural set-up, where cells are attached to a solid surface. The flagellar rotation of the predivisional cell induces in some cases a bending of the predivisional cell, leading to a larger surface sampling area of the flagellum. This also increases the surface finding area of the pili and gives cells with the free cell pole not close enough to a surface the opportunity to attach, possibly leading to a permanent attachment of the daughter cell (Figure 8.1). It is also possible that the rotation of the flagellum induces a spreading of the pili, therefore further increasing the surface sampling area.

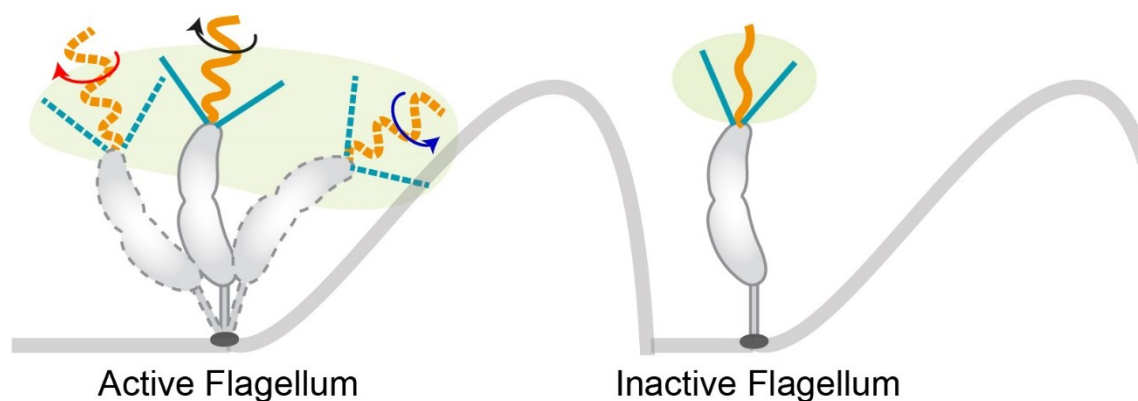


**Figure 8.1: Surface finding area of pili with (left) and without (right) an active flagellum in the predivisional stage.** The active flagellum bends the predivisional cell and allows the sampling a much larger area, therefore increasing the likelihood of pili attachment.

This effect could be especially useful in flow-free environments, where the cells tend to be aligned perpendicular to the surface. Because of this effect, it seems that the flagellum and pili are not counterparts, but cooperate. For a bacterial colony, it is a high risk to produce exclusively swarmer or fast-attaching cells. The cooperation of flagellum and pili could allow the colony a bet-hedging strategy. The colony is maximizing the survival chances of the daughter cells by dividing its offspring into cells that attach to the surface even before cell separation occurs and cells that swim away. The attached cells will strengthen the existing colony, while the swimming cells explore new areas and might start a new colony. The mechanism how a colony or individual cells would make the decision to stay or the leave is not yet clear. Additional experiments could be performed in microfluidic channels with varying amounts of nutrition. A higher amount of nutrition could lead to more active pili or longer attachment cycles of pili, leading to more permanently attached cells due to a more favorable environment. A scarce amount of nutrients could then lead to less active pili, the flagellum would be able to rotate freely most of the time and the cells would swim away after cell separation to find better environments. The fraction of cells that permanently attach or swim away depends not only on pili and flagellum activity, but also on holdfast formation. Holdfast formation is regulated in response to cell cycle and environmental cues, limiting surface attachment under unfavorable conditions, without influencing cell cycle progression<sup>133</sup>. With this, the fraction of cells that permanently attach might be delicately balanced.

The onset of the flagellar rotation before cell separation could also be advantageous for predivisional cells that are not attached to a solid surface. The rotation of the flagellum of the predivisional daughter cell gives the mother cell a window of motility of several minutes to swim into more favorable conditions. This window is re-occurring during every replication cycle. When the predivisional daughter cell attaches to the surface before cell separation, the mother cell is released upon cell separation and has a new change for a motility window in the next replication cycle.

## 9 REFERENCES

---

1. Raddadi, N., Cherif, A., Daffonchio, D., Neifar, M. & Fava, F. Biotechnological applications of extremophiles, extremozymes and extremolytes. *Appl. Microbiol. Biotechnol.* **99**, 7907–7913 (2015).
2. Sánchez-Cañizares, C., Jorrín, B., Poole, P. S. & Tkacz, A. Understanding the holobiont: the interdependence of plants and their microbiome. *Curr. Opin. Microbiol.* **38**, 188–196 (2017).
3. Kennedy, I. R. & Tchan, Y.-T. Biological nitrogen fixation in non-leguminous field crops: Recent advances. *Plant Soil* **141**, 93–118 (1992).
4. Fang, Y. & Ramasamy, R. P. Current and Prospective Methods for Plant Disease Detection. *Biosensors* **5**, 537–561 (2015).
5. Kurilshikov, A., Wijmenga, C., Fu, J. & Zhernakova, A. Host Genetics and Gut Microbiome: Challenges and Perspectives. *Trends Immunol.* **38**, 633–647 (2017).
6. Gill, S. R. Metagenomic analysis of the human distal gut microbiome. *Science* **312**, 1355–1359 (2006).
7. Romeo, Tony, (Ed.). *Bacterial Biofilms*. **322**, (Springer Science & Business Media, 2008).
8. Stewart, P. S. & William Costerton, J. Antibiotic resistance of bacteria in biofilms. *Lancet* **358**, 135–138 (2001).
9. Strelnikova, N. *et al.* Live cell X-ray imaging of autophagic vacuoles formation and chromatin dynamics in fission yeast. *Sci. Rep.* **7**, 13775 (2017).
10. Purcell, E. M. Life at Low Reynolds Number. *Am. J. Phys.* **45**, 3–11 (1977).
11. Purcell, E. M. The efficiency of propulsion by a rotating flagellum. *Proc. Nat. Acad. Sci.* **94**, 11307–11311 (1997).
12. Berg, H. C. & Anderson, R. A. Bacteria Swim by Rotating their Flagellar Filaments. *Nature* **245**, 380–382 (1973).
13. Ghosh, A. & Albers, S.-V. Assembly and function of the archaeal flagellum. *Biochem. Soc. Trans.* **39**, 64–69 (2011).
14. Henrici, A. T. & Johnson, D. E. Studies of Freshwater Bacteria. *J. Bacteriol.* **30**, 61–93 (1935).
15. Poindexter, J. S. The caulobacters: ubiquitous unusual bacteria. *Microbiol. Rev.* **45**, 123–179 (1981).
16. Margolin, W. Bacterial shape: Concave coiled coils curve Caulobacter. *Curr. Biol.* **14**, 242–244 (2004).
17. Ausmees, N., Kuhn, J. R. & Jacobs-Wagner, C. The bacterial cytoskeleton: An intermediate filament-like function in cell shape. *Cell* **115**, 705–713 (2003).
18. Charbon, G., Cabeen, M. T. & Jacobs-Wagner, C. Bacterial intermediate filaments: In vivo assembly, organization, and dynamics of crescentin. *Genes Dev.* **23**, 1131–1144 (2009).
19. Jin, S. K. & Sun, S. X. Morphology of Caulobacter crescentus and the mechanical role of

- crescentin. *Biophys. J.* **96**, L47–L49 (2009).
20. Stove, J. L. & Stanier, R. Y. Cellular Differentiation in Stalked Bacteria. *Nature* **196**, 1189–1192 (1962).
  21. Wortinger, M., Sackett, M. J. & Brun, Y. V. CtrA mediates a DNA replication checkpoint that prevents cell division in *Caulobacter crescentus*. *EMBO J.* **19**, 4503–4512 (2000).
  22. Li, G. *et al.* Surface contact stimulates the just-in-time deployment of bacterial adhesins. *Mol. Microbiol.* **83**, 41–51 (2012).
  23. Persat, A., Stone, H. A. & Gitai, Z. The curved shape of *caulobacter crescentus* enhances surface colonization in flow. *Nat. Commun.* **5**, 3824 (2014).
  24. Lino, T. Genetics of structure and function of bacterial flagella. *Annu. Rev. Genet.* **11**, 161–182 (1977).
  25. Manson, M. D., Tedesco, P., Berg, H. C., Harold, F. M. & Van der Drift, C. A protonmotive force drives bacterial flagella. *Proc. Natl. Acad. Sci.* **74**, 3060–3064 (1977).
  26. Larsen, S. H., Adler, J., Gargus, J. J. A. Y. & Hogg, R. W. Chemomechanical Coupling without ATP : The Source of Energy for Motility and Chemotaxis in Bacteria. *Proc. Nat. Acad. Sci.* **71**, 1239–1243 (1974).
  27. Shioi, J., Matsuura, S. & Imae, Y. Quantitative Measurements of Proton Motive Force and Motility in *Bacillus subtilis*. *J. Bacteriol.* **144**, 891–897 (1980).
  28. Blair, D. F. Flagellar movement driven by proton translocation. *FEBS Lett.* **545**, 86–95 (2003).
  29. Li, G. & Tang, J. X. Low flagellar motor torque and high swimming efficiency of *Caulobacter crescentus* swarmer cells. *Biophys. J.* **91**, 2726–2734 (2006).
  30. Hirota, N. & Imae, Y. Na<sup>+</sup>-driven Flagellar Motors of an Alkalophilic. *J. Biol. Chem.* **258**, 10577–10581 (1983).
  31. Koyasu, S. & Shirakihara, Y. *Caulobacter crescentus* flagellar filament has a right-handed helical form. *J. Mol. Biol.* **173**, 125–130 (1984).
  32. Samatey, F. A. *et al.* Structure of the bacterial flagellar protofilament and implications for a switch for supercoiling. *Nature* **410**, 331–337 (2001).
  33. Depamphilis, M. L. & Adler, J. Fine Structure and Isolation of the Hook-Basal Body Complex of Flagella from *Escherichia coli* and *Bacillus subtilis*. *J. Bacteriol.* **105**, 384–395 (1971).
  34. Xie, L., Altindal, T., Chattopadhyay, S. & Wu, X. Bacterial flagellum as a propeller and as a rudder for efficient chemotaxis. *Proc. Natl. Acad. Sci.* **108**, 2246–2251 (2010).
  35. Hug, I., Deshpande, S., Sprecher, K. S., Pfohl, T. & Jenal, U. Second messenger-mediated tactile response by a bacterial rotary motor. *Science* **358**, 531–534 (2017).
  36. O’Toole, G. a & Kolter, R. Flagellar and twitching motility are necessary for *Pseudomonas aeruginosa* biofilm development. *Mol Microbiol* **30**, 295–304 (1998).
  37. Giltner, C. L., Nguyen, Y. & Burrows, L. L. Type IV Pilin Proteins: Versatile Molecular Modules. *Microbiol. Mol. Biol. Rev.* **76**, 740–772 (2012).

38. Hospenthal, M. K., Costa, T. R. D. & Waksman, G. A comprehensive guide to pilus biogenesis in Gram-negative bacteria. *Nat. Rev. Microbiol.* **15**, 365–379 (2017).
39. Flores-Mireles, A. L., Walker, J. N., Caparon, M. & Hultgren, S. J. Urinary tract infections: Epidemiology, mechanisms of infection and treatment options. *Nat. Rev. Microbiol.* **13**, 269–284 (2015).
40. Persat, A., Inclan, Y. F., Engel, J. N., Stone, H. A. & Gitai, Z. Type IV pili mechanochemically regulate virulence factors in *Pseudomonas aeruginosa*. *Proc. Natl. Acad. Sci.* **112**, 7563–7568 (2015).
41. Merz, A. J., So, M. & Sheetz, M. P. Pilus retraction powers bacterial twitching motility. *Nature* **407**, 98–102 (2000).
42. Skerker, J. M. & Berg, H. C. Direct observation of extension and retraction of type IV pili. *Proc. Natl. Acad. Sci.* **98**, 6901–6904 (2001).
43. Chang, Y.-W. *et al.* Architecture of the type IVa pilus machine. *Science* **351**, aad2001 (2016).
44. McCallum, M., Tammam, S., Khan, A., Burrows, L. L. & Lynne Howell, P. The molecular mechanism of the type IVa pilus motors. *Nat. Commun.* **8**, 15091 (2017).
45. Berry, J. L. & Pelicic, V. Exceptionally widespread nanomachines composed of type IV pilins: The prokaryotic Swiss Army knives. *FEMS Microbiol. Rev.* **39**, 134–154 (2015).
46. Pelicic, V. Type IV pili: e pluribus unum? *Mol. Microbiol.* **68**, 827–837 (2008).
47. Tomich, M., Planet, P. J. & Figurski, D. H. The tad locus: postcards from the widespread colonization island. *Nat. Rev. Microbiol.* **5**, 363–375 (2007).
48. Kachlany, S. C. *et al.* flp-1, the first representative of a new pilin gene subfamily, is required for non-specific adherence of *Actinobacillus actinomycetemcomitans*. *Mol. Microbiol.* **40**, 542–554 (2001).
49. Nykyri, J. *et al.* Role and Regulation of the Flp/Tad Pilus in the Virulence of *Pectobacterium atrosepticum* SCRI1043 and *Pectobacterium wasabiae* SCC3193. *PLoS One* **8**, e73718 (2013).
50. Ellison, C. K. *et al.* Obstruction of pilus retraction stimulates bacterial surface sensing. *Science* **358**, 535–538 (2017).
51. Jiang, C., Brown, P. J. B., Ducret, A. & Brun, Y. V. Sequential evolution of bacterial morphology by co-option of a developmental regulator. *Nature* **506**, 489–493 (2014).
52. Ireland, M. M. E., Karty, J. A., Quardokus, E. M., Reilly, J. P. & Brun, Y. V. Proteomic analysis of the *Caulobacter crescentus* stalk indicates competence for nutrient uptake. *Mol. Microbiol.* **45**, 1029–1041 (2002).
53. Tsang, P. H., Li, G., Brun, Y. V., Freund, L. B. & Tang, J. X. Adhesion of single bacterial cells in the micronewton range. *Proc. Natl. Acad. Sci.* **103**, 5764–5768 (2006).
54. Li, G., Smith, C. S., Brun, Y. V. & Tang, J. X. The Elastic Properties of the *Caulobacter crescentus* Adhesive Holdfast Are Dependent on Oligomers of N-Acetylglucosamine. *J. Bacteriol.* **187**, 257–265 (2005).
55. Merker, R. I. & Smit, J. Characterization of the adhesive holdfast of marine and freshwater

- caulobacters. *Appl. Environ. Microbiol.* **54**, 2078–2085 (1988).
56. Berne, C. *et al.* Physicochemical Properties of Caulobacter crescentus Holdfast: A Localized Bacterial Adhesive. *J. Phys. Chem. B* **117**, 10492–10503 (2013).
  57. Wan, Z., Brown, P. J. B., Elliott, E. N. & Brun, Y. V. The adhesive and cohesive properties of a bacterial polysaccharide adhesin are modulated by a deacetylase. *Mol. Microbiol.* **88**, 486–500 (2013).
  58. Ong, C. J., Wong, M. L. Y. & Smit, J. Attachment of the adhesive holdfast organelle to the cellular stalk of Caulobacter crescentus. *J. Bacteriol.* **172**, 1448–1456 (1990).
  59. Turner, L., Ryu, W. S. & Berg, H. C. Real-time imaging of fluorescent flagellar filaments. *J. Bacteriol.* **182**, 2793–2801 (2000).
  60. Darnton, N. C., Turner, L., Rojevsky, S. & Berg, H. C. On torque and tumbling in swimming Escherichia coli. *J. Bacteriol.* **189**, 1756–1764 (2007).
  61. Berg, H. C. & Brown, D. A. Chemotaxis in Escherichia coli analysed by Three-dimensional Tracking. *Nature* **239**, 500–504 (1972).
  62. Tso, W.-W. & Adler, J. Negative chemotaxis in Escherichia coli. *J. Bacteriol.* **118**, 560–576 (1974).
  63. Lauga, E. & Powers, T. R. The hydrodynamics of swimming microorganisms. *Reports Prog. Phys.* **72**, 096601 (2009).
  64. Liu, B. *et al.* Helical motion of the cell body enhances Caulobacter crescentus motility. *Proc. Natl. Acad. Sci.* **111**, 11252–11256 (2014).
  65. Lele, P. P., Roland, T., Shrivastava, A., Chen, Y. & Berg, H. C. The flagellar motor of Caulobacter crescentus generates more torque when a cell swims backwards. *Nat. Phys.* **12**, 175–178 (2016).
  66. Chen, X. & Berg, H. C. Torque-Speed Relationship of the Flagellar Rotary Motor of Escherichia coli. *Biophys. J.* **78**, 1036–1041 (2000).
  67. Sowa, Y., Hotta, H., Homma, M. & Ishijima, A. Torque–speed Relationship of the Na<sup>+</sup>-driven Flagellar Motor of Vibrio alginolyticus. *J. Mol. Biol.* **327**, 1043–1051 (2003).
  68. Morse, M., Bell, J., Li, G. & Tang, J. X. Flagellar Motor Switching in Caulobacter Crescentus Obeys First Passage Time Statistics. *Phys. Rev. Lett.* **115**, 198103 (2015).
  69. Son, K., Guasto, J. S. & Stocker, R. Bacteria can exploit a flagellar buckling instability to change direction. *Nat. Phys.* **9**, 494–498 (2013).
  70. Taute, K. M., Gude, S., Tans, S. J. & Shimizu, T. S. High-throughput 3D tracking of bacteria on a standard phase contrast microscope. *Nat. Commun.* **6**, 8776 (2015).
  71. Morse, M., Colin, R., Wilson, L. G. & Tang, J. X. The Aerotactic Response of Caulobacter crescentus. *Biophys. J.* **110**, 2076–2084 (2016).
  72. Jenal, U., Reinders, A. & Lori, C. Cyclic di-GMP: Second messenger extraordinaire. *Nat. Rev. Microbiol.* **15**, 271–284 (2017).
  73. Egli, M. *et al.* Atomic-resolution structure of the cellulose synthase regulator cyclic diguanylic acid. *Proc. Natl. Acad. Sci.* **87**, 3235–3239 (1990).

74. Tal, R. *et al.* Three *cdg* operons control cellular turnover of cyclic di-GMP in *Acetobacter xylinum*: Genetic organization and occurrence of conserved domains in isoenzymes. *J. Bacteriol.* **180**, 4416–4425 (1998).
75. Romling, U., Galperin, M. Y. & Gomelsky, M. Cyclic di-GMP: the First 25 Years of a Universal Bacterial Second Messenger. *Microbiol. Mol. Biol. Rev.* **77**, 1–52 (2013).
76. Christen, M. *et al.* Asymmetrical Distribution of the Second Messenger c-di-GMP upon Bacterial Cell Division. *Science* **328**, 1295–1297 (2010).
77. Hengge, R. Principles of c-di-GMP signalling in bacteria. *Nat. Rev. Microbiol.* **7**, 263–273 (2009).
78. Abel, S. *et al.* Bi-modal distribution of the second messenger c-di-GMP controls cell fate and asymmetry during the caulobacter cell cycle. *PLoS Genet.* **9**, e1003744 (2013).
79. Albert, E. Über einen die Erzeugung und Verwandlung des Lichts betreffenden heuristischen Gesichtspunkt. *Ann. Phys.* **17**, 132–148 (1905).
80. Ashkin, A. Acceleration and trapping of particles by radiation pressure. *Phys. Rev. Lett.* **24**, 156–159 (1970).
81. Neuman, K. C. & Block, S. M. Optical trapping. *Rev. Sci. Instrum.* **75**, 2787–2809 (2004).
82. Ashkin, A. Forces of a single-beam gradient laser trap on a dielectric sphere in the ray optics regime. *Biophys. J.* **61**, 569–582 (1992).
83. Svoboda, K. & Block, S. M. Biological Applications of Optical Forces. *Annu. Rev. Biophys. Biomol. Struct.* **23**, 247–285 (1994).
84. Neuman, K. C., Chadd, E. H., Liou, G. F., Bergman, K. & Block, S. M. Characterization of photodamage to *Escherichia coli* in optical traps. *Biophys. J.* **77**, 2856–2863 (1999).
85. Grange, W., Husale, S., Güntherodt, H. J. & Hegner, M. Optical tweezers system measuring the change in light momentum flux. *Rev. Sci. Instrum.* **73**, 2308–2316 (2002).
86. Deshpande, S. & Pfohl, T. Real-time dynamics of emerging actin networks in cell-mimicking compartments. *PLoS One* **10**, e0116521 (2015).
87. Swank, Z., Deshpande, S. & Pfohl, T. Trapping, entrainment and synchronization of semiflexible polymers in narrow, asymmetric confinements. *Soft Matter* **12**, 87–92 (2016).
88. Eddington, D. T., Puccinelli, J. P. & Beebe, D. J. Thermal aging and reduced hydrophobic recovery of polydimethylsiloxane. *Sensors Actuators, B Chem.* **114**, 170–172 (2006).
89. Ely, B. Genetics of *Caulobacter crescentus*. in *Methods in enzymology* **204**, 372–384 (Academic Press, 1991).
90. Cabeen, M. T. *et al.* Bacterial cell curvature through mechanical control of cell growth. *EMBO J.* **28**, 1208–1219 (2009).
91. Briegel, A., Beeby, M., Thanbichler, M. & Jensen, G. J. Activated chemoreceptor arrays remain intact and hexagonally packed. *Mol. Microbiol.* **82**, 748–757 (2011).
92. Cordeli, F. Manual Tracking. *NIH* (2005).
93. Skerker, J. M. & Shapiro, L. Identification and cell cycle control of a novel pilus system in

- Caulobacter crescentus. *EMBO J.* **19**, 3223–3234 (2000).
94. Conrad, J. C. *et al.* Flagella and pili-mediated near-surface single-cell motility mechanisms in *P. aeruginosa*. *Biophys. J.* **100**, 1608–1616 (2011).
  95. Utada, A. S. *et al.* *Vibrio cholerae* use pili and flagella synergistically to effect motility switching and conditional surface attachment. *Nat. Commun.* **5**, 4913 (2014).
  96. McCarter, L., Hilmen, M. & Silverman, M. Flagellar dynamometer controls swarmer cell differentiation of *V. parahaemolyticus*. *Cell* **54**, 345–351 (1988).
  97. Berg, H. C. The Rotary Motor of Bacterial Flagella. *Annu. Rev. Biochem.* **72**, 19–54 (2003).
  98. Minamino, T. & Imada, K. The bacterial flagellar motor and its structural diversity. *Trends Microbiol.* **23**, 267–274 (2015).
  99. Leifson, E., Cosenza, B., Murchelano, R. & Cleverdon, R. Motile Marine Bacteria. *J. Bacteriol.* **87**, 652–666 (1964).
  100. Stocker, R. Reverse and flick: Hybrid locomotion in bacteria. *Proc. Natl. Acad. Sci.* **108**, 2635–2636 (2011).
  101. Drescher, K., Dunkel, J., Cisneros, L. H., Ganguly, S. & Goldstein, R. E. Fluid dynamics and noise in bacterial cell – cell and cell – surface scattering. *Proc. Natl. Acad. Sci.* **108**, 10940–10945 (2011).
  102. POINDEXTER, J. S. Biological Properties and Classification of the Caulobacter Group. *Bacteriol. Rev.* **28**, 231–295 (1964).
  103. Johnson, R. C. & Ely, B. Isolation of Spontaneously Derived Mutants of *Caulobacter Crescentus*. *Genetics* **86**, 25–32 (1977).
  104. Nesper, J. *et al.* Cyclic di-GMP differentially tunes a bacterial flagellar motor through a novel class of cheY-like regulators. *Elife* **6**, e28842 (2017).
  105. Welch, M., Oosawa, K., Aizawa, S. & Eisenbach, M. Phosphorylation-dependent binding of a signal molecule to the flagellar switch of bacteria. *Proc. Nat. Acad. Sci.* **90**, 8787–8791 (1993).
  106. Sarkar, M. K., Paul, K. & Blair, D. Chemotaxis signaling protein CheY binds to the rotor protein FliN to control the direction of flagellar rotation in *Escherichia coli*. *Proc. Natl. Acad. Sci.* **107**, 9370–9375 (2010).
  107. Hughes, K. T. & Berg, H. C. The bacterium has landed. *Science* **358**, 446–447 (2017).
  108. Quardokus, E. M., Din, N. & Brun, Y. V. Cell cycle and positional constraints on FtsZ localization and the initiation of cell division in *Caulobacter crescentus*. *Mol. Microbiol.* **39**, 949–959 (2001).
  109. Judd, E. M., Ryan, K. R., Moerner, W. E., Shapiro, L. & McAdams, H. H. Fluorescence bleaching reveals asymmetric compartment formation prior to cell division in *Caulobacter*. *Proc. Nat. Acad. Sci.* **100**, 8235–8240 (2003).
  110. Judd, E. M. *et al.* Distinct Constrictive Processes, Separated in Time and Space, Divide *Caulobacter* Inner and Outer Membranes. *J. Bacteriol.* **187**, 6874–6882 (2005).
  111. Craig, L., Pique, M. E. & Tainer, J. A. Type IV pilus structure and bacterial pathogenicity. *Nat. Rev. Microbiol.* **2**, 363–378 (2004).

112. Chang, Y. W. *et al.* Architecture of the *Vibrio cholerae* toxin-coregulated pilus machine revealed by electron cryotomography. *Nat. Microbiol.* **2**, 16269 (2017).
113. Gold, V. A. M., Salzer, R., Averhoff, B. & Kühlbrandt, W. Structure of a type IV pilus machinery in the open and closed state. *Elife* **4**, e07380 (2015).
114. Schilling, J. *et al.* Transcriptional activation of the tad type IVb pilus operon by PypB in *Yersinia enterocolitica*. *J. Bacteriol.* **192**, 3809–3821 (2010).
115. Wang, Y., Haitjema, C. H. & Fuqua, C. The Ctp type IVb pilus locus of *Agrobacterium tumefaciens* directs formation of the common pili and contributes to reversible surface attachment. *J. Bacteriol.* **196**, 2979–2988 (2014).
116. Bernier, S. P. *et al.* *Pseudomonas aeruginosa*-derived rhamnolipids and other detergents modulate colony morphotype and motility in the *Burkholderia cepacia* complex. *J. Bacteriol.* **199**, e00171-17 (2017).
117. Ng, D. *et al.* The *Vibrio cholerae* Minor Pilin TcpB Initiates Assembly and Retraction of the Toxin-Coregulated Pilus. *PLoS Pathog.* **12**, e1006109 (2016).
118. Viollier, P. H., Sternheim, N. & Shapiro, L. Identification of a localization factor for the polar positioning of bacterial structural and regulatory proteins. *Proc. Natl. Acad. Sci.* **99**, 13831–13836 (2002).
119. Marks, M. E. *et al.* The genetic basis of laboratory adaptation in *Caulobacter crescentus*. *J. Bacteriol.* **192**, 3678–3688 (2010).
120. Mignolet, J., Panis, G. L. & Viollier, P. H. More than a Tad: spatiotemporal control of *Caulobacter* pili This review comes from a themed issue on Cell regulation. *Curr. Opin. Microbiol.* **42**, 79–86 (2018).
121. Sprecher, K. S. *et al.* Cohesive Properties of the *Caulobacter crescentus* Holdfast Adhesin are Regulated by a Novel c-di-GMP Effector Protein. *MBio* **8**, e00294-17 (2017).
122. Craig, L. *et al.* Type IV Pilus Structure by Cryo-Electron Microscopy and Crystallography: Implications for Pilus Assembly and Functions. *Mol. Cell* **23**, 651–662 (2006).
123. Maier, B. & Wong, G. C. L. How Bacteria Use Type IV Pili Machinery on Surfaces. *Trends Microbiol.* **23**, 775–788 (2015).
124. Kolappan, S. *et al.* Structure of the *neisseria meningitidis* type IV pilus. *Nat. Commun.* **7**, 13015 (2016).
125. Biais, N., Higashi, D. L., Brujic, J., So, M. & Sheetz, M. P. Force-dependent polymorphism in type IV pili reveals hidden epitopes. *Proc. Natl. Acad. Sci.* **107**, 11358–11363 (2010).
126. Sauer, M. M. *et al.* Catch-bond mechanism of the bacterial adhesin FimH. *Nat. Commun.* **7**, 10738 (2016).
127. Shen, Y., Siryaporn, A., Lecuyer, S., Gitai, Z. & Stone, H. A. Flow directs surface-attached bacteria to twitch upstream. *Biophys. J.* **103**, 146–151 (2012).
128. Deshpande, S. & Pfohl, T. Hierarchical self-assembly of actin in micro-confinements using microfluidics. *Biomicrofluidics* **6**, 34120 (2012).
129. Göllner, M., Toma, A. C., Strelnikova, N., Deshpande, S. & Pfohl, T. A self-filling microfluidic device for noninvasive and time-resolved single red blood cell experiments.

*Biomicrofluidics* **10**, 054121 (2016).

130. Sliusarenko, O., Heinritz, J., Emonet, T. & Jacobs-Wagner, C. High-throughput, subpixel precision analysis of bacterial morphogenesis and intracellular spatio-temporal dynamics. *Mol. Microbiol.* **80**, 612–627 (2011).
131. Happel, J. & Brenner, H. *Low Reynolds number hydrodynamics: with special applications to particulate media*. (Springer Science & Business Media, 1983). doi:10.1007/978-94-009-8352-6
132. Berke, A. P., Turner, L., Berg, H. C. & Lauga, E. Hydrodynamic attraction of swimming microorganisms by surfaces. *Phys. Rev. Lett.* **101**, 038102 (2008).
133. Fiebig, A. *et al.* A Cell Cycle and Nutritional Checkpoint Controlling Bacterial Surface Adhesion. *PLoS Genet.* **10**, e1004101 (2014).

## 10 ACKNOWLEDGMENTS

---

Thomas P., thank you so much for all your good ideas, advices and discussions we had. I greatly appreciated your passion and curiosity about science. You supported me in every possible way to bring the project to a successful end.

I'm deeply grateful to Urs who provided me always with good advice, everything I needed to master the biological aspect of the project and gave me the opportunity to work in his lab.

I want to thank Thomas B. for being the Co-referee of my thesis.

Matteo, you are like a swiss army knife. Whatever I needed help with, you were there to help. You taught me everything about handling Caulos and I'm most thankful for your Matlab scripts, they made the analysis of my data so much easier and better. You were my partner in crime, always going back and forth between two groups, two buildings and two labs.

I thank Isabelle, Siddharth and Beni for starting the project. Isa, I am especially thankful for your insight into this project, your advices, the discussions and the good times we had during lunch.

I am also very thankful to my old lab members, Michael Ge. for so many things, especially for your advices and your help with the calibration of the optical tweezers, Raphael for being my desktop-neighbor and introducing me to the life in the group, Natalja for the time in Grenoble and at the PSI. Even though it was not successful the first time, it is unforgettable, and what a success it was the second time! Cora, Michael Gö., Axel, Zoe and Marzia for creating such a great workplace.

Furthermore I'd like to thank all members of the new lab, especially Antje, Alexander, Viktoriya, Shogo, Pablo, Benoit, Dominique, Enea and Isabella who granted me space in their office or lab.

I thank the SNI for founding this project, creating the SNI PhD-school and for organizing all the courses, conferences and retreats. The mechanical workshop in the physical chemistry for their friendly and very helpful support. Whatever the problem was, you came up with a solution! I thank everyone in the secretary and the media kitchen for their support. It's great to just come to work and not having to worry about organizational manners or producing media.

I want to thank Beat & Rosmarie for always supporting me and teaching me to follow my heart. I thank Dave, Myriam and Julian for the good company in life.

Christoph, you are the best thing that ever happened to me.

# 11 APPENDIX

---

## 11.1 MEDIA

### 11.1.1 PYE

For 1 l

Bacto Peptone:	2 g	(BD, Art. Nr. 211677)
Yeast Extract:	1 g	(Oxoid, Art. Nr. L21)
MgSO <sub>4</sub> 0.5 M:	1.6 ml	(MgSO <sub>4</sub> * 7 H <sub>2</sub> O, Merck, Art. Nr. 1.05886.0500)
Dest. H <sub>2</sub> O:	1 l	

The ingredients were dissolved in water, poured into smaller glass bottles and autoclaved. After autoclaving the bottles were stored at room temperature. Before use 0.5 mM CaCl<sub>2</sub> was added.

### 11.1.2 PYE Agar Plates

For 1 l

Bacto Peptone:	2 g	(BD, Art. Nr. 211677)
Yeast Extract:	1 g	(Oxoid, Art. Nr. L21)
Difco Agar:	15 g	(BD, Art. Nr. 214530)
MgSO <sub>4</sub> 0.5 M:	1.6 ml	(MgSO <sub>4</sub> * 7 H <sub>2</sub> O, Merck, Art. Nr. 1.05886.0500)
CaCl <sub>2</sub> 0.5 M:	1 ml	
Dest. H <sub>2</sub> O:	1 l	

The ingredients were dissolved in water and the media was autoclaved. After autoclaving the media was cooled to 56 °C, poured into the petri-dishes and let dry overnight before stored at 4 °C.

### 11.1.3 CaCl<sub>2</sub> 0.5 M

For 1 l

CaCl <sub>2</sub> :	73.5 g	(CaCl <sub>2</sub> * 2 H <sub>2</sub> O, Merck, Art. Nr. 1.02382)
Dest. H <sub>2</sub> O:	1 l	

The ingredient was dissolved in water, poured into smaller glass bottles and autoclaved. After autoclaving the bottles were stored at room temperature.

## 11.2 MATLAB SCRIPTS

### 11.2.1 MSD Determination (Credit: Michael A. Gerspach)

The MSD in  $x$ - and  $y$ -direction of the bead for different laser power was calculated with the  $x$ - and  $y$ -direction of the recorded trajectories with the following script:

```
%Michael Gerspach
%
%This code is for calculating the MSD in an oscillator or harmonic
%potential (The Langevin oscillator). Here, MSD should reach a plateau for
%big lagtimes.
%lim t->infin. MSD = lim t->infin. <x^2> = kB*T/(M*w0^2), were w0^2 = K/M
% --> trapp stiffness K = kB*T/<x^2>X
%
%MSD
%
function [MSD] = MSD_Scatter_v2_0(x0, y0, frametime, percent)

%tracks a list of tracks of of the particles containing:
%no frame, time, x-value (px), y-value (px), x-value (um), y-value (um)

% x0 = collum1: collum2:                collum3:  collum4:  collum5:
collum6:                                collum7:
%      frame  part. center in [px]    pos error  neg error  mean part.center in [px]
part. center mean corrected in [px]    part. center mean corrected in [nm]

% y0 = collum1: collum2:                collum3:  collum4:  collum5:
collum6:                                collum7:
%      frame  part. center in [px]    pos error  neg error  mean part.center in [px]
part. center mean corrected in [px]    part. center mean corrected in [nm]

%frametime = frametime in sec
%percent = percentage of MSD plot (how many timeintervals are used. This
%shoule be normally between 0.25 and 0.5.

size_x0 = size(x0);
MSD(1,:) = [0, 0, 0, 0, 0, 0, 0, 0, 0, 0, 0];
for m = 1:1:(size_x0(1,1)-1)*percent
%for m = 1:1:3
    MSDx_all = [];
    MSDy_all = [];
    MSDxy_all = [];
%display(m);
    for i = 1:1:size_x0(1,1)-m
        MSDx_all(i,1) = (x0(i,7)-x0(i+m,7))^2;
        MSDy_all(i,1) = (y0(i,7)-y0(i+m,7))^2;
        MSDxy_all(i,1) = (sqrt((x0(i+m,7)-x0(i,7))^2 + (y0(i+m,7)-y0(i,7))^2))^2;
%display(i);
    end
    %display(MSDx_all(:,1));

    MSDx = sum(MSDx_all)/size(MSDx_all,1);
    MSDx_stddev = std(MSDx_all);
    MSDx_stderr = MSDx_stddev/sqrt(size(MSDx_all,1));

    MSDy = sum(MSDy_all)/size(MSDy_all,1);
    MSDy_stddev = std(MSDy_all);
    MSDy_stderr = MSDy_stddev/sqrt(size(MSDy_all,1));

    MSDxy = sum(MSDxy_all)/size(MSDxy_all,1);
    MSDxy_stddev = std(MSDxy_all);
    MSDxy_stderr = MSDxy_stddev/sqrt(size(MSDxy_all,1));
```

```

        MSD(m+1,:) = [m*frametime, MSDx, MSDx_stddev, MSDx_stderr, MSDy, MSDy_stddev,
MSDy_stderr, MSDxy, MSDxy_stddev, MSDxy_stderr];

        %figure,
        %plot(MSD(:,1),MSD(:,2),'o',MSD(:,1),MSD(:,3),'o', MSD(:,1), MSD(:,4),'o');

    end
% Create figure
figure1 = figure;

% Create axes
axes1 = axes('Parent',figure1,'FontSize',20);
box(axes1,'on');
hold(axes1,'on');

% Create ylabel
ylabel('MSD [nm^2]','FontSize',20);

% Create xlabel
xlabel('time [s]','FontSize',20);

% Create multiple lines using matrix input to plot
plot(MSD(:,1),MSD(:,2),'Marker','.', 'LineStyle','none','Parent',axes1,'DisplayName','MSD
x');
plot(MSD(:,1),MSD(:,5),'Marker','.', 'LineStyle','none','Parent',axes1,'DisplayName','MSD
y');
plot(MSD(:,1),MSD(:,8),'Marker','.', 'LineStyle','none','Parent',axes1,'DisplayName','MSD
xy');

% Create legend
legend1 = legend(axes1,'show');
set(legend1,...
    'Position',[0.591518299867412 0.760830666278731 0.112459877664729
0.114052953156823],...
    'FontSize',18);

figure, plot(MSD(:,1),MSD(:,2),'-',MSD(:,1),MSD(:,5),'-',MSD(:,1),MSD(:,8),'-');

end

```

### 11.2.2 Calculation of Optical Tweezers Stiffness (Credit: Michael A. Gerspach)

The stiffness  $\kappa$  of the optical tweezers was calculated from the *MSD* in *x*- and *y*-direction for different laser power with the following script:

```
function [result] = createFitAndCalculateTrapStiffness(x, y)
%CREATEFIT(X,Y)
% Create a fit.
%
% Data for 'untitled fit 1' fit:
%   X Input : x
%   Y Output: y
% Output:
%   fitresult : a fit object representing the fit.
%   gof : structure with goodness-of fit info.
%
% See also FIT, CFIT, SFIT.

% Auto-generated by MATLAB on 08-Aug-2016 13:28:13

%% Fit: 'untitled fit 1'.
[xData, yData] = prepareCurveData( x, y );

% Set up fittype and options.
ft = fittype( '0*x+d', 'independent', 'x', 'dependent', 'y' );
excludedPoints = excludeddata( xData, yData, 'Indices', [1 2 3 4 5] );
opts = fitoptions( 'Method', 'NonlinearLeastSquares' );
opts.Display = 'Off';
opts.StartPoint = 0.421761282626275;
opts.Exclude = excludedPoints;

% Fit model to data.
[fitresult, gof] = fit( xData, yData, ft, opts );
val = coeffvalues(fitresult); %collecting coefficient values of fit
err = confint(fitresult); %collecting goodness of fit values

stiffness = (4 * 1.38064852 * 10^-23 * 293.2 * 10^9 * 10^12)/val;
stiffness_err = (4 * 1.38064852 * 10^-23 * 293.2 * 10^9 * 10^12)/err(2,1);
stiffness_std = (4 * 1.38064852 * 10^-23 * 293.2 * 10^9 * 10^12)/(val+std(y(6:end)));

result(1,:) = [val, val-err(1,1), std(y(6:end)), stiffness, stiffness-stiffness_err,
stiffness-stiffness_std];

% Plot fit with data.
figure( 'Name', 'untitled fit 1' );
h = plot( fitresult, xData, yData, excludedPoints );
legend( h, 'y vs. x', 'Excluded y vs. x', 'untitled fit 1', 'Location', 'NorthEast' );
% Label axes
xlabel x
ylabel y
grid on
```

## 11.2.3 Bead Tracking and Rotation Determination (Credit: Matteo Sangermani)

### 11.2.3.1 Fit Circle

To track the position of the bead a circle was fitted onto the bead for each frame. To fit the position and the size of the circle the following script was applied:

```
function [z, r, residual] = fit_circle(x, varargin)
%FITCIRCLE    least squares circle fit
%
% [Z, R] = FITCIRCLE(X) fits a circle to the N points in X minimising
% geometric error (sum of squared distances from the points to the fitted
% circle) using nonlinear least squares (Gauss Newton)
% Input
% X : 2xN array of N 2D points, with N >= 3
% Output
% Z : center of the fitted circle
% R : radius of the fitted circle
%
% [Z, R] = FITCIRCLE(X, 'linear') fits a circle using linear least
% squares minimising the algebraic error (residual from fitting system
% of the form ax^2 + b'x + c = 0)
%
% [Z, R] = FITCIRCLE(X, Property, Value, ...) allows parameters to be
% passed to the internal Gauss Newton method. Property names can be
% supplied as any unambiguous contraction of the property name and are
% case insensitive, e.g. FITCIRCLE(X, 't', 1e-4) is equivalent to
% FITCIRCLE(X, 'tol', 1e-4). Valid properties are:
%
% Property:                Value:
% -----
% maxits                    positive integer, default 100
%   Sets the maximum number of iterations of the Gauss Newton
%   method
%
% tol                       positive constant, default 1e-5
%   Gauss Newton converges when the relative change in the solution
%   is less than tol
%
% [X, R, RES] = fitcircle(...) returns the 2 norm of the residual from
% the least squares fit
%
% Example:
% x = [1 2 5 7 9 3; 7 6 8 7 5 7];
% % Get linear least squares fit
% [z1, r1] = fitcircle(x, 'linear')
% % Get true best fit
% [z, r] = fitcircle(x)
%
% Reference: "Least-squares fitting of circles and ellipses", W. Gander,
% G. Golub, R. Strebler - BIT Numerical Mathematics, 1994, Springer
%
% This implementation copyright Richard Brown, 2007, but is freely
% available to copy, use, or modify as long as this line is maintained
%
% nargchk is not recommended. Use narginchk instead.
% error(nargchk(1, 5, nargin, 'struct'))
narginchk(1,5)
%
% Default parameters for Gauss Newton minimisation
params.maxits = 100;
params.tol     = 1e-5;
%
% Check x and get user supplied parameters
[x, fNonlinear, params] = parseinputs(x, params, varargin{:});
%
% Convenience variables
m = size(x, 2);
x1 = x(1, :);
x2 = x(2, :);
```

```

% 1) Compute best fit w.r.t. algebraic error using linear least squares
%
% Circle is represented as a matrix quadratic form
%  $ax^2 + b^2x + c = 0$ 
% Linear least squares estimate found by minimising  $Bu = 0$  s.t.  $\text{norm}(u) = 1$ 
% where  $u = [a; b; c]$ 

% Form the coefficient matrix
B = [x1.^2 + x2.^2, x1, x2, ones(m, 1)];

% Least squares estimate is right singular vector corresp. to smallest
% singular value of B
[U, S, V] = svd(B);
u = V(:, 4);

% For clarity, set the quadratic form variables
a = u(1);
b = u(2:3);
c = u(4);

% Convert to centre/radius
z = -b / (2*a);
r = sqrt((norm(b)/(2*a))^2 - c/a);

% 2) Nonlinear refinement to minimise geometric error, and compute residual
if fNonlinear
    [z, r, residual] = fitcircle_geometric(x, z, r);
else
    residual = norm(B * u);
end

% END MAIN FUNCTION BODY -----

% NESTED FUNCTIONS
function [z, r, residual] = fitcircle_geometric(x, z0, r0)
    % Use a simple Gauss Newton method to minimize the geometric error
    fConverged = false;

    % Set initial u
    u = [z0; r0];

    % Delta is the norm of current step, scaled by the norm of u
    delta = inf;
    nIts = 0;

    for nIts = 1:params.maxits
        % Find the function and Jacobian
        [f, J] = sys(u);

        % Solve for the step and update u
        h = -J \ f;
        u = u + h;

        % Check for convergence
        delta = norm(h, inf) / norm(u, inf);
        if delta < params.tol
            fConverged = true;
            break
        end
    end

    if ~fConverged
        warning('fitcircle:FailureToConverge', ...
            'Gauss Newton iteration failed to converge');
    end
    z = u(1:2);
    r = u(3);
    f = sys(u);
    residual = norm(f);
end

```

```

function [f, J] = sys(u)
    %SYS Nonlinear system to be minimised - the objective
    %function is the distance to each point from the fitted circle
    %contained in u

    % Objective function
    f = (sqrt(sum(( repmat(u(1:2), 1, m) - x).^2) - u(3))');

    % Jacobian
    denom = sqrt( (u(1) - x1).^2 + (u(2) - x2).^2 );
    J = [(u(1) - x1) ./ denom, (u(2) - x2) ./ denom, repmat(-1, m, 1)];
end % sys

end % fitcircle_geometric

% END NESTED FUNCTIONS

end % fitcircle

function [x, fNonlinear, params] = parseinputs(x, params, varargin)
% Make sure x is 2xN where N > 3
if size(x, 2) == 2
    x = x';
end

if size(x, 1) ~= 2
    error('fitcircle:InvalidDimension', ...
        'Input matrix must be two dimensional')
end

if size(x, 2) < 3
    error('fitcircle:InsufficientPoints', ...
        'At least 3 points required to compute fit')
end

% determine whether we are measuring geometric error (nonlinear), or
% algebraic error (linear)
fNonlinear = true;
switch length(varargin)
    % No arguments means a nonlinear least squares with default parameters
    case 0
        return

    % One argument can only be 'linear', specifying linear least squares
    case 1
        if strcmpi(varargin{1}, 'linear', length(varargin{1}))
            fNonlinear = false;
            return
        else
            error('fitcircle:UnknownOption', 'Unknown Option')
        end

    % Otherwise we're left with user supplied parameters for Gauss Newton
    otherwise
        if rem(length(varargin), 2) ~= 0
            error('fitcircle:propertyValueNotPair', ...
                'Additional arguments must take the form of Property/Value pairs');
        end

        % Cell array of valid property names
        properties = {'maxits', 'tol'};

        while length(varargin) ~= 0
            property = varargin{1};

```

```

value    = varargin{2};

% If the property has been supplied in a shortened form, lengthen it
iProperty = find(strncmpi(property, properties, length(property)));
if isempty(iProperty)
    error('fitcircle:UnkownProperty', 'Unkown Property');
elseif length(iProperty) > 1
    error('fitcircle:AmbiguousProperty', ...
        'Supplied shortened property name is ambiguous');
end

% Expand property to its full name
property = properties{iProperty};

switch property
    case 'maxits'
        if value <= 0
            error('fitcircle:InvalidMaxits', ...
                'maxits must be an integer greater than 0')
        end
        params.maxits = value;
    case 'tol'
        if value <= 0
            error('fitcircle:InvalidTol', ...
                'tol must be a positive real number')
        end
        params.tol = value;
end
varargin(1:2) = [];
end

end

end

```

### 11.2.3.2 Prova Autofit

```

ml=[];
sd={};

for ff = 1 : 1 : 710
    dd = abs(255-(eDATA(ff,:)));
    %    idd = interp1([1:length(dd)],dd, [1:0.1:length(dd)]);

    ds = smooth(dd,9,'sgolay');

    [pks,locs] = findpeaks(ds,'MinPeakProminence',20, 'Annotate','extents');
    if ~isempty(locs)
        ml(ff) = max(locs);
    end
    sd{ff} = [pks,locs];

    pause(0.001)

end

figure
hold on;
for ii = 1 : length(sd)
    plot( sd{ii}(:,2), sd{ii}(:,1),'.b')
end

```

### 11.2.3.3 Movie Maker

```
% =====> MOVIE MAKER <=====

% Import detection file.txt, where all data for the movie is already present

% Reduce the output analysis if necessary to do movies of cropped time lapses:
% Frame = Frame([1: 10 : length(Disp)]) ;
% nX_1 = nX_1([1: 10 : length(Disp)]) ;
% X_1 = X_1([1: 10 : length(Disp)]) ;
% Y_1 = Y_1([1: 10 : length(Disp)]) ;
% nY_1 = nY_1([1: 10 : length(Disp)]) ;
% Radius_1 = Radius_1([1: 10 : length(Disp)]) ;
% Ori_Disp = Ori_Disp([1: 10 : length(Disp)]) ;

delimiters = {'_', '.'};
srcSTART = -1;           % start and end frame of the analysis
srcLAST = -1;
tot_dig = 0;           % total digits in .tif name after the last '_'
theta = 0:pi/60:2*pi;  % array of angle theta from 0 to 2*pi

AxesCol = [.2 .2 .2];
LabelCol = [.2 .2 .2];
TxtSize = 18;

% Access stack folder and index all the file inside that folder
[PathName, FoldName] = fileparts(uigetdir) ;
srcFiles = dir([PathName '/' FoldName]);

% RANGE OF ANALYSIS: find the range of the frames and user defined range
% Sort the names of all the files in the folder
cell_srcFiles = struct2cell(srcFiles);
[sort_name] = sort( cell_srcFiles(1,:) );
% The last in the list is the last frame. Take its number
file_Name = strsplit(sort_name{end} , delimiters);
% Create prefix name of image files, by joining strings up to the last '_' separation.
file_Prefix = strsplit(sort_name{end} , '_');
file_Prefix = file_Prefix(1:end-1);
file_Prefix = strjoin(file_Prefix , '_');

fr_num = file_Name{end-1};
tot_dig = length(fr_num);           % Count number of digits
srcLAST = str2num(fr_num);          % Assign last frame number
% Assign the first frame and its number: it can only be 1
srcSTART = 1;

Len = length(Ori_Disp);           % Length of movie and detectio
fps = 75 ;                        % frame rate of the movie acquisition
time = Frame./fps;                % time in fps
figure('Position', [100 300 1200 800]);

for ff = srcSTART : srcLAST
    % Define .tif filename and number
    N_digits = length(num2str(ff));
    N_zeros = repmat('0', [1, 5 - N_digits]);
    filesave_tif = ['G:\Jenal_Lab_Data\Lab Members Data\Matteo\Movie_170621_01 -
version_2 - 75 fps\Mv_' N_zeros num2str(ff) '.tif'];

    IMGname = [file_Prefix '_' N_zeros num2str(ff+(srcSTART-1)) '.tif'];
    IMG = (imread([PathName '/' FoldName '/' IMGname]));

% ---> show the BF frame and detection <-----
clf(1);
subplot(5,1, [1 2 3]);          axis equal;          hold on;
% imshow(imadjust(imread(filename)))
imshow(IMG, [min(min(IMG)), max(max(IMG))] , 'InitialMagnification',100) ;
% calc the bead detection circle coordinates and plot it
xs = Radius_1(ff) * cos(theta) + X_1(ff);
ys = Radius_1(ff) * sin(theta) + Y_1(ff);
plot(xs, ys, '-', 'Color', [0.4 0.75 1], 'LineWidth', 2);
```

```

% % % % % % % calc "SEARCH" circles coordinates and plot them
% % % % % % % xs = (Radius_1(ff)*0.8) * cos(theta) + X_1(ff);
% % % % % % % ys = (Radius_1(ff)*0.8) * sin(theta) + Y_1(ff);
% % % % % % % plot(xs, ys, '--y', 'LineWidth', 1.25);
% % % % % % % xs = (Radius_1(ff)*1.2) * cos(theta) + X_1(ff);
% % % % % % % ys = (Radius_1(ff)*1.2) * sin(theta) + Y_1(ff);
% % % % % % % plot(xs, ys, '--y', 'LineWidth', 1.25);

% plot line of displacement from OT-center to Bead-center
plot( [X_1(ff) X_1(2)], [Y_1(ff) Y_1(2)], '-.', 'Color', [.7 .1 .0], ...
      'LineWidth', 1.5, 'MarkerSize', 10);

% ----> show displacement <-----
subplot(5,1, [4 5 ]); hold on;
tw = [srcSTART : ff] ;
pxum = 15.14;
plot( tw, -nX_1(srcSTART : ff) ./pxum, ':', 'Color', [.0 .7 .0], 'LineWidth', 1.5 );
plot( tw, -nY_1(srcSTART : ff) ./pxum, ':', 'Color', [.0 .6 .9], 'LineWidth', 1.5 );
plot( tw, Ori_Disp(srcSTART : ff) ./pxum, 'Color', [.7 .1 .0], 'LineWidth', 2.2 );
% plot baseline at zero
plot([0,Len],[0,0], '--', 'Color',[.5 .5 .5], 'LineWidth', 0.5);

ax = gca;
ax.FontSize = TxtSize; ax.Box = 'on';
ax.XColor = AxesCol; ax.YColor = AxesCol;
ax.TickDir = 'out'; ax.LineWidth = 2;

xlabel('time [s]', 'Color',LabelCol, 'FontSize', TxtSize);
ylabel('\Delta disp [\mum]', 'Color',LabelCol, 'FontSize', TxtSize);

ax.YLim = [-0.5 2];
ax.YTick = [-0.5 : 0.5 : 2];
ax.YTickLabels = [-0.5 : 0.5 : 2];

% Choose XLIM so that it moves with the movie
if ff - srcSTART <= 50
    ax.XLim = [0 , 80];
elseif srcLAST - ff <= 30
    ax.XLim = [srcLAST-80 , srcLAST];
else
    ax.XLim = [ff-50 , ff+30]
end
ax.XTick = [0: 37.5 : Frame(end)];
ax.XTickLabels = [0: 37.5 : Frame(end)]./fps;

% For last frame, show all displacement graph
if ff == srcLAST
    ax.XLim = [0 , srcLAST]
    ax.XTick = [0: 22.5*10 : Frame(end)];
    ax.XTickLabels = [0: 22.5*10 : Frame(end)]./fps;
end

set(gcf, 'Color', [1,1,1]);

saveas(gcf, filesave_tif )
pause(0.0001)
end

% =====

```

### 11.2.3.4 Main Bead Tracker

```

function MAIN_BeadTracker(app)
%-----
% BEAD TRACKER main function
%-----

```

```

% The function is created to track a single bead in a timelapse movie.
% The script use multilevel image thresholds to find the biggest object
% in the frame and then fit its perimeter to a circle.
% There is the option to use a pseudo-Gaussian method, where we delimit two
% rings that encompass the bright diffraction ring of the bead and then find
% the highest pixel value in that ring circumference. Those are then used
% to fit in a circle.
% The function, accordin to proper choises, display the analysis fitting
% and masks created.
%
%
% ... PARAMETERS .....
% OPT.T_levels      perform threshold with N threshold levels
% OPT.f1            decrease bead "Dark" circle of F%
% OPT.f2            increase bead "Dark" circle of F%
% [ those are then used to create two circles and delimit the area where to
%   search for the bright diffraction ring ]
% OPT.Range         frame range in which to perform the analysis
% OPT.Exp_name      name of the experiment to assign at the .txt output file
%
%
% ... other INPUTs .....
% OPT.Disp_Masks
% OPT.Disp_Bea
% OPT.Disp_Dark_C
% OPT.Disp_Light_C
% OPT.Disp_Search_C
% OPT.Method_2
%
%
%-----
clc;      clearvars -except OPT app;

global OPT;

delimiters = {'_', '.'};
srcSTART = -1;          % start and end frame of the analysis
srcLAST = -1;
tot_dig = 0;           % total digits in .tif name after the last '_'
theta = 0:pi/60:2*pi; % array of angle theta from 0 to 2*pi
rr = 1;                % row counter of .txt file

% Access stack folder and index all the file inside that folder
% [PathName, FoldName] = fileparts(uigetdir) ;
% OPT.path = PathName ;
% OPT.fold = FoldName ;
srcFiles = dir([OPT.path '/' OPT.fold]);

% Determine name of output file and initialize the first row
if isempty(OPT.Exp_name)
    filename_txt = [ OPT.path '/Track_' OPT.fold '.txt'];
else
    filename_txt = [ OPT.path '/Track_' OPT.Exp_name '.txt'];
end
file_C = fopen(filename_txt, 'w+');
if OPT.Method_2 == 1
    fprintf( file_C, 'Frame \tX_1 \tY_1 \tnX_1 \tnY_1 \tDisp \tOri_Disp \tRadius_1 \t');
    fprintf( file_C, '\tX_2 \tY_2 \tnX_2 \tnY_2 \tDisp \tOri_Disp \tRadius_2 \n'
);
else
    fprintf( file_C, 'Frame \tX_1 \tY_1 \tnX_1 \tnY_1 \tDisp \tOri_Disp \tRadius_1 \n'
);
end

% RANGE OF ANALYSIS: find the range of the frames and user defined range
% Sort the names of all the files in the folder
cell_srcFiles = struct2cell(srcFiles);
srcFiles_2 = srcFiles(~[cell_srcFiles{5,:}]);

[sort_name] = sort( cell_srcFiles(1,:) );

```

```

% The last in the list is the last frame. Take its number
file_Name = strsplit(sort_name{end} , delimiters);
% Create prefix name of image files, by joining strings up to the last '_' separation.
file_Prefix = strsplit(sort_name{end} , '_');
file_Prefix = file_Prefix(1:end-1);
file_Prefix = strjoin(file_Prefix , '_');

fr_num = file_Name{end-1};
tot_dig = length(fr_num);          % Count number of digits
srcLAST = str2num(fr_num);        % Assign last frame number
% Assign the first frame and its number: it can only be 1
srcSTART = 1;

if ~strcmp( OPT.Range , 'S:E')
    RR = strsplit(OPT.Range,{' ':'});
    if str2num(RR{1}) > str2num(RR{2}) || length(RR) ~= 2 || ...
isstring(str2num(RR{1})) || isstring(str2num(RR{2}))
        app.TextOut.Value = sprintf('%s', ['Invalid Range!!!']);
        OPT.ERROR = 1;
        return
    end
    if str2num(RR{2}) > srcLAST || str2num(RR{2}) < srcSTART
        app.TextOut.Value = sprintf('%s', ['Range exceed limits !!!']);
        OPT.ERROR = 1;
        return
    end
    srcSTART = str2num(RR{1});
    srcLAST = str2num(RR{2});
end

%+++++
% ANALYSIS -----
for ff = srcSTART : srcLAST

    if OPT.STOP == 1;
        OPT.STOP = 1;
        return
    end

    % Reset the variables
    idx_XY_1 = [];    peri_XY_1 = [];
    idx_XY_2 = [];    peri_XY_2 = [];

    N_dig = length(num2str(ff));
    N_null = repmat('0', [1, tot_dig - N_dig]);

    IMGname = [file_Prefix '_' N_null num2str(ff+(srcSTART-1)) '.tif'];
    IMG = (imread([OPT.path '/' OPT.fold '/' IMGname]));

% ----> FIRST THRES: dark inner core <-----
% Find the multilevel image thresholds using Otsu's method
thrs_1 = multithresh(IMG, OPT.T_levels) ;

% Quantize image using specified quantization levels and output values
seg_IMG_1 = imquantize(IMG, thrs_1);

% Create a mask of all detected objects with the given OPT.T_levels threshold
Mask_1 = seg_IMG_1 ;
Mask_1( seg_IMG_1 ~= 1) = 0 ;

% Find connected components in the Bead_Mask
Mask_1 = imfill(Mask_1, 'holes');
temp = bwconncomp(Mask_1, 4);

% Find the largest component in the mask, it should be the bead, and save
% linear coordintes (idx_LIN) and as xy-coord (idx_XY).
% Then create a mask of the bead (Mask_Bd_1)
Len_idx_1 = cellfun(@length, temp.PixelIdxList);
idx_LIN_1 = temp.PixelIdxList{ find(Len_idx_1 == max(Len_idx_1)) };
[idx_XY_1(:,2), idx_XY_1(:,1)] = ind2sub(temp.ImageSize, idx_LIN_1);
Mask_Bd_1 = zeros(temp.ImageSize);
Mask_Bd_1(idx_LIN_1) = 1;

```

```

% Find the Perimeter of the bead and its coordinates
Mask_Bd_Peri_1 = bwperim(Mask_Bd_1);
[peri_XY_1(:,2), peri_XY_1(:,1)] = ind2sub(temp.ImageSize, find(Mask_Bd_Peri_1 ==
1)) ;

% Fit the bead's perimeter coordinate into a circle function and find center.
[cntr, Fit_R_1(ff) ] = fit_circle(peri_XY_1, 'linear');
Fit_C_1(ff,:) = cntr';

% ----> SECOND THRES: light outer ring <-----
if OPT.Method_2 == 1
% Define the outer and inner search circle that enclose the light diffraction
% pattern of the bead
x_sIn = OPT.f1 *Fit_R_1(ff) * cos(theta) + Fit_C_1(ff,1);
y_sIn = OPT.f1 *Fit_R_1(ff) * sin(theta) + Fit_C_1(ff,2);
x_sOut = OPT.f2 *Fit_R_1(ff) * cos(theta) + Fit_C_1(ff,1);
y_sOut = OPT.f2 *Fit_R_1(ff) * sin(theta) + Fit_C_1(ff,2);

% Create radial profile lines between the two search circles. Save the
% variables G (Px values), and line coordinates (Gx and Gy)
G = {}; Gx = {}; Gy = {}; Cxy = [];
for jj = 1 : length(x_sIn)
[Gx{jj},Gy{jj}, G{jj}] = improfile(IMG, [x_sIn(jj); x_sOut(jj)], [y_sIn(jj);
y_sOut(jj)]);
end

% Go through each line profile and search max (peak) value and store
% its coordinates in Cxy
for jj = 1 : length(x_sIn)
Px_peak = find( G{jj} == max(G{jj})) ;
if length(Px_peak) == 1
Cxy(jj,1) = Gx{jj}(Px_peak) ;
Cxy(jj,2) = Gy{jj}(Px_peak) ;
% if there are >2 equal values, then take the mean for the coordinates
elseif length(Px_peak) > 1
Cxy(jj,1) = mean(Gx{jj}(Px_peak)) ;
Cxy(jj,2) = mean(Gy{jj}(Px_peak)) ;
end
end

% Fit the Cxy coordinate into a circle function and find circle center.
[cntr, Fit_R_2(ff) ] = fit_circle(Cxy, 'linear');
Fit_C_2(ff,:) = cntr';
end

% ----> DISPLAY ANALYSIS <-----
if OPT.Disp_Masks == 1
if OPT.Disp_Bead == 1
col = 3
else
col = 2;
end
fig1 = figure(1);
% fig1.Position(1:2) = [50 500];
hold on;
% subplot(1,col,1);
imshow(seg_IMG_1,[1,OPT.T_levels+1]) ;
% title('Raw "Quanta" detection');
% subplot(1,col,2); imshow(Mask_Bd_1);
% title('Bead and Perimeter');
%
%
if OPT.Disp_Bead == 1
subplot(1,col,3); imshow(IMG); hold on;
title('Bright Field and circle Fitting');
% Plot the search ring
if OPT.Disp_Search_C == 1 && OPT.Method_2 == 1
plot( x_sIn, y_sIn, '--y');
plot(x_sOut, y_sOut, '--y');
end
end

```

```

% Define and draw the fitted circles
if OPT.Disp_Dark_C == 1
    xs_1 = Fit_R_1(ff) * cos(theta) + Fit_C_1(ff,1);
    ys_1 = Fit_R_1(ff) * sin(theta) + Fit_C_1(ff,2);
    plot(xs_1, ys_1, '-', 'Color', [0.4 0.75 1], 'LineWidth', 1.5);
    plot(Fit_C_1(ff,1), Fit_C_1(ff,2), '.', 'Color', [0.4 0.75 1],
'MarkerSize', 15);
end

if OPT.Disp_Light_C == 1 && OPT.Method_2 == 1
    xs_2 = Fit_R_2(ff) * cos(theta) + Fit_C_2(ff,1);
    ys_2 = Fit_R_2(ff) * sin(theta) + Fit_C_2(ff,2);
    plot(xs_2, ys_2, '-r', 'LineWidth', 1.5);
    plot(Fit_C_2(ff,1), Fit_C_2(ff,2), '.r', 'MarkerSize', 15);
end
end

if OPT.Disp_Bead == 1 && OPT.Disp_Masks == 0
    fig2 = figure(2);
    fig2.Position(1:2) = [50 100];

    imshow(IMG); hold on;
    title('Bright Field and circle Fitting');
    % Plot the search ring
    if OPT.Disp_Search_C == 1 && OPT.Method_2 == 1
        plot(x_sIn, y_sIn, '--y');
        plot(x_sOut, y_sOut, '--y');
    end

    % Define and draw the fitted circles
    if OPT.Disp_Dark_C == 1
        xs_1 = Fit_R_1(ff) * cos(theta) + Fit_C_1(ff,1);
        ys_1 = Fit_R_1(ff) * sin(theta) + Fit_C_1(ff,2);
        plot(xs_1, ys_1, '-', 'Color', [0.4 0.75 1], 'LineWidth', 1.5);
        plot(Fit_C_1(ff,1), Fit_C_1(ff,2), '.', 'Color', [0.4 0.75 1], 'MarkerSize',
15);
    end

    if OPT.Disp_Light_C == 1 && OPT.Method_2 == 1
        xs_2 = Fit_R_2(ff) * cos(theta) + Fit_C_2(ff,1);
        ys_2 = Fit_R_2(ff) * sin(theta) + Fit_C_2(ff,2);
        plot(xs_2, ys_2, '-r', 'LineWidth', 1.5);
        plot(Fit_C_2(ff,1), Fit_C_2(ff,2), '.r', 'MarkerSize', 15);
    end
end

% ----> SAVE DATA in txt file <-----
Mat(rr,1) = ff; % Frame number
% XY coord and R^2, raw and normalized
Mat(rr,2) = Fit_C_1(ff,1); Mat(rr,3) = Fit_C_1(ff,2);
if ff ~= srcSTART
    Mat(rr,4) = Fit_C_1(ff,1)-Fit_C_1(1,1); Mat(rr,5) = Fit_C_1(ff,2)-
Fit_C_1(1,2);
    Mat(rr,6) = sqrt((Fit_C_1(ff,1) -Fit_C_1(ff-1,1))^2 + (Fit_C_1(ff,2) -
Fit_C_1(ff-1,2))^2);
    Mat(rr,7) = sqrt((Fit_C_1(ff,1) -Fit_C_1(1,1))^2 + (Fit_C_1(ff,2) -
Fit_C_1(1,2))^2);
elseif ff == srcSTART
    Mat(rr,4) = 0; Mat(rr,5) = 0;
    Mat(rr,6) = 0;
    Mat(rr,7) = 0;
end
Mat(rr,8) = Fit_R_1(ff) ;

if OPT.Method_2 == 1
    Mat(rr,10) = Fit_C_2(ff,1); Mat(rr,11) = Fit_C_2(ff,2);
    if ff ~= srcSTART
        Mat(rr,12) = Fit_C_2(ff,1)-Fit_C_2(1,1); Mat(rr,13) = Fit_C_2(ff,2)-
Fit_C_2(1,2);
        Mat(rr,14) = sqrt((Fit_C_2(ff,1) -Fit_C_2(ff-1,1))^2 + (Fit_C_2(ff,2) -
Fit_C_2(ff-1,2))^2);
    end
end

```

```

        Mat(rr,15) = sqrt((Fit_C_2(ff,1) -Fit_C_2(1,1))^2 + (Fit_C_2(ff,2) -
Fit_C_2(1,2))^2);
        elseif ff == srcSTART
            Mat(rr,12) = 0;           Mat(rr,13) = 0;
            Mat(rr,14) = 0 ;
            Mat(rr,15) = 0 ;
        end
        Mat(rr,16) = Fit_R_2(ff) ;
    end
    % Write in the .txt file and show status of analysis
    fprintf( file_C , '%f\t', Mat(rr,:) );
    fprintf( file_C , '\n');

    pause(0.001);
    app.TextOut.Value = sprintf('%s', ['Frame ' num2str(rr) ' of ' num2str(srcLAST-
srcSTART+1)] );
    rr = rr +1;

end

% ----> DISPLAY PREVIEW ANALYSIS <-----
if OPT.PreviewPlot == 1
    Preview_Plot(Mat)
end

fclose(file_C) ;

end

% =====
function Preview_Plot(Mat_Dat)
    global OPT;
    hnd.figure1 = figure(3);
    clf(3);
    hnd.figure1.Position = [400 50 1400 350];

    subplot(2,1,1);           hold on;
                                plot(Mat_Dat(:,1), Mat_Dat(:,6), 'Color', [0.4 0.75 1]);
    if OPT.Method_2 == 1;     plot(Mat_Dat(:,1), Mat_Dat(:,14));           end
    hnd.axes = gca;
    hnd.axes.XLim = [min(Mat_Dat(:,1)), max(Mat_Dat(:,1))];
    hnd.axes.TickDir = 'out';
    hnd.axes.XColor = [.3 .3 .3];           hnd.axes.YColor = [.3 .3 .3];
    ylabel('Displacement R^2');

    subplot(2,1,2);           hold on;
                                plot(Mat_Dat(:,1), Mat_Dat(:,8), 'Color', [0.4 0.75 1]);
    if OPT.Method_2 == 1;     plot(Mat_Dat(:,1), Mat_Dat(:,16));           end

    hnd.axes = gca;
    hnd.axes.XLim = [min(Mat_Dat(:,1)), max(Mat_Dat(:,1))];
    hnd.axes.TickDir = 'out';
    hnd.axes.XColor = [.3 .3 .3];           hnd.axes.YColor = [.3 .3 .3];
    ylabel('Radius');
end

```

### 11.2.3.5 Main Rotation

```

function MAIN_BeadTracker(app)
%-----
% ROTATION main function
%-----
% Describe an ellipse/circle object around the bead. Then the algorithm
% will take the values for all the pixels that describe the ellipse and
% save them in a linear array. This process is done for all frames and save

```

```

% as e_DATA.txt
% The algorithm also does the same for the "vertices" describing the ellipse
% resulting in a more condensed data (saved as v_DATA.txt)
%-----

clc;      clearvars -except OPT app;

global OPT;

delimiters = {'_', '.'};
srcSTART = -1;      % start and end frame of the analysis
srcLAST = -1;
tot_dig = 0;      % total digits in .tif name after the last '_'

% Access stack folder and index all the file inside that folder
% [PathName, FoldName] = fileparts(uigetdir) ;
% OPT.path = PathName ;
% OPT.fold = FoldName ;
srcFiles = dir([OPT.path '/' OPT.fold]);

% RANGE OF ANALYSIS: find the range of the frames and user defined range
% Sort the names of all the files in the folder
cell_srcFiles = struct2cell(srcFiles);

[sort_name] = sort( cell_srcFiles(1,:) );
% The last in the list is the last frame. Take its number
file_Name = strsplit(sort_name{end}, delimiters);
% Create prefix name of image files, by joining strings up to the last '_' separation.
file_Prefix = strsplit(sort_name{end}, '_');
file_Prefix = file_Prefix(1:end-1);
file_Prefix = strjoin(file_Prefix, '_');

fr_num = file_Name{end-1};
tot_dig = length(fr_num);      % Count number of digits
srcLAST = str2num(fr_num);      % Assign last frame number
% Assign the first frame and its number: it can only be 1
srcSTART = 1;

if ~strcmp( OPT.Range, 'S:E')
    RR = strsplit(OPT.Range, ':');
    if str2num(RR{1}) > str2num(RR{2}) || length(RR) ~= 2 || ...
        isstring(str2num(RR{1})) || isstring(str2num(RR{2}))
        app.TextOut.Value = sprintf('%s', ['Invalid Range!!!']);
        OPT.ERROR = 1;
        return
    end
    if str2num(RR{2}) > srcLAST || str2num(RR{2}) < srcSTART
        app.TextOut.Value = sprintf('%s', ['Range exceed limits !!!']);
        OPT.ERROR = 1;
        return
    end
    srcSTART = str2num(RR{1});
    srcLAST = str2num(RR{2});
end

%::::::::::::::::::::::::::::::::::::::::::::::::::::::::::::::::::::::::::::::::::
%::::::::::::::::::::::::::::
% FIRST FRAME : analysed independently
%::::::::::::::::::::::::::::::::::::::::::::::::::::::::::::::::::::::::::::::::::

N_null = repmat('0', [1, tot_dig - length(num2str(srcSTART)) ]);
IMGname = [file_Prefix '_' N_null num2str(srcSTART) '.tif'];
firstIMG = [ OPT.path '/' OPT.fold '/' IMGname ] ;
im_A = imread(firstIMG);

% Select manually the OBJ to use as reference:
% -----
% Place an ellipse object in first frame of movie. Then create a mask of
% the ellipse perimeter.
fg2 = figure(2); clf(2);

```

```

imshow(im_A) ;
hnd = imellipse ; % draw ellipse
vert = wait(hnd) ; % allow resize, and wait untill doubleclick to
continue
row = round(vert(:,2));
col = round(vert(:,1));

% Find the 1+8-neighborings pixels of the vertexes:
Row_9 = [ row row-1, row-1, row-1, row ,...
          row, row+1, row+1, row+1, ];
Col_9 = [ col col-1, col, col, col-1 ,...
          col+1, col-1, col, col+1 ];

% create the binary perimeted mask of the ellipse
Mask_elip = bwperim(createMask(hnd));
% Extract the pixel coordinates subscripts and indexes
% bwboundaries --> start from one pixel and goes from one to the next
% neighbour describing a circle of the perimeter.If we
% plot in microbeTracker we then have circular line.
% NB : the coordinates are given as [Y,X], opposite order than usual
stats = bwboundaries(Mask_elip,'noholes');
e_sub(:,1) = stats{1}(:,2) ;
e_sub(:,2) = stats{1}(:,1) ;
e_ind = sub2ind(size(Mask_elip), e_sub(:,2), e_sub(:,1)) ;

%+++++
% ALL FRAMES
%+++++
jj=1; % counter for saving data
for ff = srcSTART+1 : srcLAST-1

    N_dig = length(num2str(ff));
    N_null = repmat('0', [1, tot_dig - N_dig]);

    IMGname = [file_Prefix '_' N_null num2str(ff+(srcSTART-1)) '.tif'];
    im_A = (imread([OPT.path '/' OPT.fold '/' IMGname]));

    % -----
    eDATA(ff,:) = im_A(e_ind)';

    % Save value of the mean of the 1+8-neighboring pixels
    vDATA(ff,:) = mean(im_A( sub2ind(size(im_A), Row_9, Col_9) ), 2);

    jj = jj+1 ;
    app.TextOut.Value = sprintf('%s', ['Fr: ' num2str(ff) ' of ' num2str(srcLAST-
srcSTART+1)] );
end

% Save results in .txt files
dlmwrite( [OPT.path '/e_DATA.txt'] , eDATA, 'delimiter', '\t')
dlmwrite( [OPT.path '/v_DATA.txt'] , vDATA, 'delimiter', '\t')

```

